

Electromagnetic Modeling and Control Aspects of a Reaction Sphere for Satellite Attitude Control

THÈSE N° 6311 (2014)

PRÉSENTÉE LE 14 AOÛT 2014

À LA FACULTÉ DES SCIENCES ET TECHNIQUES DE L'INGÉNIEUR
LABORATOIRE D'ACTIONNEURS INTÉGRÉS
PROGRAMME DOCTORAL EN SYSTÈMES DE PRODUCTION ET ROBOTIQUE

ÉCOLE POLYTECHNIQUE FÉDÉRALE DE LAUSANNE

POUR L'OBTENTION DU GRADE DE DOCTEUR ÈS SCIENCES

PAR

Leopoldo ROSSINI

acceptée sur proposition du jury:

Prof. F. Mondada, président du jury
Prof. Y. Perriard, directeur de thèse
Prof. H. Bleuler, rapporteur
Dr O. Chételat, rapporteur
Prof. B. Dehez, rapporteur



ÉCOLE POLYTECHNIQUE
FÉDÉRALE DE LAUSANNE

Suisse
2014

A mia mamma Manuela e mio papà Enrico.

Acknowledgements

This research work was carried out at the Swiss Center for Electronics and Microtechnology (CSEM) in Neuchâtel, Switzerland, in collaboration with the Integrated Actuators Laboratory (LAI) of the Swiss Federal Institute of Technology in Lausanne (EPFL), Switzerland.

I gratefully acknowledge the funding sources that made this dissertation possible:

- The European Space Agency (ESA) under the Networking/Partnering Initiative (NPI) contract 40000101313/10/NL/PA. I am indebted to my advisor at ESA Claudia Allegranza for her valuable technical advises and heartfelt support. Moreover, I would like to extend my deepest appreciation to Gerard Migliorero for continuously encouraging the development of the reaction sphere activity. Finally, I would also like to thank the team of the Structures and Mechanisms Section for providing a comfortable working environment during my 3-month stay at ESA/ESTEC.
- Maxon motor AG in Sachseln, Switzerland, which supported the NPI program cited above and collaborated in the design optimization of the spherical rotor (see Chapter 6). I am particularly grateful for all the insightful comments and suggestions received by Alexis Boletis and Stefan Mingard during the rotor design optimization. Finally, I would also like to express my sincere gratitude to Eugenio Forzani for his efforts throughout this activity while at maxon motor.
- The Swiss Space Office of the State Secretariat for Education, Research and Innovation (SERI) that funded the development of the spherical rotor (see Chapter 6) under the positioning measures call 2010.
- The European Union's Seventh Framework Programme (FP7/2007-2013) under grant agreement No. 283223.

I owe my deepest gratitude to my academic advisor Professor Yves Perriard of LAI for accepting to follow this PhD thesis and for his friendly guidance and unconditioned availability throughout these years. I also would like to thank the former and current members at LAI, and in particular Paolo Germano and Miroslav Markovic.

Acknowledgements

I would like to express my sincere appreciation to CSEM for providing me with this unique opportunity to carry out a research work on such a fascinating topic. First, I would particularly like to thank Jens Krauss for offering me the most agreeable conditions during these four years as a PhD student. Before this thesis work, Olivier Chételat made enormous contributions to the reaction sphere concept (see patent in reference [1]) especially in designing the rotor and stator of the first prototype (see Section 1.4.2). His suggestions and comments during these four years of research were invaluable. Then, I would also like to acknowledge Joseph Moerschell for his seminal work on the reaction sphere while at CSEM and subsequently at the University of Applied Sciences Western Switzerland (HES-SO). I am also deeply grateful to Emmanuel Onillon for his enthusiasm in this research and his warm technical and human support. Moreover, I am particularly indebted for the assistance received by Leszek Lisowski, who designed and developed the control electronics (see Section 1.4.2), Serge Droz, who designed and manufactured the test bench prototypes, and René Maurer, who always contributed with passion in manufacturing mechanical parts. A particular acknowledgement goes also to Ivar Kjelberg for his unlimited guidance concerning COMSOL Multiphysics. Throughout this research, I also received generous technical support from Patrick Theurillat, Yves-Julien Regamey, and Christophe Meier. Then, I would also like to express my gratitude to Jean-Marc Breguet for all the constructive discussions while at CSEM. Finally, a special thank goes to all the people of the Systems Division of CSEM who supported the reaction sphere program.

I would like to acknowledge the generous assistance of Professor Michel Rappaz at EPFL who guided me in deriving the spectral content conditions corresponding to the octupole cubic symmetry that are reported in Section 2.4.6.

Infine, questo lavoro non sarebbe stato possibile senza il supporto morale e l'amore ricevuto da Paola, dagli amici, e da tutta la mia famiglia. Desidero in particolare ringraziare i miei genitori Manuela ed Enrico, mia sorella Sabrina, e i miei fratelli Gionata e Federico per essermi sempre stati vicini anche nei momenti più difficili.

Neuchâtel, July 17, 2014

Leopoldo Rossini

Abstract

The Attitude Determination and Control System (ADCS) is responsible for the orbital behavior and pointing precision of stabilized satellites. The ADCS of three-axis stabilized spacecraft requires a minimum of three Reaction Wheels (RWs), but in practice, four wheels are common for optimization and redundancy purposes. As potential alternative, reaction spheres were introduced more than 60 years ago, but none of the suggested designs has reached a level of performance comparable to that of a four-wheel scheme. The leading idea is to replace the four rotating masses of RWs by a single spherical (hollow) mass, which can be levitated inside the surrounding stator and torqued about any direction to provide three-axis attitude control with a unique device.

In this thesis, we study a novel concept of reaction sphere actuator, in which the spherical rotor is supported by magnetic bearing and can be torqued electronically about any desired axis. The proposed reaction sphere is composed of an 8-pole permanent magnet spherical rotor and of a 20-pole stator with electromagnets. One of the key challenging aspects of permanent magnet spherical actuators consists in determining the orientation of the rotor inside the stator. In this thesis, we introduce a novel approach to parametrize the orientation of the rotor by considering the “magnetic orientation” rather than the “mechanical”. This approach constitutes an essential ingredient for the models proposed throughout this work and it allows reducing the computational complexity, which represents another important element for the experimental demonstration.

Magnetic flux density models, necessary for design optimization and to derive force and torque models, are developed using both analytical and hybrid FEM-analytical approaches. In these models, properties of spherical harmonics under rotation are employed to parametrize the orientation of the rotor inside the stator. Hence, the proposed approach allows expressing the force and torque as linear combinations, in which spherical harmonic decomposition coefficients (the magnetic state) include all the information relative to the orientation of the rotor. Then, the proposed procedure to determine the magnetic state, required to update force and torque models in real-time, is based on measuring the radial component of the magnetic flux density to subsequently solve the associated linear estimation problem. This procedure requires a minimum of seven measurements collected at different locations equidistant from the rotor surface. To measure the magnetic flux density, sensors are arranged to minimize the condition number

Acknowledgements

of the linear estimation problem so as to reduce the impact of measurement noise and high-order harmonics on force and torque relative errors. Subsequently, for closed-loop angular velocity control of the reaction sphere, algorithms are proposed to determine the back-EMF voltage induced in the stator coils and the angular velocity of the rotor. These two procedures, derived by applying the Faraday law of electromagnetic induction and the energy conservation principle, are linear and are expressed in closed-form. Finally, magnetic bearing and angular velocity control algorithms are experimentally validated using the developed laboratory prototype showing the ability of simultaneously levitating the rotor while rotating it about a given arbitrary axis.

We believe that this work represents a step forward concerning the study of reaction spheres. However, the development of these actuators remains an important challenge for future research, especially concerning the demanding manufacturing requirements, the estimation and control techniques, as well as the spatialization aspects.

Keywords: satellite attitude control, reaction sphere, spherical actuator, electromagnetic modeling, magnetic flux density model, spherical harmonics, force and torque model, magnetic state, magnetic bearing, design optimization.

Résumé

Le Système de Commande d'Attitude et d'Orbite (SCAO) est responsable du comportement orbital et de la précision de pointage des satellites stabilisés. Le SCAO des satellites stabilisés à trois axes nécessite un minimum de trois roues de réaction, toutefois, dans la pratique, quatre roues sont utilisées pour des raisons d'optimisation et de redondance. Comme alternative potentielle, les sphères de réaction ont été introduites il y a plus de 60 ans, mais aucune des solutions proposées n'a atteint un niveau de performance comparable à celui d'une approche basée sur quatre roues. L'idée principale est de remplacer les quatre masses tournantes des roues de réaction par une seule masse sphérique (creuse), pouvant être soutenue sans contact ainsi qu'entraînée dans toutes les directions possibles par un stator, permettant de contrôler l'attitude des trois axes du satellite avec un seul actionneur.

Dans cette thèse, nous étudions un nouveau concept de sphère de réaction, dans lequel le rotor est soutenu par un palier magnétique et peut être entraîné électroniquement dans toutes les directions possibles. La sphère de réaction proposée est composée d'un rotor sphérique ayant 8 pôles à aimants permanents et d'un stator ayant 20 pôles avec électroaimants. Un des défis essentiels des actionneurs sphériques basés sur des aimants permanents réside dans la détermination de l'orientation du rotor à l'intérieur du stator. Dans cette thèse, nous introduisons une nouvelle approche afin de paramétrer l'orientation du rotor considérant l'orientation « magnétique » plutôt que celle « mécanique ». Cette approche constitue un ingrédient essentiel pour les modèles proposés dans ce travail et permet de réduire la complexité de calcul, représentant un aspect fondamental pour la démonstration expérimentale.

Les modèles de champ magnétique, nécessaires pour l'optimisation du design et pour dériver les modèles de force et couple, sont développés en utilisant une approche analytique ainsi qu'une méthode hybride (éléments finis et analytiques). Dans ces modèles, les propriétés des harmoniques sphériques sous rotation sont employées afin de paramétrer l'orientation du rotor dans le stator. Ainsi, les approches proposées permettent d'exprimer la force et le couple comme combinaisons linéaires, dans lesquels les coefficients de décomposition sphérique (état magnétique) englobent toute l'information concernant l'orientation du rotor. Ensuite, la procédure proposée pour déterminer l'état magnétique, requise pour la mise à jour des modèles de force et couple en temps réel, est basée sur une

Acknowledgements

mesure de la composante radiale du champ magnétique pour ensuite résoudre le système d'estimation linéaire associé. Cette procédure nécessite un minimum de sept mesures collectionnées à des endroits différents et équidistants de la surface du rotor. Pour mesurer le champ magnétique, les capteurs sont disposés en minimisant le conditionnement du problème d'estimation linéaire afin de réduire l'impact du bruit de mesure et des harmoniques d'ordre supérieur sur les erreurs relatives de force et couple. Ensuite, pour le contrôle de la vitesse angulaire de la sphère en boucle fermée, des algorithmes sont proposés afin de déterminer les tensions induites dans le stator et la vitesse angulaire du rotor. Les deux procédures, dérivées en appliquant la loi de Faraday et le principe de conservation d'énergie, sont linéaires et sont exprimées en forme fermée. Pour terminer, les algorithmes de contrôle de sustentation magnétique (contrôle de position) et de vitesse angulaire sont validés expérimentalement utilisant le prototype développé. Cela a démontré l'habilité de faire léviter le rotor et simultanément le faire tourner sur un axe arbitraire.

Nous sommes persuadés que ce travail représente un pas en avant concernant les études des sphères de réaction. Cependant, le développement de ces actionneurs reste un défi important pour la recherche future, notamment au niveau des besoins exigeants de fabrication, des techniques d'estimation et de contrôle avancées, ainsi que des aspects de spatialisation.

Mots-clés : contrôle d'attitude des satellites, sphère de réaction, actuateur sphérique, modélisation électromagnétique, modèle de champ magnétique, harmoniques sphériques, modèles de force et couple, état magnétique, palier magnétique, optimisation de design.

Contents

Acknowledgements	v
Abstract (English/Français)	vii
1 Introduction	1
1.1 Concepts of Satellite Attitude Control	1
1.1.1 Attitude Determination and Control System	3
1.1.2 Attitude Control Methods	4
1.1.3 Actuators for Attitude Control	5
1.2 Literature Review of Reaction Sphere Concepts	8
1.3 Literature Review of 3-DOF Spherical Actuators	14
1.4 The Proposed Reaction Sphere	26
1.4.1 General Description	26
1.4.2 Developed Hardware and Prototype	29
1.5 Motivation and Problem Definition of the Thesis	32
1.6 Outline of the Thesis	34
2 Magnetic Flux Density Models	37
2.1 Introduction	37
2.2 System Description	39
2.2.1 Rotor and Stator Reference Frames	39
2.2.2 Twenty-pole Stator	42
2.2.3 Eight-pole Rotor	42
2.3 Analytical Model with an Ideal Octupole Rotor	44
2.3.1 Region Definitions and Relevant Dimensions	44
2.3.2 Constitutive Relations	45
2.3.3 Rotor Magnetization	45
2.3.4 Governing Equations	46
2.3.5 General Solution to Laplace's and Poisson's Equations	47
2.3.6 Boundary Conditions	47
2.3.7 Solution	47
2.3.8 Solution for Rotated Rotor (Stator Coordinates)	49
2.3.9 Verification with FEM Simulations	51

Contents

2.4	Hybrid FEM-Analytical Model	56
2.4.1	Region Definitions and Relevant Dimensions	56
2.4.2	Constitutive Relations	57
2.4.3	Governing Equations	57
2.4.4	General Solutions	57
2.4.5	Analytical Boundary Conditions	57
2.4.6	Measured or Simulated Boundary Conditions	58
2.4.7	Solution	60
2.4.8	Solution for Rotated Rotor (Stator Coordinates)	61
2.5	Summary	62
3	Force and Torque Models	63
3.1	Introduction	63
3.2	Definitions	66
3.2.1	Coil Reference Frame	66
3.2.2	Coordinate Transformations	66
3.3	Rotor Orientation Parametrized with SH Coefficients	68
3.3.1	Force Generated by a Coil	68
3.3.2	Torque Generated by a Coil	69
3.3.3	Complete Force and Torque Model	69
3.4	Orientation Parametrized with Rotation Matrix	71
3.4.1	Force Generated by a Coil	71
3.4.2	Torque Generated by a Coil	72
3.4.3	Complete Force and Torque Model	72
3.5	Force and Torque Inverse Models	73
3.6	Verification with FEM Simulations	75
3.6.1	Simulation Setup	75
3.6.2	Results	76
3.7	Summary	76
4	Magnetic State Estimation and Optimal Sensor Placement	81
4.1	Introduction	81
4.2	Magnetic State Estimation	83
4.2.1	Introduction	83
4.2.2	Least-squares Determination of Magnetic State	85
4.2.3	Update of Force and Torque Models	86
4.2.4	Implementation Procedure	87
4.3	Magnetic Flux Density Optimal Sensor Placement	89
4.3.1	Perturbed Measurement Equation	90
4.3.2	Derivation of an Optimization Criterion	90
4.3.3	Problem Defintion	91
4.3.4	Results	92
4.4	Summary	99

5	Back-EMF and Rotor Angular Velocity Estimation	101
5.1	Introduction	101
5.2	Electromechanical Model	103
5.2.1	Dynamic and Kinematic Rotational Model	103
5.2.2	Electrical Model	104
5.3	Rotor Angular Velocity Estimation	104
5.4	Back-EMF Estimation	105
5.4.1	Back-EMF in a Single Coil	105
5.4.2	Complete Back-EMF Model	107
5.5	Verification with FEM Simulations	108
5.5.1	Simulation Setup and Verification Procedure	108
5.5.2	Results	108
5.6	Summary	108
 6	 Design Optimization of a Spherical Rotor	 111
6.1	Introduction	111
6.2	Rotor Specifications and Design Optimization Problem Definition	112
6.2.1	Rotor Magnetic Flux Density over Mass Ratio	112
6.2.2	Model Agreement Criterion	113
6.2.3	Rotor Specifications and Problem Definition	114
6.3	Design Optimization with FEM Simulations	114
6.3.1	Influence of Rotor Pole Eccentricity and Permanent Magnet Mass on the Radial Component of the Flux Density	114
6.3.2	Influence of Rotor Pole Eccentricity on Model Agreement Criterion and Rotor Magnetic Flux Density over PM Mass Ratio	115
6.3.3	Back-iron Thickness Optimization with Nonlinear Simulations	116
6.3.4	Back-iron Mass Optimization with Non-linear Simulations	118
6.4	Spherical Harmonic Analysis	124
6.5	Summary	125
 7	 Experimental Results	 127
7.1	Introduction	127
7.2	Magnetic Flux Density Model - Monoblock Rotor	128
7.2.1	Introduction	128
7.2.2	Experimental Setup	128
7.2.3	Results	129
7.2.4	Conclusions	134
7.3	Force and Torque Models	135
7.3.1	Introduction	135
7.3.2	Experiments with Discrete Rotor	135
7.3.3	Simulations with Discrete Rotor	141
7.3.4	Experiments with Monoblock Rotor	148
7.3.5	Conclusions	149

Contents

7.4	Magnetic State Estimation	150
7.4.1	Introduction	150
7.4.2	Optimal Sensor Placement	150
7.4.3	Sensor Position Calibration	150
7.4.4	Magnetic Flux Density Reconstruction	154
7.4.5	Conclusions	154
7.5	Back-EMF and Rotor Angular Velocity Estimation	154
7.5.1	Introduction	154
7.5.2	Experimental Setup	154
7.5.3	Results	156
7.5.4	Conclusions	156
7.6	Design Optimization of a Spherical Rotor	158
7.6.1	Introduction	158
7.6.2	Experimental Setup and Method	158
7.6.3	Results	159
7.6.4	Conclusions	159
7.7	Closed-loop Levitation and Angular Velocity Control	160
7.7.1	Introduction	160
7.7.2	Control Scheme and Design	160
7.7.3	Experimental Setup	169
7.7.4	Results	170
7.7.5	Conclusions	174
7.8	Summary	174
8	Conclusions	177
8.1	Overview	177
8.2	Summary of Results and Contributions	179
8.3	Research Perspectives	182
A	Spherical Harmonics	187
A.1	Introduction	187
A.2	Definition	187
A.3	Properties	190
A.3.1	Orthonormality	190
A.3.2	Projection and Expansion/Reconstruction	190
A.3.3	Rotation	191
B	Illustration of Propositions	195
B.1	Illustration of Proposition 1	195
B.2	Illustration of Proposition 2	198
B.3	Illustration of Proposition 3	198
B.4	Illustration of Proposition 4	200

Bibliography	216
Nomenclature	222
Curriculum Vitae	223

1 Introduction

This document concentrates on modeling, estimation, and control aspects of a novel reaction sphere actuator for satellite attitude control. This chapter begins with an introductory section on satellite attitude control, which is intended to provide general aspects to define the framework for the application of the reaction sphere. Then, we review the existing literature concerning reaction sphere actuators. Subsequently, since the reaction sphere considered in this thesis can be classified into the family of 3-DOF electromagnetic spherical actuators, a literature review of this kind of actuators is presented. Afterwards, we introduce the reaction sphere concept that is under investigation in this thesis. Finally, we provide the motivation of the research performed in the frame of the thesis and we conclude the chapter with an outline of the remainder of this document.

1.1 Concepts of Satellite Attitude Control

Satellites can be classified in a number of ways such as by orbit altitude or according to the final application. Based on the intended applications, the satellites are broadly classified as communication satellites, navigation satellites, weather forecasting satellites, earth observation satellites, scientific satellites, and military satellites [2]. Irrespective from the intended application, the spacecraft can be divided conveniently in two principal elements, the payload, and the bus [3]. The payload is the combination of hardware and software on the spacecraft that interacts with the subject (the portion of the outside world that the spacecraft is looking at or interacting with) to accomplish the mission objectives. Payloads are typically unique to each mission and are the fundamental reason that the spacecraft is flown [4]. In order that the payload may function it requires certain resources that are provided by the bus. Requirements on the bus lead on the breakdown into subsystems that are summarized in Table 1.1 [2, 3, 5] (note that in [2] the authors include the payload in the subsystems).

Table 1.1. Spacecraft subsystems.

Subsystem	Function
Mechanical structure	Provide the framework for mounting other subsystems of the satellite and also an interface between the satellite and the launch vehicle [2].
Propulsion	Provide the translational velocity necessary to establish and maintain the required orbit. Provide vehicle rotation about all axes at the command of the attitude control system [5].
Thermal control	Maintain temperature of all spacecraft equipment within allowable limits for all mission modes [5].
Power supply	Generate, store, regulate, and distribute electrical power for all equipment in all mission modes. Switch all spacecraft equipment as required by the command system [5].
Telemetry, tracking, and command	Monitor and control the satellite from the lift-off stage to the end of its operational life in space. The tracking part of the subsystem determines the position of the spacecraft and follows its travel using angle, range, and velocity information. The telemetry part gathers information on the health of various subsystems of the satellites. The command element receives and executes remote control commands to effect changes to the platform functions, position, and velocity [2].
Attitude determination and control	Determine vehicle attitude and correct it to desired attitude. Implement and control commanded changes in velocity or attitude [5].
Telecommunication	Receive commands from the ground communication facility (uplink). Transmit payload and engineering data to the ground facility (downlink). Receive and re-transmit signals for navigation and tracking [5].

Among these subsystems, the Attitude Determination and Control System (ADCS) will be illustrated in more details because of its relevance for the thesis.

1.1.1 Attitude Determination and Control System

The motion of a rigid spacecraft is specified by its position, velocity, attitude, and attitude motion. The first two quantities describe the translational motion of the center of mass of the spacecraft. The latter two quantities describe the rotational motion of the body of the spacecraft about the center of mass and are relevant for the ADCS [6].

Typically, the purpose of putting a satellite in orbit is to point an instrument (payload) at something. For example, for an astronomy mission, the objective is to point a telescope at a distant solar star or some other astronomical feature. For an earth observation satellite, the purpose is to point a camera, radar or other instrument toward a desired location on the earth below. For a communication satellite, the transmitting and receiving antennas need to point toward the earth. What it means is that the attitude (orientation) of the spacecraft needs to be stabilized to some desired attitude [7].

Attitude determination is the process of forecasting the future orientation of the spacecraft relative to either an inertial reference or some object of interest, such as the earth. This typically involves several types of sensors and sophisticated data processing procedures [6]. Attitude control is the process of orienting the spacecraft in a specified, predetermined direction. It consists of two areas: attitude stabilization, which is the process of maintaining an existing orientation and attitude maneuver control, which is the process of controlling the reorientation of the spacecraft from one attitude to another [6].

The ADCS stabilizes the vehicle and orients it in desired directions during the mission despite the external disturbance torque acting on it [4]. As matter of fact, any uncontrolled body in space, for example an asteroid, will tumble about all axes in response to natural forces, notably solar pressure, gravity gradients, and magnetic torques [5]. Natural tumbling is not normally acceptable for a spacecraft because solar panels must be pointed at the sun for power, antennas must be pointed at an earth station for communication, and science instruments must be pointed at their targets. As a result, spacecraft attitude must be controlled. A spinning spacecraft tends to hold one axis, the spin axis, fixed in inertial coordinates. Having one axis fixed is already adequate for many missions. For example, if the spin axis is perpendicular to the sun vector the body can be populated with solar cells to provide the power needs. Omnidirectional antennas can be used, and some payloads need no more than one fixed axis. In today's complex missions, many spacecraft have requirements too diverse for the one-axis control. It is not unusual for spacecraft to need solar panels pointed to the sun, science payload (a camera for example) pointed at the planet surface, and a high-gain antenna pointed at the ground station. For complex situations three-axis control is required [5]. Finally, in addition to rejecting

disturbances, for many spacecraft, the ADCS must control vehicle attitude during firing of large liquid or solid rocket motors, which may be used during orbit insertion or for orbit changes. Large motors create large disturbance torques, which can drive the design to larger actuators than needed once on station [4].

1.1.2 Attitude Control Methods

Several methods of controlling the spacecraft have been proposed. This can be done both actively or passively, depending on the desired attitude, and how accurately it must be maintained. Passive methods of attitude stabilization make use of the spacecraft's natural dynamics to ensure a stable equilibrium at the desired attitude, and are useful when accuracy requirements are coarse. For active control, actuators capable of affecting the attitude are installed on the spacecraft. In many cases, passive control methods are augmented by active control methods [7]. The most common attitude control systems include spin-stabilized systems, dual-spin systems, gravity-gradient systems, three-axis-stabilized systems, and momentum bias systems [5]. A spin-stabilized spacecraft is one in which the entire spacecraft spins around the axis with the highest moment of inertia. A dual-spin spacecraft has a spinning segment and an inertially fixed section. Gravity-gradient control is completely passive and takes advantage of the spacecraft tendency to align the long axis with the gravity gradient. A three-axis controlled spacecraft actively controls the inertial position of all the three axes. A momentum bias system uses a momentum wheel to provide stiffness in two axes and wheel speed to control the third axis [5]. In the next section, we present in more detail three-axis-stabilized systems, to which this thesis is mostly concerned.

Three-axis-stabilized System

A three-axis-stabilized system actively maintains the vehicle axis system aligned with a reference system, usually orbital reference or nadir reference [5]. Spacecraft stabilized in three axes are more common today than those using spin gravity gradient. They maneuver and can be stable and accurate, depending on their sensors and actuators [4]. In a zero-momentum system, Reaction Wheels (RWs) respond to disturbances on the vehicle. For example, a vehicle pointing error creates a signal which speeds up the wheel, initially at zero. This torque corrects the vehicle and leaves the wheel spinning at low speed, until another pointing error speeds the wheel further or slows it down again. If the disturbance is cyclic during each orbit, the wheel may not approach saturation speed for several orbits. Non-periodic disturbances (secular disturbances), however, cause the wheel to drift toward saturation. We then must apply an external torque, usually with a thruster or magnetic torquer, to force the wheel speed back to zero. This process, called desaturation, momentum unloading, or momentum dumping, can be done automatically or by command from the ground [4]. When high torque is required for large vehicles or

fast slews, a variation of three-axis control is possible using control moment gyroscopes (CMGs).

Advantages of three-axis stabilized systems include an unlimited pointing capability in any direction and the best pointing accuracy, limited only by sensor accuracy. Pointing accuracy of greater than 0.001° can be achieved [5]. Solar panels can make full use of the available solar energy. This type is the most adaptable to changing requirements. On the other hand, ADCS hardware (gyros, RWs, star scanner, computers) are complex, heavy, high-power consumers, failure sources, and expensive. Moreover, redundancy schemes are more complex. Examples of three-axis-controlled spacecraft are Magellan, INTELSAT VIII, the Hubble Telescope, and GPS.

1.1.3 Actuators for Attitude Control

There are at least four distinct means of producing torque for the attitude control of spacecraft, based on [8]:

1. earth's magnetic field (magnetic torqrods);
2. reaction forces produce by expulsion of gas or ion particles (thrusters);
3. solar radiation pressure on spacecraft surfaces; and
4. rotating bodies inside the spacecraft (momentum exchange devices).

The first three techniques listed are inertial controllers (or external), in the sense that they change the overall inertial angular momentum of the satellite. The remaining option is based on rotating masses inside the spacecraft body, so that that angular momentum is transferred between different part of the satellite without changing its overall inertial angular momentum [8].

Magnetic Torqrods

Magnetic actuations is generally obtained using torqrods (also known as torque rods, torque bars, or magnetotorquers), which consist of a magnetic core and a coil. When the coil is energized, the torqrod generates a magnetic moment. Torqrods are extensively used in the attitude control of spacecraft. However, the level of torques that can be achieved with magnetic torqrods is normally low (in the range of 1 mNm to 10 mNm) and generally insufficient for fast attitude maneuvers. Moreover, magnetic torques are also dependent on the chosen orbit inclination and they are excluded for spacecraft not revolving about the earth, since it its based on the earth's magnetic field [8].

Thrusters

Most spacecraft use reaction forces obtained using thrusters as actuators. They provide momentum to the spacecraft by ejecting mass overboard in the form of high velocity exhaust gas. Thrusters can be used directly to control the spacecraft attitude or used as momentum desaturation actuators for the RWs. Primary thruster control can be very costly in terms of propellant mass if there are noticeable disturbance torques [5]. Moreover, reaction controllers are not linear, in the sense that they provide reaction torques of constant amplitude and modulated time duration [8]. The level that can be achieved with reaction pulses is almost unbounded. However, no smooth control can be achieved due to the inherent nature of thrusters [8].

Solar Pressure

Torques obtained from solar pressure cannot be used for attitude maneuvering since the level of torques that can be produced (when the spacecraft sees the sun) are of the order of tens of μNm only, which are insufficient for attitude maneuvers [8]. Moreover, they cannot produce torques about the three spacecraft axes.

Momentum Exchange Devices

The remaining option is based on rotating masses inside the spacecraft body, so that angular momentum is transferred between different parts of the satellite without changing its overall inertial angular momentum. The resulting actuators are called momentum exchange devices, and include RWs, momentum wheels, and Control Moment Gyroscopes (CMGs) [8]. With CMGs (used in manned spacecraft) torques of 200 Nm are achievable. However, such CMGs are very heavy and are seldom used in the ADCS of ordinary-sized satellites [8]. Momentum wheels are used primarily to provide the spacecraft with the momentum bias necessary for inertial stability. As a byproduct, the momentum wheel can also develop torque for controlling the attitude of the satellite's axis that is parallel to the momentum wheel's axis of rotation. The range of angular momentum provided by such wheels is 1 Nms to 300 Nms [8]. For very accurate attitude control systems and for moderately fast maneuvers, the RWs are preferred because they allow continuous and smooth control of torque with the lowest possible parasitic disturbing torques. The level of torques that can be achieved with RWs is of the order of 0.05 Nm to 2 Nm [8].

Reaction wheels are simply small flywheels powered by an electrical motor, which exchanges momentum with the spacecraft by changing wheel speed. The flywheel is designed to increase the motor's angular momentum of inertia. The rotating wheel may have an initial constant momentum. By accelerating the wheel in one direction about the wheel spin-axis, the wheel applies a reaction torque to the spacecraft structure in the opposite direction (also about the wheel spin axis). This is the principle of conservation of

angular momentum [7]. In the absence of an external torque acting on the spacecraft, the total angular momentum of the spacecraft remains constant. Therefore, in the absence of external torques, if the angular momentum of the wheels is changed, there must be a corresponding opposite change in the angular momentum of the spacecraft structure [7]. External disturbance torques result in a change in overall spacecraft angular momentum. When the spacecraft attitude is controlled using RWs, this change in overall spacecraft angular momentum manifests itself as a change in stored angular momentum in the wheels. Therefore, external disturbances result in a build-up of wheel angular momentum. In the case of secular disturbances, wheels may drift toward saturation. External thruster or magnetic torquer are necessary for desaturation.

For three-axis control, three orthogonal RWs, with each one's rotational axis parallel to one of the spacecraft body axes, make up the simplest control system. However, if one of the assemblies becomes damaged then the satellite's attitude can no longer be adequately corrected. For this reason, a fourth RW is installed in order to increase the reliability of the entire system [8]. The additional wheel is installed with its axis "off" the three principal spacecraft axes, enabling (reduced) torque control about any one of those axes. Reaction wheels are also used in a four-wheel pyramid scheme, with the spin axes pointing normal to the faces of a pyramid. This configuration provides redundancy as well as greater flexibility in the distribution of wheel angular momentum [9].

The rotor bearings of momentum exchange devices deserves special attention: we distinguish between mechanical and magnetic bearings. Momentum exchange devices are designed to work without interruption for long time periods (5–12 years). In the space environment of subpressure, lubrication of (mechanical) ball bearings is a major problem that has not been completely solved. Moreover, the ball bearing suffers from excessive friction loading. In recent years, the development of magnetic bearings has taken a decided upturn, with good prospects for the future [8]. Magnetic bearings improve the torque-to-noise ratio by eliminating the parasitic torque noises characteristic of ball bearing [8].

Multi-axis Momentum Exchange Devices

Multi-axis momentum exchange devices capable of producing torque in any direction have also been proposed although their credibility has still to be demonstrated in space. The idea behind these devices is to provide a compact solution for three-axis attitude control by combining the four-wheel scheme in a unique actuator.

A fully active magnetic bearing wheel with five actively controlled axes is presented in [10]. The wheel can be actively tilted by 1° enabling to use it simultaneously as a RW and CMG. This enables three-axis attitude control of the spacecraft with only one wheel. The five degrees of freedom are actively controlled and a special decoupling tilt control

law assures that the tilt responses are not deteriorated by gyroscopic effects. Furthermore, the magnetic bearing wheel can be used as actuator for active damping of structure oscillations since active damping forces can be generated by moving the rotor within the mechanical gap. Another attractive feature of the magnetic bearing wheel is the active vibration suppression, enabling the rotor to rotate about its natural axis of inertia and to suppress all the resulting noise components without affecting the suspension stability. The work reported in [10] is continued in [11, 12] under the same principle and general architecture. The rotor gimbaling capability has been increased to $\pm 1.7^\circ$ and special signal processing techniques are employed to enhance the microvibration signatures due to both static and dynamic imbalance of the wheel. The above discussed actuator, which is displayed in Fig. 1.1, is currently offered as a product under the name of MWI Magnetic Bearing Momentum and Reaction Wheels by Rockwell Collins Deutschland GmbH.

In the next section, we discuss a special kind of multi-axis momentum exchange devices, which are called reaction spheres.



Figure 1.1. Five axes magnetic bearing reaction wheel developed by Rockwell Collins [12].

1.2 Literature Review of Reaction Sphere Concepts

In line with the effort of dealing with the RW problematic aspects such as bearing and gyroscopic cross coupling between axes, reaction spheres were proposed more than 50 years ago, in 1960, three years after the launch of Sputnik 1 [13–15]. The leading idea was to replace the three rotating masses of RWs by a single spherical (hollow) mass, which can be torqued about any direction to provide three-axis attitude control with a unique device.

A spherical reaction member for a three-axis attitude control is described in [15]. Control of the space vehicle with the spherical reaction member, torquing of the sphere, its bearing, and its angular velocity measurement are discussed. The author points out the advantage of using a sphere to avoid coupling effects commonly present with three RWs and to reduce the number of actuators from three to one. For the suspension of the sphere, air bearing and magnetic levitation are proposed. Magnetic bearing in vacuum conditions is indicated as most promising due to lower losses. As depicted in Fig. 1.2, a

1.2. Literature Review of Reaction Sphere Concepts

set of four or more stabilizing coils allow the proper centering of the sphere, which has to be made of ferromagnetic material. For torquing the sphere about the three orthogonal axes, the author proposes to use air nozzles and electrical means. Air nozzles require considerable power and torques are produced inefficiently. Hence, the most promising torquing method is by electrical means with two or more phase AC torquers that can produce torque due to hysteresis and eddy current effects on the magnetic sphere.

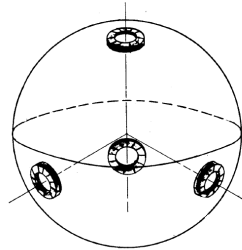


Figure 1.2. Suspension coils in tetrahedron configuration proposed by Haeussermann. Drawing adapted from [15].

The author in [13] considers an inertial sphere consisting of a spherical conducting shell positioned by a high-frequency magnetic field, and subject to torques by another magnetic field rotating at lower frequency. The configuration has the advantage that only one system is needed and the gyroscopic effects that appear with multiple rotating wheels are absent.

An outgrowth of the study in [13] is proposed by [16] for attitude control of earth satellites. In this study the sphere would be suspended with the aid of a spatially nonuniform, high frequency alternating magnetic field. The force is produced by the interaction between the applied magnetic field and the eddy current induced in the sphere. To generate the torque, three sets of mutually perpendicular coils are proposed. The difference from [13] is that the accumulated angular momentum is passively dumped by eddy currents interaction with the earth's magnetic field.

An electrically suspended free reaction sphere was firstly invented in [14]. The principle is to suspend a spherical metal rotor by electric field attraction forces and transfer angular momentum from the satellite to the rotor through the spin coils. Electric, magnetic, and air bearing suspension have been considered. Magnetic suspension has been discarded due to retarding torques acting upon the spinning rotor. Air bearing requires gas to be stored on board and was also discarded. As depicted in Fig. 1.3, the spherical rotor is held at the center of the spherical cavity by the forces of attraction from mutually orthogonal electrodes. Three pairs of induction motor stator windings are located in the orthogonal planes to provide for generating control torques around the three axes (in Fig. 1.3 only two windings are displayed). Equipment to demonstrate single-axis electric field suspension for the free reaction sphere was developed.

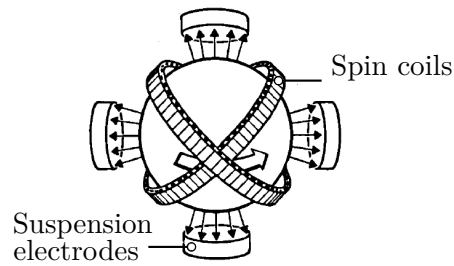


Figure 1.3. Illustration of the free reaction sphere by Ormsby. Drawing adapted from [14].

A similar reaction sphere concept is discussed by the same authors in reference [17]. The authors present some important characteristics of an electrically suspended reaction sphere designed with three induction motor stator winding in orthogonal planes to provide attitude control of the spacecraft about any axis. As illustrated in Fig. 1.4, the stator has eight available areas to provide four pairs of electrodes which can be paired to obtain four independent suspension forces. The electrodes cover the surface of the stator sphere except for the areas needed for the motor stators. The major limitation of the electric field suspension was the maximum positioning force which can be generated. The torque system constitutes a set of three orthogonal stators, any one of which resembles a short electric induction motor stator in its electric and geometric characteristics. Despite the detailed analysis of the design, there is no evidence of any manufactured prototype or experimental result.

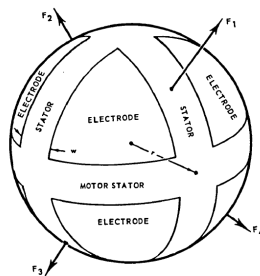


Figure 1.4. Four-point suspension geometry for reaction sphere presented by Ormsby and Smith. Drawing adapted from [17].

The same configuration of [17] is proposed in [18] by another group. The basic elements of the reaction sphere are a thin-walled spherical rotor within a spherical cavity bounded by eight electrodes and three motor stators. As in [17], the electrode arrangement perfectly suits the necessary orthogonal arrangement of stators, which divide the surface into octants. Each of the orthogonal stators consists of a two-phase induction motor that creates a rotating magnetic field in the suspension gap, torquing the sphere about any axis. Authors reported two major problems concerning voltage breakdown in a vacuum and dynamic stability of the four-point suspension servo loop. A bench model of the

1.2. Literature Review of Reaction Sphere Concepts

controller was constructed to provide a four-point suspension system and an analogue computer was utilized to mechanize the analytic configuration of the suspension system. Despite any evidence of experimental results, authors claim that dynamic suspension was achieved.

The use of reaction sphere for satellite attitude stabilization was also discussed some years later in [19]. The author recognizes that the advantages provided by the use of a reaction sphere come with the price of a relatively complex bearing, which is identified as the greatest difficulty. Moreover, the author classifies the conceptual problems into the following categories: a) type of bearing, b) storage capacity for angular momentum, c) torque resolution and maximum torque, d) cross-coupling in the three dimensional drive, e) vectorial rpm measurement, f) mechanical stability, g) testing possibilities before blastoff, h) reliability. Various bearing possibilities are discussed. Gas bearing and fluid bearing are not identified as possible solutions due to excessive friction. The main drawback of magnetic bearing suspension is identified as the coupling of the magnetic moments with the drive motor (at that time inductive). Electrostatic bearing seemed to be the preferred solution despite the lower supporting forces. Concerning the drive motor, the author discusses only the stator composed of three separate winding arranged in three perpendicular planes (as above [14, 17, 18]). The measurement of the angular velocity is also discussed and author seems to be in favor of using the stator coils as tachometer. Motor windings serve simultaneously as exciter and sensings windings.

Twenty years later, in 1986, author in [20] patented the idea of a single magnetically supported torqued reaction sphere mounted in a spherical housing without physical contact with the housing. The rotor comprises a massive spherical body having at least an outer layer, which is both electrical conductor and a magnetizable material. Three pair of sectors mounted mutually orthogonal comprise an accurate set of laminations carrying a centering winding (bearings) and a torquing winding. Centering of the rotor (bearing) is accomplished by automatic regulation of the current in centering windings of the sectors as the inner spherical rotor moves off center. Rotation of the spherical rotor in this unit is accomplished by a three-axis torque motor as depicted in Fig. 1.5. The forces acting to produce the torque result from the interplay of eddy currents, induced in the sphere by the magnetic flux of the centering winding, reacting with fluxes produced by the torquing winding.

In 1990, the idea of a magnetic bearing suspension system with the rotor that can be gimballed about 360 degrees was patented in [21]. Rotor includes annular magnet and a flywheel attached to the magnet. The flywheel is machined to a spherical shape to provide constant gap width between it and spherical housing. As shown in Fig. 1.6, three orthogonal pairs of ring inductive motors are used to control the bearing of the rotor. Three additional orthogonal pairs of coils with cylindrical shape are employed to apply torques to the flywheel to control direction of the rotating axis. It is claimed that by providing a gyroscope in which the flywheel can completely gimballed without contact

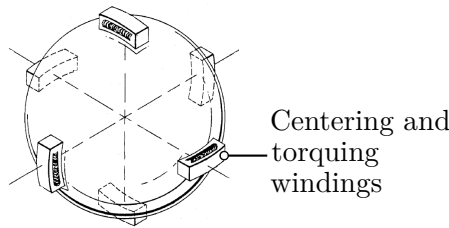


Figure 1.5. Schematic of reaction sphere with centering and torquing windings proposed by Isely. Drawing adapted from [20].

with the housing, the spin axis of the flywheel can be placed as desired to properly turn the spacecraft.

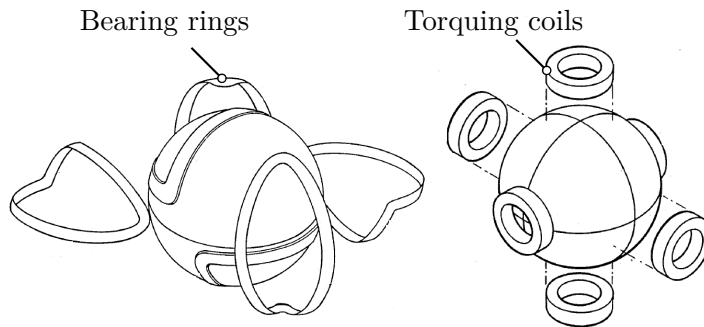


Figure 1.6. (Left) Schematic of reaction sphere with bearing rings proposed by Downer et al. (Right) Torquing coils. Drawing adapted from [21].

A general concept for multi-freedom motion that can also be used as attitude control actuator is proposed in patent [22] in 1995. Authors provide various embodiments of their invention. In general, the electrical motor includes a spherical (hollow) rotor with a plurality of magnets disposed on an outer surface of the rotor with polarities of the respective adjacent magnetic poles being different from one another. The stator is provided along the outer surface of the rotor, and a plurality of magnets opposed to the magnets of the rotor are disposed on an inner surface of the stator. Either magnets on the rotor or stator could be electromagnets. Several bearings are proposed: hydrostatic bearing, magnetic bearing, sliding bearing, and roller bearing.

In 2006, author in [1] patented the idea of a reaction-gyro sphere with magnetic bearing. The reaction-gyro sphere may consist of a concentric assembly of a spherical rotor and a spherical stator. The rotor has magnetic poles such that, when radially projected on a concentric octahedron, the same symmetrical pattern is obtained on all faces of the octahedron, the polarity of the poles projected on two opposite faces of the octahedron

1.2. Literature Review of Reaction Sphere Concepts

being opposite. The rotor is perfectly isotropic regarding its dynamic properties. The stator has at least twenty poles magnetized with coils and such that, when radially projected on a concentric icosahedron, the same symmetrical patterns is obtained on all faces of the icosahedron. As the rotor has a constant source of magnetic field, on the one hand, the system is linear, allowing the decoupling of the motor and bearing functions by superposition, and on the other hand, the efficiency is potentially better with the possibility to recover the kinetic energy stored in the rotor. In one of the possible embodiment shown in Fig. 1.7, the rotor has eight permanent magnet poles located at each faces of an octahedron (vertexes of a cube), with two opposite faces of the octahedron having opposite polarity. The stator has twenty poles located at the center of each face of a icosahedron (vertexes of a dodecahedron).

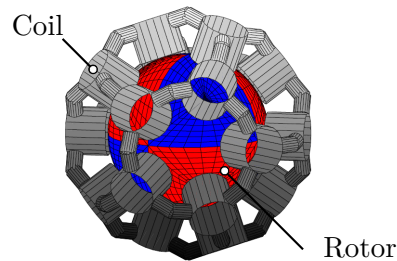


Figure 1.7. Schematic of rotor and stator arrangement proposed by Chételat [1].

The reaction sphere concept proposed in invention [23] consists of an electromagnetic stator that surrounds a spherical conductive rotor to provide rotation of the rotor in a frictionless environment, as well as allows the rotor to be driven in any axis. In one embodiment displayed in Fig. 1.8, the stator includes twenty ferrite poles pieces. Each pole piece has a copper wire winding about the pole and the twenty poles are arranged to form the shape of a truncated icosahedron around the spherical rotor. The rotor in this embodiment is a hollow copper sphere.

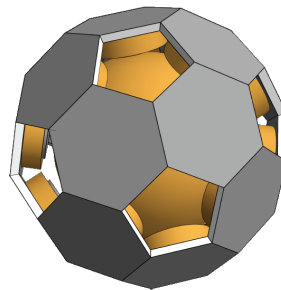


Figure 1.8. Schematic of the conductive rotor contained in stator with 20 ferrite pole pieces proposed by Doty [23].

1.3 Literature Review of 3-DOF Spherical Actuators

Reaction spheres can be classified into the family of spherical actuators, which are devices capable of performing three degree-of-freedom (3-DOF) rotational motion in a single joint. Spherical actuators are especially presented in the robotic literature, where researchers investigate new solutions to design compact and high performance 3-DOF rotary actuators without the inconvenient of combined multi-DOF actuators, such as friction and backlash, low dynamic performance, and kinematic singularities [24].

A variety of different designs have been proposed in the last five decades. In general, the proposed designs consist in a rotating spherical rotor enclosed in a stator. Then, a mechanical shaft emerges from the rotor to export the torque. Although ultrasonic and piezoelectric spherical drives have been developed [25–31], electromagnetic devices are the most common and have attracted the attention of several research groups and industries throughout the world. We will first rapidly review inductive and variable reluctance electromagnetic spherical actuator concepts to subsequently focus our attention on Permanent Magnet (PM) synchronous actuators, which are more concerned with this thesis.

The first 2-DOF spherical induction motor has been designed by Williams et al. in 1959 [32]. As depicted in Fig. 1.9, the motor is composed of a conductive spherical barrel-shaped rotor and two stator winding blocks. Conduction of the rotor surface in any directions is achieved by wounding rotor slots with conducting rings joined at all points to form a grid. The stator block is wound with a polyphase winding designed to produce a rotating magnetic field. The interaction between the induced current and the stator magnetic field produces a 2-DOF motion of the rotor. The speed of the motor is changed by modifying the direction of the moving magnetic field relative to the direction of movement of the rotor surface by twisting the stator about an axis perpendicular to the axis of the rotor. A method for field analysis and torque prediction based on Maxwell stress tensor for this kind of spherical induction motor is presented by [33]. Vachtsevanos et al. [34] proposed a robotic manipulator incorporating a spherical motor capable of three degrees of motion in a single joint. The rotor consists of a conducting ball filled with a high permeability material. The rotor is driven by three sets of windings mounted on the stator and excited to generate induced current on the rotor surface. No prototype has been constructed for this conceptualized spherical actuator due to the complexity in mechanical design [24]. Despite magnet technology has improved with high powered permanent rare earth magnets now being commonly available, spherical induction motors are still subject of investigation. For example, a double excited spherical motor with three-phase excitation coils in the stator placed perpendicularly to each other has been modeled and simulated by Ruan et al. [35]. More recently, Dehez et al. developed a 2-DOF spherical induction motor prototype whose stator is obtained by superimposing two sets of three-phase windings placed orthogonally to each other. The rotor consists of a two-layer spherical shell with teeth and is held in position by aerostatic bearings [36].

1.3. Literature Review of 3-DOF Spherical Actuators

The developed prototype is displayed in Fig. 1.10. Driven by specifications without high dynamics and precision, a preliminary model design of a spherical induction motor is proposed by Zenter [37]. The first spherical induction motor operated in closed-loop is claimed by [38] and reported in Fig. 1.11. This 3-DOF actuator is capable of 300 rpm rotation in arbitrary axis with 4 Nm torque on the spherical rotor of 246 mm diameter. The rotor is a two-layer copper-over-iron spherical shell. The stator has four independent inductors that generate thrust forces on the rotor surface. The motor is also equipped with four optical mouse sensors that measure surface velocity to estimate the rotor's angular velocity, which is used for vector control of the inductors and control of angular velocity and orientation.

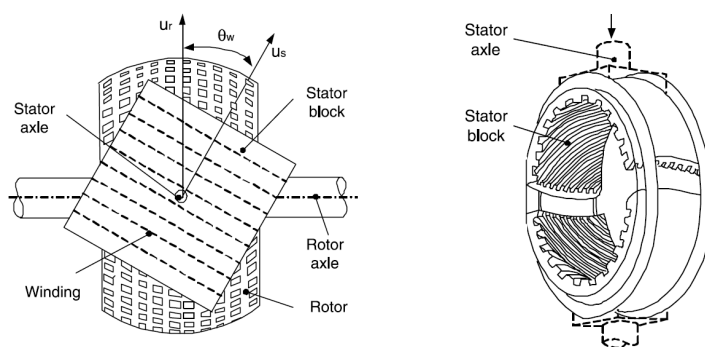


Figure 1.9. A 2-DOF spherical induction motor proposed by Williams et al. [32]. (Left) Rotor and stator block. (Right) Structure of the stator. Drawing taken from [24].

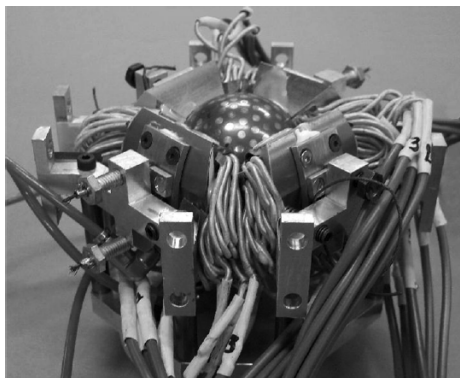


Figure 1.10. Prototype of 2-DOF spherical induction motor proposed by Dehez et al. [36].

A hybrid permanent magnet and variable reluctance spherical stepper motor with 3-DOF has been investigated by Lee et al. [39, 40]. The motor consists of a hemispherical stator housing iron-cored coils and a rotor with a pair of permanent magnets.

Subsequently, a Variable Reluctance Spherical Motor (VRSM) has been studied and developed by Lee et al. [41–45]. This motor is illustrated in Fig. 1.12. In general, the motor consists of a hemispherical stator housing a distribution of electromagnets and a

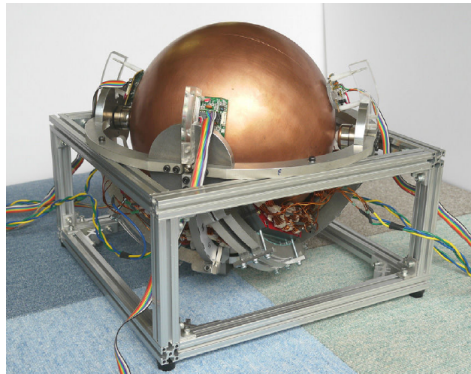


Figure 1.11. Prototype of 3-DOF spherical induction motor proposed by Kumagai and Hollis [38].

rotor with a number of poles made up of ferromagnetic materials or permanent magnets. By energizing the coils individually, a magnetic energy function of the relative position of the rotor and stator is created in the airgap. The motion of the rotor is generated as the rotor tends to move to a minimal energy position. First rotor dynamic and torque models as well as a motion control strategy for this actuator have been developed in [41]. The torque model of the VRSM actuator is expressed in a quadratic form with respect to the stator current and is function of the permanence and its derivative. Permeance functions are determined experimentally by measuring the static torque at a series of positions as a function of the current input. Hence, the current vector is calculated using an inverse problem, solved by nonlinear optimization and stored in look-up tables. A reaction-free control strategy for the spherical stepper to establish a non-contact support mechanism through partial magnetic levitation has been proposed [42]. More recently, the interest to derive a closed-form solution to the inverse torque model has led to consider alternative configurations of the VRSM characterized by a linear torque-current relationship. To this end, iron rotor poles have been replaced by high coercitive PMs whereas coils are wound on non-ferromagnetic cores [43]. Six cylindrical PMs with their magnetization axes meeting at the center of the rotor are adjusted on the rotor equator with alternate polarity. Two different configurations of the coils are suggested. The resulting torque-current is approximately linear and it is function of a torque constant, which is computed using Finite Element Method (FEM). The optimal control input to generate a requested torque is computed by minimizing the dissipated energy using weighted least squares. A design study based on Computer-Aided Design (CAD) and FEM iterative procedures to optimize this kind of actuators are discussed in [44, 45].

Subsequently, Lee et al. have proposed a particular form of VRSM that is referred as Spherical Wheel Motor (SWM) [46, 47]. Unlike VRSM, where the focus has been on controlling the three-DOF angular displacements, the SWM offers a means to control in open-loop the orientation of its rotating shaft with a single spherical joint. As shown in Fig. 1.13, the SWM consists of a spherical rotor with cylindrical magnets and a stator

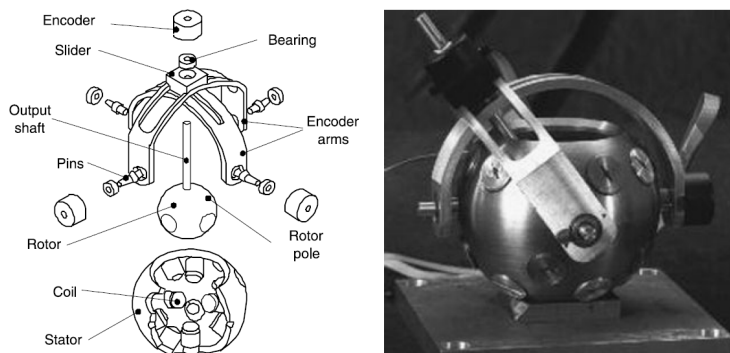


Figure 1.12. Variable reluctance spherical motor proposed by Lee et al. [41–45]. (Left) Exploded view. (Right) Prototype. Drawing taken from [24].

with aluminum-core electromagnets. Permanent magnets and electromagnets are placed at locations following the vertices of a regular polygon. The setup consists of two layers of 8 equally-spaced magnetic poles placed alternatively (for a total of 16 permanent magnets) and two layers of 10 stator coils (for a total of 20 coils). A dynamic model of the rotor is derived to predict its dynamics. As in [43], the resulting torque-current characteristic is approximately linear, with the torque constant computed using FEM. Then, an open-loop method based on switching sequences to control the rotor orientation while allowing it to spin continuously is proposed and experimentally validated using the prototype. An alternative approach to characterize torque models, while reducing the computational time, was proposed by Lee et al. and consists in modeling both the stator coils and the permanent magnets as Distributed Multipoles (DMP) [48]. Unlike the Lorentz force or the Maxwell stress tensor methods that require integration, the dipole force computation is expressed in closed form. An alternative open-loop control strategy to decouple the spin from the inclination of the rotating shaft is proposed by Son et al. [49]. Specifically, the open-loop controller combines a multispeed switching control law for controlling the spin motion and a dynamic model-based control law for regulating the rotor inclination.

Yan et al. [50] proposed a prototype of ball-joint-like 3-DOF PM spherical actuator that is depicted in Fig. 1.14. The rotor has eight PMs assembled evenly spaced with alternate polarities around the rotor equator. Each magnet has the shape of a dihedral cone. Then, two layers of 12 air-core coils for each layer are assembled on the stator. The magnetic flux density in the spherical actuator is formulated solving the Laplace equation in spherical coordinates and resulted in a torque model, which connects linearly a set of currents to a torque vector. Details of this design can be found in [51] and [24]. Then, Yan et al. [52] studied the effect of an iron stator on the magnetic field and torque output of this spherical actuator. Their results show that the iron stator can increase the radial component of the flux density and thus the actuator torque output significantly. In parallel, driven by the high manufacturing costs and system complications, Yan et

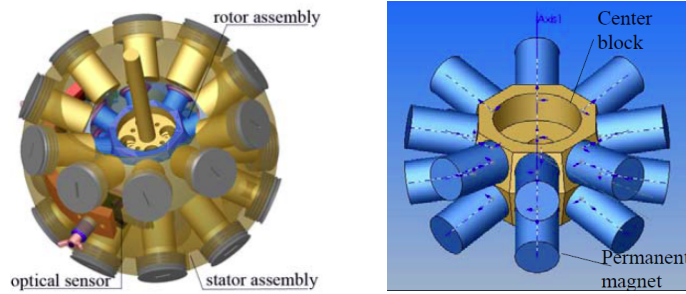


Figure 1.13. 3-DOF spherical wheel motor proposed by Lee et al. [46,47]. (Left) Actuator assembly. (Right) Rotor assembly.

al. [53,54] proposed to substitute the dihedral-shaped magnets with a specific distribution of stacked cylindrical magnets. One layer of eight cylindrical-shaped PM poles are mounted along the rotor equator, and two layers of air-core coils (12 per layer) are fixed on the stator symmetrically with respect to the stator equator. The developed prototype is displayed in Fig. 1.15. Torque output of the spherical actuator is formulated with a hybrid method, i.e., using both analytical and experimental methodologies. Yan et al. [55] also presented a generic design concept of 3-DOF spherical actuator with a rotor consisting of multiple layers of PM poles that is concentrically housed in a spherical-shell-like stator with multiple layers of air-core coils. It is shown that the tilting torque in double-layer configuration is higher than that of single-layer configuration whereas the single-layer configuration has a higher spinning torque about the rotor shaft.

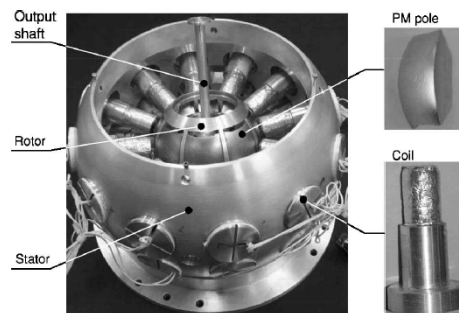


Figure 1.14. Prototype of ball-joint-like 3-DOF spherical actuator proposed by Yan et al. [50].

A permanent magnet spherical motor for haptic applications in presented by Bai et al. [56] and reported here in Fig. 1.16. The device can be operated in rotational and displacement modes. With the two-mode configuration, the actuator can offer 6-DOF motion commands for manipulating a target in a virtual computer-aided engineering

1.3. Literature Review of 3-DOF Spherical Actuators

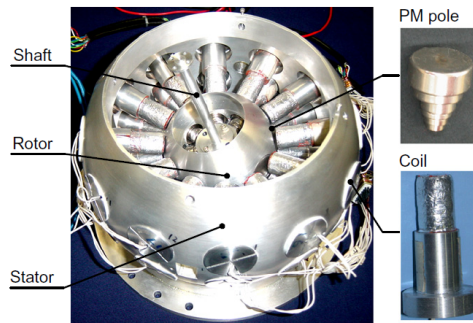


Figure 1.15. Prototype of ball-joint-like 3-DOF spherical actuator with cylindrical-shaped PM poles proposed by Yan et al. [53,54].

environment while providing force/torque feedback in real-time. The spherical motor consists of 24 cylindrical electromagnets housed on the outer surface of the ball like stator which concentrically supports the socket-like rotor (where 24 cylindrical PMs with alternating polarities are embedded on its inner surface) by means of a low-friction spherical bearing. The magnetization axes of both stator EMs and rotor PMs radially pass through the spherical center. A direct mapping based on an artificial neural network is used to compute the magnetic torque and provide the required force/torque feedback without explicit orientation measurements in real-time. A direct field-feedback control of this actuator is presented by Bai and Lee [57]. Specifically, unlike other spherical actuators based on rotor orientation feedback [58], magnetic flux density measurements (uniquely corresponding to the rotor orientation) are used for feedback, allowing parallel computation of the control law and computation of the torque model, which is computed using flux density measurements through an artificial neural network. Magnetic flux density measurements are provided by 24 single-axis or two-axis Hall sensors, which are adjusted on the middle of each coil.

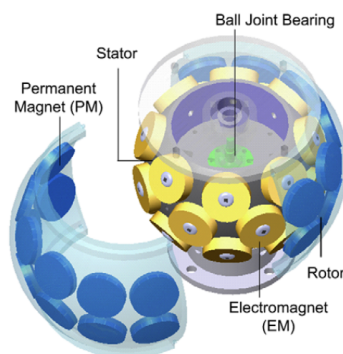


Figure 1.16. CAD model of the two-mode 6-DOF permanent magnet spherical motor proposed by Bai et al. [56].

Chirikjian and Stein [59] developed a spherical stepper actuator consisting of a plastic rotor with 89 PMs that is partially encapsulated in the stator, which is composed of 16 iron-cored coils arranged on a hemisphere. The developed prototype is displayed in Fig. 1.17. The rotor and stator pole arrangement is carried out using recursive semi regular packing, which resulted in an octahedral symmetry for the rotor and icosahedral symmetry for the stator. Difference in rotor-pole and stator-pole symmetry allows to change the orientation of the rotor when the coils are appropriately energized. The commutation problem is addressed by approximating the interaction of the magnetic fields of one rotor pole and one stator pole as potential functions. These potential functions are approximated using spherical harmonics and thanks to rotational invariant properties of the latter the computations are simplified. Experimental results are presented in reference [60]. The measurement of the orientation of the rotor uses a vision-based approach combined with a recursive nonlinear optimization algorithm [61,62].

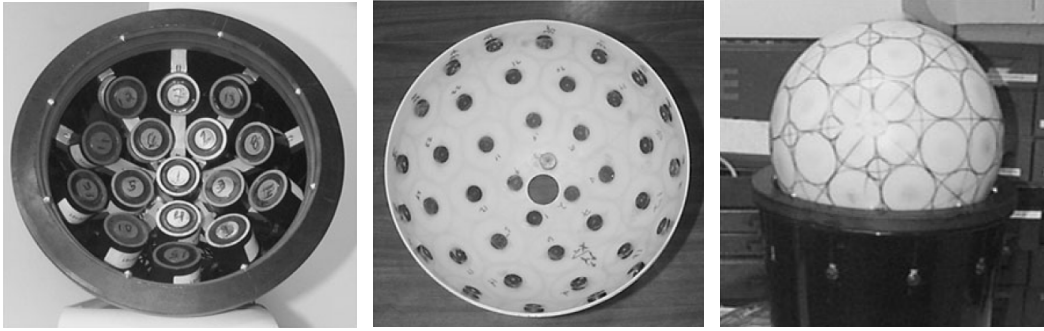


Figure 1.17. Prototype of 3-DOF stepper actuator proposed by Chirikjian and Stein [59]. (Left) Stator. (Center) Rotor. (Right) Assembly. Figure adapted from [24].

A similar electromagnetic spherical actuator was developed by Li et al. [63]. The rotor consists of two half spheres each placed symmetrically by 80 rare-earth magnets along the inside surface. The stator consists of 16 coils with soft iron cores. A model of the magnetic field inside the permanent magnet spherical motor is developed using integral equation method (IEM). Subsequently, the analysis of the electromagnetic system for robust control based trajectory algorithm development is done considering individual rotor and stator pair interactions [64]. The structure of the torque model is similar to that of the SWM [46,47] and the resulting torque-current characteristic is linear. Then, based on the latter model, a fuzzy inference system is used to predict the rotor orientation and perform the activation operation of the stepping motor [65]. Finally, based on a nonlinear system dynamic model, a robust neural network control scheme is presented to eliminate uncertainties and to improve the trajectory tracking [66,67]. Finally, using 3-D FEM simulations, Li et al. have analyzed the magnetic flux density distribution and the torque of a novel structure. The rotor is composed of four PM parts with alternate polarity distribution (see [58,68]) and the stator has two layers of four electromagnets [69].

1.3. Literature Review of 3-DOF Spherical Actuators

Another geometrical design scheme to arrange stator and rotor poles in order to achieve a fine discretized motion is presented by [70]. The design resulted in a rotor with 212 permanent magnet poles and a stator with 58 electromagnet poles. Finite element simulations for force computation and control algorithm design for motion planning are also reported. A fuzzy control algorithm is used to map the motor inputs (motor orientations and coil currents of the activated EM pole) to the motor output represented by the resulted torque that determines rotor dynamic conditions.

Wang et al. created a 2-DOF spherical actuator composed by a 2-pole rotor with PMs diametrically magnetized and a stator with 3-phase winding arrangement [71]. The tilt excursion is limited to $\pm 45^\circ$ and the continuous torque estimated to 0.15 Nm. Kinematic and dynamic equations are derived in terms of Euler angles. The derived dynamic equations possess the same properties of those in robot manipulators. A robust outer Proportional-Derivative (PD) position-control law is used in conjunction with an inner Proportional-Integral (PI) current-control law. The role of the inner current-tracking loop is to minimize the effects of back-EMF and current transients on the outer position-servo loop. Subsequently, thanks to a 4-pole PM rotor formed by two pairs of parallel magnetized quarter spheres, they obtained a 3-DOF actuator capable of a continuous torque of 0.25 Nm [72]. In this case, the stator has four sets of windings, which are arranged so that three independently controllable torque components can be developed. The rotor bearing is a low-friction surface coating. An image of the developed prototype is shown in Fig. 1.18. Based on the latter design, Wang et al. presented an analytical model of the magnetic field for force and torque prediction based on the Laplace equation. They also developed a model for the rotor dynamics and proposed rotor position sensing and control algorithms [58]. As the actuator has four coils and only three independent torque inputs, the extra degree of freedom is used to minimize the power consumption of the command using a generalized Moore-Penrose inverse of the torque matrix. An application of this spherical actuator as high-fidelity force-feedback joystick can be found in [73].

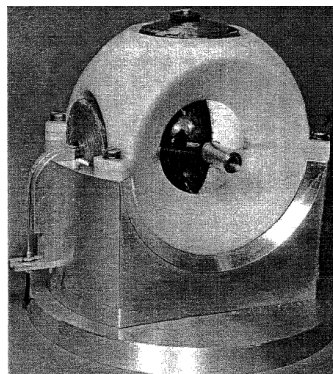


Figure 1.18. Prototype of 3-DOF spherical actuator proposed by Wang et al. [58, 72].

Kahlen et al. [74] developed a spherical machine with 3-DOF and variable pole pitch.

Chapter 1. Introduction

As can be observed in Fig. 1.19, the spherical rotor is composed by 112 magnets with dihedral shape that are arranged in seven rows each having 16 magnets with alternating north and south orientation. A total of 96 electromagnet poles are arranged on the stator yoke, which is made of a soft magnetic powder composite with relative permeability equal to 500. The movement of the rotor is limited to $\pm 60^\circ$ and the specified torque is 40 Nm in all positions. With an air gap of 40 μm , the rotor is supported by hydrostatic oil bearings built into the stator case. The position control is realized by an outer control loop with position feedback whereas the torque control is in open-loop with no feedback because torque sensors are not available. Force characteristics are carried out using FEM simulations. The force characteristics are stored in look-up tables for the high nonlinearity.

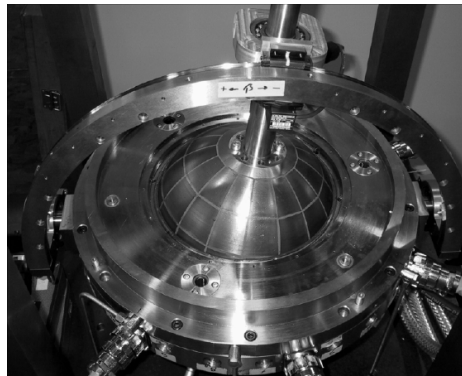


Figure 1.19. Prototype of 3-DOF spherical machine proposed by Kahlen et al. [74].

Xia et al. [75] studied a variation of the design proposed in [50], where a Halbach array of PM is located on the rotor. Multiple layers of air-core coils are mounted on the stator along different latitudes. The permanent magnets on the rotor have the shape of a dihedral cone and are placed around the rotor equator according to a discrete set of Halbach array. Each magnet segment is parallel magnetized. There are a total of four poles and 3/4/5 Halbach segments per pole are used. It is found that, compared to a conventional parallel magnetized array, the Halbach array PM spherical motor has greater torque and its magnetic field distribution is more sinusoidal. A similar study, employing Halbach-like PM array with only radial and tangential magnetized variable arcs is proposed in [76]. Based on a harmonic model of the magnetic flux density distribution, the optimization of four-pole magnet array is performed in which the higher harmonics of the radial airgap flux density are minimized to reduce the torque ripple.

Chen et al. [77] studied and manufactured a spherical actuator consisting of a rotor with eight PM poles and a two-layer stator with a total of 24 air-core coils. The rotor shell is made of aluminum with PM poles arranged in an alternative polarization pattern along the rotor equator. An image of the developed prototype is reported in Fig. 1.20. Maximum tilt angle is $\pm 15^\circ$. The study covers actuator design, torque modeling, and motion control. The orientation of the rotor is measured by a rotary encoder and two-axis

1.3. Literature Review of 3-DOF Spherical Actuators

tilt sensor incorporated with the joint.

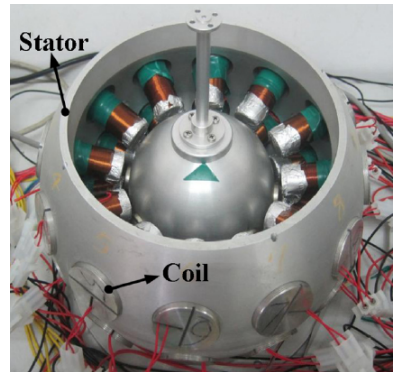


Figure 1.20. Prototype of 3-DOF spherical actuator proposed by Chen et al. [77].

To maximize the field interaction with the stator coils, Jinjun et al. [78] proposed a new design concept and procedure for utilizing rotor PMs both inside and outside of stator coils, which are arranged in a two-layer configuration. The optimization of design parameters to maximize the inclination torque without spinning is carried out using finite element numerical analysis.

Yano et al. [79] manufactured a multi-pole synchronous motor with rotor supported by gimbals and a stator with two pair of air-cored poles placed perpendicularly to each other (four electromagnets in total). The developed prototype is depicted in Fig. 1.21. The rotor, which has a diameter of 130 mm, consists of a pavement 260 small cylindrical permanent magnets attached on its surface so that the north and south poles appear on concentric circles alternately. The maximum torque of the motor is 0.49 Nm and the working area is $\pm 45^\circ$ about two axes. Subsequently, this group developed a polyhedron based spherical stepper motor [80–82], where regular polyhedra are used to place the poles on the rotor and the stator. As illustrated in Fig. 1.22, the rotor consists of eight PMs attached on the spherical shell at the vertex of a (virtual) hexahedron so that the north and south poles are located alternately. Six iron cores are also attached on the spherical shell at the center of the faces of the hexahedron inscribed in the rotor for the purpose of fixing rotation axis. The spherical shell is made of iron covered with acrylic spherical shell with thickness 4 mm. Twenty-five air-cored coils are attached on the stator, which is an acrylic spherical shell. The configuration of the coils on the (virtual) octahedron is the following: six of these coils are adjusted at the vertexes, 12 coils are attached at the center of the edges, and the remaining seven of them attached at the center of the faces. Thus, the upper face is open for the output shaft. The actuator is called 6-8 spherical stepping motor, since there are six faces on the hexahedron (rotor), and eight faces on the octahedron (stator). As pointed out in [83], if the number of vertexes of the polygon of the rotor is the same as the number of vertexes of the polygon of the stator, then the rotor would develop some singularities when the two polygons are face to face. A three-phase sinusoidal current excitation provided to six pairs of

armature coils will rotate the rotor about the axis passing to the center of the three coils (Figure 2 in [81]). Finally, rotational characteristics on the 6-8 spherical stepping motor are obtained by 3-D electromagnetic and motion coupled simulations [84]. Static torque, frequency-velocity, and torque characteristics are reported. In parallel to this development, Yano et al. [83, 85] developed a polyhedron based spherical stepper motor that can rotate about six axes. The developed prototype is shown in Fig. 1.23. The rotor is a spherical shell with 24 PMs and 12 iron bolts covered by an acrylic spherical shell. Permanent magnets are arranged at the vertices of a truncated regular octahedron with two facing faces having opposite polarities. An iron bolt is placed at the gravity center of each face, square or hexagonal, for the purpose of fixing rotation axis. The stator is an acrylic shell with 62 electromagnets to generate the rotation force. Electromagnets are placed at the vertices, the midpoints of the edges, and at the gravity center of a regular dodecahedron. The actuator is called 14-12 spherical stepping motor, since there are 14 faces on the truncated octahedron, and 12 faces on the dodecahedron. Because two given parallel faces of the truncated octahedron (rotor, square or hexagon) and the dodecahedron (stator, pentagon) have different number of vertexes, rotation about an axis passing through the middle of the dodecahedron face is possible using a five-phase excitation. There are a total of six possible rotation axis (one for each face of the dodecahedron). Basic experimental results using this actuator are presented in [85, 86].

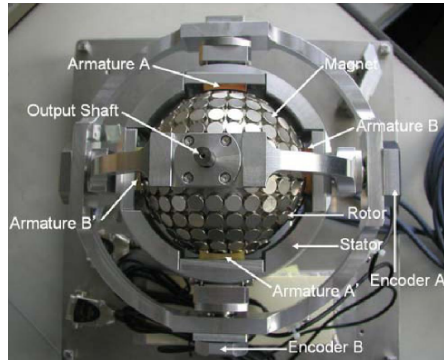


Figure 1.21. Prototype of multi-pole synchronous motor developed by Yano et al. [79].

We conclude this literature review on spherical actuators by mentioning the three-axis micro magnetic bearing device developed by Boletis [87] that we report in Fig. 1.24. The stator consists of five vertically arranged electromagnets; the central electromagnet and the four lateral electromagnets actively control the axial and radial position of the rotor, respectively. Moreover, the four lateral electromagnets are simultaneously employed as a two-phase induction motor, making it possible to accelerate the rotor about the vertical axis. The rotor consists of a steel spherical ball with diameters ranging from 1 mm down to 0.4 mm. The position of the rotor inside the airgap is measured with two orthogonally arranged optical subsystems. Each subsystem is composed of a red laser source and a four-segment photodiode. With a 1 mm diameter rotor, the maximum achieved rotating speed is 180 000 rpm at atmospheric pressure and $2.88 \cdot 10^6$ rpm at $5 \cdot 10^{-5}$ bar.

1.3. Literature Review of 3-DOF Spherical Actuators

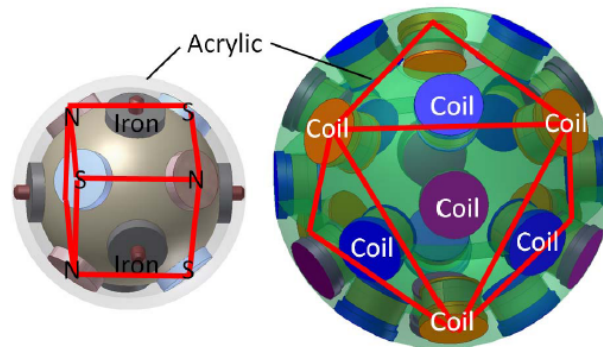


Figure 1.22. Polyhedron based 6-8 spherical stepper motor proposed by Yano et al. [80–82]. (Left) Rotor. (right) Stator.

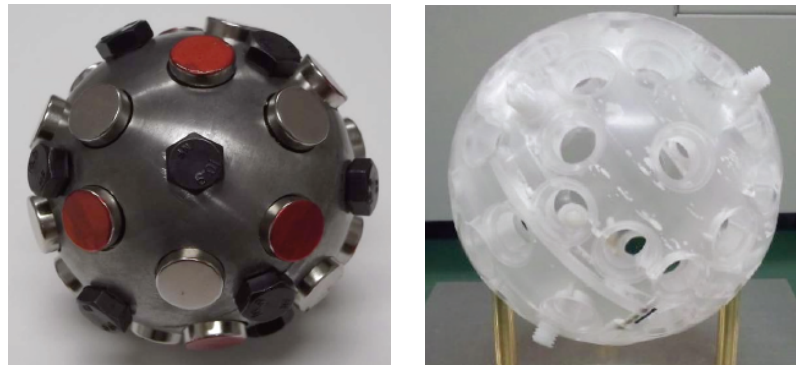


Figure 1.23. Developed prototype of polyhedron based 14-12 spherical stepper motor proposed by Yano et al. [83, 85]. (Left) Rotor. (Right) Stator without coils.

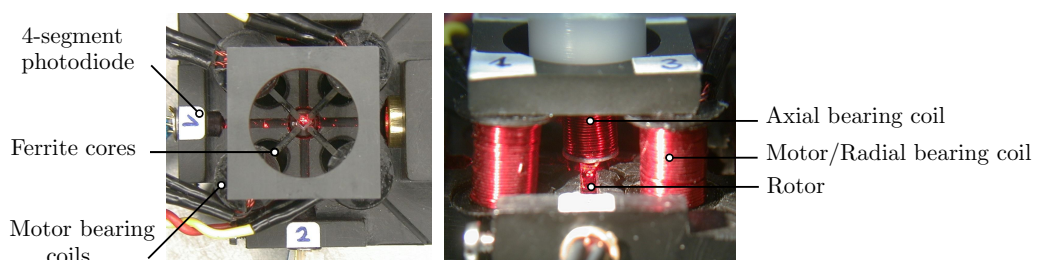


Figure 1.24. (Left) Top-view of prototype (without central coil). (Right) Levitation of the 0.6 mm rotor. Drawing adapted from Boletis [87].

1.4 The Proposed Reaction Sphere

This thesis deals with modeling, estimation, and control issues of a novel concept of reaction sphere that is based on invention [1]. In this reaction sphere concept, a permanent magnet solution was preferred to reluctant and inductive approaches because it guarantees linearity, i.e., decoupling of the motor and bearing function (see Section 3.5), and a potential better efficiency with the possibility to recover the kinetic energy stored in the rotor. In this section, we provide a general description of the proposed reaction sphere concept as well as we present the manufactured hardware and prototype.

1.4.1 General Description

The reaction sphere is a PM synchronous spherical actuator whose rotor is magnetically levitated and can be accelerated about any desired axis. The 3-DOF motor is synchronous and has PMs and electromagnets placed at the vertices of regular polyhedra. A schematic representation of the reaction sphere and its elements is presented in Fig. 1.25. The permanent magnet rotor in Fig. 1.25a is composed of eight poles, each of them being either a north pole if $xyz > 0$ or a south pole otherwise (x , y , and z are the coordinates of a given point of the sphere). As shown in Fig. 1.25b, permanent magnets have a spherical shell shape and are adjusted on a back-iron hollow spherical shell. The rotor is hollow to optimize the inertia-moment-to-mass ratio. The stator has 20 air-core electromagnets, each corresponding to one vertex of a virtual dodecahedron as displayed in Fig. 1.25c. As illustrated in Fig. 1.25d, electromagnets are mounted on a spherical support, which could possibly be ferromagnetic. Notice that a ferromagnetic stator increases the actuator forces and torques and at the same time provides an important shielding role [52].

Before selecting the eight-pole permanent magnet configuration of the rotor, several alternative arrangements have been considered. A two-pole rotor, obtained by dividing a sphere into two equal hemispheres, one of them being the north pole of a magnet and the other the south pole, cannot be used because no torque can be applied about the pole axis. Therefore, only a 2-D motor can be realized with such configuration. A two-pole rotor was used by Wang et al. in [71]. The four-pole rotor proposed in [58, 68, 69], obtained by splitting the sphere into four equal segments, is capable of 3-DOF motion. However, such a PM pole arrangement would most likely lead to an anisotropic inertia tensor, which is not acceptable for the reaction sphere, as the rotor dynamics would depend on the instantaneous rotation axis. Therefore, in order to keep as much symmetry as possible, rotor and stator poles were arranged following the vertices of regular polyhedra, among which possible choices are the tetrahedron (4 vertices), the octahedron (6 vertices), the cube (8 vertices), the icosahedron (12 vertices), and the dodecahedron (20 vertices). Of these five polyhedra, only the cube has faces with an even number of edges and only its vertices can alternatively be the north and south poles of a PM. Therefore, a cubic (eight-pole) distribution was selected for the spherical rotor, which is ideally

split into eight quarters, each of them being either a north pole if $xyz > 0$ or a south pole otherwise. The eight-pole permanent magnet rotor is displayed in Fig. 1.25a and Fig. 1.25b. An eight-pole arrangement was also considered by Ninhuijs et al. for their spherical permanent magnet gravity compensator [88, 89].

Given the 8-pole PM spherical rotor, numerical simulations performed using different stator pole arrangements on regular polyhedra have shown that the minimum necessary number of vertices is 20 [1, 90]. As a matter of fact, using a lower number of poles, for instance with the icosahedron (12 vertices), resulted in ill-conditioned torque characteristics matrices (see Section 3.5 for definition of these matrices) or singular configurations, where no torque could be exported in certain directions for given randomly-generated rotor orientations [90]. Monitoring the condition number of the torque characteristic matrix to study workspace non-singularity of spherical actuators was also proposed in [24]. Therefore, 20 air-core electromagnets were arranged on the stator following the vertices of a virtual dodecahedron as displayed in Fig. 1.25c. Finally, notice that these 20 electromagnets are simultaneously employed to levitate the rotor inside the stator and, at the same time, to accelerate it about any desired axis in order to produce the appropriate torque. The 20 air-cored electromagnets are rigidly attached to a stator spherical shell.

The rotor arranged in the stator is depicted in Fig. 1.25e where, for illustrative purposes, only a half stator is shown. A section view of the complete reaction sphere is displayed in Fig. 1.25f.

Contrary to many of the discussed spherical actuators in Section 1.3, as in the aimed application the torque is exported to the satellite by conservation of the angular momentum [8], the structure of the proposed reaction sphere is symmetric with no physical constraints on the rotation. Moreover, thanks to its magnetic and mechanical symmetric design, the reaction sphere rotor is isotropic, i.e., the inertia matrix is diagonal and all of the diagonal terms are equal. An isotropic rotor guarantees the same behavior independently from the axis of rotation. Finally, the reaction sphere rotor is magnetically levitated, and no friction occurs during operation.

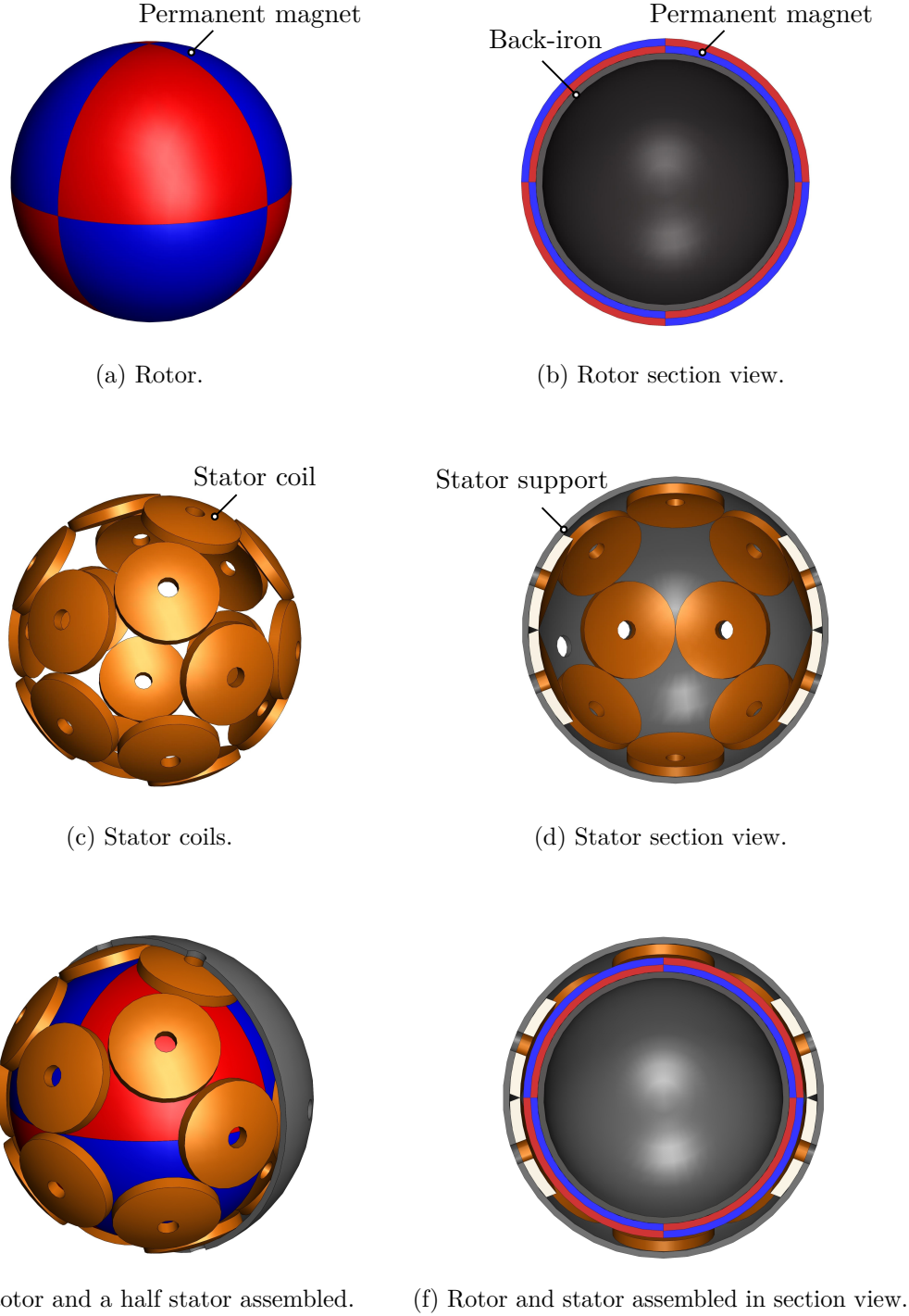


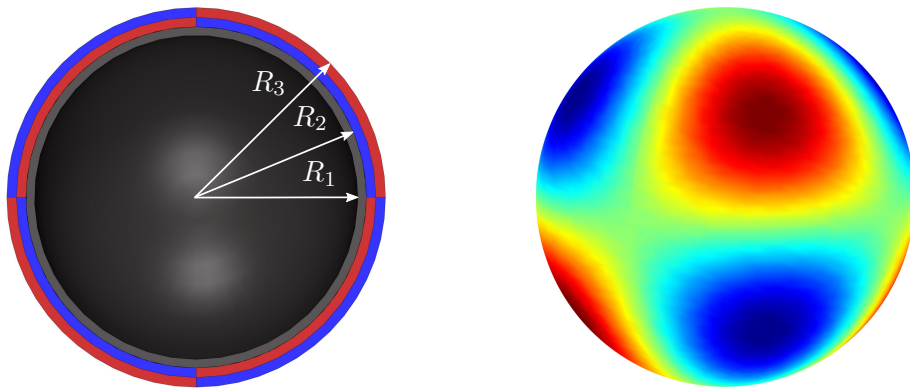
Figure 1.25. Components of the reaction sphere actuator discussed in the thesis.

1.4.2 Developed Hardware and Prototype

A first laboratory prototype of the reaction sphere that includes a permanent magnet rotor, a stator, and a control electronics was initially manufactured to validate some of the postulated characteristics. The objective of this section is to provide a general overview of the hardware and prototype, which have been developed before this thesis work. For a detailed description of these components we refer the reader to Reference [91].

Rotor

The selected eight-pole PM rotor with some relevant dimensions is displayed in Fig. 1.26a. In this conceptual configuration, the eight PM poles are ideally radially magnetized with the strength of magnetization modulated according to the octupole harmonics (real spherical harmonic of degree three and order two), which we report in Fig. 1.26b. An analytical model of the magnetic flux density corresponding to this configuration will be discussed in Section 2.3.



(a) Ideal eight-pole rotor with dimensions. (b) Fundamental octupole harmonic.

Figure 1.26. Section view of the reaction sphere ideal rotor and fundamental octupole spherical harmonic.

Notice that manufacturing permanent magnets with the spherical shape depicted in Fig. 1.26a to obtain the proposed theoretical distribution in Fig. 1.26b is both technologically challenging and expensive. Therefore, in order to obtain a valid approximation of the desired magnetic distribution, the spherical permanent magnet has been discretized using a mosaic of 728 cylindrical magnets glued on the surface of the rotor back-iron spherical shell. As depicted in Fig. 1.27, these permanent magnets have the same magnetic remanence and their height is varied to approximate the desired spherical harmonic distribution.

The back-iron hollow spherical shell in Fig. 1.26a is manufactured with iron material.

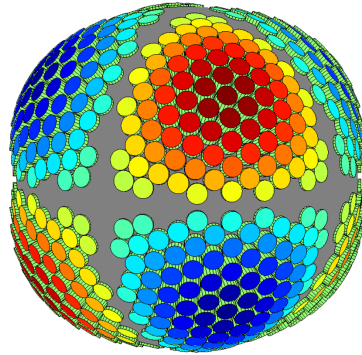


Figure 1.27. Illustration of the developed rotor composed of a mosaic with 728 cylindrical permanent magnets.

The inner back-iron radius R_1 is equal to 75 mm and the outer back-iron radius R_2 is 80 mm. Permanent magnets are made of Neodymium iron boron (NdFeB) with magnetic remanence equal to 1.4 T. Their diameters are 10.1 mm and their height is varied from 0.8 mm to 9.0 mm. The rotor during the assembly phase is displayed in Fig. 1.28 (left). Permanent magnets are glued on the back-iron hollow sphere using a pattern of pre-machined support composed of non-magnetic Acrylonitrile Butadiene Styrene (ABS) material. Then, the rotor is surrounded by a non-magnetic cover to protect the PMs and to obtain a smooth spherical surface, which is necessary to measure the position of the rotor inside the stator. Finally, six balancing masses could be used for the dynamic counterbalance of the rotor. The total rotor mass is 5.5 kg.

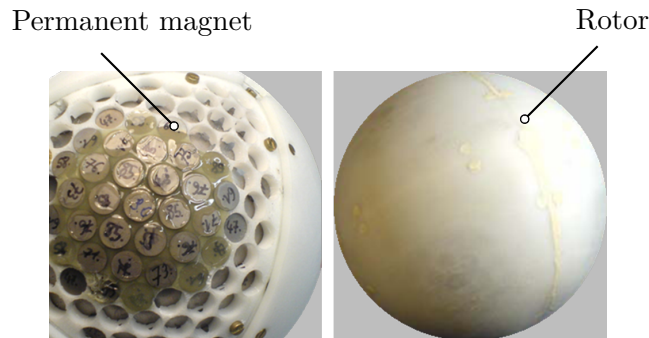


Figure 1.28. (Left) Spherical rotor during assembly showing cylindrical permanent magnets with different heights. (Right) Final rotor.

Stator

The selected stator comprises 20 air-core electromagnets arranged at the vertexes of a dodecahedron. A section view of the stator configuration with some relevant dimensions is depicted in Fig. 1.29. Initially, the spherical shell of the stator was manufactured using

a magnetic material to benefit from a higher magnetic flux density in the airgap and a sufficient shielding capability, which is essential for the electromagnetic compatibility of the reaction sphere. However, with the use of a magnetic stator, we experimented strong sticking reluctant forces between the stator and the rotor when the latter was not centered. For this reason, we manufactured a non-magnetic spherical shell using ABS. There are several advantages using a non-magnetic stator including the absence of iron losses due to eddy currents, less density and thus less weight, no rotor-stator sticking forces leading to easier assembly and control, no saturation effects, and less perturbations of coil currents on magnetic flux density measurements. On the other hand, however, the disadvantages with respect to a magnetic stator include a reduced magnetic flux density in the airgap (weaker motor), the necessity of a supplementary external magnetic shield, and less thermal conductivity.

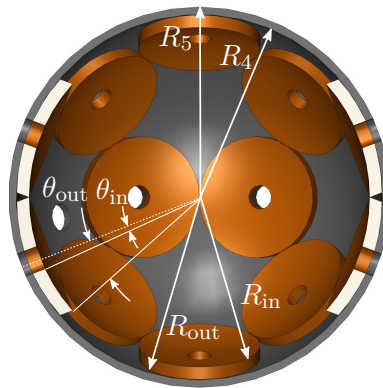


Figure 1.29. Section view of the reaction sphere 20-pole stator with relevant dimensions.

In Fig. 1.30 (left) we display one half stator composed of a hemispherical shell manufactured with ABS material and 10 air-core coils, which have been manufactured with the desired spherical shape. Moreover, the stator is equipped with a total of 12 ABS cells, which besides protecting the coils they also support magnetic flux density sensors necessary to compute force and torque models for any possible orientation of the rotor (see Chapter 4). Relevant geometrical measurements of rotor and stator are summarized in Table 1.2. Coil resistances and inductances are approximately $5.40\ \Omega$ and $6.65\ \text{mH}$, respectively.

Table 1.2. Geometrical parameters of reaction sphere rotor and stator.

Inner back-iron R_1	75 mm	Outer back-iron R_2	80 mm
Inner stator R_4	99 mm	Outer stator R_5	103 mm
Inner coil R_{in}	92 mm	Outer coil R_{out}	99 mm
Inner coil angle θ_{in}	3.7°	Inner coil angle θ_{out}	16.0°

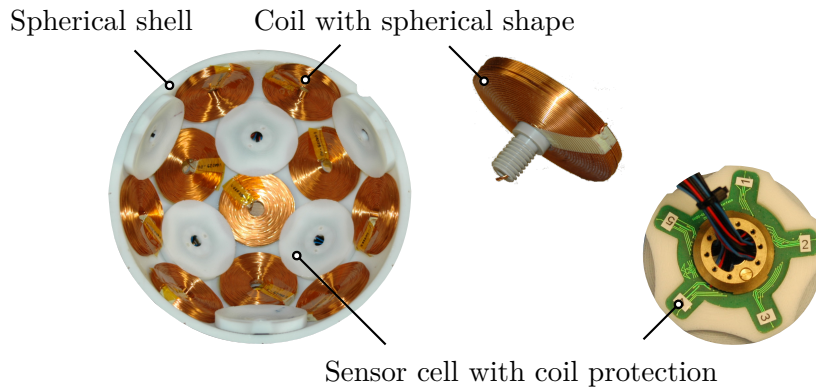


Figure 1.30. One of the two plastic stator hemispheres with air-cored coils and sensor cells with plastic protections.

Control Electronics

The control electronics is composed of a dedicated control rack electronics combined with a commercial DSpace DS1005 PowerPC external computational platform, on which the control algorithms are embedded for real-time control. The control rack electronics, which is displayed in Fig. 1.31, includes 20 linear PI current regulators responsible to supply the necessary current to the coils. The closed-loop bandwidth of the current regulators is approximately 1.2 kHz. The power supply voltage is ± 36 V. Additionally, the control rack comprises an analogical treatment of various sensor signals, including temperatures, coil currents, optical displacement measurements, and magnetic flux density measurements. These pre-processed signals are dispatched to the DSpace platform for digital conversion and processing.

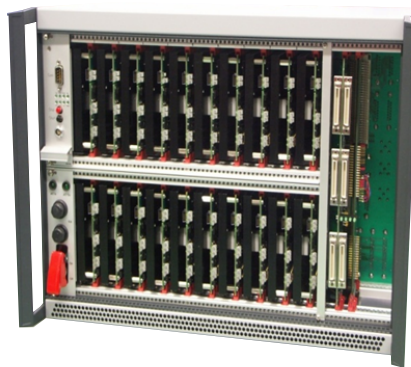


Figure 1.31. Developed control rack electronics for the reaction sphere prototype.

1.5 Motivation and Problem Definition of the Thesis

As discussed in Section 1.2, a reaction sphere is a valuable alternative to a four-wheel configuration for spacecraft attitude control. However, none of the presented designs or

1.5. Motivation and Problem Definition of the Thesis

concepts have reached the technology readiness level needed for a commercial product. The difficulty is in the 3-DOF motor, the bearing, and its combination. Recent advances in simulation and modeling, power electronics, sensing, and especially in high-power space-qualified processors give a totally new chance to the concept.

Among the challenges related to the proposed reaction sphere concept, the magnetic bearing of the rotor has to be taken in serious consideration. Although magnetic bearing in single-axis rotatory devices [92] and ferromagnetic spheres [87] is already successfully established, to the knowledge of the author, no magnetic bearing of PM spherical actuators has been reported yet. Therefore, development of a magnetic bearing control strategy will be of pivotal importance for a possible employment of the proposed reaction sphere as a momentum exchange device.

In order to address magnetic levitation, modeling aspects of the spherical actuator have to be investigated. In particular, force and torque models need to be available to understand the relation between a given set of stator currents and the resulting force and torque outputs. A crucial aspect of these models is the real-time implementability. As a matter of fact, although terrestrial validation can be carried out with state-of-the art computing platforms leading to large computational capabilities, available computational power in space is generally more limited due to lag of space qualified processors.

The derivation of force and torque models requires knowledge of the magnetic flux density model of the actuator, which is also important for model-based rotor orientation determination. Because a model describing the magnetic flux density distribution relative to the proposed rotor architecture is not available in the literature, this model needs to be addressed.

One of the most critical aspect related to forces and torques developed by the actuators is their dependence to the orientation of the rotor inside the stator. The estimation of the orientation of the rotor (not necessarily the physical/mechanical orientation but possibly also the magnetic orientation) in magnetic bearing motor technology is an essential aspect for the automatic control [92], which is responsible for closed-loop performance and stabilization of the actuator. Therefore, the orientation of the rotor is measured, or estimated, at each sampling interval and used to compute the actuation for the bearing and motor control loops. Furthermore, the rotor estimation accuracy for a spherical actuator used as momentum exchange device will have a dramatic impact on the pointing performances and exported vibrations as rotor estimation errors would result in undesired force and torque components. Therefore, a precise and reliable information of the rotor orientation at every sampling time is highly desired and necessary for the automatic control of the reaction sphere.

Furthermore, to manage the stored angular momentum, and for attitude control purposes, measurement of the angular velocity of the rotor inside the stator is required by the

ADCS. Therefore, techniques to estimate the angular velocity of the rotor should also be considered as fundamental ingredients for a potential use of the reaction sphere in space. Similarly to force and torque models, real-time implementation should be a driving constraint for the investigation of possible estimation schemes.

1.6 Outline of the Thesis

In Chapter 2 we present two distinct approaches to develop expressions of the magnetic flux density produced by the PM rotor. First, the magnetic flux density distribution is derived using an analytical approach, which assumes a purely octupole radial magnetization of the rotor as discussed in Section 1.4 above. The derivation of the analytical model is based on solving Laplace's and Poisson's equations. Second, to take into account higher order harmonics, the magnetic flux density model is derived using a hybrid FEM-analytical approach, in which FEM or measured derived values are combined with other boundary conditions on a known analytical structure. Finally, the developed models are validated using FEM simulations.

Chapter 3 discusses the development of forward and inverse force and torque analytical models for the reaction sphere actuator. The development of these models is based on the Lorentz force law taking into account a general expression of the magnetic flux density within the airgap derived in Chapter 2. To derive these models, we first consider the interaction between the rotor magnetic flux density and one stator coil and subsequently invoke the superposition principle to calculate forces and torques generated by the complete set of coils. Afterwards, we discuss force and torque inverse models, which allow calculating a minimum-energy current vector to satisfy a given force and torque pair. To conclude, we validate the developed force and torque models using FEM simulations.

Chapter 4 presents a method to estimate the magnetic state of the rotor and an optimal arrangement of magnetic flux density sensors. As will be shown, the magnetic state is defined as a vector of spherical harmonic decomposition coefficients, which deliver to force and torque models all the information relative to the orientation of the rotor inside the stator. To estimate the magnetic state, several magnetic flux density sensors are necessary. Therefore, in Chapter 4 we also propose an optimization strategy to position these sensors so that the influence of the measurement noise on force and torque relative errors is minimized. To conclude, we perform numerical simulations to verify the effectiveness of the proposed optimization strategy.

Chapter 5 is dedicated to the estimation of the back-EMF voltage and the rotor angular velocity, both necessary for closed-loop operation of the reaction sphere actuator and, as discussed above, requested by the ADCS for angular momentum management. The estimation of the back-EMF voltages is based on using Faraday's law of electromagnetic induction whereas the rotor angular velocity is determined using the energy conservation

principle. Finally, the estimation procedures are validated using FEM simulations.

Chapter 6 presents the design optimization of a new concept of spherical rotor, which consists of eight bulk PM poles with truncated spherical shape that are parallel magnetized and adjusted on the back-iron structure, which has truncated octahedral shape. This new concept of spherical rotor was proposed as an alternative to the first developed rotor introduced in Section 1.4 with the objective of improving its manufacturability. The optimization of the rotor is performed using FEM simulations based on a set of specifications that are defined taking into account the previously developed stator and power electronics presented in Section 1.4.

In Chapter 7 we report a variety of experimental activities related to the material developed throughout the document including rotor magnetic flux density measurements, force and torque measurements, and results obtained during the first closed-loop experimental validation campaign.

Chapter 8 concludes the document with an overview of this thesis. Main contributions of this thesis and research perspectives are discussed.

2 Magnetic Flux Density Models

In this chapter magnetic flux density models for the reaction sphere rotor are presented. To begin with, we discuss various approaches to derive such models that are available in the literature related to permanent magnet spherical actuators. Then, we describe the rotor and stator reference frames as well as the locations of the stator/rotor pole coordinates. Subsequently, the magnetic flux density distribution is derived using an analytical approach, which assumes a purely octupole radial magnetization of the rotor. Next, to take into account higher order harmonics, the magnetic flux density model is derived using a hybrid FEM-analytical approach. To develop these models, we employ spherical harmonic functions and exploit their properties, which we introduce in Appendix A. Finally, the developed magnetic flux density models are validated using FEM simulations.

2.1 Introduction

The magnetic flux density model of a spherical actuator denotes the formulation of the spatial distribution of the magnetic flux density produced by the permanent magnet rotor.

The magnetic flux density model is a necessary ingredient for the formulation of force and torque models, which are necessary for position and angular velocity control of the spherical actuator. As it will be discussed in the next chapter, force and torque models are generally based on utilizing the Lorentz force law or the Maxwell stress tensor, which require knowing the spatial distribution of the magnetic flux density within the airgap. An additional motivation to develop a magnetic flux density model is the process of design optimization of the spherical actuator. In this case, knowing the magnetic flux density distribution allows the designer to find optimal parameters to satisfy given specifications.

Depending on the practical case, the magnetic flux density model can be formulated with

a variety of methods.

An analytical model of the magnetic flux density can be derived by solving Maxwell's equations under certain boundary conditions, which generally results in Laplace's or Poisson's equations in spherical coordinates [50, 52, 55, 58, 71, 72, 75, 76, 93–97]. The analytical solution is conveniently expressed as a series of space spherical harmonics functions.

An alternative approach to characterize the magnetic flux density model consists in modeling both the stator coils and the permanent magnets as DMP [48, 56, 98–101]. The method utilizes an assembly of appropriately distributed dipoles to account for the shape and magnetization of the physical magnet. The distribution and number of dipoles can be obtained by minimizing an error function between the magnetic potential at any point given by all the dipoles of the model and a known solution of magnetic potential. As it will be recalled in the next chapter, with the DMP formulation the dipole force computation is expressed in closed-form. To account for the effects of magnetic conducting materials on the DMP method, an image method can be applied [102].

The Magnetic Equivalent Circuit (MEC) method has also been employed to analyze the magnetic flux density of a spherical actuator [103]. Similarly to FEM, the model of PM spherical motor is evenly meshed into a lumped element network, and the expressions of reluctances in the element are deduced. Changes in PM topology require construction of a new MEC model.

The charge model is another analytical method to derive a magnetic flux density model [89, 104, 105]. In this technique, PMs are replaced by an equivalent spatial (volume or surface) distribution of “magnetic charges”. Then, the charge distribution is used as a source term in the magnetostatic field equations. If the PM is in free space, its magnetic flux density is obtained by integration of the volume and surface charge densities [106]. Since this method requires integration, it is not suitable for complex pole geometries.

Finally, Finite Element Analysis (FEA) is widely adopted in the design optimization, model verification of spherical actuators. Examples of references employing this method are [68, 69, 107, 108].

Magnetic flux density models are generally derived in a reference frame attached to the rotor. Then, because forces and torques are produced by the interaction of the rotor magnetic flux density with the stator coil currents, a change of coordinates is performed to express the magnetic flux density in the stator reference frame. Generally, this change of coordinates is parametrized with a set of three Euler angles to account for the orientation of the rotor [41, 43, 48, 51, 58, 97, 98, 109].

To derive the magnetic flux density model for the reaction sphere, we consider in this chapter two distinct approaches. The first approach is purely analytical, and it is based

on solving Laplace's and Poisson's equations. Thanks to the selected octupole cubic magnetization, the magnetic flux density distribution within the airgap can be expressed as a linear combination of a finite number of spherical harmonic functions. In the second approach, we adopt a hybrid FEM-analytical method, in which FEM or measured derived values are combined with other boundary conditions on a known analytical structure to derive expressions for the magnetic flux density. This hybrid FEM-analytical approach was proposed to derive an expression of the magnetic flux density for highly complex rotor geometries. In both approaches, the magnetic flux density is initially derived in rotor coordinates. Subsequently, two distinct change of coordinates are proposed. In the first one, the change of coordinate frame is performed by exploiting spherical harmonic properties under rotation. The second method is based on the conventional change of reference frames operated with a rotation matrix (parametrized using Euler angles or quaternions).

2.2 System Description

2.2.1 Rotor and Stator Reference Frames

Definitions

As depicted in Fig. 2.1, let \mathcal{B} be the rotor fixed reference frame with a corresponding triad of mutually orthogonal base vectors $\{\hat{\mathbf{x}}_b, \hat{\mathbf{y}}_b, \hat{\mathbf{z}}_b\}$ with origin at $O_{\mathcal{B}}$. Similarly, let \mathcal{S} be the stator fixed reference frame with base vectors $\{\hat{\mathbf{x}}_s, \hat{\mathbf{y}}_s, \hat{\mathbf{z}}_s\}$ with origin at $O_{\mathcal{S}}$. Note that for the derivation of the magnetic flux density model, the origin of the rotor reference frame coincides with the origin of the stator reference frame. Then, a position vector \mathbf{r} can be written in the stator reference frame as

$$\mathbf{r} = {}^{\mathcal{S}}\mathbf{r} = \begin{bmatrix} x_s \\ y_s \\ z_s \end{bmatrix} = x_s \hat{\mathbf{x}}_s + y_s \hat{\mathbf{y}}_s + z_s \hat{\mathbf{z}}_s, \quad (2.1)$$

where $\{x_s, y_s, z_s\}$ are the Cartesian coordinates of \mathcal{S} . The notation ${}^{\mathcal{S}}\mathbf{r}$ is used to specify that the vector components of \mathbf{r} are taken along the unit directions vectors of the \mathcal{S} coordinate systems. Similarly, \mathbf{r} can be written in the rotor reference frames as

$${}^{\mathcal{B}}\mathbf{r} = \begin{bmatrix} x_b \\ y_b \\ z_b \end{bmatrix} = x_b \hat{\mathbf{x}}_b + y_b \hat{\mathbf{y}}_b + z_b \hat{\mathbf{z}}_b, \quad (2.2)$$

Chapter 2. Magnetic Flux Density Models

where $\{x_b, y_b, z_b\}$ are the Cartesian coordinates of \mathcal{B} . Then, a vector-valued function \mathbf{A} can be expressed in the stator and rotor frames as

$${}^S\mathbf{A} = \begin{bmatrix} A_{x_s}(x_s, y_s, z_s) \\ A_{y_s}(x_s, y_s, z_s) \\ A_{z_s}(x_s, y_s, z_s) \end{bmatrix} = A_{x_s}(x_s, y_s, z_s)\hat{\mathbf{x}}_s + A_{y_s}(x_s, y_s, z_s)\hat{\mathbf{y}}_s + A_{z_s}(x_s, y_s, z_s)\hat{\mathbf{z}}_s, \quad (2.3)$$

and

$${}^B\mathbf{A} = \begin{bmatrix} A_{x_b}(x_b, y_b, z_b) \\ A_{y_b}(x_b, y_b, z_b) \\ A_{z_b}(x_b, y_b, z_b) \end{bmatrix} = A_{x_b}(x_b, y_b, z_b)\hat{\mathbf{x}}_b + A_{y_b}(x_b, y_b, z_b)\hat{\mathbf{y}}_b + A_{z_b}(x_b, y_b, z_b)\hat{\mathbf{z}}_b. \quad (2.4)$$

The stator and rotor spherical polar coordinates (r_s, θ_s, ϕ_s) and (r_b, θ_b, ϕ_b) of a point P are defined in Fig. 2.1. As shown in this figure, the two angles θ_s and ϕ_s completely define the orientation of the unit vectors $\hat{\mathbf{r}}_s$, $\hat{\boldsymbol{\theta}}_s$, and $\hat{\boldsymbol{\phi}}_s$ relative to $\{\hat{\mathbf{x}}_s, \hat{\mathbf{y}}_s, \hat{\mathbf{z}}_s\}$. Similarly, the two angles θ_b and ϕ_b completely define the orientation of the unit vectors $\hat{\mathbf{r}}_b$, $\hat{\boldsymbol{\theta}}_b$, and $\hat{\boldsymbol{\phi}}_b$ relative to $\{\hat{\mathbf{x}}_b, \hat{\mathbf{y}}_b, \hat{\mathbf{z}}_b\}$.

Two spherical coordinate systems are defined for the rotor and stator reference frames. The stator spherical coordinate system \mathcal{S}^S is defined through the triad of unit vectors $\{\hat{\mathbf{r}}_s, \hat{\boldsymbol{\theta}}_s, \hat{\boldsymbol{\phi}}_s\}$. Similarly, we define the rotor spherical coordinate system \mathcal{B}^S with the triad of unit vectors $\{\hat{\mathbf{r}}_b, \hat{\boldsymbol{\theta}}_b, \hat{\boldsymbol{\phi}}_b\}$. Then, any vector \mathbf{A} in the stator frame can be expressed in terms of \mathcal{S}^S as

$$\mathbf{A} = {}^S\mathbf{A} = \begin{bmatrix} A_{r_s} \\ A_{\theta_s} \\ A_{\phi_s} \end{bmatrix} = A_{r_s}\hat{\mathbf{r}}_s + A_{\theta_s}\hat{\boldsymbol{\theta}}_s + A_{\phi_s}\hat{\boldsymbol{\phi}}_s, \quad (2.5)$$

where $\{\hat{\mathbf{r}}_s, \hat{\boldsymbol{\theta}}_s, \hat{\boldsymbol{\phi}}_s\}$ are also spatially-varying functions that can be written in terms of the Cartesian unit vectors $\{\hat{\mathbf{x}}_s, \hat{\mathbf{y}}_s, \hat{\mathbf{z}}_s\}$. Transformations from and to stator spherical coordinates are summarized in Table 2.1 and Table 2.2. The notation and transformations are similar for the rotor spherical coordinates.

Table 2.1. Transformations from Cartesian to spherical coordinates [106].

Cartesian	Spherical
$\hat{\mathbf{x}}_s$	$= \sin \theta_s \cos \phi_s \hat{\mathbf{r}}_s + \cos \theta_s \cos \phi_s \hat{\boldsymbol{\theta}}_s - \sin \phi_s \hat{\boldsymbol{\phi}}_s$
$\hat{\mathbf{y}}_s$	$= \sin \theta_s \sin \phi_s \hat{\mathbf{r}}_s + \cos \theta_s \sin \phi_s \hat{\boldsymbol{\theta}}_s + \cos \phi_s \hat{\boldsymbol{\phi}}_s$
$\hat{\mathbf{z}}_s$	$= \cos \theta_s \hat{\mathbf{r}}_s - \sin \theta_s \hat{\boldsymbol{\theta}}_s$
x_s	$= r_s \sin \theta_s \cos \phi_s$
y_s	$= r_s \sin \theta_s \sin \phi_s$
z_s	$= r_s \cos \theta_s$
A_{x_s}	$= \sin \theta_s \cos \phi_s A_{r_s} + \cos \theta_s \cos \phi_s A_{\theta_s} - \sin \phi_s A_{\phi_s}$
A_{y_s}	$= \sin \theta_s \sin \phi_s A_{r_s} + \cos \theta_s \sin \phi_s A_{\theta_s} + \cos \phi_s A_{\phi_s}$
A_{z_s}	$= \cos \theta_s A_{r_s} - \sin \theta_s A_{\theta_s}$

Table 2.2. Transformations from spherical to Cartesian coordinates [106].

Spherical	Cartesian
$\hat{\mathbf{r}}_s$	$= \sin \theta_s \cos \phi_s \hat{\mathbf{x}}_s + \sin \theta_s \sin \phi_s \hat{\mathbf{y}}_s + \cos \theta_s \hat{\mathbf{z}}_s$
$\hat{\boldsymbol{\theta}}_s$	$= \cos \theta_s \cos \phi_s \hat{\mathbf{x}}_s + \cos \theta_s \sin \phi_s \hat{\mathbf{y}}_s - \sin \theta_s \hat{\mathbf{z}}_s$
$\hat{\boldsymbol{\phi}}_s$	$= -\sin \phi_s \hat{\mathbf{x}}_s + \cos \phi_s \hat{\mathbf{y}}_s$
r_s	$= \sqrt{x_s^2 + y_s^2 + z_s^2}$
θ_s	$= \cos^{-1} \frac{z_s}{r_s}$
ϕ_s	$= \tan^{-1} \frac{y_s}{x_s}$
A_{r_s}	$= A_{x_s} \sin \theta_s \cos \phi_s + A_{y_s} \sin \theta_s \sin \phi_s + A_{z_s} \cos \theta_s$
A_{θ_s}	$= A_{x_s} \cos \theta_s \cos \phi_s + A_{y_s} \cos \theta_s \sin \phi_s - A_{z_s} \sin \theta_s$
A_{ϕ_s}	$= -A_{x_s} \sin \phi_s + A_{y_s} \cos \phi_s$

Finally, in nominal orientation, the rotor frame is superimposed to the stator frame.

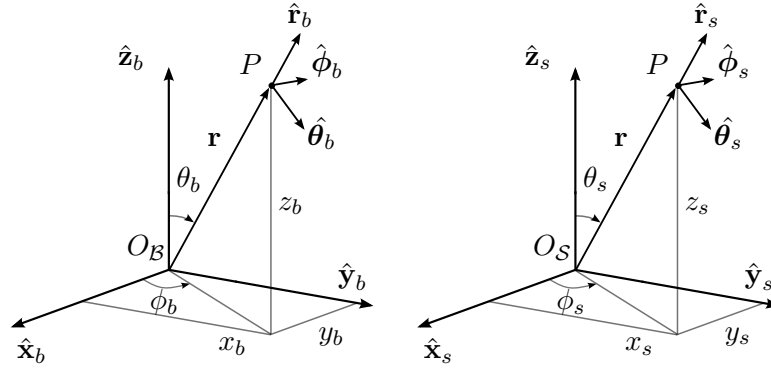


Figure 2.1. (Left) Rotor reference frame. (Right) stator reference frame.

Transformation between Rotor and Stator Reference Frames

The unit vectors of the stator reference frame are related to those of the rotor reference frame by

$$R_{\mathcal{S} \rightarrow \mathcal{B}} \{ \hat{\mathbf{x}}_s, \hat{\mathbf{y}}_s, \hat{\mathbf{z}}_s \} = \{ \hat{\mathbf{x}}_b, \hat{\mathbf{y}}_b, \hat{\mathbf{z}}_b \}, \quad (2.6)$$

where $R_{\mathcal{S} \rightarrow \mathcal{B}} \in \mathbb{R}^{3 \times 3}$ is a rotation matrix belonging to the rotation group $SO(3)$. The rotation matrix $R_{\mathcal{S} \rightarrow \mathcal{B}}$ can be parametrized, for example, using Euler angles or quaternions. For a complete description of rotation matrix parametrization see [8]. In this section, to be consistent with the theory of spherical harmonics rotation, we adopt the ZYZ Euler parameterization using angles α , β , and γ .

2.2.2 Twenty-pole Stator

Figure 2.2 shows the motor with the rotor in nominal position. The stator comprises 20 poles evenly spread on the sphere and arranged at the vertices of a dodecahedron. The coordinates of the stator coils \mathbf{P}_k , with $k = 1, 2, \dots, 10$, are expressed in the stator reference frame \mathcal{S} as

$$\mathbf{P}_1 = \frac{1}{\sqrt{3}} \begin{bmatrix} 0 \\ 1-G \\ -G \end{bmatrix}, \quad \mathbf{P}_2 = \frac{1}{\sqrt{3}} \begin{bmatrix} 0 \\ G-1 \\ -G \end{bmatrix}, \quad \mathbf{P}_3 = \frac{1}{\sqrt{3}} \begin{bmatrix} -1 \\ -1 \\ -1 \end{bmatrix}, \quad (2.7)$$

$$\mathbf{P}_4 = \frac{1}{\sqrt{3}} \begin{bmatrix} 1 \\ -1 \\ 1 \end{bmatrix}, \quad \mathbf{P}_5 = \frac{1}{\sqrt{3}} \begin{bmatrix} -1 \\ 1 \\ -1 \end{bmatrix}, \quad \mathbf{P}_6 = \frac{1}{\sqrt{3}} \begin{bmatrix} 1 \\ 1 \\ -1 \end{bmatrix}, \quad (2.8)$$

$$\mathbf{P}_7 = \frac{1}{\sqrt{3}} \begin{bmatrix} -G \\ 0 \\ 1-G \end{bmatrix}, \quad \mathbf{P}_8 = \frac{1}{\sqrt{3}} \begin{bmatrix} G \\ 0 \\ 1-G \end{bmatrix}, \quad \mathbf{P}_9 = \frac{1}{\sqrt{3}} \begin{bmatrix} 1-G \\ -G \\ 0 \end{bmatrix}, \quad (2.9)$$

$$\mathbf{P}_{10} = \frac{1}{\sqrt{3}} \begin{bmatrix} G-1 \\ -G \\ 0 \end{bmatrix}, \quad (2.10)$$

where G is the golden ratio defined as $G = \frac{1+\sqrt{5}}{2}$. As the 20 poles are evenly spread on the sphere, each pole faces another. Therefore, the remaining coil coordinates can be computed as $\mathbf{P}_{20+1-k} = -\mathbf{P}_k$, with $k = 1, 2, \dots, 10$.

2.2.3 Eight-pole Rotor

The rotor is a cubic arrangement of four north and four south magnetic poles. The coordinates $\mathbf{Q}_1, \dots, \mathbf{Q}_4$ of the south poles expressed in the rotor frame are given by

$$\mathbf{Q}_1 = \frac{1}{\sqrt{3}} \begin{bmatrix} 1 \\ 1 \\ 1 \end{bmatrix}, \quad \mathbf{Q}_2 = \frac{1}{\sqrt{3}} \begin{bmatrix} 1 \\ -1 \\ -1 \end{bmatrix}, \quad \mathbf{Q}_3 = \frac{1}{\sqrt{3}} \begin{bmatrix} -1 \\ 1 \\ -1 \end{bmatrix}, \quad \mathbf{Q}_4 = \frac{1}{\sqrt{3}} \begin{bmatrix} -1 \\ -1 \\ 1 \end{bmatrix}. \quad (2.11)$$

Note that there is a north pole opposite to any south pole and vice-versa. Hence, the coordinates $\mathbf{Q}_5, \dots, \mathbf{Q}_8$ of the north poles can be computed as $\mathbf{Q}_{8+1-k} = -\mathbf{Q}_k$, with $k = 1, \dots, 4$. In nominal position and orientation, as shown in Fig. 2.2, the rotor poles exactly match height stator poles.

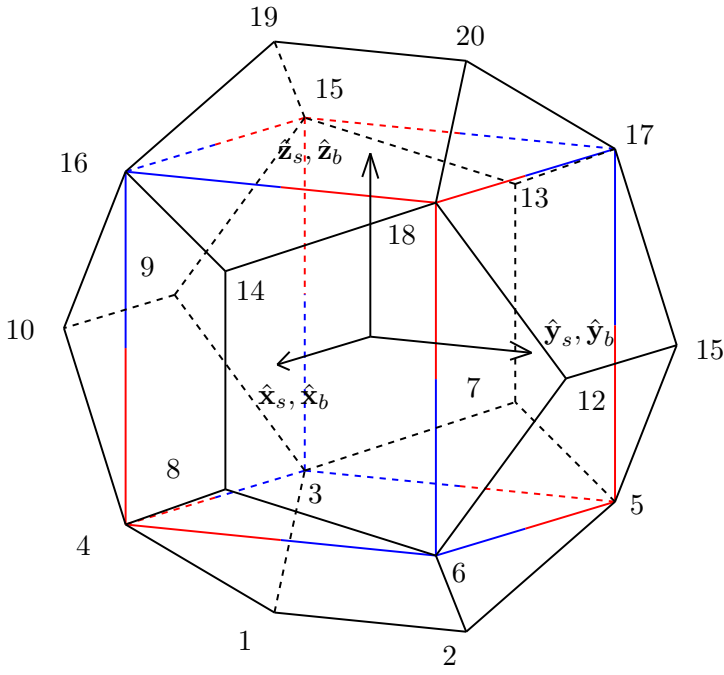


Figure 2.2. Rotor and stator reference frames with pole locations.

2.3 Analytical Model with an Ideal Octupole Rotor

In this section we derive the magnetic flux density model assuming that the rotor is ideally magnetized radially with the strength of magnetization modulated according to the octupole spherical harmonics (real spherical harmonic of degree three and order two).

2.3.1 Region Definitions and Relevant Dimensions

For the formulation of the analytical model, we use the rotor and stator model reported in Fig. 2.3 with the respective relevant dimensions. The reaction sphere is composed of a rotor back-iron (region 2) a permanent magnet (region 3), an airgap that includes the coils (region 4), and an iron stator (region 5). The rotor back-iron is hollow (region 1) and the reaction sphere is surrounded by air (region 6).

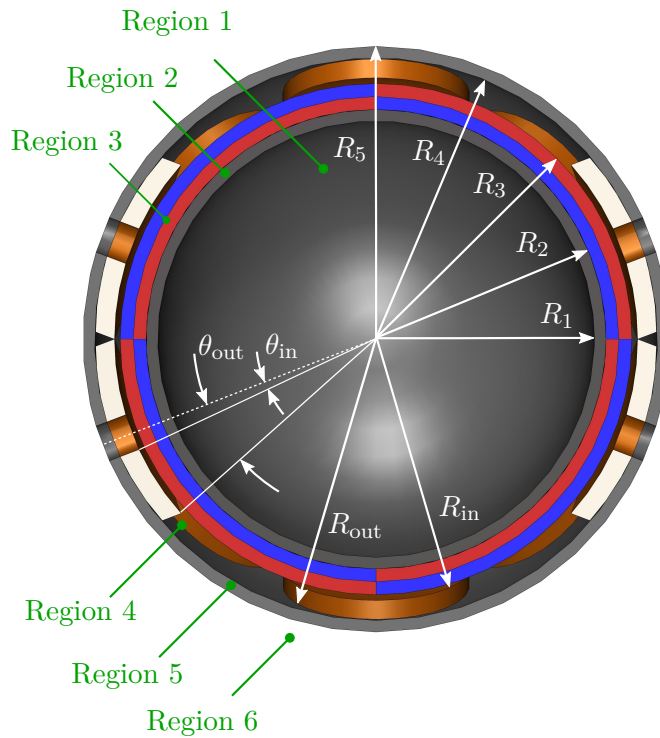


Figure 2.3. Section view of the reaction sphere for development of analytical model with ideal octupole rotor.

2.3.2 Constitutive Relations

The constitutive relations describing the magnetic effects inside the six regions are characterized by

$$\mathcal{B}^S \mathbf{B}_i = \begin{bmatrix} B_{i,r_b} \\ B_{i,\theta_b} \\ B_{i,\phi_b} \end{bmatrix} = \begin{cases} \mu_0 \mathbf{H}_i, & \text{for } i = 1, 4, 6 \\ \mu_0 \mu_R \mathbf{H}_i, & \text{for } i = 2, 5 \\ \mu_0 \mu_{PM} \mathbf{H}_i + \mathbf{B}_{rem}, & \text{for } i = 3 \end{cases} \quad (2.12)$$

where the subscript i denotes the region numbers; \mathbf{B} and \mathbf{H} are the magnetic flux density and the magnetic field respectively; μ_0 is the vacuum magnetic permeability while μ_R is the magnetic permeability of the rotor back-iron and the stator; μ_{PM} is the magnetic permeability of the permanent magnet material. Finally, \mathbf{B}_{rem} is the remanence of the permanent magnet.

2.3.3 Rotor Magnetization

In order to obtain an eight-pole spherical rotor, the remanence of the permanent magnet expressed in rotor spherical coordinates \mathcal{B}^S is

$$\mathcal{B}^S \mathbf{B}_{rem}(\theta_b, \phi_b) = \begin{bmatrix} B_{rem,r_b} \\ B_{rem,\theta_b} \\ B_{rem,\phi_b} \end{bmatrix} \quad (2.13)$$

$$= \begin{bmatrix} \frac{Y_3^2(\theta_b, \phi_b) - Y_3^{-2}(\theta_b, \phi_b)}{Y_3^2(\theta_{pole}, \phi_{pole}) - Y_3^{-2}(\theta_{pole}, \phi_{pole})} \\ 0 \\ 0 \end{bmatrix} B_{rem}, \quad (2.14)$$

where B_{rem} is the constant magnetic remanence modulated by the complex spherical harmonics $Y_3^{-2}(\theta_b, \phi_b)$ and $Y_3^2(\theta_b, \phi_b)$, while $\theta_{pole} = \cos^{-1}(1/\sqrt{3})$ and $\phi_{pole} = \pi/4$ are the coordinates defining a pole. For convenience, the radial component of the magnetization of the immobile rotor in equation (2.14) is decomposed in terms of spherical harmonics of degree three as

$$B_{rem,r_b}(\theta_b, \phi_b) = B_{rem} \sum_{m=-3}^3 c_{3,imm}^m Y_3^m(\theta_b, \phi_b), \quad (2.15)$$

where, by the orthogonality property of spherical harmonics, the decomposition coefficients $c_{3,imm}^m$ for the immobile rotor can be expressed as

$$c_{3,imm}^m = \begin{cases} \pm \frac{1}{Y_3^2(\theta_{pole}, \phi_{pole}) - Y_3^{-2}(\theta_{pole}, \phi_{pole})}, & \text{if } m = \pm 2 \\ 0, & \text{otherwise.} \end{cases} \quad (2.16)$$

Therefore, the remanence of the permanent magnet expressed in rotor spherical coordinates \mathcal{B}^S can be rewritten as

$${}^{\mathcal{B}^S} \mathbf{B}_{\text{rem}}(\theta_b, \phi_b) = \begin{bmatrix} B_{\text{rem}} \sum_{m=-3}^3 c_{3,\text{imm}}^m Y_3^m(\theta_b, \phi_b) \\ 0 \\ 0 \end{bmatrix}. \quad (2.17)$$

2.3.4 Governing Equations

Starting from the magnetostatic field equation for current-free regions $\nabla \times \mathbf{H} = 0$, the magnetic field \mathbf{H} in region i is calculated as the gradient of a magnetic scalar potential $\varphi(r_b, \theta_b, \phi_b)$ [106]

$${}^{\mathcal{B}^S} \mathbf{H}_i(r_b, \theta_b, \phi_b) = \begin{bmatrix} H_{i,r_b} \\ H_{i,\theta_b} \\ H_{i,\phi_b} \end{bmatrix} = -\nabla \varphi_i(r_b, \theta_b, \phi_b) = \begin{bmatrix} -\frac{\partial \varphi_i}{\partial r_b} \\ -\frac{1}{r_b} \frac{\partial \varphi_i}{\partial \theta_b} \\ -\frac{1}{r_b \sin \theta_b} \frac{\partial \varphi_i}{\partial \phi_b} \end{bmatrix}. \quad (2.18)$$

Then, substituting the constitutive relations in equation (2.12) into $\nabla \cdot \mathbf{B} = 0$, and employing equation (2.18), we obtain the Laplace equations for regions $i = 1, 2, 4, 5, 6$

$$\nabla^2 \varphi_i(r_b, \theta_b, \phi_b) = 0 \quad (2.19)$$

and the Poisson equation for the permanent magnet in region $i = 3$

$$\nabla^2 \varphi_3(r_b, \theta_b, \phi_b) = \frac{1}{\mu_0 \mu_R} \nabla \cdot \mathbf{B}_{\text{rem}}(\theta_b, \phi_b). \quad (2.20)$$

With definition (2.17), the Poisson equation (2.20) for the permanent magnet can be rewritten as

$$\nabla^2 \varphi_3(r_b, \theta_b, \phi_b) = \frac{2}{\mu_0 \mu_R} \frac{1}{r_b} B_{\text{rem}} \sum_{m=-3}^3 c_{3,\text{imm}}^m Y_3^m(\theta_b, \phi_b). \quad (2.21)$$

The solutions $\varphi_i(r_b, \theta_b, \phi_b)$ of equations (2.19) and (2.21) are the magnetic scalar potentials inside the six regions that are expressed in rotor spherical coordinates \mathcal{B}^S . Once these equations are solved, the magnetic flux density within region i can be calculated by first employing definition (2.18) and subsequently applying the respective constitutive relations (2.12).

2.3.5 General Solution to Laplace's and Poisson's Equations

The general solution of the Laplace equation in spherical coordinates \mathcal{B}^S characterizing region $i = 1, 2, 4, 5, 6$ is [24]

$$\varphi_i(r_b, \theta_b, \phi_b) = \sum_{n=0}^{\infty} \sum_{m=-n}^n \left(\kappa_{n,i}^m r_b^n + \xi_{n,i}^m r_b^{-(n+1)} \right) Y_n^m(\theta_b, \phi_b), \quad (2.22)$$

where $\kappa_{n,i}^m$ and $\xi_{n,i}^m$ are coefficients to be defined using boundary conditions while $Y_n^m(\theta_b, \phi_b)$ are complex-valued spherical harmonic functions. The general solution to the Poisson equation (2.21) is obtained by including an additional term to solution (2.22) so as to satisfy the conditions imposed by the excitation term on the right-hand side of equation (2.21). Therefore,

$$\begin{aligned} \varphi_3(r_b, \theta_b, \phi_b) = & \sum_{n=0}^{\infty} \sum_{m=-n}^n \left(\kappa_{n,3}^m r_b^n + \xi_{n,3}^m r_b^{-(n+1)} \right) Y_n^m(\theta, \phi) \\ & - \frac{r_b}{5\mu_0\mu_R} B_{\text{rem}} \sum_{m=-3}^3 c_{3,\text{imm}}^m Y_3^m(\theta_b, \phi_b). \end{aligned} \quad (2.23)$$

2.3.6 Boundary Conditions

A set of boundary conditions is necessary to determine coefficients $\kappa_{n,i}^m$ and $\xi_{n,i}^m$, $i = 1, 2, \dots, 6$, that provide particular solutions to (2.19) and (2.21). Boundary conditions for the reaction sphere configuration can be summarized as

$$B_{6,r_b}|_{r_b \rightarrow \infty} = 0, \quad B_{6,\theta_b}|_{r \rightarrow \infty} = 0, \quad B_{6,\phi_b}|_{r_b \rightarrow \infty} = 0, \quad (2.24)$$

$$B_{1,r_b}|_{r_b=0} \neq \infty, \quad B_{1,\theta_b}|_{r_b=0} \neq \infty, \quad B_{1,\phi_b}|_{r_b=0} \neq \infty, \quad (2.25)$$

$$B_{i,r_b}|_{r_b=R_i} = B_{i+1,r_b}|_{r=R_i}, \quad \text{and} \quad (2.26)$$

$$H_{i,\theta_b}|_{r_b=R_i} = H_{i+1,\theta_b}|_{r=R_i}, \quad H_{i,\phi_b}|_{r=R_i} = H_{i+1,\phi_b}|_{r=R_i}. \quad (2.27)$$

Expressions (2.24) and (2.25) are the boundary conditions to be satisfied at the far field and at the origin, where the magnetic flux density approaches zero when $r_b \rightarrow \infty$ and must be finite at $r_b = 0$. Furthermore, boundary conditions (2.26) specify that the radial component of \mathbf{B} must be continuous across the interface i and $i + 1$. Finally, conditions (2.27) indicate that, in absence of a free surface current density, the tangential component of \mathbf{H} must also be continuous at the interface [106].

2.3.7 Solution

Forces and torques are produced by the interaction of the magnetic flux density with the stator coils located in region 4. Hence, only the magnetic scalar potential φ_4 within

Chapter 2. Magnetic Flux Density Models

the airgap will be calculated. Invoking the orthogonal property of spherical harmonics, using the definition in equation (2.18) together with general solutions (2.22) and (2.23), boundary conditions (2.24)-(2.27) result in

$$\left\{ \begin{array}{l} \kappa_{3,6}^m = 0 \\ \xi_{3,1}^m = 0 \\ \kappa_{3,1}^m R_1^3 - \kappa_{3,2}^m R_1^3 - \xi_{3,2} R_1^{-4} = 0 \\ \kappa_{3,2}^m R_2^3 + \xi_{3,2}^m R_2^{-4} - \kappa_{3,3}^m R_2^3 - \xi_{3,3}^m R_2^{-4} = 0 \\ \kappa_{3,3}^m R_3^3 + \xi_{3,3}^m R_3^{-4} - \kappa_{3,4}^m R_3^3 - \xi_{3,4}^m R_3^{-4} = 0 \\ \kappa_{3,4}^m R_4^3 + \xi_{3,4}^m R_4^{-4} - \kappa_{3,5}^m R_4^3 - \xi_{3,5}^m R_4^{-4} = 0 \\ \kappa_{3,5}^m R_5^3 + \xi_{3,5}^m R_5^{-4} - \xi_{3,6}^m R_5^{-4} = 0 \\ 3\kappa_{3,1}^m R_1^2 - 3\mu_R \kappa_{3,2}^m R_1^2 + 4\mu_R \xi_{3,2}^m R_1^{-5} = 0 \\ 3\mu_R \kappa_{3,2}^m R_2^2 - 4\mu_R \xi_{3,2}^m R_2^{-5} - 3\mu_{PM} \kappa_{3,3}^m R_2^2 + 4\mu_{PM} \xi_{3,3}^m R_2^{-5} + 6B_{rem}/\mu_0 c_{3,imm}^m = 0 \\ 3\mu_{PM} \kappa_{3,3}^m R_3^2 - 4\mu_{PM} \xi_{3,3}^m R_3^{-5} - 6B_{rem}/\mu_0 c_{3,imm}^m - 3\kappa_{3,4}^m R_3^2 + 4\xi_{3,4}^m R_3^{-5} = 0 \\ 3\kappa_{3,4}^m R_4^2 - 4\xi_{3,4}^m R_4^{-5} - 3\mu_R \kappa_{3,5}^m R_4^2 + 4\mu_R \xi_{3,5}^m R_4^{-5} = 0 \\ 3\mu_R \kappa_{3,5}^m R_5^2 - 4\mu_R \xi_{3,5}^m R_5^{-5} + 4\xi_{3,6}^m R_5^{-5} = 0 \end{array} \right. \quad (2.28)$$

that is a system of 12 linear equations for the 12 unknowns coefficients $\kappa_{3,i}^m$ and $\xi_{3,i}^m$, $i = 1, 2, \dots, 6$. Defining

$$K_1 = \frac{\xi_{3,4}^m}{B_{rem} c_{3,imm}^m} \mu_0, \quad K_2 = \frac{\kappa_{3,4}^m}{B_{rem} c_{3,imm}^m} \mu_0, \quad (2.29)$$

and solving the system of linear equations (2.28) for the desired coefficients $\kappa_{3,4}^m$ and $\xi_{3,4}^m$, expression (2.22) for the magnetic scalar potential within the airgap can be rewritten as

$$\varphi_4(r_b, \theta_b, \phi_b) = r_b^{-4} \left(K_1 + K_2 r_b^7 \right) \frac{B_{rem}}{\mu_0} \sum_{m=-3}^3 c_{3,imm}^m Y_3^m(\theta_b, \phi_b). \quad (2.30)$$

Note that K_1 and K_2 in (2.30) are constant and their dependence to the spherical harmonic order m is removed by dividing $\xi_{3,4}^m$ and $\kappa_{3,4}^m$ (both proportional to $c_{3,imm}^m$) in (2.29) by $c_{3,imm}^m$. Although easily calculated using a program of symbolic calculation, expressions for K_1 and K_2 are excessively long for a finite value of the permeability μ_R . Therefore, we will assume that the back-iron and stator material is infinitely permeable ($\mu_R \rightarrow \infty$). Notice that with this assumption, the number of conditions in (2.28) reduces to 4 and coefficients $\kappa_{3,i}^m = 0$ and $\xi_{3,i}^m = 0$, $\forall i \neq 3, 4$. Therefore,

$$K_1 = \frac{R_3^5 \hat{K}_1}{5 \check{K}_1}, \quad K_2 = -K_1 R_4^{-7}, \quad (2.31)$$

with

$$\hat{K}_1 = \frac{\left(1 + 3/4R_2^{-7}R_3^7\right)\left(1 - R_2^{-2}R_3^2\right)}{\left(1 + 3/4R_4^{-7}R_3^7\right)\left(1 - R_2^{-7}R_3^7\right)} + \frac{3/2\left(1 - 1/2R_2^{-2}R_3^2\right)}{\left(1 + 3/4R_4^{-7}R_3^7\right)}, \quad (2.32)$$

and

$$\check{K}_1 = 1 - \mu_{\text{PM}} \frac{\left(1 + 3/4R_2^{-7}R_3^7\right)\left(1 - R_4^{-7}R_3^7\right)}{\left(1 + 3/4R_4^{-7}R_3^7\right)\left(1 - R_2^{-7}R_3^7\right)}. \quad (2.33)$$

Then, the magnetic scalar potential (2.30) becomes

$$\varphi_4(r_b, \theta_b, \phi_b) = r_b^{-4} \left(1 - R_4^{-7}r_b^7\right) \frac{K_1 B_{\text{rem}}}{\mu_0} \sum_{m=-3}^3 c_{3,\text{imm}}^m Y_3^m(\theta_b, \phi_b). \quad (2.34)$$

Finally, the magnetic flux density in the airgap is calculated using expression (2.18) and the constitutive relation in air $\mathbf{B}_4 = \mu_0 \mathbf{H}_4$ as

$${}^{\mathcal{B}^S} \mathbf{B}_4(r_b, \theta_b, \phi_b) = K_1 B_{\text{rem}} \sum_{m=-3}^3 c_{3,\text{imm}}^m \nabla \left[r_b^{-4} \left(R_4^{-7} r_b^7 - 1 \right) Y_3^m(\theta_b, \phi_b) \right], \quad (2.35)$$

which can also be expressed as the sum of the magnetic flux densities $\mathbf{B}_{4,3}^m$ generated by each spherical harmonic of degree 3 and order m as

$${}^{\mathcal{B}^S} \mathbf{B}_4(r_b, \theta_b, \phi_b) = \sum_{m=-3}^3 c_{3,\text{imm}}^m \mathbf{B}_{4,3}^m(r_b, \theta_b, \phi_b), \quad (2.36)$$

where

$$\mathbf{B}_{4,3}^m(r_b, \theta_b, \phi_b) = K_1 B_{\text{rem}} \nabla \left[r_b^{-4} \left(R_4^{-7} r_b^7 - 1 \right) Y_3^m(\theta_b, \phi_b) \right]. \quad (2.37)$$

2.3.8 Solution for Rotated Rotor (Stator Coordinates)

During operation, the reaction sphere rotor reference frame \mathcal{B} is constantly changing with respect to the stator reference frame \mathcal{S} . Forces and torques are generated by the interaction of the rotor magnetic flux density with the stator coils. Therefore, in order to compute the force and torque models, the magnetic flux density has to be expressed in the stator (fixed) reference frame. As introduced, two distinct change of coordinates are proposed. In the first one, the change of coordinate frame is performed by exploiting spherical harmonic properties under rotation. The second method is based on the conventional change of reference frames operated with a rotation matrix (parametrized using Euler angles or quaternions).

Rotation Operation Parametrized with Spherical Harmonic Coefficients

The magnetic scalar potential within the airgap in (2.34) is expressed in rotor coordinates and depends on the evaluation (application) point defined by r_b , θ_b , and ϕ_b . The magnetic scalar potential expressed in terms of stator coordinates \mathcal{S} can be calculated by considering the effect of a rotation operator $R(\alpha, \beta, \gamma)$, parametrized using ZYZ Euler angles α , β , and γ . Then, writing spherical harmonic functions in terms of stator coordinates as developed in (A.17), the magnetic scalar potential (2.34) is expressed in stator inertial coordinates as

$$\varphi_4(r_s, \theta_s, \phi_s) = r_s^{-4} \left(1 - R_4^{-7} r_s^7\right) \frac{K_1 B_{\text{rem}}}{\mu_0} \sum_{m=-3}^3 c_{3,\text{imm}}^m \sum_{m'=-n}^n D_{m'm}^n(R) Y_n^{m'}(\theta_s, \phi_s). \quad (2.38)$$

However, by also taking into account the expansion property of spherical harmonic introduced in Section A.3.2, and considering the effect that a rotation operator $R(\alpha, \beta, \gamma)$ has on spherical harmonic coefficients $c_{3,\text{imm}}^m$, the magnetic scalar potential (2.34) is more conveniently expressed in stator inertial coordinates as

$$\varphi_4(r_s, \theta_s, \phi_s) = r_s^{-4} \left(1 - R_4^{-7} r_s^7\right) \frac{K_1 B_{\text{rem}}}{\mu_0} \sum_{m=-3}^3 c_3^m(\alpha, \beta, \gamma) Y_3^m(\theta_s, \phi_s), \quad (2.39)$$

with $c_3^m(\alpha, \beta, \gamma)$ given by expression (A.22), which we report here for convenience,

$$c_n^m(\alpha, \beta, \gamma) = \sum_{m'=-n}^n D_{m'm}^n(\alpha, \beta, \gamma) c_{n,\text{imm}}^{m'}. \quad (2.40)$$

Then, similarly to (2.35), the magnetic flux density in the airgap expressed in the stator spherical coordinates \mathcal{S}^S can be written as

$${}^{\mathcal{S}^S} \mathbf{B}_4(r_s, \theta_s, \phi_s) = K_1 B_{\text{rem}} \sum_{m=-3}^3 c_3^m(\alpha, \beta, \gamma) \nabla \left[r_s^{-4} \left(R_4^{-7} r_s^7 - 1 \right) Y_3^m(\theta_s, \phi_s) \right]. \quad (2.41)$$

Again, this result can also be expressed as the sum of the magnetic flux densities $\mathbf{B}_{4,3}^m$ generated by each spherical harmonic of degree 3 and order m as

$${}^{\mathcal{S}^S} \mathbf{B}_4(r_s, \theta_s, \phi_s) = \sum_{m=-3}^3 c_3^m(\alpha, \beta, \gamma) \mathbf{B}_{4,3}^m(r_s, \theta_s, \phi_s), \quad (2.42)$$

where

$$\mathbf{B}_{4,3}^m(r_s, \theta_s, \phi_s) = K_1 B_{\text{rem}} \nabla \left[r_s^{-4} \left(R_4^{-7} r_s^7 - 1 \right) Y_3^m(\theta_s, \phi_s) \right]. \quad (2.43)$$

Rotation Operation Parametrized with Rotation Matrix

The magnetic flux density in (2.36) can be expressed in the stator frame \mathcal{S} by means of the rotation matrix $R_{\mathcal{S} \rightarrow \mathcal{B}}(\alpha, \beta, \gamma)$ defined in (2.6). To do this, first, ${}^{\mathcal{B}^S} \mathbf{B}_4(r_b, \theta_b, \phi_b)$ in (2.36) needs to be transformed from rotor spherical coordinates \mathcal{B}^S to rotor cartesian coordinates \mathcal{B} . Hence, for example, ${}^{\mathcal{B}} \mathbf{B}_4(x_b, y_b, z_b)$ can be computed from (2.36) by using transformations $r_b = \sqrt{x_b^2 + y_b^2 + z_b^2}$, $\theta_b = \cos^{-1} \frac{z_b}{r_b}$, $\phi_b = \tan^{-1} \frac{y_b}{x_b}$ listed in Table 2.2, and by employing the gradient operator in cartesian coordinates as $\nabla = [\partial/\partial x_b \quad \partial/\partial y_b \quad \partial/\partial z_b]^\top$. Other methods to compute ${}^{\mathcal{B}} \mathbf{B}_4(x_b, y_b, z_b)$ are proposed in Table 2.2. Finally, the magnetic flux density expressed in cartesian coordinates can be calculated as

$${}^{\mathcal{S}} \mathbf{B}_4(x_s, y_s, z_s) = R_{\mathcal{S} \rightarrow \mathcal{B}}(\alpha, \beta, \gamma) {}^{\mathcal{B}} \mathbf{B}_4(x_b, y_b, z_b) \quad (2.44)$$

with

$$\begin{bmatrix} x_b \\ y_b \\ z_b \end{bmatrix} = R_{\mathcal{S} \rightarrow \mathcal{B}}(\alpha, \beta, \gamma)^\top \begin{bmatrix} x_s \\ y_s \\ z_s \end{bmatrix} \quad (2.45)$$

2.3.9 Verification with FEM Simulations

Simulation Setup

In this section, the magnetic flux density model is verified using FEM simulations. Electromagnetic 3-D FEM simulations are performed using the AC/DC module of COMSOL Multiphysics v4.3 running on a Win7 64-bit system equipped with two Intel six-core 3.33-GHz CPUs and 48-GB RAM. Simulation parameters are summarized in Table 2.3. Notice that the verification is performed using a non-ferromagnetic stator. Hence, the analytical expression of the magnetic flux density without the metallic stator can be easily obtained from equation (2.35) by calculating the limit for the inner stator radius $R_4 \rightarrow \infty$.

Table 2.3. Parameters for FEM verification of magnetic flux density model with an ideal octupole rotor.

Inner back-iron R_1	75 mm	Outer coil R_b	99 mm
Back-iron R_2	80 mm	Inner coil angle θ_a	3.7°
Magnet R_3	89 mm	Inner coil angle θ_b	16°
Inner stator R_4	99 mm	Iron permeability μ_R	500
Outer stator R_5	103 mm	Magnet permeability μ_R	1.0
Inner coil R_a	92 mm	Magnet remanence B_r	1.4 T

Simulations

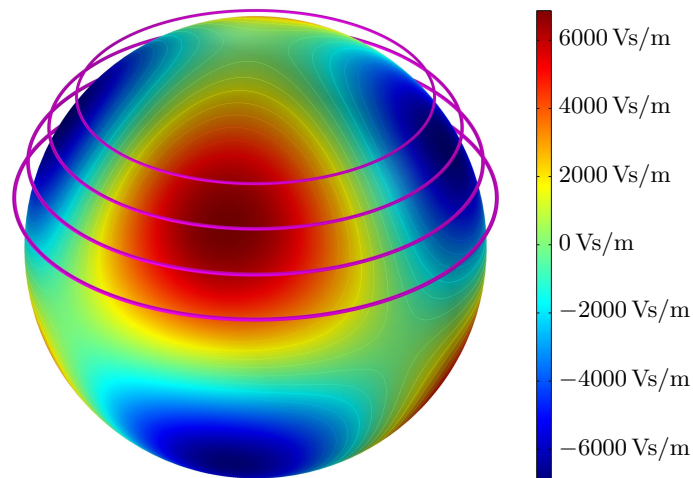
The three components of the magnetic flux density are evaluated about a parametric circular path, which is described in spherical coordinates as $r_{b,p}\hat{\mathbf{r}}_b + \theta_{b,p}\hat{\boldsymbol{\theta}}_b + \phi_{b,p}\hat{\boldsymbol{\phi}}_b$, where $r_{b,p} = 95.5$ mm and $\phi_{b,p} \in [0^\circ, 360^\circ]$. The evaluation is repeated about four different values of the polar angle $\theta_{b,p} = \{45^\circ, 55^\circ, 65^\circ, 75^\circ\}$. Therefore, for an immobile rotor with a non-ferromagnetic stator, the expected radial component of the flux density about these parametric circular paths can be calculated in rotor spherical coordinates from (2.34) as

$$\begin{aligned} B_{4,r_b}(r_{b,p}, \theta_{b,p}, \phi_{b,p}) &= \lim_{R_4 \rightarrow \infty} \left\{ K_1 B_{\text{rem}} \frac{\partial}{\partial r_b} \left[r_b^{-4} \left(R_4^{-7} r_b^7 - 1 \right) \right] \Big|_{r_b=r_{b,p}} \right\} \\ &\quad \cdot \sum_{m=-3}^3 c_{3,\text{imm}}^m Y_3^m(\theta_{b,p}, \phi_{b,p}) \\ &= \lim_{R_4 \rightarrow \infty} (K_1) \frac{6\sqrt{3}B_{\text{rem}}}{r_{b,p}^5} \sin^2 \theta_{b,p} \cos \theta_{b,p} \sin 2\phi_{b,p}. \end{aligned} \quad (2.46)$$

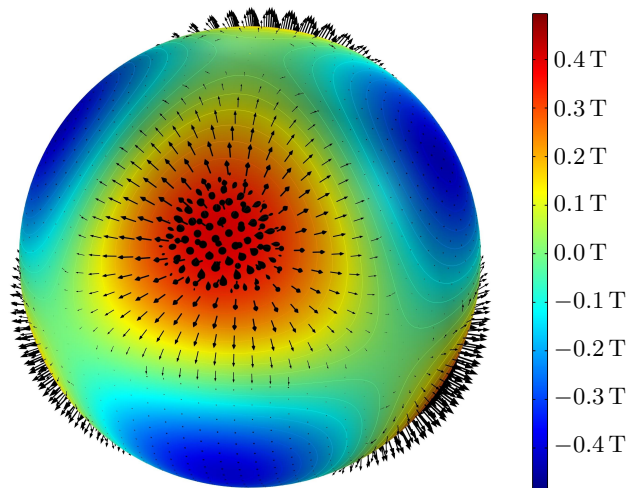
The tangential components B_{4,θ_b} and B_{4,ϕ_b} can be derived in a similar way. For illustration, a surface plot of the simulated magnetic scalar potential at the surface of the rotor with the four circular paths is reported in Fig. 2.4a. A surface plot of the radial component of the simulated magnetic flux density with arrows is shown in Fig. 2.4b.

Simulated values of the magnetic flux density are compared to the analytical model in Fig. 2.5-2.8. As one can notice, all the three components of the simulated flux density are in strong accordance with the analytical expression of the model.

2.3. Analytical Model with an Ideal Octupole Rotor



(a) Surface plot of the simulated magnetic scalar potential at the surface of the rotor (maximum value in red is 6870 Vs/m). The four circular paths for evaluation of magnetic flux density are shown in magenta.



(b) Surface plot of the radial component of the simulated magnetic flux density at the surface of the rotor (maximum value in red is 0.49 T). Arrow plot showing the magnetic flux density is displayed in black.

Figure 2.4. Surface plots of the simulated magnetic scalar potential and radial component of magnetic flux density with ideal octupole rotor.

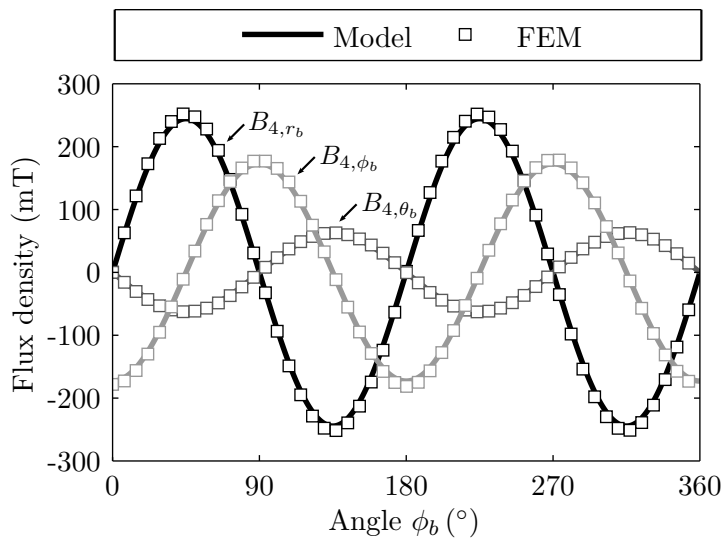


Figure 2.5. Analytical and simulated magnetic flux density at polar angle $\theta_p = 45^\circ$ with ideal octupole rotor.

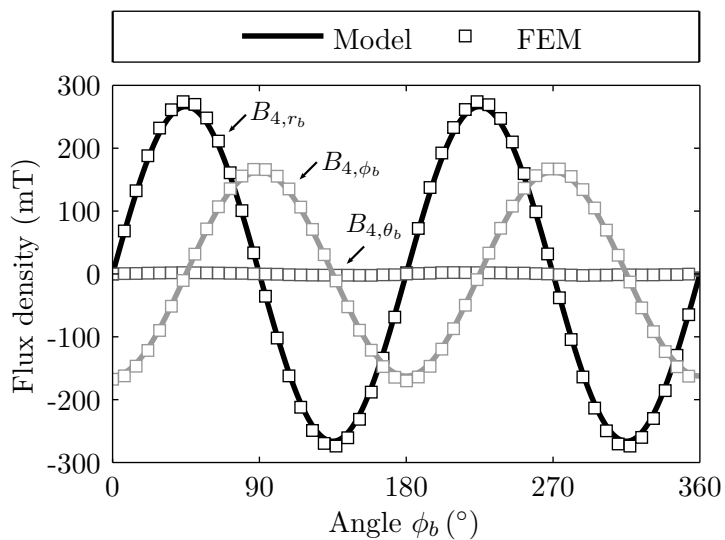


Figure 2.6. Analytical and simulated magnetic flux density at polar angle $\theta_p = 55^\circ$ with ideal octupole rotor.

2.3. Analytical Model with an Ideal Octupole Rotor

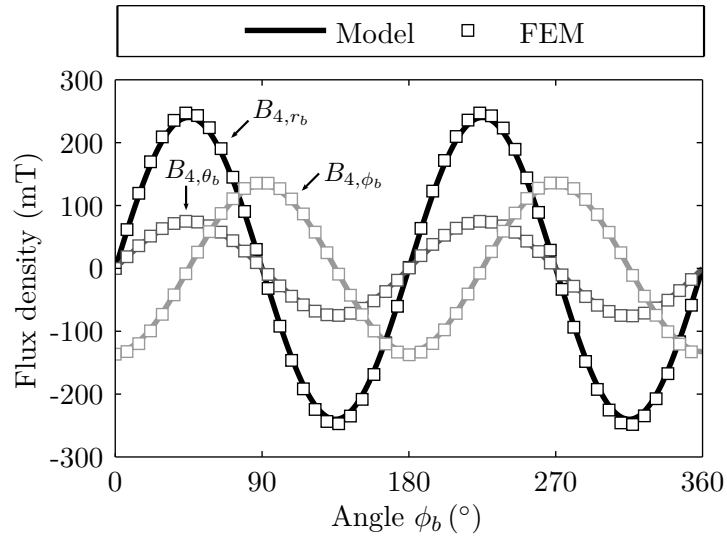


Figure 2.7. Analytical and simulated magnetic flux density at polar angle $\theta_p = 65^\circ$ with ideal octupole rotor.

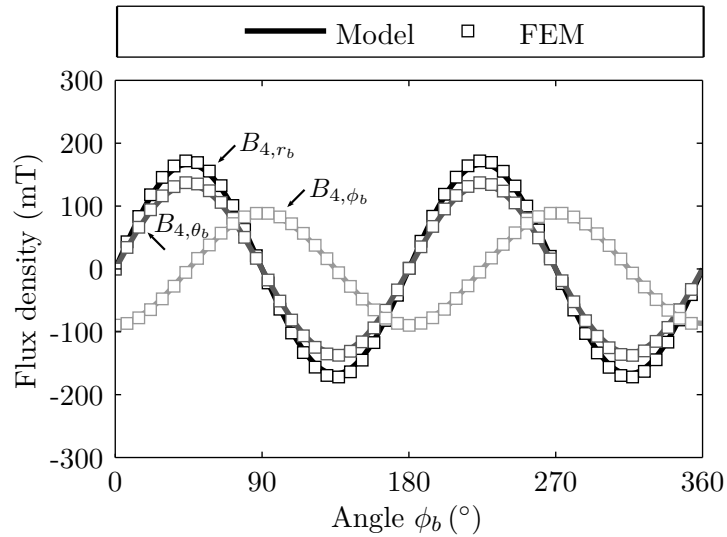


Figure 2.8. Analytical and simulated magnetic flux density at polar angle $\theta_p = 75^\circ$ with ideal octupole rotor.

2.4 Hybrid FEM-Analytical Model

2.4.1 Region Definitions and Relevant Dimensions

For the derivation of the magnetic flux density model using the hybrid FEM-analytical approach, we use the rotor and stator schematic in Fig. 2.9 with the respective relevant dimensions. The difference between this schematic and the one used for the ideal octopole magnetization in Fig. 2.3 is that, in Fig. 2.9, the rotor is treated as a black-box, with given mechanical and magnetic symmetries. As before, we are interested in computing the magnetic flux density in the airgap (region 4), which is enclosed in the stator (region 5), which in turn is surrounded by air (region 6).

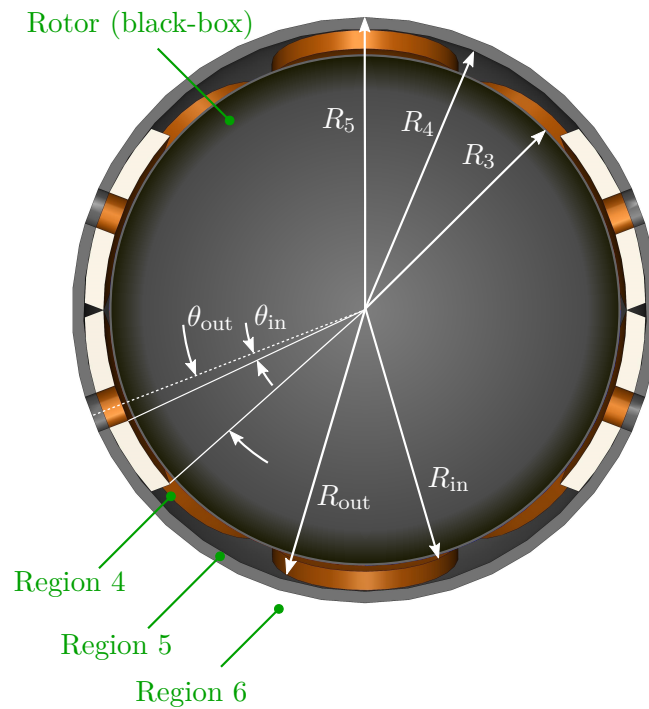


Figure 2.9. Section view of the reaction sphere for development of hybrid FEM-analytical model.

2.4.2 Constitutive Relations

As with the ideal octopole magnetization, the constitutive relations describing the magnetic effects inside the three regions are characterized by

$$\mathbf{B}_i = \begin{bmatrix} B_{i,r_b} \\ B_{i,\theta_b} \\ B_{i,\phi_b} \end{bmatrix} = \begin{cases} \mu_0 \mathbf{H}_i, & \text{for } i = 4, 6 \\ \mu_0 \mu_R \mathbf{H}_i, & \text{for } i = 5 \end{cases} \quad (2.47)$$

where the subscript i denotes the region numbers.

2.4.3 Governing Equations

The magnetic scalar potential inside the airgap, the stator, and the surrounding air satisfies the Laplace equations (2.19)

$$\nabla^2 \varphi_i(r_b, \theta_b, \phi_b) = 0. \quad (2.48)$$

Potentials $\varphi_i(r_b, \theta_b, \phi_b)$, with $i = 4, 5, 6$, are expressed in rotor coordinates \mathcal{B}^S . Once these equations are solved, the magnetic flux density within region i can be calculated by first employing definition (2.18) and subsequently applying the respective constitutive relations (2.47).

2.4.4 General Solutions

The general solution of the Laplace equation in spherical coordinates \mathcal{B}^S characterizing region $i = 4, 5, 6$ is given in (2.22) and is reported here for convenience

$$\varphi_i(r_b, \theta_b, \phi_b) = \sum_{n=0}^{\infty} \sum_{m=-n}^n \left(\kappa_{n,i}^m r_b^n + \xi_{n,i}^m r_b^{-(n+1)} \right) Y_n^m(\theta_b, \phi_b). \quad (2.49)$$

2.4.5 Analytical Boundary Conditions

A set of boundary conditions is necessary to determine coefficients $\kappa_{n,i}^m$ and $\xi_{n,i}^m$, $i = 4, 5, 6$, that provide particular solutions to (2.49). Boundary conditions can be summarized as

$$B_{6,r_b}|_{r_b \rightarrow \infty} = 0, \quad B_{6,\theta_b}|_{r_b \rightarrow \infty} = 0, \quad B_{6,\phi_b}|_{r_b \rightarrow \infty} = 0, \quad (2.50)$$

$$B_{i,r_b}|_{r_b=R_i} = B_{i+1,r_b}|_{r_b=R_i}, \quad \text{and} \quad (2.51)$$

$$H_{i,\theta_b}|_{r_b=R_i} = H_{i+1,\theta_b}|_{r_b=R_i}, \quad H_{i,\phi_b}|_{r_b=R_i} = H_{i+1,\phi_b}|_{r_b=R_i}. \quad (2.52)$$

As before, expressions (2.50) are the boundary conditions to be satisfied at the far field, where the magnetic flux density approaches zero when $r_b \rightarrow \infty$. Furthermore, boundary

conditions (2.51) and (2.52) specify that the radial component of \mathbf{B} must be continuous across the interfaces and that, in absence of a free surface current density, the tangential component of \mathbf{H} must also be continuous [106].

2.4.6 Measured or Simulated Boundary Conditions

In the proposed hybrid approach, the analytical expression of the magnetic flux density within the rotor cannot be calculated because the rotor is treated as a black-box, with some given mechanical and magnetic symmetries. Therefore, no analytical expression of the magnetic flux density is available as boundary condition at the surface of the rotor, where $r_b = R_3$. Similarly as [110, 111], in absence of an analytical expression, the boundary condition can either be simulated (for instance during the design optimization phase) or measured. Suppose that the simulated (or measured) radial component of the magnetic flux density B_{4,r_b}^{dec} is available on the entire spherical surface at $r_b = R_{\text{dec}}$ with $R_{\text{dec}} \in [R_3, R_4]$. Then, we can decompose B_{4,r_b}^{dec} on a spherical harmonic basis up to degree N_h as

$$B_{4,r_b}^{\text{dec}} = \sum_{n=0}^{N_h} \sum_{m=-n}^n c_{n,\text{imm}}^m(R_{\text{dec}}) Y_n^m(\theta_b, \phi_b), \quad (2.53)$$

where $c_{n,\text{imm}}^m$ are spherical harmonic decomposition coefficients for the immobile rotor. These coefficients can be computed using integration as

$$c_{n,\text{imm}}^m(R_{\text{dec}}) = \int_0^{2\pi} \int_0^\pi B_{4,r_b}^{\text{dec}}(R_{\text{dec}}, \theta_b, \phi_b) \overline{Y_n^m(\theta_b, \phi_b)} \sin \theta_b d\theta_b d\phi_b. \quad (2.54)$$

Notice, however, that if B_{4,r_b}^{dec} is only available at discrete points, for instance on the equiangular latitude-longitude grid, the computation of $c_{n,\text{imm}}^m(R_{\text{dec}})$ can also be performed using the sampling theorem [112]. Hence, by comparing the measurement equation (2.53) to

$$B_{4,r_b}|_{r_b=R_{\text{dec}}} = -\mu_0 \left. \frac{\partial \varphi_4}{\partial r_b} \right|_{r_b=R_{\text{dec}}}, \quad (2.55)$$

the measured boundary condition for the immobile rotor can be expressed as

$$c_{n,\text{imm}}^m(R_{\text{dec}}) = -\mu_0 n k_{n,4}^m R_{\text{dec}}^{(n-1)} + \mu_0 (n+1) \xi_{n,4}^m R_{\text{dec}}^{-(n+2)}. \quad (2.56)$$

As mentioned above, although in the proposed hybrid approach the rotor is treated as a black-box, we will assume that any of its practical realization has some symmetry properties. These symmetries result from the intention to obtain a rotor with a scalar inertia tensor and possibly a magnetic flux density profile similar to the octupole cubic harmonic. By considering these symmetries, as it will be shown in the next section, only harmonic of a given degree and order can appear in the spectrum.

Spectral Content of Octupole Cubic Symmetry

We define the function $f(r_b, \theta_b, \phi_b)$ to be the radial component of the magnetic flux density within the airgap. Then, expression (2.53) can be reformulated as

$$\begin{aligned} f(r_b, \theta_b, \phi_b) &= \sum_{n=0}^{N_h} \sum_{m=-n}^n c_{n,\text{imm}}^m Y_n^m(\theta_b, \phi_b) \\ &= \sum_{n=0}^{N_h} \sum_{m=-n}^n c_{n,\text{imm}}^m K_n^m P_n^m(\cos \theta_b) e^{im\phi_b}. \end{aligned} \quad (2.57)$$

Because in the proposed reaction sphere concept the rotor has eight permanent magnet poles located at each faces of an octahedron, with two opposite faces of the octahedron having opposite polarity [1], the following properties need to be satisfied in the proposed octupole cubic rotor:

1. $f(r_b, \theta_b, \phi_b) = f(r_b, \theta_b, \phi_b + \pi)$,
2. $f(r_b, \theta_b, \phi_b) = -f(r_b, \theta_b, \phi_b + \pi/2)$,
3. $f(r_b, \theta_b, \phi_b) = -f(r_b, \pi - \theta_b, \phi_b)$.

For any n and $|m| < n$ in equation (2.57), the term $e^{im\phi_b}$ is the only that depends on the azimuthal angle ϕ_b . Therefore, to satisfy symmetry property 1, the following shall hold

$$\cos(m\phi_b) + i \sin(m\phi_b) = \cos(m\phi_b + m\pi) + i \sin(m\phi_b + m\pi). \quad (2.58)$$

Thus, by equating the real parts in (2.58) we obtain

$$\cos(m\phi_b) = \cos(m\phi_b + m\pi). \quad (2.59)$$

Therefore, since $\cos(\phi_b) = \cos(\phi_b + k2\pi)$ for $k \in \mathbb{Z}$, it follows that symmetry 1 holds for $m = 2k = 0, \pm 2, \pm 4, \pm 6, \dots$. The same condition can be obtained by equating the imaginary parts in (2.58).

For symmetry property 2, for $m = 2k$, the following holds

$$\begin{aligned} \cos(2k\phi_b) + i \sin(2k\phi_b) &= -\cos(2k\phi_b + 2k\pi/2) - i \sin(2k\phi_b + 2k\pi/2), \\ &= -\cos(2k\phi_b + k\pi) - i \sin(2k\phi_b + k\pi), \end{aligned} \quad (2.60)$$

which is satisfied for $k \in \mathbb{Z}^*$ and odd, namely for $k = \pm 1, \pm 3, \pm 5, \dots$. Therefore, by combining the first two symmetry conditions, we conclude that only spherical harmonics with order $m = 2k = \pm 2, \pm 6, \pm 10, \pm 14 \dots$ can appear in the spectrum. Hence, for $k \in \mathbb{Z}$, $m = 4k + 2$.

Chapter 2. Magnetic Flux Density Models

Symmetry property 3 is related to polar angle θ_b . Therefore, the only polar-dependent terms in (2.57) are the associated Legendre polynomials $P_n^m(\cos \theta_b)$ previously defined in (A.4). To satisfy symmetry property 3, we look for spherical harmonic degree satisfying

$$\begin{aligned} P_n^m(\cos(\theta_b)) &= -P_n^m(\cos(\pi - \theta_b)) \\ &= -P_n^m(-\cos(\theta_b)). \end{aligned} \quad (2.61)$$

From definition of associated Legendre polynomials in (A.3) and because $P_n(-x) = (-1)^n P_n(x)$ [113], we have that $P_n^m(-x) = (-1)^{n+m} P_n^m(x)$. Therefore, condition (2.61) is rewritten as

$$P_n^m(\cos(\theta_b)) = -(-1)^{n+m} P_n^m(\cos(\theta_b)), \quad (2.62)$$

from which we see that $n + m$ must be odd (and positive since $|m| < n$). Therefore, because $m = \pm 2, \pm 6, \pm 10, \pm 14 \dots$, $n = 1, 3, 5, 7, \dots$. Finally, since $|m| < n$, spherical harmonics can only occur for $n = 3, 5, 7, 9, \dots$, namely n odd and $n \geq 3$.

Based on the above findings, we can introduce the following two sets

$$\mathbb{I}_m = \{ m \in \mathbb{Z} \mid m = 4k + 2, k \in \mathbb{Z} \} = \{ \pm 2, \pm 6, \pm 10, \pm 14, \pm 18, \dots \}, \quad (2.63)$$

$$\mathbb{I}_n = \{ n \in \mathbb{N}^0 \mid n = 2k + 3, k \in \mathbb{N} \} = \{ 3, 5, 7, 9, 11, 13, 15, 17, 19, \dots \}, \quad (2.64)$$

and rewrite (2.53) as

$$B_{4,r_b}^{\text{dec}} = \sum_{\substack{n \in \mathbb{I}_n \\ n \leq N_h}} \sum_{\substack{m \in \mathbb{I}_m \\ m \leq n}} c_{n,\text{imm}}^m(R_{\text{dec}}) Y_n^m(\theta_b, \phi_b). \quad (2.65)$$

2.4.7 Solution

Invoking the orthogonal property of spherical harmonics, using the definition in equation (2.18) together with general solution (2.49), analytical boundary conditions (2.50)-(2.52) and measured boundary condition (2.56) result in

$$\left\{ \begin{array}{l} \kappa_{n,6}^m = 0 \\ n\mu_R \kappa_{n,5}^m R_5^{n-1} - (n+1)\mu_R \xi_{n,5}^m R_5^{-(n+2)} = n\kappa_{n,6}^m R_5^{n-1} - (n+1)\xi_{n,6}^m R_5^{-(n+2)} \\ n\kappa_{n,4}^m R_4^{n-1} - (n+1)\xi_{n,4}^m R_4^{-(n+2)} = n\mu_R \kappa_{n,5}^m R_4^{n-1} - (n+1)\mu_R \xi_{n,5}^m R_4^{-(n+2)} \\ \kappa_{n,5}^m R_5^n + \xi_{n,5}^m R_5^{-(n+1)} = \kappa_{n,6}^m R_5^n + \xi_{n,6}^m R_5^{-(n+1)} \\ \kappa_{n,4}^m R_4^n + \xi_{n,4}^m R_4^{-(n+1)} = \kappa_{n,5}^m R_4^n + \xi_{n,5}^m R_4^{-(n+1)} \\ c_{n,\text{imm}}^m(R_{\text{dec}}) = -\mu_0 n \kappa_{n,4}^m R_{\text{dec}}^{n-1} + \mu_0 (n+1) \xi_{n,4}^m R_{\text{dec}}^{-(n+2)}, \end{array} \right. \quad (2.66)$$

which is a system of 6 linear equations for the 6 unknown coefficients $\kappa_{n,i}^m$ and $\xi_{n,i}^m$, $i = 4, 5, 6$. Although the values of $\kappa_{n,i}^m$ and $\xi_{n,i}^m$ can be easily calculated using a program

of symbolic calculation to solve the linear system of equations (2.66), their expressions are relatively long for a finite value of stator permeability μ_R . Therefore, solving (2.66) for an infinitely permeable stator ($\mu_R \rightarrow \infty$), using general solution (2.49), and expression (2.18), the magnetic scalar potential within the airgap (region 4) can be formulated as

$$\varphi_4(r_b, \theta_b, \phi_b) = \frac{1}{\mu_0} \sum_{\substack{n \in \mathbb{I}_n \\ n \leq N_h}} \sum_{\substack{m \in \mathbb{I}_m \\ m \leq n}} c_{n,\text{imm}}^m \frac{r_b^{-(n+1)} (1 - R_4^{-(2n+1)} r_b^{2n+1})}{n R_{\text{dec}}^{n-1} R_4^{-(2n+1)} + (n+1) R_{\text{dec}}^{-(n+2)}} Y_n^m(\theta_b, \phi_b). \quad (2.67)$$

Finally, using constitutive relations (2.47), the magnetic flux density becomes

$${}^{\mathcal{B}^S} \mathbf{B}_4(r_b, \theta_b, \phi_b) = \sum_{\substack{n \in \mathbb{I}_n \\ n \leq N_h}} \sum_{\substack{m \in \mathbb{I}_m \\ m \leq n}} c_{n,\text{imm}}^m \tilde{\mathbf{B}}_{4,n}^m, \quad (2.68)$$

where

$$\tilde{\mathbf{B}}_{4,n}^m = \nabla \left[\frac{r_b^{-(n+1)} (R_4^{-(2n+1)} r_b^{2n+1} - 1)}{n R_{\text{dec}}^{n-1} R_4^{-(2n+1)} + (n+1) R_{\text{dec}}^{-(n+2)}} Y_n^m(\theta_b, \phi_b) \right]. \quad (2.69)$$

It is worth observing that solution in (2.68) and (2.69) have the same structure of the solution calculated in (2.36) and (2.37) for the analytical model with ideal octupole magnetization. As a matter of fact, solution in (2.36) is a special case of (2.68), in which we consider only the fundamental harmonic of degree $n = 3$ and with

$$\tilde{\mathbf{B}}_{4,3}^m = \mathbf{B}_{4,3}^m \frac{1}{K_1 B_{\text{rem}} (3 R_{\text{dec}}^2 R_4^{-7} + 4 R_{\text{dec}}^{-5})}. \quad (2.70)$$

2.4.8 Solution for Rotated Rotor (Stator Coordinates)

Rotation Operation Parametrized with Spherical Harmonic Coefficients

Following the same procedure explained in Section 2.3.8, which exploits spherical harmonics properties under rotation, the magnetic scalar potential in terms of stator inertial coordinates can be written as

$$\varphi_4(r_s, \theta_s, \phi_s) = \frac{1}{\mu_0} \sum_{\substack{n \in \mathbb{I}_n \\ n \leq N_h}} \sum_{m=-n}^n c_n^m(\alpha, \beta, \gamma) \frac{r_s^{-(n+1)} (1 - R_4^{-(2n+1)} r_s^{2n+1})}{n R_{\text{dec}}^{n-1} R_4^{-(2n+1)} + (n+1) R_{\text{dec}}^{-(n+2)}} Y_n^m(\theta_s, \phi_s). \quad (2.71)$$

Therefore, the magnetic flux density in stator inertial coordinates can be readily written as

$${}^{\mathcal{S}^S} \mathbf{B}_4(r_s, \theta_s, \phi_s) = \sum_{\substack{n \in \mathbb{I}_n \\ n \leq N_h}} \sum_{m=-n}^n c_n^m(\alpha, \beta, \gamma) \tilde{\mathbf{B}}_{4,n}^m, \quad (2.72)$$

where

$$\tilde{\mathbf{B}}_{4,n}^m = \nabla \left[\frac{r_s^{-(n+1)} \left(R_4^{-(2n+1)} r_s^{2n+1} - 1 \right)}{n R_{\text{dec}}^{n-1} R_4^{-(2n+1)} + (n+1) R_{\text{dec}}^{-(n+2)}} Y_n^m(\theta_s, \phi_s) \right]. \quad (2.73)$$

Rotation Operation Parametrized with Rotation Matrix

Precisely like with the ideal octupole case in Sec. 2.3.8, the magnetic flux density in the stator reference frame can be expressed as

$${}^S \mathbf{B}_4(x_s, y_s, z_s) = R_{S \rightarrow B}(\alpha, \beta, \gamma) {}^B \mathbf{B}_4(x_b, y_b, z_b) \quad (2.74)$$

with

$$\begin{bmatrix} x_b \\ y_b \\ z_b \end{bmatrix} = R_{S \rightarrow B}(\alpha, \beta, \gamma)^\top \begin{bmatrix} x_s \\ y_s \\ z_s \end{bmatrix} \quad (2.75)$$

where ${}^B \mathbf{B}_4(x_b, y_b, z_b)$ is expressed in rotor cartesian coordinates.

2.5 Summary

In this chapter we derived models of the magnetic flux density distribution relative to a PM spherical rotor with octupole magnetization pattern. Two different approaches to derive these models have been proposed.

In the first approach, we adopted a pure octupole magnetization of the rotor permanent magnet. This magnetization is presently challenging to achieve in practice but this model will serve as an ideal reference for validation of methodologies presented in the remaining part of this document. This first approach is purely analytical and it is based on solving Laplace's and Poisson's equations. Finally, thanks to properties of spherical harmonic functions under rotation, the magnetic flux density distribution is expressed as a linear combination of seven spherical harmonic components, with decomposition coefficients conveying to the model all the information relative to the rotor orientation.

The second approach is based on a hybrid FEM-analytical method and it allows deriving expressions of the magnetic flux density for highly complex rotor geometries, taking into account higher order components of the magnetic flux density. In this approach, FEM or measured derived values are combined with other boundary conditions, and the magnetic flux density can again be expressed as a linear combination of a finite number of spherical harmonic components. We have shown that the magnetic flux density distribution derived with the first analytical approach is a special case of the general solution developed using the hybrid FEM-analytical method. Finally, the hybrid FEM-analytical model will be validated experimentally in Chapter 7.

3 Force and Torque Models

In this chapter forward/inverse force and torque models for the reaction sphere actuator are presented. We start by motivating the necessity of these models and by discussing the various approaches presented in the literature. Then, we introduce the coil reference frame and propose transformations to and from the rotor and stator reference frames. Force and torque forward models are derived in stator coordinates. First, we derive force and torque models for a rotor orientation parametrized using spherical harmonic coefficients. Subsequently, the same models are derived for the rotor orientation parametrized with a rotation matrix. Afterwards, we discuss force and torque inverse models, which allow calculating a minimum-energy current vector to satisfy a given force and torque pair. To conclude, we validate the developed force and torque models using FEM simulations.

3.1 Introduction

Force and torque models are necessary for design analysis and real-time control of spherical actuators as they allow relating a given set of stator currents to force and torque outputs. First, the use of these models in combination with actuator dynamic equations allows simulating the actuator dynamic motion. Moreover, force and torque models are necessary for the design of closed-loop dynamic controllers. We use the term “forward model” to indicate the model that provides the force and torque output for a given input current vector. Then, an “inverse model” computes an optimal set of currents to deliver the requested force and torque pair. On one hand, the force is required to control the position of the rotor inside the stator. On the other hand, the torque allows controlling the rotation of the rotor so as to influence the attitude of the satellite.

Depending on the architecture of the design, force and torque forward models between stator coils and the permanent magnet rotor can be obtained with multiple approaches.

To begin with, force and torque analytical models can be derived using the coenergy (or virtual work) method, which is based on the conservation of energy [106]. Forces and torques are obtained by differentiating the coenergy with respect to the linear or angular displacement parameters [24]. This approach was used by Lee et al. to derive the torque of the VRSM [41]. In [43,46], the coenergy method is employed in combination with FEM simulations, which are performed to determine the torque characteristic as a function of the separation angle between a stator pole and two permanent magnet pole pairs. A similar approach is proposed in [67,77,78]. One prerequisite of the implementation of coenergy method for force and torque modeling is that the magnetic energy stored in the airgap of the actuator can be formulated readily [24]. As a matter of fact, due to the existence of large airgap or air-core coils in some cases, the magnetic energy cannot be formulated analytically and the coenergy method becomes ineffective [24].

Another method to derive analytical force and torque models is the Maxwell stress tensor approach. With this method, force and torques are computed by integrating the so called Maxwell stress tensor over the surface surrounding the body [106]. This approach is particularly useful for evaluating the force and torque on soft magnetic materials that have high permeability in free space and it is widely employed in FEM simulations. References of authors that derived the torque model of a spherical actuator using the Maxwell stress tensor include [34,36,114]. This method was also adopted by Ninhuijs et al. [89] to compute the torque of a multi-degree-of-freedom spherical permanent magnet gravity compensator and by Lee et al. [48,100] as a comparative approach.

One of the most employed method to derive force and torque models is based on the Lorentz force law. Lorentz force law is especially useful when the force/torque is generated by a current-carrying conductor laying in the magnetic field of PM [24]. Examples of reference that adopted this method to compute the force and torque models of a permanent magnet spherical actuator include [50,52,55,58,71,72,75,94,97,105,115–117].

Both the Maxwell stress tensor and the Lorentz force methods require knowing the magnetic flux distribution in the region of interest. An alternative method is to compute the magnetic force using the Lorentz force law in analogy to that on an electric charge, which provides closed-form solution if PMs and electromagnets and their magnetic boundaries can be modeled as dipoles [48,98,100]. With both the PMs and electromagnets modeled as DMP, the magnetic forces on the system can be calculated using the Maxwell stress tensor method or the dipole force equation [48]. Unlike the commonly used Lorentz force equation and the Maxwell stress tensor method, the dipole force equation, which replaces integrations with summations, can reduce the computation time [48].

FEM simulations to compute force characteristics between a stator coil and the rotor of a spherical machine with variable pole pitch were proposed in [74]. The force characteristics are stored in look-up tables for the high nonlinearity. FEM simulations are extensively used in combination with experimental measurements as a verification approach.

Another category of approaches to derive expressions for the force and torque are the so-called hybrid methods, in which FEM or measured derived values are used in combination with an analytical model [53, 54]. For instance, in case of reference [54], an analytical torque model of spherical actuator with dihedral-shaped PM poles is derived. Then experimental torque measurements are performed using a research prototype with cylindrical-shaped PM poles. Since the torque characteristic using two different types of PM poles with respect to the rotor orientation is similar, parameters in the analytical model are adjusted to fit with the experimental measurements. The resulting torque model can be employed for real-time motion control of the actuator.

To our understanding, a common characteristics of these modeling techniques is that force and torque models are intrinsically dependent on the orientation of the rotor. Thus, force and torque calculations are carried out by applying a change of coordinates in the derived magnetic flux models, generally parametrized with a set of three Euler angles to account for the orientation of the rotor. To this end, several non-contact based methods were proposed to measure the orientation of the spherical rotor. An overview of these methods is proposed in the next chapter. Computing the orientation is not an easy task. In general, although the relation between current and force and torque is linear, the relation between the rotor orientation parameters and the force and torque is nonlinear.

The difficulty of estimating the rotor orientation has led Bai et al. [57] to develop a direct field-feedback control strategy. As the direct field-feedback control system requires only measured magnetic fields, it eliminates the need of an external orientation sensing system. In the paper, the method for determining the bijective relationship between the rotor orientation and measured magnetic field is presented, which enables the replacement of the orientation error, see for instance [58], by the magnetic field error in the control law. Moreover, a direct mapping based on an artificial neural network is used to compute the magnetic torque model given magnetic flux density measurements provided by 24 single-axis or two-axis Hall sensors adjusted on the middle of each stator coil.

In this chapter we propose a development of forward and inverse force and torque analytical models for the reaction sphere actuator based on the Lorentz force law. As studied in the previous chapter, the rotor magnetic flux density can be expressed in stator coordinates by operating the change of coordinates directly on the spherical harmonic decomposition coefficients or through a classical change of coordinates carried out with a rotation matrix. Similarly, in this chapter we develop force and torque analytical models in stator coordinates with both coordinate transformations treated separately. Moreover, because the magnetic flux density relative to the ideal octupole magnetization in (2.36) is a special case of the general solution in (2.68), force and torque models will be derived by considering the distribution of the magnetic flux density in (2.68). Force and torque models are derived by first considering the interaction between the rotor magnetic flux density and one stator coil and by subsequently invoking the superposition principle to calculate forces and torques generated by the complete set of coils. For the derivation of

force and torque models, we assume that the rotor is positioned exactly at the center of the stator. Finally, we present the derivation of the force and torque inverse model, which allows computing the optimal current vector to satisfy a given force and torque pair.

3.2 Definitions

3.2.1 Coil Reference Frame

As depicted in Fig. 3.1, we define a coil reference frame with the $\hat{\mathbf{z}}_c$ -axis passing through the center of the coil. Moreover, to calculate the force and torque produced by a single coil, we consider the latter as a spherical portion about the $\hat{\mathbf{z}}_c$ -axis delimited by angles θ_{in} and θ_{out} , and by the spherical radii R_{in} and R_{out} as illustrated in Fig. 2.3 and Fig. 2.9. In the following section, we define the coordinate transformations to and from stator and rotor reference frames.

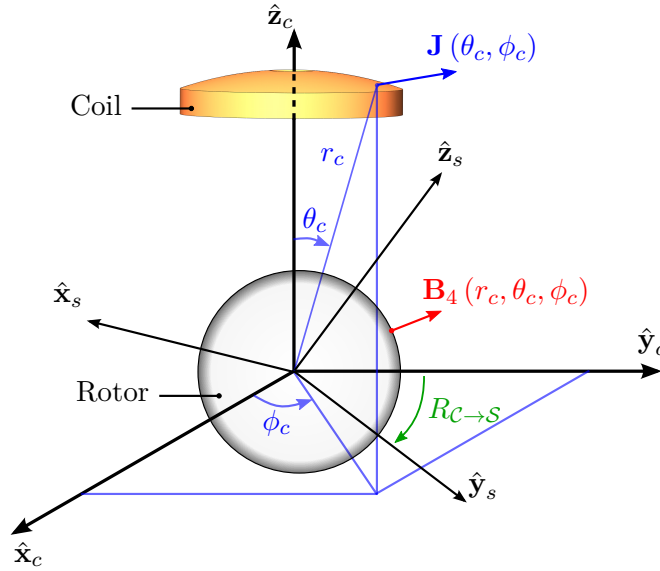


Figure 3.1. Coil reference frame for development of force and torque analytical models.

3.2.2 Coordinate Transformations

Stator ↔ Coil Reference Frames

The angular position of the coil $k = 1, 2, \dots, 20$ in the stator frame \mathcal{S} can be described by a rotation matrix $R_{\mathcal{C} \rightarrow \mathcal{S}, k}(\zeta_k, \eta_k)$, which combines a rotation ζ_k about the $\hat{\mathbf{z}}_s$ -axis, followed by a rotation η_k about the $\hat{\mathbf{x}}_s$ -axis. This rotation allows bringing the stator

$\hat{\mathbf{z}}_s$ -axis parallel to the coil $\hat{\mathbf{z}}_c$ -axis. This rotation matrix takes the form

$$R_{\mathcal{C} \rightarrow \mathcal{S},k}(\zeta_k, \eta_k) = \begin{bmatrix} 1 & 0 & 0 \\ 0 & \cos \eta_k & -\sin \eta_k \\ 0 & \sin \eta_k & \cos \eta_k \end{bmatrix} \begin{bmatrix} \cos \zeta_k & -\sin \zeta_k & 0 \\ \sin \zeta_k & \cos \zeta_k & 0 \\ 0 & 0 & 1 \end{bmatrix} \quad (3.1)$$

$$= \begin{bmatrix} \cos \zeta_k & -\sin \zeta_k & 0 \\ \sin \zeta_k \cos \eta_k & \cos \zeta_k \cos \eta_k & -\sin \eta_k \\ \sin \zeta_k \sin \eta_k & \cos \zeta_k \sin \eta_k & \cos \eta_k \end{bmatrix}. \quad (3.2)$$

Then, given the coil location \mathbf{P}_k , which is expressed in stator coordinates, the following condition shall hold

$$R_{\mathcal{C} \rightarrow \mathcal{S},k}(\zeta_k, \eta_k) \mathbf{P}_k = \begin{bmatrix} 0 \\ 0 \\ 1 \end{bmatrix}, \quad (3.3)$$

which can be used to compute ζ_k and η_k given \mathbf{P}_k . Finally, the unit vectors of the stator reference frame are related to those of the coil reference frame by

$$R_{\mathcal{C} \rightarrow \mathcal{S}} \{ \hat{\mathbf{x}}_c, \hat{\mathbf{y}}_c, \hat{\mathbf{z}}_c \} = \{ \hat{\mathbf{x}}_s, \hat{\mathbf{y}}_s, \hat{\mathbf{z}}_s \}. \quad (3.4)$$

Note that the matrix $R_{\mathcal{C} \rightarrow \mathcal{S},k}(\zeta_k, \eta_k)$ is constant and does not vary with the rotor orientation.

Coil \leftrightarrow Rotor Reference Frames

For the derivation of force and torque models when the rotor orientation is parametrized using the rotation matrix $R_{\mathcal{S} \rightarrow \mathcal{B}}(\alpha, \beta, \gamma)$, which relates the rotor fixed reference frame and the stator reference frame, we introduce a new matrix transformation $R_{\mathcal{C} \rightarrow \mathcal{B}}$. This matrix relates the unit vectors of the rotor reference frame to those of the coil reference frame. As above, the angular position of the coil k in the rotor frame \mathcal{B} can be described in the coil frame by a rotation matrix $R_{\mathcal{C} \rightarrow \mathcal{B},k}(\zeta_k, \eta_k)$, which combines a rotation ζ_k about the $\hat{\mathbf{z}}_b$ -axis, followed by a rotation η_k about the $\hat{\mathbf{x}}_b$ -axis. This rotation allows bringing the rotor $\hat{\mathbf{z}}_b$ -axis parallel to the coil $\hat{\mathbf{z}}_c$ -axis. As for the stator \leftrightarrow coil transformation, this rotation matrix takes the form

$$R_{\mathcal{C} \rightarrow \mathcal{B},k}(\zeta_k, \eta_k) = \begin{bmatrix} \cos \zeta_k & -\sin \zeta_k & 0 \\ \sin \zeta_k \cos \eta_k & \cos \zeta_k \cos \eta_k & -\sin \eta_k \\ \sin \zeta_k \sin \eta_k & \cos \zeta_k \sin \eta_k & \cos \eta_k \end{bmatrix}. \quad (3.5)$$

Notice that we will parametrize $R_{\mathcal{C} \rightarrow \mathcal{B},k}$ using the same angles as above since the two matrices will be used in two separated frameworks. Therefore, for a given orientation of

the rotor described by the matrix $R_{\mathcal{S} \rightarrow \mathcal{B}}(\alpha, \beta, \gamma)$, the following condition shall hold

$$R_{\mathcal{C} \rightarrow \mathcal{B},k}(\zeta_k, \eta_k) R_{\mathcal{S} \rightarrow \mathcal{B}}(\alpha, \beta, \gamma)^\top \mathbf{P}_k = \begin{bmatrix} 0 \\ 0 \\ 1 \end{bmatrix}, \quad (3.6)$$

and can be used to compute ζ_k and η_k given \mathbf{P}_k . Contrary to the angles in (3.3), which do not vary with the rotor orientation, $R_{\mathcal{C} \rightarrow \mathcal{B},k}(\zeta_k, \eta_k)$ is orientation dependent. Finally, the unit vectors of the reference frame are related to the unit vectors of the coil frame through the following relation

$$R_{\mathcal{C} \rightarrow \mathcal{B}} \{ \hat{\mathbf{x}}_c, \hat{\mathbf{y}}_c, \hat{\mathbf{z}}_c \} = \{ \hat{\mathbf{x}}_b, \hat{\mathbf{y}}_b, \hat{\mathbf{z}}_b \}. \quad (3.7)$$

3.3 Rotor Orientation Parametrized with SH Coefficients

3.3.1 Force Generated by a Coil

The force ${}^{\mathcal{C}}\tilde{\mathbf{F}}_k$ generated by the coil k and expressed in the coil reference frame \mathcal{C} depicted in Fig. 3.1 can be calculated using the Lorentz force law as

$${}^{\mathcal{C}}\tilde{\mathbf{F}}_k = \int_{R_{\text{in}}}^{R_{\text{out}}} \int_{\theta_{\text{in}}}^{\theta_{\text{out}}} \int_{-\pi}^{\pi} \mathbf{J}_k \times {}^{\mathcal{C}}\mathbf{B}_4(r_c, \theta_c, \phi_c) r_c^2 \sin \theta_c d\phi_c d\theta_c dr_c \quad (3.8)$$

$$= \int_{R_{\text{in}}}^{R_{\text{out}}} \int_{\theta_{\text{in}}}^{\theta_{\text{out}}} \int_{-\pi}^{\pi} \mathbf{J}_k \times R_{\mathcal{C} \rightarrow \mathcal{S},k} {}^{\mathcal{S}}\mathbf{B}_4(x_s, y_s, z_s) r_c^2 \sin \theta_c d\phi_c d\theta_c dr_c, \quad (3.9)$$

with

$$\begin{bmatrix} x_s \\ y_s \\ z_s \end{bmatrix} = R_{\mathcal{C} \rightarrow \mathcal{S},k}^\top \begin{bmatrix} r_c \sin \theta_c \cos \phi_c \\ r_c \sin \theta_c \sin \phi_c \\ r_c \cos \theta_c \end{bmatrix}. \quad (3.10)$$

The current density in the coil reference frame is expressed by

$$\mathbf{J}_k = J_k \begin{bmatrix} -\sin \phi_c \\ \cos \phi_c \\ 0 \end{bmatrix}, \quad (3.11)$$

where J_k is the amplitude of the vector field. The magnetic flux density for any orientation is calculated using equation (2.72). Therefore, from (3.9), we obtain the force generated by a coil and by the spherical harmonic of degree n and order m as

$${}^{\mathcal{C}}\tilde{\mathbf{F}}_{k,n}^m = \int_{R_{\text{in}}}^{R_{\text{out}}} \int_{\theta_{\text{in}}}^{\theta_{\text{out}}} \int_{-\pi}^{\pi} \mathbf{J}_k \times R_{\mathcal{C} \rightarrow \mathcal{S},k} {}^{\mathcal{S}}\mathbf{B}_{4,n}^m(x_s, y_s, z_s) r_c^2 \sin \theta_c d\phi_c d\theta_c dr_c. \quad (3.12)$$

Then, the net force generated by a single coil is obtained by summing forces generated

3.3. Rotor Orientation Parametrized with SH Coefficients

by each spherical harmonic as

$${}^c\tilde{\mathbf{F}}_k = \sum_{\substack{n \in \mathbb{I}_n \\ n \leq N_h}} \sum_{m=-n}^n c_n^m(\alpha, \beta, \gamma) {}^c\tilde{\mathbf{F}}_{k,n}^m. \quad (3.13)$$

Recall that \mathbb{I}_n is the set of possible spherical harmonic degree of the rotor magnetic flux density previously defined in (2.64) and N_h is the maximum spherical harmonic degree taken into account. Finally, notice that the integral (3.12) can be expressed in closed-form using a program of symbolic computation.

3.3.2 Torque Generated by a Coil

Following the same development used to calculate the force, the torque ${}^c\tilde{\mathbf{T}}_k$ generated by coil k and expressed in its reference frame is obtained by making the cross product of the application points of the infinitesimal forces by their values

$${}^c\tilde{\mathbf{T}}_k = \int_{R_{\text{in}}}^{R_{\text{out}}} \int_{\theta_{\text{in}}}^{\theta_{\text{out}}} \int_{-\pi}^{\pi} \mathbf{r} \times \mathbf{J}_k \times {}^c\mathbf{B}_4(r_c, \theta_c, \phi_c) r_c^2 \sin \theta_c d\phi_c d\theta_c dr_c \quad (3.14)$$

$$= \int_{R_{\text{in}}}^{R_{\text{out}}} \int_{\theta_{\text{in}}}^{\theta_{\text{out}}} \int_{-\pi}^{\pi} \mathbf{r} \times \mathbf{J}_k \times R_{C \rightarrow S, k} {}^S\mathbf{B}_4(x_s, y_s, z_s) r_c^2 \sin \theta_c d\phi_c d\theta_c dr_c, \quad (3.15)$$

where

$$\mathbf{r} = \begin{bmatrix} r_c \sin \theta_c \cos \phi_c \\ r_c \sin \theta_c \sin \phi_c \\ r_c \cos \theta_c \end{bmatrix}. \quad (3.16)$$

Then, the torque generated by a single coil and by the spherical harmonic of degree n and order m becomes

$${}^c\tilde{\mathbf{T}}_{k,n}^m = \int_{R_{\text{in}}}^{R_{\text{out}}} \int_{\theta_{\text{in}}}^{\theta_{\text{out}}} \int_{-\pi}^{\pi} \mathbf{r} \times \mathbf{J}_k \times R_{C \rightarrow S, k} {}^S\mathbf{B}_{4,n}^m(x_s, y_s, z_s) r_c^2 \sin \theta_c d\phi_c d\theta_c dr_c. \quad (3.17)$$

Finally, the net torque provided by the coil is calculated summing the contribution of each spherical harmonic as

$${}^c\tilde{\mathbf{T}}_k = \sum_{\substack{n \in \mathbb{I}_n \\ n \leq N_h}} \sum_{m=-n}^n c_n^m(\alpha, \beta, \gamma) {}^c\tilde{\mathbf{T}}_{k,n}^m. \quad (3.18)$$

3.3.3 Complete Force and Torque Model

Given a set of 20-coil coordinates \mathbf{P}_k , each having a current density norm J_k , the force ${}^c\tilde{\mathbf{F}}_k$ and torque ${}^c\tilde{\mathbf{T}}_k$ generated by a coil can be computed using expressions (3.13) and (3.18), respectively. Summing forces and torques given by each individual coil in the

stator frame \mathcal{S} results in the complete force and torque models

$${}^{\mathcal{S}}\mathbf{F} = \sum_{k=1}^{20} R_{\mathcal{C} \rightarrow \mathcal{S}, k}^{\top} {}^{\mathcal{C}}\tilde{\mathbf{F}}_k(J_k) = \sum_{\substack{n \in \mathbb{I}_n \\ n \leq N_h}} \sum_{m=-n}^n c_n^m(\alpha, \beta, \gamma) \sum_{k=1}^{20} R_{\mathcal{C} \rightarrow \mathcal{S}, k}^{\top} {}^{\mathcal{C}}\tilde{\mathbf{F}}_{k,n}^m(J_k) \quad (3.19)$$

and

$${}^{\mathcal{S}}\mathbf{T} = \sum_{k=1}^{20} R_{\mathcal{C} \rightarrow \mathcal{S}, k}^{\top} {}^{\mathcal{C}}\tilde{\mathbf{T}}_k(J_k) = \sum_{\substack{n \in \mathbb{I}_n \\ n \leq N_h}} \sum_{m=-n}^n c_n^m(\alpha, \beta, \gamma) \sum_{k=1}^{20} R_{\mathcal{C} \rightarrow \mathcal{S}, k}^{\top} {}^{\mathcal{C}}\tilde{\mathbf{T}}_{k,n}^m(J_k). \quad (3.20)$$

By applying the current density norm substitution

$$J_k = \frac{2N_t}{(R_{\text{out}}^2 - R_{\text{in}}^2)(\theta_{\text{out}} - \theta_{\text{in}})}, \quad (3.21)$$

where N_t is the number of turns in each coil, expressions (3.19) and (3.20) can be written as

$${}^{\mathcal{S}}\mathbf{F} = \sum_{\substack{n \in \mathbb{I}_n \\ n \leq N_h}} \sum_{m=-n}^n c_n^m(\alpha, \beta, \gamma) K_{\mathbf{F}, n}^m \mathbf{i}, \quad \text{and} \quad {}^{\mathcal{S}}\mathbf{T} = \sum_{\substack{n \in \mathbb{I}_n \\ n \leq N_h}} \sum_{m=-n}^n c_n^m(\alpha, \beta, \gamma) K_{\mathbf{T}, n}^m \mathbf{i}, \quad (3.22)$$

where $\mathbf{i} \in \mathbb{R}^{20 \times 1}$ is a current vector, and $K_{\mathbf{F}, n}^m \in \mathbb{R}^{3 \times 20}$ and $K_{\mathbf{T}, n}^m \in \mathbb{R}^{3 \times 20}$ are respectively force and torque matrices for the harmonic of degree n and order m and are defined as

$$\begin{aligned} K_{\mathbf{F}, n}^m &= \left[R_{\mathcal{C} \rightarrow \mathcal{S}, 1}^{\top} {}^{\mathcal{C}}\tilde{\mathbf{F}}_{1,n}^m \quad R_{\mathcal{C} \rightarrow \mathcal{S}, 2}^{\top} {}^{\mathcal{C}}\tilde{\mathbf{F}}_{2,n}^m \quad \cdots \quad R_{\mathcal{C} \rightarrow \mathcal{S}, 20}^{\top} {}^{\mathcal{C}}\tilde{\mathbf{F}}_{20,n}^m \right], \quad \text{and} \\ K_{\mathbf{T}, n}^m &= \left[R_{\mathcal{C} \rightarrow \mathcal{S}, 1}^{\top} {}^{\mathcal{C}}\tilde{\mathbf{T}}_{1,n}^m \quad R_{\mathcal{C} \rightarrow \mathcal{S}, 2}^{\top} {}^{\mathcal{C}}\tilde{\mathbf{T}}_{2,n}^m \quad \cdots \quad R_{\mathcal{C} \rightarrow \mathcal{S}, 20}^{\top} {}^{\mathcal{C}}\tilde{\mathbf{T}}_{20,n}^m \right]. \end{aligned} \quad (3.23)$$

We emphasize that in (3.22), forces and torques are expressed as a linear combination of forces and torques provided by each spherical harmonic of degree n and order m , with the coefficients c_n^m delivering to the models all the necessary information relative to the orientation of the rotor. Notice that the matrices $K_{\mathbf{F}, n}^m$ and $K_{\mathbf{T}, n}^m$ given by (3.23) are constant and can be computed offline. Finally, defining force and torque characteristic matrices $K_{\mathbf{F}} \in \mathbb{R}^{3 \times 20}$ and $K_{\mathbf{T}} \in \mathbb{R}^{3 \times 20}$ as

$$K_{\mathbf{F}} = \sum_{\substack{n \in \mathbb{I}_n \\ n \leq N_h}} \sum_{m=-n}^n c_n^m(\alpha, \beta, \gamma) K_{\mathbf{F}, n}^m, \quad \text{and} \quad K_{\mathbf{T}} = \sum_{\substack{n \in \mathbb{I}_n \\ n \leq N_h}} \sum_{m=-n}^n c_n^m(\alpha, \beta, \gamma) K_{\mathbf{T}, n}^m, \quad (3.24)$$

equations (3.22) can be rewritten in a compact form as

$${}^{\mathcal{S}}\mathbf{F} = K_{\mathbf{F}}(\mathbf{c}) \mathbf{i}, \quad \text{and} \quad {}^{\mathcal{S}}\mathbf{T} = K_{\mathbf{T}}(\mathbf{c}) \mathbf{i}, \quad (3.25)$$

with

$$\mathbf{c} = \left[c_3^{-3} \quad c_3^{-2} \quad c_3^{-1} \quad c_3^0 \quad c_3^1 \quad c_3^2 \quad c_3^3 \quad \dots \quad c_{N_h}^{-N_h} \quad c_{N_h}^{-N_h+1} \quad \dots \quad c_{N_h}^{N_h} \right]^T. \quad (3.26)$$

3.4 Orientation Parametrized with Rotation Matrix

When the change of reference frame from the rotor to the stator is carried out using a rotation matrix, we follow precisely the same procedure used above to develop the force and torque models.

3.4.1 Force Generated by a Coil

We begin to calculate the force ${}^C \tilde{\mathbf{F}}_k$ generated by the coil expressed in the coil reference frame as

$${}^C \tilde{\mathbf{F}}_k = \int_{R_{\text{in}}}^{R_{\text{out}}} \int_{\theta_{\text{in}}}^{\theta_{\text{out}}} \int_{-\pi}^{\pi} \mathbf{J}_k \times {}^C \mathbf{B}_4(r_c, \theta_c, \phi_c) r_c^2 \sin \theta_c d\phi_c d\theta_c dr_c \quad (3.27)$$

$$= \int_{R_{\text{in}}}^{R_{\text{out}}} \int_{\theta_{\text{in}}}^{\theta_{\text{out}}} \int_{-\pi}^{\pi} \mathbf{J}_k \times R_{C \rightarrow \mathcal{B}, k} {}^{\mathcal{B}} \mathbf{B}_4(x_b, y_b, z_b) r_c^2 \sin \theta_c d\phi_c d\theta_c dr_c, \quad (3.28)$$

with

$$\begin{bmatrix} x_b \\ y_b \\ z_b \end{bmatrix} = R_{C \rightarrow \mathcal{B}, k}^T \begin{bmatrix} r_c \sin \theta_c \cos \phi_c \\ r_c \sin \theta_c \sin \phi_c \\ r_c \cos \theta_c \end{bmatrix}. \quad (3.29)$$

Notice that, contrary to equation (3.9) where the magnetic flux density is expressed in the stator frame, in (3.28) the flux density is expressed in the rotor frame.

The current density \mathbf{J}_k in the coil reference frame is expressed by (3.11). Again, we consider the force generated by coil k and by the spherical harmonic of degree n and order m as

$${}^C \tilde{\mathbf{F}}_{k,n}^m = \int_{R_{\text{in}}}^{R_{\text{out}}} \int_{\theta_{\text{in}}}^{\theta_{\text{out}}} \int_{-\pi}^{\pi} \mathbf{J}_k \times R_{C \rightarrow \mathcal{B}, k} {}^{\mathcal{B}} \mathbf{B}_{4,n}^m(x_b, y_b, z_b) r_c^2 \sin \theta_c d\phi_c d\theta_c dr_c. \quad (3.30)$$

Then, the net force generated by a single coil is obtained by summing forces generated by each spherical harmonic as

$${}^C \tilde{\mathbf{F}}_k = \sum_{\substack{n \in \mathbb{L}_n \\ n \leq N_h}} \sum_{m=-n}^n c_{n, \text{imm}}^m {}^C \tilde{\mathbf{F}}_{k,n}^m. \quad (3.31)$$

3.4.2 Torque Generated by a Coil

Similarly, the torque ${}^C\tilde{\mathbf{T}}_k$ generated by coil k and expressed in its reference frame can be written as

$${}^C\tilde{\mathbf{T}}_k = \int_{R_{\text{in}}}^{R_{\text{out}}} \int_{\theta_{\text{in}}}^{\theta_{\text{out}}} \int_{-\pi}^{\pi} \mathbf{r} \times \mathbf{J}_k \times {}^C\mathbf{B}_4(r_c, \theta_c, \phi_c) r_c^2 \sin \theta_c d\phi_c d\theta_c dr_c \quad (3.32)$$

$$= \int_{R_{\text{in}}}^{R_{\text{out}}} \int_{\theta_{\text{in}}}^{\theta_{\text{out}}} \int_{-\pi}^{\pi} \mathbf{r} \times \mathbf{J}_k \times R_{\mathcal{C} \rightarrow \mathcal{B}, k} {}^B\mathbf{B}_4(x_b, y_b, z_b) r_c^2 \sin \theta_c d\phi_c d\theta_c dr_c, \quad (3.33)$$

with \mathbf{r} given by (3.16). Then, the torque generated by a single coil and by the spherical harmonic of degree n and order m becomes

$${}^C\tilde{\mathbf{T}}_{k,n}^m = \int_{R_{\text{in}}}^{R_{\text{out}}} \int_{\theta_{\text{in}}}^{\theta_{\text{out}}} \int_{-\pi}^{\pi} \mathbf{r} \times \mathbf{J}_k \times R_{\mathcal{C} \rightarrow \mathcal{B}, k} {}^B\mathbf{B}_{4,n}^m(x_b, y_b, z_b) r_c^2 \sin \theta_c d\phi_c d\theta_c dr_c. \quad (3.34)$$

Finally, the net torque provided by the coil is calculated summing the contribution of each spherical harmonic as

$${}^C\tilde{\mathbf{T}}_k = \sum_{\substack{n \in \mathbb{L}_n \\ n \leq N_h}} \sum_{m=-n}^n c_{n,\text{imm}}^m {}^C\tilde{\mathbf{T}}_{k,n}^m. \quad (3.35)$$

Notice that in this expression, as in (3.31), spherical harmonic coefficients $c_{n,\text{imm}}^m$ are constant and do not depend on the rotor orientation.

3.4.3 Complete Force and Torque Model

The force ${}^C\tilde{\mathbf{F}}_k$ and torque ${}^C\tilde{\mathbf{T}}_k$ generated by coil k , and expressed in the coil reference frame can be computed using expressions (3.31) and (3.35), respectively. Now, the force and torque given by each coil have to be summed in the stator reference frame. To do this, we first express forces and torques in the rotor frame using the matrix $R_{\mathcal{C} \rightarrow \mathcal{B}}$ and subsequently express them in the stator frame using $R_{\mathcal{S} \rightarrow \mathcal{B}}$. Therefore, given a set of 20-coil coordinates \mathbf{P}_k , each having a current density norm J_k , the complete force and torque models are written as

$${}^S\mathbf{F} = R_{\mathcal{S} \rightarrow \mathcal{B}} \sum_{k=1}^{20} R_{\mathcal{C} \rightarrow \mathcal{B}, k}^T {}^C\tilde{\mathbf{F}}_k(J_k) = R_{\mathcal{S} \rightarrow \mathcal{B}} \sum_{\substack{n \in \mathbb{L}_n \\ n \leq N_h}} \sum_{m=-n}^n c_{n,\text{imm}}^m \sum_{k=1}^{20} R_{\mathcal{C} \rightarrow \mathcal{B}, k}^T {}^C\tilde{\mathbf{F}}_{k,n}^m(J_k) \quad (3.36)$$

and

$${}^S\mathbf{T} = R_{\mathcal{S} \rightarrow \mathcal{B}} \sum_{k=1}^{20} R_{\mathcal{C} \rightarrow \mathcal{B}, k}^T {}^C\tilde{\mathbf{T}}_k(J_k) = R_{\mathcal{S} \rightarrow \mathcal{B}} \sum_{\substack{n \in \mathbb{L}_n \\ n \leq N_h}} \sum_{m=-n}^n c_{n,\text{imm}}^m \sum_{k=1}^{20} R_{\mathcal{C} \rightarrow \mathcal{B}, k}^T {}^C\tilde{\mathbf{T}}_{k,n}^m(J_k), \quad (3.37)$$

where $R_{\mathcal{C} \rightarrow \mathcal{B},k}$ shall satisfy (3.6).

By applying the current density norm substitution (3.21), expressions (3.36) and (3.37) can be written as

$${}^S\mathbf{F} = R_{\mathcal{S} \rightarrow \mathcal{B}} \sum_{\substack{n \in \mathbb{L}_n \\ n \leq N_h}} \sum_{m=-n}^n c_{n,\text{imm}}^m K_{\mathbf{F},n}^m \mathbf{i}, \quad \text{and} \quad {}^S\mathbf{T} = R_{\mathcal{S} \rightarrow \mathcal{B}} \sum_{\substack{n \in \mathbb{L}_n \\ n \leq N_h}} \sum_{m=-n}^n c_{n,\text{imm}}^m K_{\mathbf{T},n}^m \mathbf{i}, \quad (3.38)$$

where, as above, \mathbf{i} is a current vector, and $K_{\mathbf{F},n}^m$ and $K_{\mathbf{T},n}^m$ are respectively force and torque matrices for the harmonic of degree n and order m and are defined as

$$\begin{aligned} K_{\mathbf{F},n}^m &= \left[R_{\mathcal{C} \rightarrow \mathcal{B},1}^\top \tilde{\mathbf{F}}_{1,n}^m \quad R_{\mathcal{C} \rightarrow \mathcal{B},2}^\top \tilde{\mathbf{F}}_{2,n}^m \quad \cdots \quad R_{\mathcal{C} \rightarrow \mathcal{B},20}^\top \tilde{\mathbf{F}}_{20,n}^m \right], \quad \text{and} \\ K_{\mathbf{T},n}^m &= \left[R_{\mathcal{C} \rightarrow \mathcal{B},1}^\top \tilde{\mathbf{T}}_{1,n}^m \quad R_{\mathcal{C} \rightarrow \mathcal{B},2}^\top \tilde{\mathbf{T}}_{2,n}^m \quad \cdots \quad R_{\mathcal{C} \rightarrow \mathcal{B},20}^\top \tilde{\mathbf{T}}_{20,n}^m \right]. \end{aligned} \quad (3.39)$$

We emphasize that in (3.38), forces and torques are expressed as a linear combination of forces and torques provided by each spherical harmonic of degree n and order m . Notice that the matrices $K_{\mathbf{F},n}^m$ and $K_{\mathbf{T},n}^m$ given by (3.39) are constant and can be computed offline. Finally, defining force and torque characteristic matrices $K_{\mathbf{F}}$ and $K_{\mathbf{T}}$ as

$$K_{\mathbf{F}}(R_{\mathcal{S} \rightarrow \mathcal{B}}) = R_{\mathcal{S} \rightarrow \mathcal{B}} \sum_{\substack{n \in \mathbb{L}_n \\ n \leq N_h}} \sum_{m=-n}^n c_{n,\text{imm}}^m K_{\mathbf{F},n}^m, \quad \text{and} \quad (3.40)$$

$$K_{\mathbf{T}}(R_{\mathcal{S} \rightarrow \mathcal{B}}) = R_{\mathcal{S} \rightarrow \mathcal{B}} \sum_{\substack{n \in \mathbb{L}_n \\ n \leq N_h}} \sum_{m=-n}^n c_{n,\text{imm}}^m K_{\mathbf{T},n}^m, \quad (3.41)$$

equations (3.38) can be rewritten in a compact form as

$${}^S\mathbf{F} = K_{\mathbf{F}}(R_{\mathcal{S} \rightarrow \mathcal{B}}) \mathbf{i}, \quad \text{and} \quad {}^S\mathbf{T} = K_{\mathbf{T}}(R_{\mathcal{S} \rightarrow \mathcal{B}}) \mathbf{i}. \quad (3.42)$$

3.5 Force and Torque Inverse Models

In the previous two sections we have derived force and torque forward models using different parametrizations for the rotor orientation. Independently from the rotor orientation parametrization, force and torque models resulted in the following structure

$$\mathbf{F} = K_{\mathbf{F}} \mathbf{i}, \quad \text{and} \quad \mathbf{T} = K_{\mathbf{T}} \mathbf{i}, \quad (3.43)$$

which can also be written compactly as

$$\begin{bmatrix} \mathbf{F} \\ \mathbf{T} \end{bmatrix} = \begin{bmatrix} K_{\mathbf{F}} \\ K_{\mathbf{T}} \end{bmatrix} \mathbf{i} = K_{\mathbf{F},\mathbf{T}} \mathbf{i}. \quad (3.44)$$

For control purposes, an inverse model that determines a current vector \mathbf{i} for a desired force \mathbf{F} and torque \mathbf{T} needs to be derived. The difficulty of the inverse model is that there are 20 degrees of freedom for the current and only 6 degrees of freedom for forces and torques making the system (3.44) underdetermined.

Because forces and torques generated by the stator span a three-dimensional space, the rank of the matrices K_F and K_T is equal to three. For the proposed stator configuration, where coils are located at the vertexes of a dodecahedron, this rank property remains valid for any possible orientation of the rotor (it can be shown with numerical simulations that this is not the case if we consider a stator with only 12 coils located at the vertexes of an icosahedron). Next, we introduce the following proposition.

Proposition 1. *Force and torque are mutually orthogonal. Therefore, given $K_F \in \mathbb{R}^{3 \times 20}$ and $K_T \in \mathbb{R}^{3 \times 20}$, we have that $K_F K_T^T = 0$.*

Illustration. The illustration is proposed in Appendix B.1. □

Therefore, because force and torque characteristic matrices are mutually orthogonal, i.e., $K_F K_T^T = 0$, the matrix $K_{F,T}$ in (3.44) is full rank (the rank is equal to six), which implies that (3.44) has infinitely many solutions. In other words, there are infinitely many current vectors \mathbf{i} that satisfy a given force and torque pair. Therefore, to calculate the current vector \mathbf{i} , we consider the least-squares solution of (3.44)

$$\mathbf{i}_{LS} = K_{F,T}^T \left(K_{F,T} K_{F,T}^T \right)^{-1} \begin{bmatrix} \mathbf{F} \\ \mathbf{T} \end{bmatrix}. \quad (3.45)$$

Notice that $\left(K_{F,T} K_{F,T}^T \right)^{-1}$ exists because $K_{F,T} K_{F,T}^T$ is full rank since $K_{F,T}$ is full rank ($K_{F,T}$ is full rank as discussed above).

Proposition 2. *Solution \mathbf{i}_{LS} is the unique least-squares solution that minimizes the electrical energy.*

Illustration. The illustration is proposed in Appendix B.2. □

Proposition 2 guarantees that the current vector computed using (3.45) is the unique minimum-energy least-squares solution of (3.44). The least-squares solution approach to compute the current vector satisfying a given torque reference has also been adopted by other authors [48, 49, 56, 58, 77, 98, 118].

The minimum-energy solution in (3.45) can be expanded as

$$\mathbf{i}_{LS} = \begin{bmatrix} K_F^T & K_T^T \end{bmatrix} \left(\begin{bmatrix} K_F \\ K_T \end{bmatrix} \begin{bmatrix} K_F^T & K_T^T \end{bmatrix} \right)^{-1} \begin{bmatrix} \mathbf{F} \\ \mathbf{T} \end{bmatrix} \quad (3.46)$$

$$= \begin{bmatrix} K_F^T & K_T^T \end{bmatrix} \begin{bmatrix} K_F K_F^T & K_F K_T^T \\ K_T K_F^T & K_T K_T^T \end{bmatrix}^{-1} \begin{bmatrix} \mathbf{F} \\ \mathbf{T} \end{bmatrix}. \quad (3.47)$$

Since $K_F K_T^\top = 0$ (see Proposition 1), (3.47) can be rewritten as

$$\mathbf{i} = M_F \mathbf{F} + M_T \mathbf{T}, \quad (3.48)$$

where

$$M_F = K_F^\top (K_F K_F^\top)^{-1} \quad \text{and} \quad M_T = K_T^\top (K_T K_T^\top)^{-1}. \quad (3.49)$$

As discussed above, the rank of the matrices K_F and K_T is equal to three, and so is the one of $K_F K_F^\top$ and $K_T K_T^\top$. Therefore, M_F and M_T always exist. Finally, as can be noticed in 3.48, because of the decoupling characteristic of Proposition 1, force and torque can be controlled independently, which is an attractive feature to control the spherical actuator.

Proposition 3. *A current vector computed to generate a desired reference force \mathbf{F}_{ref} using the force model taking into account only the fundamental harmonics of degree $n = 3$ does not generate any torque, and vice versa. To this end, from (3.24) we define $K_F^3 = \sum_{m=-3}^3 c_3^m(\alpha, \beta, \gamma) K_{F,3}^m$ to be the force characteristic matrix with only the fundamental harmonic taken into account and $K_T^{N_h} = \sum_{\substack{n \in \mathbb{I}_n \\ n \leq N_h}} \sum_{m=-n}^n c_n^m(\alpha, \beta, \gamma) K_{T,n}^m$ to be the torque characteristic matrix with all the harmonics up to N_h . Subsequently, from (3.49) define $M_F^3 = (K_F^3)^\top [K_F^3 (K_F^3)^\top]^{-1}$. Hence, our proposition says that if $\mathbf{i} = M_F^3 \mathbf{F}_{\text{ref}}$, then $K_T^{N_h} \mathbf{i} = K_T^{N_h} M_F^3 \mathbf{F}_{\text{ref}} = K_T^{N_h} (K_F^3)^\top [K_F^3 (K_F^3)^\top]^{-1} \mathbf{F}_{\text{ref}} = 0$. In other words, since the matrix $K_F^3 (K_F^3)^\top$ is nonzero, $K_T^{N_h} (K_F^3)^\top = 0$.*

Illustration. The illustration is proposed in Appendix B.3. □

Proposition 3 has important practical consequences. As a matter of fact, as it will be discussed in the following chapter, because of the limited number of sensors, only the fundamental spherical harmonic of degree $n = 3$ can be taken into account in the force and torque models of our experimental environment. Therefore, Proposition 3 guarantees that a current vector computed through the force model considering the fundamental harmonic only does not generate torque, any vice versa.

3.6 Verification with FEM Simulations

3.6.1 Simulation Setup

The objective of this section is to illustrate the ability of the developed force and torque analytical models to produce suitable current vectors to satisfy reference forces and torques for four randomly-generated orientations of the rotor. This verification is performed using FEM simulations employing the model with ideal octupole rotor magnetization. For each of the four rotor orientations, parametrized using ZYZ Euler angles α , β , and γ , force and torque characteristic matrices are computed using (3.24), in which spherical harmonics coefficients c_n^m are computed according to (2.40) using (2.16). Then, these four pairs of force and torque characteristic matrices are employed to

compute a suitable current vector by applying the inverse model (3.48) to satisfy three randomly-generated pairs of reference forces and torques. Forces and torques are chosen with random direction but with norm equal to 25 N and 1 Nm respectively. Therefore, force and torque inverse models are verified for a total of 12 configurations. Simulations are performed by applying to the stator coils the current vector generated with the inverse model. Finally, simulated forces and torques are computed using the Maxwell stress tensor method in COMSOL Multiphysics and compared to the expected reference values. The simulation setup for this verification is identical as for flux density in Section 2.3.9. Parameters are the same as in Table 2.3.

3.6.2 Results

The three components of the reference and simulated forces for the studied configurations are reported in Fig. 3.2. Similarly, the three components of the torques are displayed in Fig. 3.3. As can be observed, forces and torques resulting from the proposed simulated model are in agreement with the reference values. Finally, for illustrative purposes, the radial component of the simulated magnetic flux density at the surface of the rotor together with coil currents are depicted in Fig. 3.4.

3.7 Summary

In this chapter we presented forward/inverse models of the force and torque resulting from the interaction of the rotor magnetic flux density with stator coil currents. These models are linear and relate a set of stator currents to the output forces and torques.

Forces and torques depend on the orientation of the rotor inside the stator, which is parametrized using two distinct approaches. In the first approach, which is commonly employed in the spherical actuator literature, the rotor orientation is described using a rotation matrix, generally parametrized with Euler angles or quaternions. In the second approach, the rotation of the rotor magnetic flux density is parametrized using a set of spherical harmonic coefficients. With this approach, forces and torques are expressed as a linear combination of forces and torques provided by each spherical harmonic degree n and order m taken into account.

Afterwards, we discussed force and torque inverse models, which allow calculating a minimum-energy current vector to satisfy a given force and torque pair. We have shown that force and torque characteristic matrices are orthogonal, which allows controlling forces and torques independently. With the proposed parametrization using spherical harmonic coefficients, as it will be discussed in the next chapter, the minimum-energy current vector can be computed linearly and in closed-form using several measurements of the radial component of the magnetic flux density. For instance, if we consider the

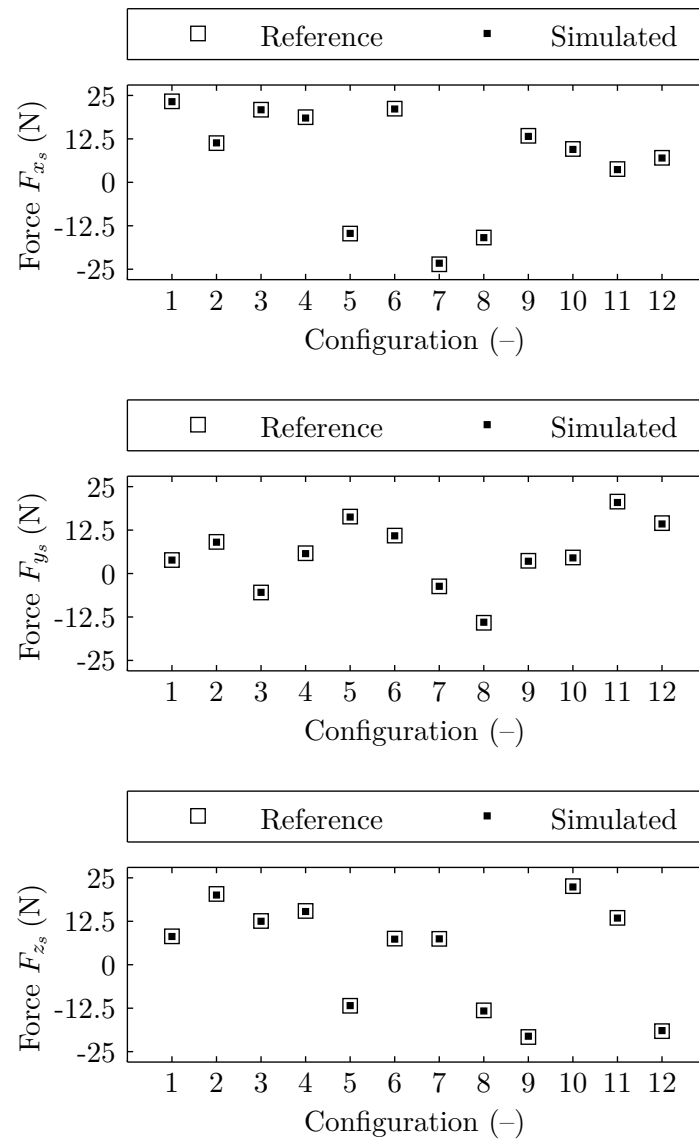


Figure 3.2. Three components of reference and simulated forces for validation of force inverse model with ideal otucpole rotor.

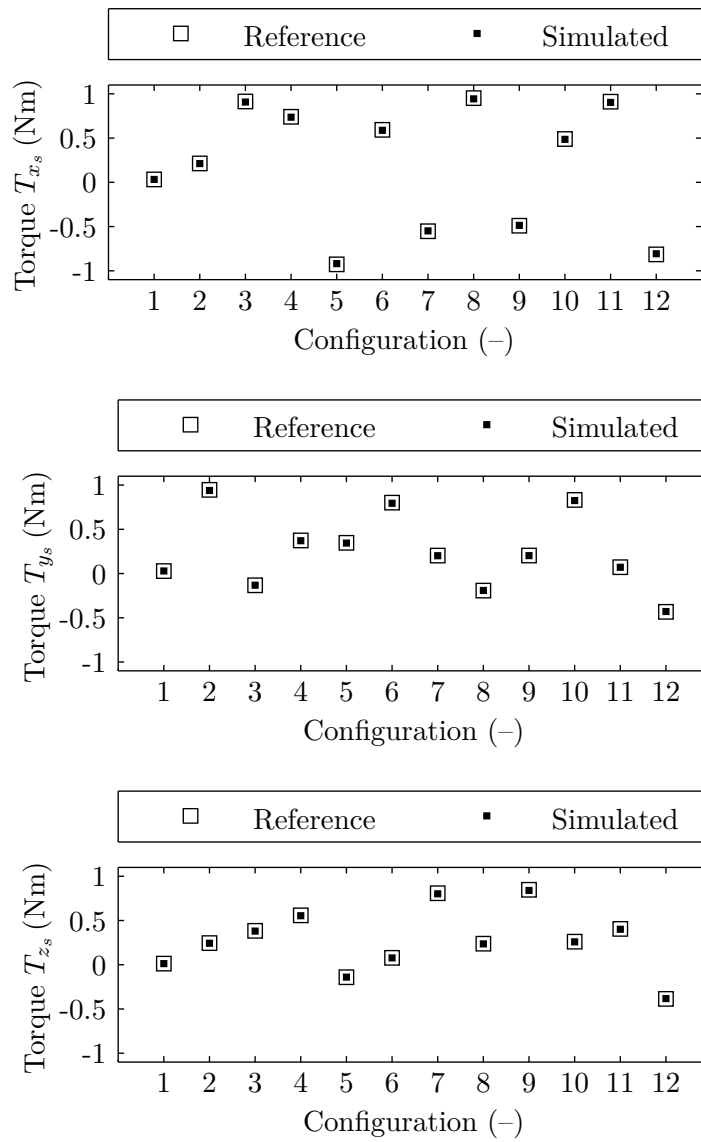


Figure 3.3. Three components of reference and simulated torques for validation of torque inverse model with ideal otucpole rotor.

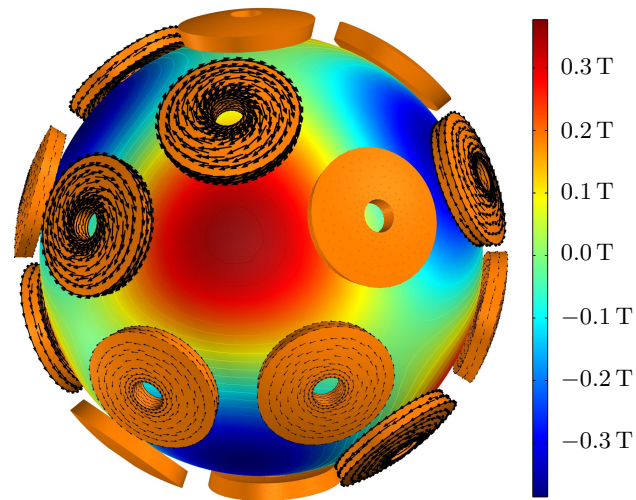


Figure 3.4. Surface plot of the radial component of the simulated magnetic flux density at the surface of the rotor with arrow coil currents relative to configuration 1. The maximum magnetic flux density at the surface of the rotor is 0.37 T while the maximum current is 1.16 A.

ideal octupole magnetization of the rotor as studied in Section 2.3, seven coefficients parametrize the rotor orientation and thus only seven measurements are theoretically required.

4 Magnetic State Estimation and Optimal Sensor Placement

In this chapter we present the magnetic state estimation and an optimal strategy to place magnetic flux density sensors. The magnetic state estimation is defined as the process of estimating spherical harmonic decomposition coefficients c_n^m , which deliver to force and torque models all the information relative to the rotor orientation. The proposed magnetic estimation strategy is based on measuring the radial component of the magnetic flux density at multiple locations equidistant from the rotor surface to subsequently solve a linear inverse problem using least-squares. The proposed procedure is linear and it is expressed in closed-form. Afterwards, we present an optimization strategy to position magnetic flux density sensors that are necessary to estimate the magnetic state. The proposed optimization procedure consists in minimizing the condition number related to the linear estimation problem of the coefficients so as to minimize the influence of the measurement noise on force and torque relative errors. Finally, numerical simulations confirm the effectiveness of the proposed optimization strategy.

4.1 Introduction

As discussed in the previous chapter, the force and the torque depend on the orientation of the rotor inside the stator. In the proposed force and torque models, the information relative to the rotor orientation can be delivered to the models with two different approaches. In the first approach, force and torque models are parametrized using spherical harmonic decomposition coefficients c_n^m as expressed in (3.25) and (3.24). Alternatively, in the second approach, information relative to the rotor orientation is conveyed through a rotation matrix $R_{S \rightarrow B}$ as expressed in (3.42) and (3.41). To employ force and torque models for real-time control operation, either the spherical harmonic coefficients or the rotor orientation matrix have to be computed at each sampling time.

Conventionally, in the 3-DOF spherical actuator literature, force and torque calculations are carried out by applying a change of coordinates in the derived magnetic flux models,

parametrized with a set of three Euler angles to account for the orientation of the rotor. Several non-contact based methods were proposed to measure the orientation of the spherical rotor. For instance, a vision based approach combined with a recursive non-linear optimization algorithm was proposed in [62]. However, the non-linear nature of the problem to solve requires a fairly good initial guess of the orientation. In [119], the authors proposed a laser-based orientation measurement but the apparatus requires a flat reflecting plate that cannot be embedded in our design. An optimization strategy for position and orientation tracking of moving objects in 3-D space is proposed in [120]. The method is based on a distributed multiple pole model of the moving object but requires 3-axis Hall sensors. Another proposed approach consists in a direct method that maps distributed 2-axis and 3-axis magnetic flux density measurements to the instantaneous orientation of the rotor [121]. The proposed mapping is based on an artificial neural network.

For the proposed reaction sphere actuator we proposed an estimation method of the seven spherical harmonic decomposition coefficients [122]. Conversely from [121], where 2-axis and 3-axis magnetic flux density measurements are necessary, the proposed estimation method is based on measuring the radial component of the magnetic flux density at multiple locations equidistant from the rotor surface. Moreover, differently from [110], where the radial component needs to be measured on all the boundary surface, the magnetic flux density in the airgap can be reconstructed with only $N_m \geq 7$ measurements. In addition, contrarily to the estimation of a set of three Euler angles in [62], the proposed procedure is linear and it is expressed in closed-form. Finally, conversely from the estimation of the rotor orientation, where due to the rotor cubic symmetry 12 different orientations can correspond to a given vector of magnetic flux density measurements, the magnetic state is unique and implicitly takes into account all the symmetries of the rotor.

In other words, for the same seven coefficients c_3^m , the rotor could be about 12 different physical orientations that could not be distinguished using magnetic measurements. However, distinguishing these orientations is currently not important since in all of these 12 orientations the rotor has exactly the same force and torque characteristics and will consequently, for a given current vector, produce the same force and torque. In linear algebra words, one would be tempted to say that the space of magnetic configurations is much smaller than the one of physical/mechanical configurations. For the presented force and torque models, the actual physical/mechanical orientation of the rotor is not relevant; what it is important, is the magnetic state, which is completely and uniquely specified by the decomposition coefficients c_n^m . A similar effort to avoid estimating the rotor orientation was recently proposed by Bai et al. [57]. In the proposed approach, magnetic flux density measurements (uniquely corresponding to the rotor orientation) are used for feedback, allowing parallel computation of the control law and computation of the torque model, which is computed using flux density measurements through an artificial neural network. Magnetic flux density measurements are provided by 24 single-axis or two-axis Hall sensors.

In this thesis, we named the process of estimating spherical harmonic decomposition coefficients c_n^m as “magnetic state estimation”. Therefore, in Section 4.2 we introduce a technique to measure the magnetic state of the rotor for offline analysis and real-time control. Then, in Section 4.3 we present an optimization strategy to position magnetic flux density sensors that are necessary for the estimation of the spherical harmonic coefficients. The proposed optimization procedure consists in minimizing the condition number related to the linear estimation problem of the coefficients so as to minimize the influence of the measurement noise on force and torque relative errors. Finally, in Section 4.3.4 we study the influence of the number of sensors, high-order spherical harmonics, and measurement noise on force and torque errors.

4.2 Magnetic State Estimation

4.2.1 Introduction

The magnetic flux density expressed in stator spherical coordinates was calculated in Chapter 2 and its is given by (2.72) and (2.73), which we report here for convenience

$$\mathbf{B}_4(r_s, \theta_s, \phi_s) = \sum_{\substack{n \in \mathbb{I}_n \\ n \leq N_h}} \sum_{m=-n}^n c_n^m \tilde{\mathbf{B}}_{4,n}^m, \quad (4.1)$$

where

$$\tilde{\mathbf{B}}_{4,n}^m = \nabla \left[\frac{r_s^{-(n+1)} \left(R_4^{-(2n+1)} r_s^{2n+1} - 1 \right)}{n R_{\text{dec}}^{n-1} R_4^{-(2n+1)} + (n+1) R_{\text{dec}}^{-(n+2)}} Y_n^m(\theta_s, \phi_s) \right]. \quad (4.2)$$

To simplify the notation, we have dropped the dependence of spherical harmonic coefficients c_n^m on Euler angles α , β , and γ . It is intended, however, that these coefficients vary as a function of the rotor orientation. Recall that R_{dec} is the radial distance where the spherical harmonic decomposition coefficients of the immobile rotor are computed using FEM simulations. Starting from (4.1), the radial component of the magnetic flux density becomes

$$B_{4,r_s}(r_s, \theta_s, \phi_s) = \sum_{\substack{n \in \mathbb{I}_n \\ n \leq N_h}} \sum_{m=-n}^n \Pi_n(R_{\text{dec}}, r_s, R_4) c_n^m Y_n^m(\theta_s, \phi_s) \quad (4.3)$$

where

$$\Pi_n(R_{\text{dec}}, r_s, R_4) = \frac{n r_s^{n-1} R_4^{-(2n+1)} + (n+1) r_s^{-(n+2)}}{n R_{\text{dec}}^{n-1} R_4^{-(2n+1)} + (n+1) R_{\text{dec}}^{-(n+2)}}. \quad (4.4)$$

Our goal here is to compute spherical harmonics coefficients c_n^m given measurements of the radial component of the magnetic flux density B_{4,r_s} .

To predict forces and torques during the actuator design optimization procedure, for

analysis purposes, or for offline operation, these spherical harmonics decomposition coefficients c_n^m can be determined from $c_{n,\text{imm}}^m$ using rotation property (2.40) or by integration as

$$c_n^m = \int_0^{2\pi} \int_0^\pi B_{4,r_s}(r_s, \theta_s, \phi_s) \overline{Y_n^m(\theta_s, \phi_s)} \sin \theta_s d\theta_s d\phi_s, \quad (4.5)$$

which is essentially the Fourier transform of B_{4,r_s} on the unit sphere. Procedures for numerical integration of (4.5) were proposed, for instance, in [112, 123, 124].

For real-time and control operation, computing these coefficients by integration is not practical because of the large amount of data required and the consequential computational effort. Nevertheless, notice that for band-limited functions, the sampling theorem allows the decomposition coefficients to be computed exactly from measurements taken on the equiangular latitude-longitude grid [112, 125, 126]. This approach is very attractive as it requires a limited number of measurements but forces the sensors to be placed on the latitude-longitude grid, which is not very practical for the reaction sphere because of the presence of the stator coils. Moreover, according to the sampling theorem [112], and taking into account symmetries of the magnetic flux density, $4B^2$ measurements are theoretically necessary to completely reconstruct a band-limited function with bandwidth B . For instance, in our situation, if we take into account a maximum spherical harmonic degree N_h , the total number of necessary measurements will be $4(N_h + 1)^2$.

We propose to solve the spherical harmonic decomposition problem using least-squares techniques as originally suggested in [127], and subsequently adopted for a variety of applications [128–131]. For the fundamental harmonics of degree $n = 3$, sampling the radial component of the magnetic flux density at $N_m \geq 7$ mutually non-collinear locations equidistant from the rotor surface to subsequently solve the decomposition problem using least-squares techniques was proposed in [122]. Extending this technique for higher spherical harmonic degrees is possible but currently not practical. As a matter of fact, the number of necessary measurements to reconstruct up to a given degree N_h is equal to $\sum_{\substack{n \in \mathbb{I}_n \\ n \leq N_h}} (2n + 1)$. Hence, for example, 22 measurements are necessary with $N_h = 7$. Therefore, reconstructing the magnetic flux density within the airgap to determine the spherical harmonics coefficients c_n^m for $n > 3$ requires a considerable number of measurements and will not be taken into consideration here. For this reason, for the real-time control model of the force and torque, only the fundamental harmonic of degree $n = 3$ will be reconstructed and only coefficients c_3^m will be computed.

4.2.2 Least-squares Determination of Magnetic State

For $N_h = 3$, expressions (4.3) and (4.4) simplify to

$$B_{4,r_s}(r_s, \theta_s, \phi_s) = \Pi_3(R_{\text{dec}}, r_s, R_4) \sum_{m=-3}^3 c_3^m Y_3^m(\theta_s, \phi_s) \quad (4.6)$$

where

$$\Pi_3(R_{\text{dec}}, r_s, R_4) = \frac{3r_s^3 R_4^{-7} + 4r_s^{-5}}{3R_{\text{dec}}^3 R_4^{-7} + 4R_{\text{dec}}^{-5}}. \quad (4.7)$$

As mentioned above, to compute the spherical harmonic decomposition coefficients c_3^m , we sample the radial component of the magnetic flux density at $N_m \geq 7$ mutually non-collinear locations equidistant from the rotor center and subsequently solve the decomposition problem using least-squares techniques. Therefore, suppose that N_m 1-axis magnetic flux density sensors are placed at $\mathbf{S}_k = (R_{\text{sens}}, \theta_k, \phi_k)$, $k = 1, 2, \dots, N_m$. Then, defining the k^{th} measurement as

$$B_{4,k}^\perp = B_{4,r_s}(R_{\text{sens}}, \theta_k, \phi_k), \quad (4.8)$$

and decomposing c_3^m in its real and imaginary parts as

$$c_3^m = a_3^m + ib_3^m, \quad |m| \leq 3, \quad (4.9)$$

we can write

$$\begin{aligned} \frac{B_{4,k}^\perp}{\Pi_3(R_{\text{dec}}, R_{\text{sens}}, R_4)} &= c_3^0 Y_3^0(\theta_k, \phi_k) + \sum_{m=1}^3 \left[c_3^{-m} Y_3^{-m}(\theta_k, \phi_k) + c_3^m Y_3^m(\theta_k, \phi_k) \right] \\ &= c_3^0 Y_3^0(\theta_k, \phi_k) + \sum_{m=1}^3 \left[\overline{c_3^m Y_3^m(\theta_k, \phi_k)} + c_3^m Y_3^m(\theta_k, \phi_k) \right] \\ &= c_3^0 Y_3^0(\theta_k, \phi_k) + 2 \sum_{m=1}^3 \text{Re} [c_3^m Y_3^m(\theta_k, \phi_k)] \\ &= \frac{a_3^0}{2} R_3^0(\theta_k, \phi_k) + \sum_{m=1}^3 a_3^m R_3^m(\theta_k, \phi_k) + \sum_{m=1}^3 b_3^m I_3^m(\theta_k, \phi_k), \end{aligned} \quad (4.10)$$

where $R_3^m(\theta_k, \phi_k) = 2\text{Re}[Y_3^m(\theta_k, \phi_k)]$ and $I_3^m(\theta_k, \phi_k) = -2\text{Im}[Y_3^m(\theta_k, \phi_k)]$. Therefore, define a vector of N_m magnetic flux measurements as

$$\mathbf{B}_4^\perp = \left[B_{4,1}^\perp \quad B_{4,2}^\perp \quad \dots \quad B_{4,N_m}^\perp \right]^\top, \quad (4.11)$$

and the $N_m \times 7$ matrix $A(\Gamma)$ as

$$A(\Gamma)^\top = \begin{bmatrix} \frac{1}{2}R_3^0(\varsigma_1) & \frac{1}{2}R_3^0(\varsigma_2) & \dots & \frac{1}{2}R_3^0(\varsigma_{N_m}) \\ R_3^1(\varsigma_1) & R_3^1(\varsigma_2) & \dots & R_3^1(\varsigma_{N_m}) \\ R_3^2(\varsigma_1) & R_3^2(\varsigma_2) & \dots & R_3^2(\varsigma_{N_m}) \\ R_3^3(\varsigma_1) & R_3^3(\varsigma_2) & \dots & R_3^3(\varsigma_{N_m}) \\ I_3^1(\varsigma_1) & I_3^1(\varsigma_2) & \dots & I_3^1(\varsigma_{N_m}) \\ I_3^2(\varsigma_1) & I_3^2(\varsigma_2) & \dots & I_3^2(\varsigma_{N_m}) \\ I_3^3(\varsigma_1) & I_3^3(\varsigma_2) & \dots & I_3^3(\varsigma_{N_m}) \end{bmatrix}, \quad (4.12)$$

where Γ is a parameter set of sensor spherical angular coordinates

$$\Gamma = \{ \varsigma_1, \varsigma_2, \dots, \varsigma_{N_m} \}, \quad (4.13)$$

with $\varsigma_k = (\theta_k, \phi_k)$, $k = 1, 2, \dots, N_m$. Then, the desired coefficients (the magnetic state)

$$\mathbf{x} = [a_3^0 \ a_3^1 \ a_3^2 \ a_3^3 \ b_3^1 \ b_3^2 \ b_3^3]^\top \quad (4.14)$$

can be computed solving

$$\Pi_3 A(\Gamma) \mathbf{x} = \mathbf{B}_4^\perp \quad (4.15)$$

using the left-inverse matrix of $A(\Gamma)$ as

$$\mathbf{x} = \frac{1}{\Pi_3} (A^\top A)^{-1} A^\top \mathbf{B}_4^\perp. \quad (4.16)$$

The matrix $A^\top A$ is nonsingular if the sensors are placed so that they are mutually non-collinear. Observe that the matrix

$$P = \frac{1}{\Pi_3} (A^\top A)^{-1} A^\top \quad (4.17)$$

of equation (4.16) is constant and can be computed offline. Hence, force and torque characteristics for the rotor in any possible orientation can be determined in closed-form by projecting the measurements of the radial component of the magnetic flux density on the column space of P .

4.2.3 Update of Force and Torque Models

Force and torque models are defined in (3.24) by their characteristic matrices K_F and K_T , whose structure is reported here for convenience

$$K_F = \sum_{\substack{n \in \mathbb{I}_n \\ n \leq N_h}} \sum_{m=-n}^n c_n^m K_{F,n}^m, \quad \text{and} \quad K_T = \sum_{\substack{n \in \mathbb{I}_n \\ n \leq N_h}} \sum_{m=-n}^n c_n^m K_{T,n}^m. \quad (4.18)$$

4.2. Magnetic State Estimation

As mentioned above, only coefficients c_3^m are available from magnetic state estimation. Therefore, with $N_h = 3$, force and torque characteristic matrices become

$$K_F = \sum_{m=-3}^3 c_3^m K_{F,3}^m, \quad \text{and} \quad K_T = \sum_{m=-3}^3 c_3^m K_{T,3}^m. \quad (4.19)$$

In the previous section, we proposed a method to measure the 7 necessary spherical harmonic decomposition coefficients c_3^m , with $|m| \leq 3$. Hence, given these coefficients, force and torque characteristic matrices are calculated using (4.19). However, applying definition (4.9) and invoking the properties employed to derive (4.10), the force characteristic matrix K_F in (4.19) can be rewritten as

$$K_F = \frac{a_3^0}{2} K_{F,R}^0 + \sum_{m=1}^3 a_3^m K_{F,R}^m + \sum_{m=1}^3 b_3^m K_{F,I}^m \quad (4.20)$$

where

$$K_{F,R}^m = 2\text{Re} \left(K_{F,3}^m \right), \quad \text{and} \quad K_{F,I}^m = -2\text{Im} \left(K_{F,3}^m \right). \quad (4.21)$$

Therefore, the force characteristic matrix can be calculated directly from (4.16) as

$$\begin{aligned} K_F = \frac{x_1}{2} \cdot K_{F,R}^0 + x_2 \cdot K_{F,R}^1 + x_3 \cdot K_{F,R}^2 + x_4 \cdot K_{F,R}^3 \\ + x_5 \cdot K_{F,I}^1 + x_6 \cdot K_{F,I}^2 + x_7 \cdot K_{F,I}^3, \end{aligned} \quad (4.22)$$

where x_k is the k^{th} entry of the solution vector \mathbf{x} . Similarly, defining

$$K_{T,R}^m = 2\text{Re} \left(K_{T,3}^m \right), \quad \text{and} \quad K_{T,I}^m = -2\text{Im} \left(K_{T,3}^m \right), \quad (4.23)$$

the torque characteristic matrix can be expressed as

$$\begin{aligned} K_T = \frac{x_1}{2} \cdot K_{T,R}^0 + x_2 \cdot K_{T,R}^1 + x_3 \cdot K_{T,R}^2 + x_4 \cdot K_{T,R}^3 \\ + x_5 \cdot K_{T,I}^1 + x_6 \cdot K_{T,I}^2 + x_7 \cdot K_{T,I}^3. \end{aligned} \quad (4.24)$$

We emphasize that the matrices $K_{F,R}^m$, $K_{F,I}^m$, $K_{T,R}^m$, and $K_{T,I}^m$ are constant and are computed offline.

4.2.4 Implementation Procedure

The implementation procedure to compute force and torque characteristic matrices for the rotor about any possible orientation is summarized by dividing the operations to be performed as offline and online.

Operations performed offline

1. Place $N_m \geq 7$ mutually non-collinear single-axis magnetic flux density sensors equidistant from the rotor surface so that the matrix $A^\top A$ in (4.16) is full-rank. An optimal placement strategy is proposed in the following section.
2. Given the set of selected sensors, compute the spherical harmonic projection matrix $P \in \mathbb{R}^{7 \times N_m}$ using definition (4.12) and (4.17).
3. Compute force and torque characteristic matrices $K_{F,R}^m \in \mathbb{R}^{3 \times 20}$, $K_{F,I}^m \in \mathbb{R}^{3 \times 20}$, $K_{T,R}^m \in \mathbb{R}^{3 \times 20}$, and $K_{T,I}^m \in \mathbb{R}^{3 \times 20}$ using expressions (4.19), with definitions (4.21) and (4.23). These matrices can be computed with a program of symbolic computation.

Operations performed online

1. Measure the radial component of the flux density and combine the N_m measurements in the vector $\mathbf{B}_4^\perp \in \mathbb{R}^{N_m \times 1}$ defined in (4.11).
2. Compute the decomposition coefficients $\mathbf{x} \in \mathbb{R}^{7 \times 1}$ projecting the measurement vector \mathbf{B}_4^\perp on the matrix P previously computed offline. Hence, $\mathbf{x} = P \cdot \mathbf{B}_4^\perp$.
3. Compute force and torque characteristic matrices $K_F \in \mathbb{R}^{3 \times 20}$ and $K_T \in \mathbb{R}^{3 \times 20}$ as linear combination of matrices $K_{F,R}^m$, $K_{F,I}^m$, $K_{T,R}^m$, and $K_{T,I}^m$ and the measured decomposition coefficients \mathbf{x} as expressed in (4.22) and (4.24).

The diagram of the procedure to compute the force characteristic matrix is reported in Fig. 4.1. Although not reported, the diagram for the torque characteristic matrix has exactly the same structure. Therefore, force and torque characteristic matrices K_F and K_T are expressed as linear combination of the matrices $K_{F,R}^m$, $K_{F,I}^m$, $K_{T,R}^m$, and $K_{T,I}^m$ with the decomposition coefficients x_1, x_2, \dots, x_7 . The matrices $K_{F,R}^m$, $K_{F,I}^m$, $K_{T,R}^m$, and $K_{T,I}^m$ as well as the projection matrix P are constant and are computed offline. Hence, we emphasize that force and torque characteristic matrices for the rotor about any possible orientation are computed non-iteratively and in a linear fashion. Finally, it should be noted that the magnetic flux density measurements will be affected by the field due to stator currents. However, as illustrated in [58], the measured radial components of the flux density are linear with respect to coil currents. Therefore, the influence of the stator currents on the sensor measurements can be compensated for by using current measurements and the information obtained in a calibration procedure.

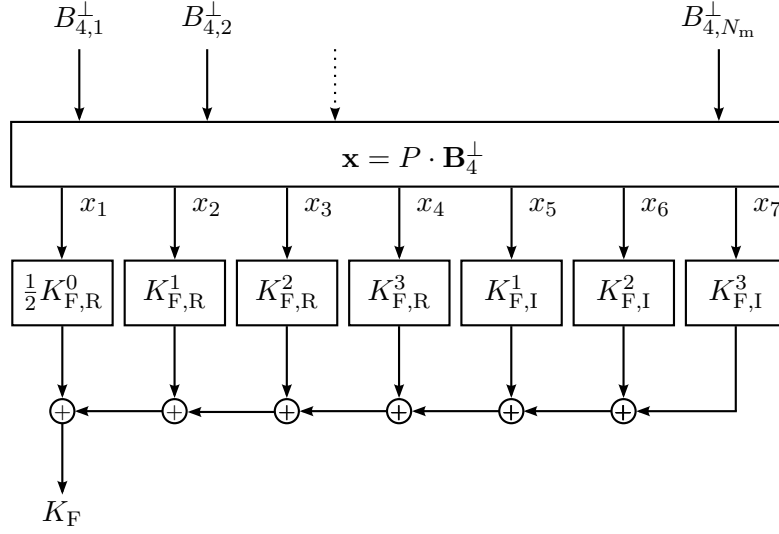


Figure 4.1. Diagram for the computation of the force characteristic matrix $K_F \in \mathbb{R}^{3 \times 20}$. The matrices $K_{F,R}^m$ and $K_{F,I}^m$ as well as the projection matrix P are constant and are computed offline.

4.3 Magnetic Flux Density Optimal Sensor Placement

A minimum of 7 single-axis magnetic flux density sensors is necessary to determine the seven spherical harmonic decomposition coefficients c_3^m , which completely define force and torque characteristics in (4.19). In this section, we propose an optimal strategy to position the magnetic flux density sensors necessary to estimate the magnetic state of the rotor. This strategy is based on minimizing the relative error between a desired reference force (or torque) and the actual force obtained in presence of possible modeling errors and measurement noise.

The optimal sensor placement problem for state or parameter estimation has been intensely investigated in several domains of engineering such as, for instance, aerospace [132], biomedical imaging [133], engine health monitoring [134], model identification [135], and robotics [136]. Although the choice of the performance indexes for the optimization could be based on minimizing a certain error statistics [134, 137], in the present section we adopt a purely deterministic approach minimizing the maximum difference between the perturbed and non-perturbed system given bounds on the largest values attainable by the modeling errors and measurement noise [138].

4.3.1 Perturbed Measurement Equation

Given $N_m \geq 7$ non-collinear magnetic flux density measurements collected in the vector \mathbf{B}_4^\perp , the spherical harmonic decomposition coefficients \mathbf{x} , which represent the magnetic state, can be computed using (4.15). In practice, however, modeling errors, uncertainties related to the position of the sensors, and measurement noise lead to perturbations of the measurement equation (4.15), and consequently to its inconsistency [138]. Assuming additive modeling errors ΔA and measurement noise $\Delta \mathbf{B}_4^\perp$, we define the perturbed measurement equation as

$$[\Pi_3 A(\Gamma) + \Delta A] \hat{\mathbf{x}} = \mathbf{B}_4^\perp + \Delta \mathbf{B}_4^\perp, \quad (4.25)$$

whose least-squares solution is given by

$$\hat{\mathbf{x}} = [\Pi_3 A(\Gamma) + \Delta A]^+ \left(\mathbf{B}_4^\perp + \Delta \mathbf{B}_4^\perp \right), \quad (4.26)$$

where $+$ denotes the Moore-Penrose pseudoinverse, which for a full-rank matrix $M \in \mathbb{R}^{m \times n}$, $m \geq n$, is expressed as $M^+ = (M^\top M)^{-1} M^\top$ [139]. Notice that the least-squares estimation $\hat{\mathbf{x}}$ in (4.26) is equivalent to the best linear unbiased estimator (BLUE) in the special case where $\Delta \mathbf{B}_4^\perp$ is a zero-mean uncorrelated normally distributed random vector and is also equivalent to the maximum-likelihood estimator if $\Delta \mathbf{B}_4^\perp$ is normally distributed [140].

4.3.2 Derivation of an Optimization Criterion

For an arbitrary current vector $\mathbf{i} \in \mathbb{R}^{20 \times 1}$, the force \mathbf{F} relative to the measurement equation (4.15), and the force $\hat{\mathbf{F}}$ relative to the perturbed measurement equation (4.25) can be calculated using (3.25) and (4.22) as

$$\mathbf{F} = K_F(\mathbf{i}) \mathbf{x}, \quad \text{and} \quad \hat{\mathbf{F}} = K_F(\mathbf{i}) \hat{\mathbf{x}}, \quad (4.27)$$

where

$$K_F(\mathbf{i}) = \begin{bmatrix} \frac{1}{2} K_{F,R}^0 \mathbf{i} & K_{F,R}^1 \mathbf{i} & K_{F,R}^2 \mathbf{i} & K_{F,R}^3 \mathbf{i} & K_{F,I}^1 \mathbf{i} & K_{F,I}^2 \mathbf{i} & K_{F,I}^3 \mathbf{i} \end{bmatrix}. \quad (4.28)$$

Then, supposing that $A(\Gamma)$ is full rank with smallest and respectively largest singular values $\sigma_{\min}(A(\Gamma))$ and $\sigma_{\max}(A(\Gamma))$, and assuming that

$$\epsilon = \max \left(\frac{\|\Delta A\|_2}{\|\Pi_3 A(\Gamma)\|_2}, \frac{\|\Delta \mathbf{B}_4^\perp\|_2}{\|\mathbf{B}_4^\perp\|_2} \right) < \frac{\sigma_{\min}(A(\Gamma))}{\sigma_{\max}(A(\Gamma))}, \quad (4.29)$$

4.3. Magnetic Flux Density Optimal Sensor Placement

the maximum relative error for the solution \mathbf{x} becomes [139]

$$\frac{\|\mathbf{x} - \hat{\mathbf{x}}\|_2}{\|\mathbf{x}\|_2} \leq 2\kappa_2(A(\Gamma)) \epsilon, \quad (4.30)$$

where $\kappa_2(A(\Gamma)) = \frac{\sigma_{\max}(A(\Gamma))}{\sigma_{\min}(A(\Gamma))}$ denotes the 2-norm condition number of $A(\Gamma)$. Then, substituting (4.27) in the inequality (4.30) results in

$$\frac{\|K_F^+(\mathbf{i}) \mathbf{F} - K_F^+(\mathbf{i}) \hat{\mathbf{F}}\|_2}{\|K_F^+(\mathbf{i}) \mathbf{F}\|_2} \leq 2\kappa_2(A(\Gamma)) \epsilon. \quad (4.31)$$

Finally, since $K_F^+(\mathbf{i})$ is full-rank by design, using the fact that

$$\|K_F^+(\mathbf{i}) \mathbf{F}\|_2 \leq \|K_F^+(\mathbf{i})\|_2 \|\mathbf{F}\|_2 = \sigma_{\max}(K_F^+(\mathbf{i})) \|\mathbf{F}\|_2 \quad (4.32)$$

and that

$$\|K_F^+(\mathbf{i}) \mathbf{F} - K_F^+(\mathbf{i}) \hat{\mathbf{F}}\|_2 \geq \sigma_{\min}(K_F^+(\mathbf{i})) \|\mathbf{F} - \hat{\mathbf{F}}\|_2, \quad (4.33)$$

inequality (4.30) can be rewritten as

$$\frac{\|\mathbf{F} - \hat{\mathbf{F}}\|_2}{\|\mathbf{F}\|_2} \leq 2\kappa_2(K_F^+(\mathbf{i})) \kappa_2(A(\Gamma)) \epsilon. \quad (4.34)$$

Therefore, in order to minimize the force relative error, sensors are placed so as to minimize the condition number $\kappa_2(A(\Gamma))$. Similar design performance indexes, for different applications, were selected in [129, 133, 141]. Moreover, the condition number is a measure of the eccentricity of the error ellipsoid and minimizing it automatically makes all singular values become more similar in magnitude and makes the hyperellipsoid closed to a hypersphere [136]. Finally, notice that, although not derived in this section, the upper bound for the relative error of the torque is equivalent to (4.34). Therefore, minimizing the condition number leads to minimal relative errors for both forces and torques.

4.3.3 Problem Definition

As derived in (4.34), the problem of finding an optimal location for $N_m \geq 7$ magnetic flux density sensors can be formulated as finding an optimal parameter vector Γ_{opt} of sensor coordinates that solves the minimization problem

$$\Gamma_{\text{opt}} = \underset{\Gamma \in \Gamma_P}{\text{argmin}} \kappa_2(A(\Gamma)), \quad (4.35)$$

where, adopting the terminology presented in [142], Γ_P is the set of possible parameter vectors defined as

$$\Gamma_P = \{ \Gamma \mid \Gamma \in \mathbb{V}, \text{rank}(A(\Gamma)) = 7 \}, \quad (4.36)$$

in which \mathbb{V} is the set of parameter vectors expressed as

$$\mathbb{V} = \{ \Gamma = \{ \varsigma_1, \varsigma_2, \dots, \varsigma_{N_m} \} \mid \varsigma_k \in \mathbb{S}, \varsigma_k \neq \varsigma_m \forall k, m = 1, 2, \dots, N_m \} \quad (4.37)$$

and \mathbb{S} is the set of coordinates where the sensors could potentially be arranged. In this study, sensors shall be placed within the airgap (region 4 in Fig. 2.3) in a number of locations limited by the presence of the stator coils, which occupy a significant portion of the airgap.

4.3.4 Results

Optimization for Various Configurations and Number of Sensors

Possible sensor locations for the first illustrative example are reported in Fig. 4.2 and are divided into three different sets:

$$\mathbb{S}_D = \{ D_1, D_2, \dots, D_{10} \}, \quad (4.38)$$

$$\mathbb{S}_I = \{ I_1, I_2, \dots, I_6 \}, \text{ and} \quad (4.39)$$

$$\mathbb{S}_S = \{ S_1, S_2, \dots, S_{30} \}. \quad (4.40)$$

\mathbb{S}_D includes the centers of 10 coils in a half stator, which are located about the vertexes of a half dodecahedron. \mathbb{S}_I represents the vertexes of an half icosahedron dual of the dodecahedron. Finally, \mathbb{S}_S consists in locations about branches of embedded sensor stars, which have already been employed for previous activities. Therefore, the minimization problem (4.35) is of combinatorial nature and will be solved for $\mathbb{S} = \mathbb{S}_D$, with $N_m = 7, 8, \dots, 10$, and for $\mathbb{S} = \mathbb{S}_D \cup \mathbb{S}_I$ and $\mathbb{S} = \mathbb{S}_S$, for $N_m = 7, 8, \dots, 16$. For \mathbb{S}_D and $\mathbb{S}_D \cup \mathbb{S}_I$ there are at most 120 and respectively 12870 possible combinations (10 choose 7 and 16 choose 8 binomial coefficients). Thus, the optimal configuration can be found by brute force. However, for \mathbb{S}_S , the magnitude of the 30 choose N_m binomial coefficient is large and the optimization problem will be solved using the Genetic Algorithm (GA) distributed with the Optimization Toolbox of MATLAB[®].

The 2-norm condition number $\kappa_2(A(\Gamma))$ as a function of the number of sensors N_m for best and worst configurations within sets \mathbb{S}_D and $\mathbb{S}_D \cup \mathbb{S}_I$ is reported in Fig. 4.3. Only the best configurations are reported for the set \mathbb{S}_S . As it can be observed, for a given number of sensors N_m , their configuration plays an important role on the optimization criterion. The condition number of the problem can be made smaller by increasing the number of sensors but more importantly by arranging them properly. As a matter of fact, a more favorable performance could be obtained by employing a reduced number of

4.3. Magnetic Flux Density Optimal Sensor Placement

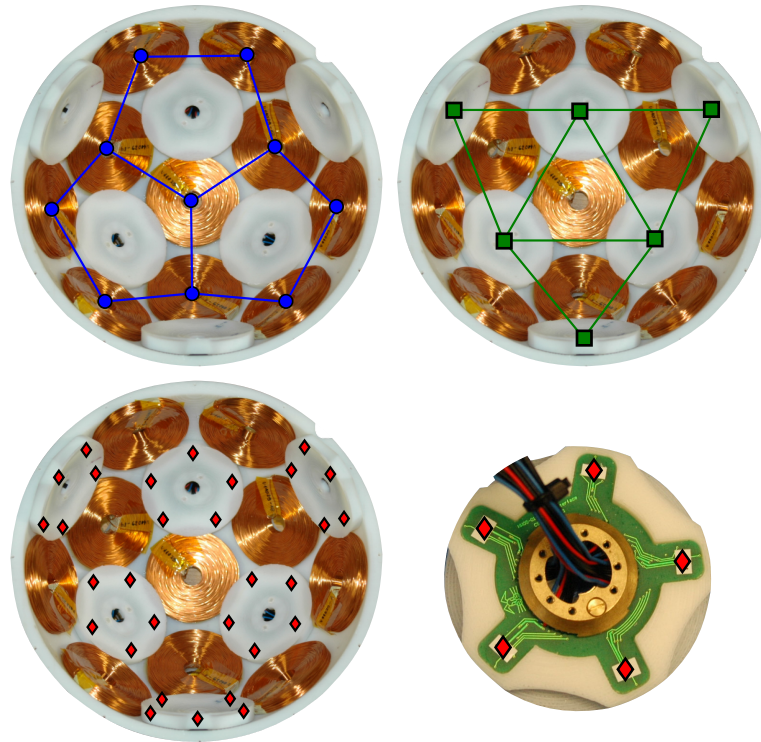


Figure 4.2. Possible locations of magnetic flux density sensors in the reaction sphere stator. (Top-left) Center of coils about dodecahedron vertexes. (Top-right) Vertexes of icosahedron dual of dodecahedron. (Bottom-left) Branches of embedded sensor stars. (Bottom-right) Detail view of an embedded sensor star.

sensors provided that they are arranged carefully. For example, within the set $\mathbb{S}_D \cup \mathbb{S}_I$, an appropriate arrangement of 7 sensors has a better condition number than an inaccurate placement of 12 sensors.

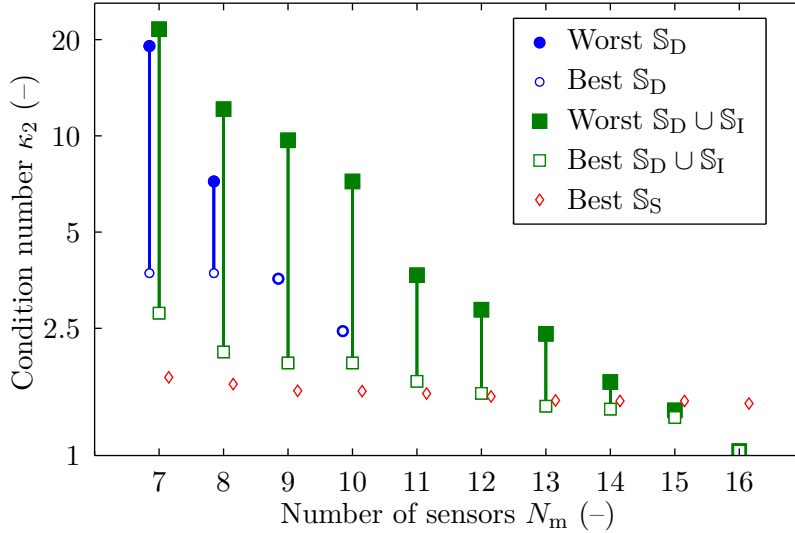


Figure 4.3. Optimization results showing the condition number $\kappa_2(A(\Gamma))$ as a function of the number of sensors N_m placed for best and worst configurations within sets \mathbb{S}_D , $\mathbb{S}_D \cup \mathbb{S}_I$, and \mathbb{S}_S .

The first reaction sphere prototype was equipped with a total of 12 sensor stars as the one in Fig. 4.2 (bottom-right) for a total of 60 sensors. The design of these sensors was performed to obtain a uniform covering of the surface of a sphere and was verified using numerical simulations, without using the presented optimization strategy. However, because the sensing electronics of the first prototype was limited to the acquisition of nine sensor measurements only, the proposed strategy was employed afterwards to select those nine sensors that provided the best result in terms of the selected optimization criterion.

More recently, the proposed optimization strategy was employed to place the sensors for the future prototype of reaction sphere, which will allow the acquisition of 15 sensors. Because of manufacturing constraints, it was decided to distribute the sensors about the three sensor stars as depicted in Fig. 4.4 (top-left). To begin with, we have studied the influence that the number of sensors and α_s have on the condition number κ_2 . As illustrated in Fig. 4.4 (top-left), α_s is defined as the angle between the vector pointing at the center of the sensor star and the vector pointing at a specific sensor in the star. Note that in the first prototype sensors were arranged considering an angle α_s of approximately 17° . Results of this study are reported in Fig. 4.5. The minimum condition number $\kappa_2 \approx 1.83$ is obtained for $\alpha_s \approx 31.71^\circ$, which is the angle corresponding to the arrangement depicted in Fig. 4.4 (top-right), where the nine external sensors are

4.3. Magnetic Flux Density Optimal Sensor Placement

located between two coils. Notice that in this situation, only $N_m = 12$ sensors are used because three central sensors are superimposed. Therefore, to use all the 15 acquisition channels, we have added three additional sensors that we have arranged at the center of the three sensor stars as displayed in Fig. 4.4 (bottom). With this arrangement, the condition number is $\kappa_2 \approx 1.73$.

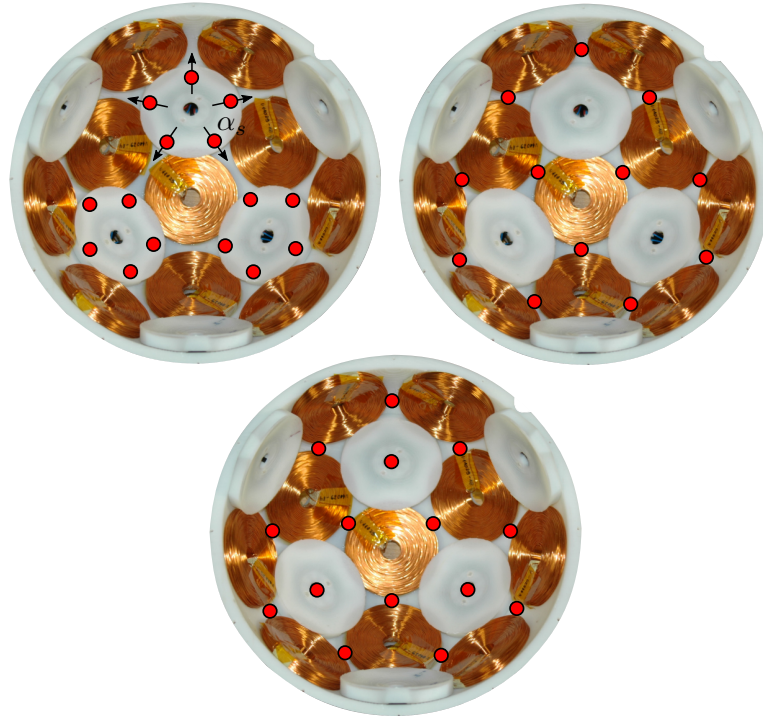


Figure 4.4. Possible locations of magnetic flux density sensors for future reaction sphere prototype.

Influence of Measurement Perturbations

The objective of this section is to illustrate by means of numerical simulations the influence of measurement noise on force relative error for various sensor configurations. This will show that the condition number κ_2 is indeed a suitable indicator for measurement noise sensitivity on the relative error. For this illustration, best and worst configurations of the set $\mathbb{S}_D \cup \mathbb{S}_I$ are taken into account. Moreover, the magnetic flux density model of the rotor is computed employing the hybrid FEM-analytical method proposed in Chapter 2 on the new developed spherical rotor that will be presented in Chapter 6. The magnetic flux density is computed using (4.3) taking into account only the fundamental octupole harmonic ($N_h = 3$).

The scheme for this illustration is depicted in Fig. 4.6. For any given sensor configuration,

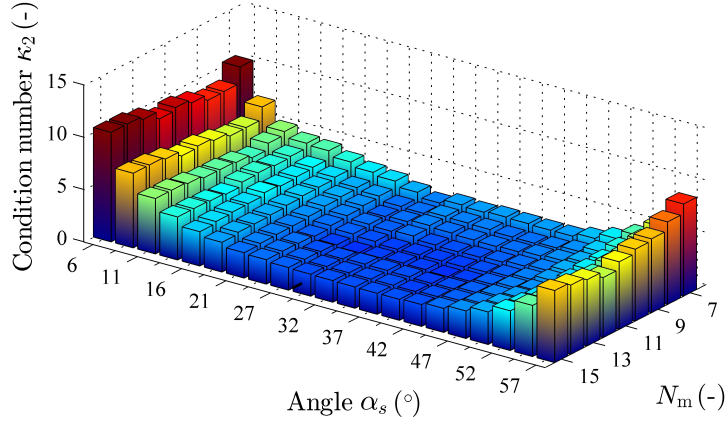


Figure 4.5. Optimization results showing the condition number $\kappa_2(A(\Gamma))$ as a function of the number of sensors N_m and the angle α_s .

which results from the optimization procedure presented in the previous section, the relative error between the reference force \mathbf{F}_{ref} and the actual force $\hat{\mathbf{F}}$ is computed. This evaluation is repeated for $2 \cdot 10^3$ randomly-generated rotor orientations parametrized using ZYZ Euler's angles (α, β, γ) . For each orientation, a vector of currents \mathbf{i} is computed within the controller subsystem so as to satisfy five randomly-generated reference forces \mathbf{F}_{ref} chosen with random direction but with same norm. Hence we have a total of $10 \cdot 10^3$ rotor orientation and force direction combinations. To compute the current vector \mathbf{i} , a set of noise-corrupted magnetic flux density measurements $\mathbf{B}_4^\perp + \Delta\mathbf{B}_4^\perp$ is first decomposed into the spherical harmonic basis to derive $\hat{\mathbf{x}}$ using (4.26) and subsequently K_F with (4.22). Finally, the minimum-energy current vector is obtained as $\mathbf{i} = K_F^+ \mathbf{F}_{\text{ref}}$. In the model subsystem, the actual force $\hat{\mathbf{F}}$ is computed from the current vector \mathbf{i} using (4.18), in which spherical harmonics coefficients c_n^m are computed according to (2.40). Finally, the non-perturbed magnetic flux density \mathbf{B}_4^\perp is computed for the current orientation (α, β, γ) using (4.1), in which c_n^m are computed according to (2.40). For illustration purposes, and although spatial correlation among measurement errors cannot be excluded *a priori*, in the present study the measurement noise $\Delta\mathbf{B}_4^\perp$ is a random vector whose entries are zero-mean uncorrelated normally-distributed random variables. The measurement noise standard deviation is fixed to 8 mT.

To compare the randomly-generated reference forces \mathbf{F}_{ref} to the actual vectors $\hat{\mathbf{F}}$, we introduce the norm relative error defined as

$$\text{Relative error (\%)} = \frac{\left| \|\hat{\mathbf{F}}\| - \|\mathbf{F}_{\text{ref}}\| \right|}{\|\mathbf{F}_{\text{ref}}\|} \cdot 100\%, \quad (4.41)$$

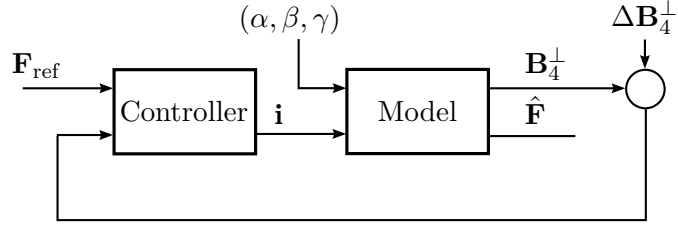


Figure 4.6. Schematic diagram for numerical simulation of the influence of the measurement noise on the force relative error.

and the angle error defined as

$$\text{Angle error } (^{\circ}) = \cos^{-1} \left(\frac{\hat{\mathbf{F}}^{\top} \mathbf{F}_{\text{ref}}}{\|\hat{\mathbf{F}}\| \|\mathbf{F}_{\text{ref}}\|} \right) \cdot \frac{180}{\pi}. \quad (4.42)$$

The norm relative and angle errors corresponding to the torque are defined similarly.

The mean and variance of the $10 \cdot 10^3$ force relative errors for best and worst sensor configurations as a function of the number of sensors is reported in Fig. 4.7. As it can be noticed, the relation between mean force relative error and the number of sensors is similar to the one between condition number and the number of sensors previously depicted in Fig. 4.3, which confirms the usefulness of using the condition number as a possible optimization criterion.

Influence of Rotor High Order Harmonics

Similarly to the above example with the measurement noise, in this section we look at the relation among higher order harmonics of the rotor magnetic flux density, number of sensors, and their arrangement. The hybrid FEM-analytical magnetic flux density model is computed as proposed in Chapter 2 using again the new developed spherical rotor that will be presented in Chapter 6. Best and worst configurations of the set $\mathbb{S}_D \cup \mathbb{S}_I$ are taken into account. The analysis is performed for a number of sensors varying from a minimum of 7 to a maximum of 15. Sensors are located at $R_{\text{sens}} = 97$ mm.

The schematics for this example is similar to the one reported in Fig. 4.6. For the control model, the maximum harmonic degree remains equal to $N_h = 3$. However, in the reference model, to study the influence of higher order harmonics, the magnetic flux density is computed using (4.3) with $N_h = 11$. The procedure to compute the current vector is also similar but we do not consider the sensor noise. The evaluation is repeated for $2 \cdot 10^3$ randomly-generated rotor orientations and a current vector is computed to satisfy 20 randomly-generated reference forces resulting in a total of $40 \cdot 10^3$ configurations.

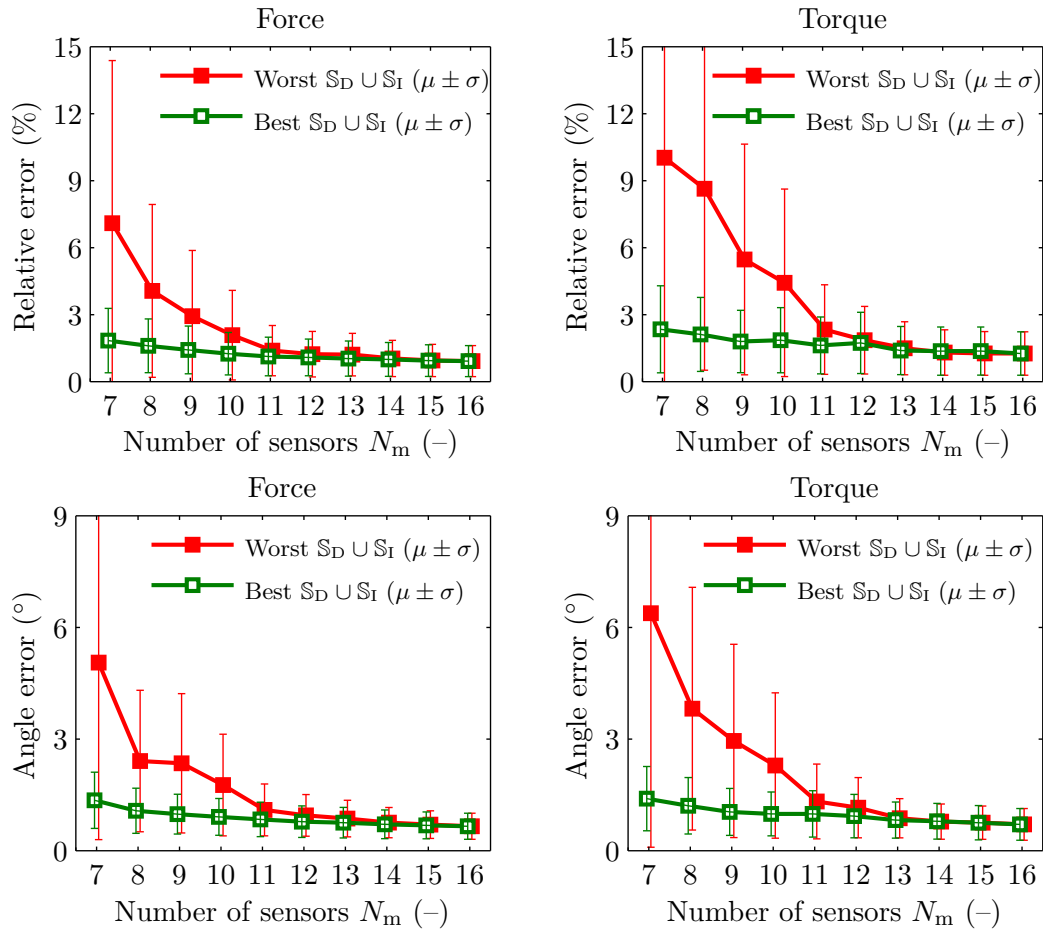


Figure 4.7. Mean force relative error of best and worst sensor configurations for the set $\mathbb{S}_D \cup \mathbb{S}_I$ as a function of the number of sensors. Magnetic flux density measurements \mathbf{B}_4 are perturbed with with zero-mean additive measurement noise $\Delta\mathbf{B}_4^\perp$ having standard deviation equal to 8 mT.

The mean and variance of the $40 \cdot 10^3$ force relative errors for best and worst sensor configurations as a function of the number of sensors is reported in Fig. 4.8. Once again, the number of sensors as well as their arrangement have an important influence in both norm relative errors and angle errors. Therefore, a careful arrangement of the sensors, employing for instance the proposed procedure, is an important aspect to minimize the negative influence of high order harmonics or sensor measurement noise.

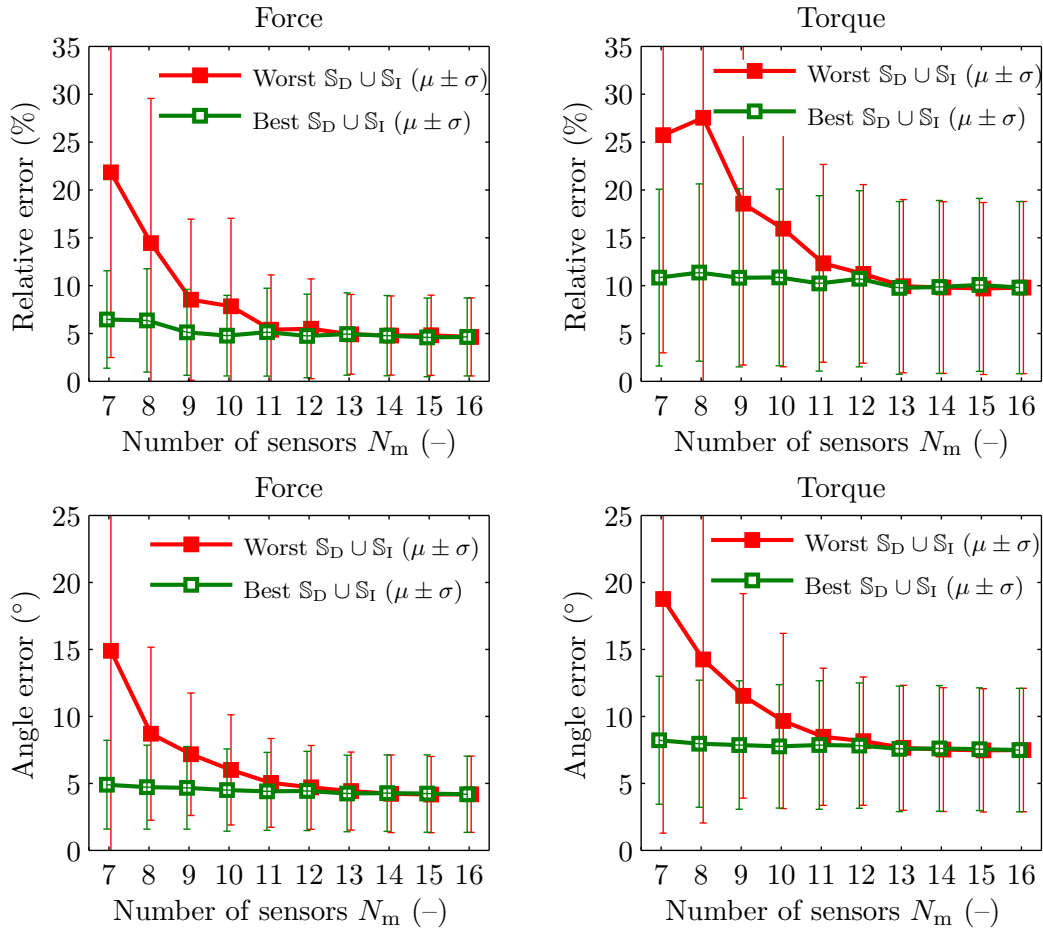


Figure 4.8. Mean force relative error of best and worst sensor configurations for the set $\mathbb{S}_D \cup \mathbb{S}_I$ as a function of the number of sensors in presence of high-order harmonics of the rotor magnetic flux density ($N_h = 11$ harmonics are used in the reference model).

4.4 Summary

In this chapter we proposed a technique to estimate the magnetic state of the reaction sphere, which was defined as the process of determining the spherical harmonic decomposition coefficients that deliver to force and torque models all the information relative to the rotor orientation. The proposed estimation strategy is based on measuring the radial component of the magnetic flux density at multiple locations equidistant from the rotor

Chapter 4. Magnetic State Estimation and Optimal Sensor Placement

surface to subsequently solve a linear inverse problem using least squares. Conversely from the estimation of the rotor orientation, the estimation of the magnetic state is linear, it is expressed in closed-form, and it implicitly takes into consideration non-uniqueness of solutions due to the cubic symmetry of the rotor magnetic flux density. The magnetic state corresponding to the ideal ocutpole model can be reconstructed with a minimum of seven measurements. Subsequently, we summarized the implementation procedure for the online computation of force and torque models, highlighting the attractive computational structure, in which several ingredients are computed offline.

Next, we presented an optimization strategy to position magnetic flux density sensors necessary to determine the magnetic state. The proposed optimization procedure consists in minimizing the condition number related to the linear estimation problem of the coefficients so as to minimize the influence of the measurement noise and high-order harmonics on force and torque relative errors. We have shown that this placement procedure can be used during the design phase to find optimal sensor locations as well as to select a subset of sensors among various pre-determined locations, the latter resulting in a combinatorial optimization problem.

5 Back-EMF and Rotor Angular Velocity Estimation

In this chapter we present a method to estimate the back-EMF voltage and the rotor angular velocity, both necessary for closed-loop operation of the reaction sphere actuator as well as requested by the ADCS for angular momentum management. The estimation of the back-EMF voltages is based on using Faraday's law of electromagnetic induction, in which the time-varying magnetic flux density of the rotor is parametrized with spherical harmonic decomposition coefficients estimated as described in the previous chapter. The technique does not require any additional measurements of the coil voltages or actuations. Then, the rotor angular velocity will be determined from the estimated back-EMF voltages using the energy conservation principle. Both procedures to determine the rotor angular velocity and the back-EMF voltages are linear and are expressed in closed-form. To conclude, the estimation procedures are validated using FEM simulations.

5.1 Introduction

In this chapter we present a technique to estimate the back-EMF voltage induced in the coils and the rotor angular velocity. These two quantities are necessary for a variety of reasons. To begin with, the magnetic flux density of a spinning rotor induces a back-EMF voltage in the coils that acts as a disturbance in the loop responsible to control the current flowing in the coils. Therefore, knowledge of the back-EMF voltage is important for feedforward compensation in the current control loop to achieve a better performance [8, 58]. Moreover, as it will be shown in this section, the back-EMF voltage allows estimating the rotor angular velocity using the energy conservation principle. The rotor angular velocity is necessary for at least two important reasons. First, a momentum exchange device (in this case the reaction sphere) can be commanded in the so called speed mode, where the ADCS provides the device with a pair of speed and acceleration references. In this mode, the angular velocity of the rotor must be measured and fed to the controller for accurate angular velocity control [8]. Second, knowledge of the angular

velocity is necessary to determine the reaction sphere total angular momentum, which is an information requested by the ADCS for momentum management [8].

To the best of our knowledge, measurement of the rotor angular velocity in the 3-DOF spherical actuator literature is only rarely addressed because, due to the proposed applications, these actuators are mostly driven in open-loop [46, 47, 49] or using closed-loop position control [43, 44, 57, 58, 74, 77]. Nevertheless, closed-loop control of the angular velocity can be found in some references. Kumagai and Hollis equipped their 3-DOF induction spherical motor with four optical mouse sensors that measure the surface velocity to estimate the rotor's angular velocity, which is used for vector control of the inductors and control of angular velocity [38]. Wang et al. employed a robust PD position control law, in which references are Euler angle trajectories and their derivatives. Euler angles are measured with a combination of magnetic flux density and optical measurements [58]. Chen et al. proposed a trajectory tracking algorithm and the desired torque is obtained from the inverse dynamics, where orientation and angular velocity is used as feedback [77]. The orientation of the rotor is measured by a rotary encoder and two-axis tilt sensor incorporated with the joint. Finally, Lee and Velinsky presented a method that uses magnetic sensors to determine the angular velocity of a spherical body for the trajectory of one of its points [143]. The approach involves tracking the time-varying magnetic field of a permanent disc magnet embedded at the center of the spherical rotor to determine the absolute orientation of the magnet axis and subsequently the instantaneous axis of rotation and the angular speed of the sphere about this axis.

The above mentioned techniques for angular velocity estimation require knowing the orientation of the rotor inside the stator. As discussed in Chapter 4, measuring the rotor orientation results in a nonlinear and iterative process with possible non-uniqueness and convergence problems. In that case, the magnetic state of the rotor was adopted to convey to force and torque models all the information relative to the rotor orientation inside the stator. Recall that the magnetic state estimation procedure is linear and it is expressed in closed-form. For this reason, in this chapter we propose to estimate the rotor angular velocity using the energy conservation principle and the estimated back-EMF voltages. The developed technique to measure the back-EMF voltages is based on using Faraday's law of electromagnetic induction, in which the time-varying magnetic flux density of the rotor is parametrized with spherical harmonic decomposition coefficients estimated as described in the previous chapter. The advantage of this approach is that the magnetic state is already available because necessary to update force and torque models, and does not require any additional measurements of the coil voltages or actuations. Finally, the proposed procedure is linear and it is expressed in closed-form.

An alternative and powerful approach for estimation of the rotor angular velocity is based on the so called Extended Kalman Filter (EKF), which is a recursive state estimator for nonlinear processes and does not require differentiation of the measurements [140]. The EKF is widely employed in a variety of different applications including, for instance,

spacecraft attitude determination [144,145], sensorless control of synchronous motors [146], and human motion tracking and orientation determination [147,148]. A perspective to employ the EKF to estimate the angular velocity of the reaction sphere will be provided in the conclusive chapter.

In this chapter, in Section 5.2, we present the electromechanical model of the reaction sphere, which consists of a dynamic and kinematic model and an electrical model. Then, techniques to estimate the rotor angular velocity and the back-EMF voltage are proposed in Section 5.3 and 5.4, respectively. Finally, these techniques will be validated using FEM simulations in Section 5.5.

5.2 Electromechanical Model

5.2.1 Dynamic and Kinematic Rotational Model

In this section we derive a dynamic and kinematic model of the rotational motion of the reaction sphere rotor. In Chapter 2 we have defined rotor and stator reference frames. Recall that \mathcal{B} denotes the rotor inertially fixed reference frame with a corresponding triad of mutually orthogonal base vectors $\{\hat{\mathbf{x}}_b, \hat{\mathbf{y}}_b, \hat{\mathbf{z}}_b\}$ with origin at O_B . Moreover, \mathcal{S} denotes the stator fixed reference frame with base vectors $\{\hat{\mathbf{x}}_s, \hat{\mathbf{y}}_s, \hat{\mathbf{z}}_s\}$ with origin at O_S . Throughout we will assume that the rotor is a rigid body with its center of mass coinciding with the origin O_B . Moreover, similarly to the derivation of force and torque models, we will assume that the origin of the rotor O_B coincides to the one of the stator O_S .

The derivation of the RS dynamic model is developed in stator coordinates, which defines our inertial reference frame. The rotational dynamics of a body are governed by the rate of change of its angular momentum as [149]

$$\frac{d}{dt}\mathbf{h} = \mathbf{T}, \quad (5.1)$$

where \mathbf{h} is the angular momentum of the body with respect to the inertial frame and \mathbf{T} is the torque applied to the body. The angular momentum can be expressed as $\mathbf{h} = J_{\text{rot}}\boldsymbol{\omega}$, where J_{rot} is the inertia tensor of the rotor and $\boldsymbol{\omega}$ is the angular velocity of the rotor expressed in stator coordinates. By design, the inertia tensor J_{rot} is diagonal with all its elements J having the same value. Thus the dynamic model of the rotating rotor becomes

$$J \frac{d}{dt}\boldsymbol{\omega} = \mathbf{T}. \quad (5.2)$$

To derive the kinematic model, let $R_{\mathcal{S} \rightarrow \mathcal{B}}$ be a rotation matrix relating stator and rotor reference frames as $\{\hat{\mathbf{x}}_b, \hat{\mathbf{y}}_b, \hat{\mathbf{z}}_b\} = R_{\mathcal{S} \rightarrow \mathcal{B}}\{\hat{\mathbf{x}}_s, \hat{\mathbf{y}}_s, \hat{\mathbf{z}}_s\}$. Then, the kinematic equation can

be formulated as [150]

$$\frac{d}{dt}R_{\mathcal{S}\rightarrow\mathcal{B}} = \boldsymbol{\omega} \times R_{\mathcal{S}\rightarrow\mathcal{B}}. \quad (5.3)$$

An alternative kinematic model can also be derived using quaternions. Finally, the mechanical power associated to the rotational motion of a body is defined as [151]

$$P_{\text{rot}} = \boldsymbol{\omega}^\top \mathbf{T}. \quad (5.4)$$

5.2.2 Electrical Model

The electrical model of a stationary circuit is given by the general expression [106]

$$\mathbf{u} = R_c \mathbf{i} + L_c \frac{d}{dt} \mathbf{i} + \mathbf{u}_{\text{emf}}, \quad (5.5)$$

where $\mathbf{u} \in \mathbb{R}^{20 \times 1}$ is the coil voltage vector, R_c is the coil resistance, $L_c \in \mathbb{R}^{20 \times 20}$ is the coil inductance tensor, and $\mathbf{u}_{\text{emf}} \in \mathbb{R}^{20 \times 1}$ is the coil back-EMF voltage vector. The coil resistance can be determined as

$$R_c = \rho N_t^2 \frac{V_c}{A_b}, \quad (5.6)$$

where ρ is the specific resistance of the coil material, N_t is the number of turns, V_c is the volume of the coil, and A_b is the section of the coil, which are calculated as

$$V_c = \frac{2\pi}{3} (R_{\text{out}}^3 - R_{\text{in}}^3) (\cos \theta_{\text{in}} - \cos \theta_{\text{out}}) \quad (5.7)$$

$$A_b = \frac{1}{2} (R_{\text{out}}^2 - R_{\text{in}}^2) (\theta_{\text{out}} - \theta_{\text{in}}). \quad (5.8)$$

Proposition 4. *Due to energy conservation, the coil back-EMF voltages can be expressed as*

$$\mathbf{u}_{\text{emf}} = K_T^\top \boldsymbol{\omega}. \quad (5.9)$$

Illustration. The illustration is proposed in Appendix B.4. \square

Proposition 5.9 guarantees that the angular velocity of the rotor can be computed using measured or estimated values of the back-EMF voltages induced in the stator coils.

5.3 Rotor Angular Velocity Estimation

Employing Proposition 4, given the back-EMF voltage \mathbf{u}_{emf} , the rotor angular velocity can be computed as

$$\boldsymbol{\omega} = (K_T^\top)^+ \mathbf{u}_{\text{emf}} = \left(K_T^+\right)^\top \mathbf{u}_{\text{emf}} = M_T^\top \mathbf{u}_{\text{emf}}, \quad (5.10)$$

where $^+$ denotes the pseudoinverse operator. Notice that the matrix M_T does not need to be computed again to estimate $\boldsymbol{\omega}$ because it is available from the inverse torque model, which is necessary for real-time control. Therefore, in order to determine the angular velocity of the rotor, we need to know the back-EMF voltage in the coils, and this will be the topic of the next section.

5.4 Back-EMF Estimation

The procedure presented in this section consists in first deriving the back-EMF independently for each coil by considering the interaction between the rotor magnetic flux density and the stator coil. Subsequently, we invoke the superposition principle to express the back-EMF induced in the complete set of coils in matrix form.

5.4.1 Back-EMF in a Single Coil

Similarly to the development of force and torque models using the Lorentz force law, to calculate the back-EMF in a specific coil we consider the latter as a spherical portion delimited by angles θ_{in} and θ_{out} , and by the spherical radii R_{in} and R_{out} as illustrated in Fig. 5.1. The position \mathbf{P}_k of the coil k in the stator frame \mathcal{S} , with $k = 1, 2, \dots, 20$, is again described by a rotation matrix $R_{\mathcal{C} \rightarrow \mathcal{S}, k}(\zeta_k, \eta_k)$, which combines a rotation ζ_k about the $\hat{\mathbf{z}}_s$ -axis, followed by a rotation η_k about the $\hat{\mathbf{x}}_s$ -axis. The matrix $R_{\mathcal{C} \rightarrow \mathcal{S}, k}(\zeta_k, \eta_k)$ shall satisfy condition (3.3), which we report here for convenience

$$R_{\mathcal{C} \rightarrow \mathcal{S}, k}(\zeta_k, \eta_k) \mathbf{P}_k = \begin{bmatrix} 0 \\ 0 \\ 1 \end{bmatrix}. \quad (5.11)$$

This condition can be used to compute ζ_k and η_k given \mathbf{P}_k .

The voltage induced in a circuit can be calculated using Faraday's law of electromagnetic induction as $\frac{d}{dt} \Lambda$, where Λ is the flux linkage through the circuit of area S , which is calculated as $\Lambda = \int_S \mathbf{B} \cdot d\mathbf{S}$ [106]. However, the calculation of the back-EMF of air-cored coils presents the difficulty that not all the windings of the coil have the same flux linkage. Therefore, the proposed approach, which we have inspired from the back-EMF calculation of a rotary actuator for a two degree-of-freedom $z\phi$ -module [152], consists in first calculating the average back-EMF of a single turn in the coil and then in calculating the total back-EMF of the coil by multiplying the average back-EMF with the number of turns in the coil. To this end, as depicted in Fig. 5.1, consider a single circular turn with cross-sectional area dA positioned at radius r_c , with declination angle α_t and spanning ϕ from 0 to 2π . The flux linked by this turn, which is a spherical cap with surface S_t , can

be expressed as

$$\begin{aligned}\Psi_{dA,k}(r_c, \alpha_t) &= \int_{S_t} c \mathbf{B}_4 \cdot d\mathbf{S} \\ &= \int_{-\alpha_t}^{\alpha_t} \int_0^{2\pi} B_{4,r_c}(x_s, y_s, z_s) r_c^2 \sin \theta_c d\phi_c d\theta_c,\end{aligned}\quad (5.12)$$

where $B_{4,r_c}(x_s, y_s, z_s) = \frac{1}{r_c} \begin{bmatrix} x_s & y_s & z_s \end{bmatrix}^S \mathbf{B}_4(x_s, y_s, z_s)$ is the radial component of the magnetic flux density evaluated at the observation point (x_s, y_s, z_s) , with

$$\begin{bmatrix} x_s \\ y_s \\ z_s \end{bmatrix} = R_{\mathcal{C} \rightarrow \mathcal{S},k}^T \begin{bmatrix} r_c \sin \theta_c \cos \phi_c \\ r_c \sin \theta_c \sin \phi_c \\ r_c \cos \theta_c \end{bmatrix}.\quad (5.13)$$

Then, by assuming that the coil contains a large number of turns, the total flux linkage (rotor only) can be calculated as

$$\begin{aligned}\Psi_k &= \int_{A_b} \Psi_{dA,k}(r_c, \alpha_t) dA \\ &= \int_{R_{in}}^{R_{out}} \int_{\theta_{in}}^{\theta_{out}} \Psi_{dA,k}(r_c, \alpha_t) r_c d\alpha_t dr_c.\end{aligned}\quad (5.14)$$

Hence, the average flux linkage per turn can be expressed as

$$\Psi_{av,k} = \frac{\Psi_k}{A_b},\quad (5.15)$$

where A_b is the cross-sectional area of the coil (see Fig. 5.1) and is calculated according to (5.8). Finally, the average back-EMF voltage for the entire coil with N_t turns is given by

$$u_{emf,k} = -N_t \frac{d}{dt} \Psi_{av,k}.\quad (5.16)$$

The magnetic flux density within the airgap in (2.72) is parameterized using spherical harmonic coefficients c_n^m that convey to the model all the information relative to the orientation of the rotor inside the stator. These coefficients are the only time-dependent components in (2.72). Therefore, by taking into account the fundamental component of degree $n = 3$ only (see discussion in Section 4.2) and invoking linearity, expression (5.16) can be reformulated as

$$u_{emf,k} = \sum_{m=-3}^3 \Psi_{av,k}^m \left(\frac{d}{dt} c_3^m \right),\quad (5.17)$$

where $\Psi_{av,k}^m$ is the rotor flux linked by the spherical harmonic of degree 3 and order m expressed as

$$\Psi_{av,k}^m = -\frac{N_t}{A_b} \int_{R_{in}}^{R_{out}} \int_{\theta_{in}}^{\theta_{out}} \int_{-\alpha_t}^{\alpha_t} \int_0^{2\pi} B_{4,r_c}^m r_c^3 \sin \theta_c d\phi_c d\theta_c d\alpha_t dr_c,\quad (5.18)$$

with $B_{4,r_c}^m = \frac{1}{r_c} \begin{bmatrix} x_s & y_s & z_s \end{bmatrix}^S \mathbf{B}_4^m(x_s, y_s, z_s)$. Therefore, similarly to force and torque models in (3.24), the back-EMF voltage induced in coil k is expressed as a linear combination of the flux linkage given by each spherical harmonic of degree 3 and order m taken into account and the time derivative of the relative spherical harmonic coefficients c_3^m . We emphasize that $\Psi_{av,k}^m$ in equation (5.17) are constant and can be computed offline.

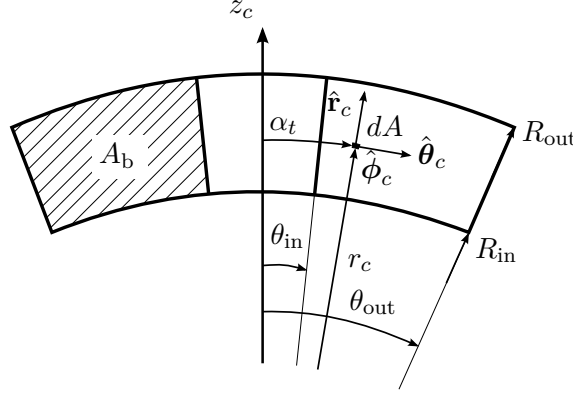


Figure 5.1. Schematic view of the coil for calculation of back-EMF.

5.4.2 Complete Back-EMF Model

The back-EMF voltage induced in the 20 coils is defined as

$$\mathbf{u}_{emf} = \begin{bmatrix} u_{emf,1} & u_{emf,2} & \dots & u_{emf,20} \end{bmatrix}^T. \quad (5.19)$$

Using expression (5.17) relative to the back-EMF induced in a single coil, by invoking linearity, the back-EMF voltage vector is expressed as

$$\mathbf{u}_{emf} = \sum_{m=-3}^3 \begin{bmatrix} \Psi_{av,1}^m & \Psi_{av,2}^m & \dots & \Psi_{av,20}^m \end{bmatrix}^T \frac{d}{dt} c_3^m, \quad (5.20)$$

or in matrix form as

$$\mathbf{u}_{emf} = \Phi \frac{d}{dt} \mathbf{c}_3, \quad (5.21)$$

where $\Phi \in \mathbb{R}^{20 \times 7}$ is given by

$$\Phi = \begin{bmatrix} \Psi_{av,1}^{-3} & \Psi_{av,1}^{-2} & \dots & \Psi_{av,1}^3 \\ \Psi_{av,2}^{-3} & \Psi_{av,2}^{-2} & \dots & \Psi_{av,2}^3 \\ \vdots & \vdots & \ddots & \vdots \\ \Psi_{av,20}^{-3} & \Psi_{av,20}^{-2} & \dots & \Psi_{av,20}^3 \end{bmatrix} \quad (5.22)$$

and $\mathbf{c}_3 = [c_3^{-3} \ c_3^{-2} \ \dots \ c_3^3]^\top$. Note that the matrix Φ is constant and is computed offline.

5.5 Verification with FEM Simulations

5.5.1 Simulation Setup and Verification Procedure

For FEM validation, we employ the model of the reaction sphere with ideal octupole cubic magnetization originally proposed in Chapter 2 and verified with FEM simulations in Section 2.3.9. The advantage of using this model is that FEM dynamic simulations are greatly simplified due to the fact that we can analytically rotate the magnetization of the rotor but leave the geometry of the model unchanged throughout all the simulations.

To simulate rotation at a given angular velocity $\omega(t)$ about a constant rotation axis $\boldsymbol{\rho}_{\text{rot}}$, we consider a rotation operator $R(\boldsymbol{\rho}_{\text{rot}}, \varphi(t))$, where $\varphi(t)$ is the angle of rotation about the axis $\boldsymbol{\rho}_{\text{rot}}$ and is computed as $\varphi(t) = \int_0^t \omega(t) dt$. From this matrix, at each time t we retrieve the ZYZ Euler angles α , β , and γ and use them to compute the rotated coefficients c_3^m using (2.40). Then, with coefficients c_3^m , we compute the back-emf voltage using equation (5.20) and the torque characteristic matrix with expression (3.24). Finally, the angular velocity is estimated according to (5.10). Geometrical dimensions and parameters for the simulation model are given in Section 2.3.9.

5.5.2 Results

In Fig. 5.2, the simulated back-EMF voltage in the first eight coils is compared to that computed using the developed technique. For this simulation, we have considered the rotation axis $\boldsymbol{\rho}_{\text{rot}} = [\sqrt{3}/4 \ 1/4 \ \sqrt{3}/2]^\top$ and the angular velocity profile $\omega(t) = \omega_0 + \Delta\omega(1 - \exp(-t/\tau))$, with $\omega_0 = 1000$ rpm, $\Delta\omega = 500$ rpm, and $\tau = 0.0385$ s. To compute values using the developed technique we assumed a sampling frequency of 20 kHz. Finally, the three angular velocity components are compared to the estimated values in Fig. 5.3. As can be observed, the estimated values are in good agreement with the simulated velocity profiles.

5.6 Summary

In this chapter we concentrated on methods to estimate the back-EMF voltage induced in the coils and the rotor angular velocity.

To estimate the back-EMF voltage we applied the Faraday's law of electromagnetic induction, where the time-varying component of magnetic flux density is conveyed to the model through the magnetic state, which can be determined as discussed in the previous

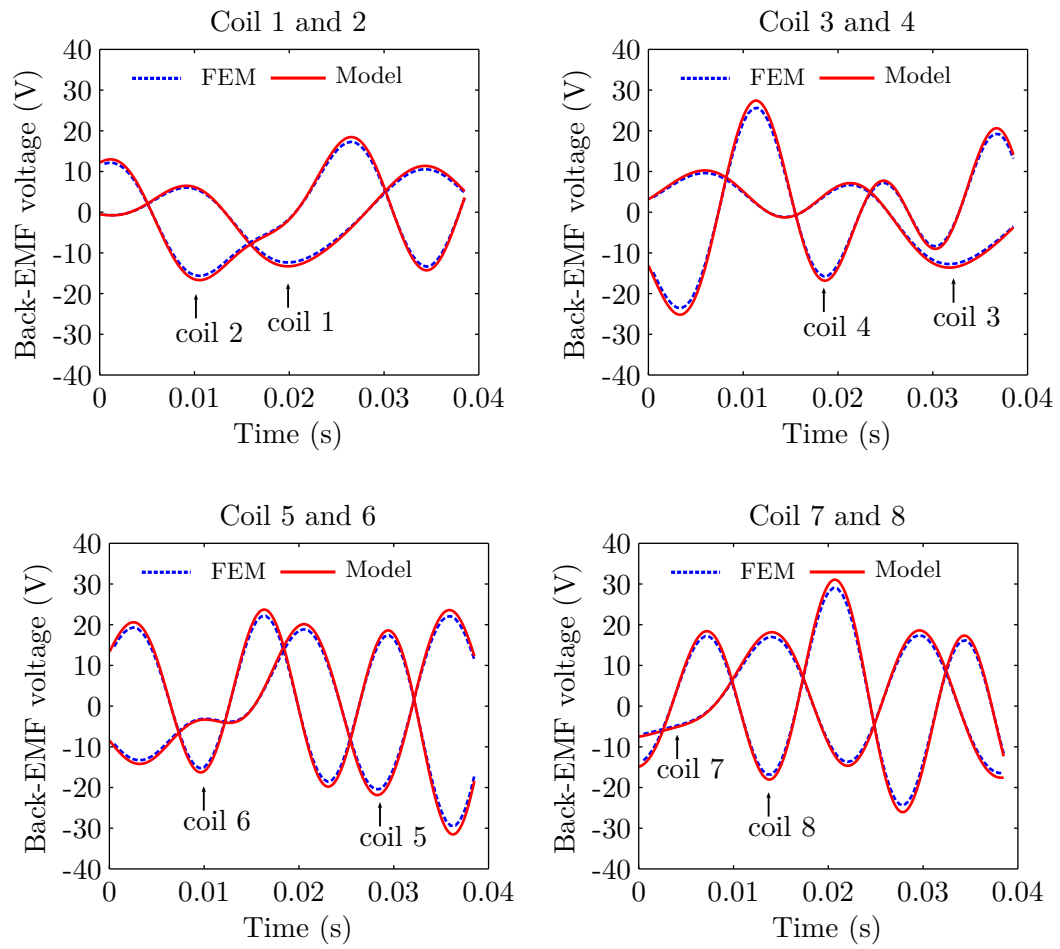


Figure 5.2. Simulated back-EMF voltage with ideal octupole rotor compared to developed analytical model.

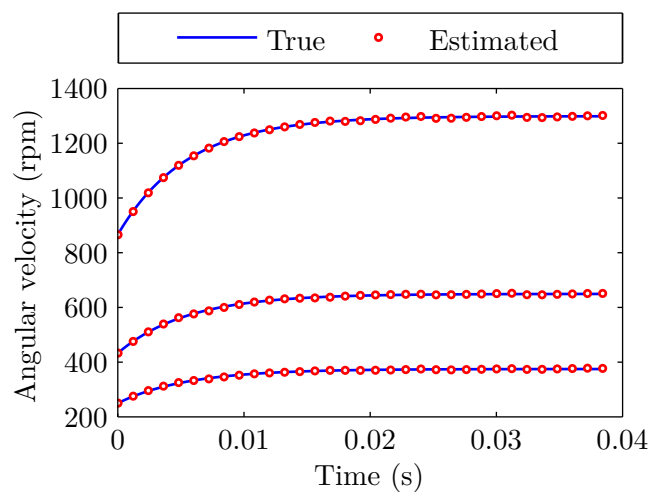


Figure 5.3. True and estimated rotor angular velocity.

Chapter 5. Back-EMF and Rotor Angular Velocity Estimation

chapter. This technique allows estimating the back-EMF voltage without additional measurements of the coil voltage or actuations, which are presently not available in the existing prototype (see Chapter 7). As mentioned above, the advantage is that the magnetic state is already available because necessary to update force and torque models. Nevertheless, the inconvenience is that the estimated magnetic state is affected by high-order harmonics of the rotor magnetic flux density and the derivative operation acting on it has a negative effect on the estimated angular velocity.

Subsequently, we have shown that the rotor angular velocity can be determined using the energy conservation principle by multiplying the estimated back-EMF voltage vector with the transpose of the torque characteristics matrix, which is a multidimensional equivalence to classical motor theory.

Both procedures to determine the back-EMF voltages and the rotor angular velocity are linear and are expressed in closed-form.

6 Design Optimization of a Spherical Rotor

In this chapter we present the design optimization of a new concept of spherical rotor, which consists of eight bulk PM poles with truncated spherical shape that are parallel-magnetized and adjusted on the back-iron structure, which has truncated octahedral shape. We will start by outlining the rotor specifications and by defining the design optimization problem. Due to the highly complex geometry of the spherical rotor, a pure analytical approach for the optimization problem is not practicable. Therefore, given a set of specifications, the optimization of design parameters is performed using FEM simulations to minimize the rotor magnetic flux density distortion with respect to the fundamental harmonic. The resulting optimized rotor is fully compliant with design specifications.

6.1 Introduction

As mentioned in Section 1.4.2, in the first developed laboratory prototype, the eight PM poles of the spherical rotor were discretized using a mosaic of 728 cylindrical magnets to approximate the desired fundamental spherical harmonic. Then, more recently, a new spherical rotor optimized to improve its manufacturability was designed and manufactured. As illustrated in Fig. 6.1, the rotor has eight bulk PM poles with truncated spherical shape that are parallel-magnetized and adjusted on the back-iron structure, which has truncated octahedral shape. Design parameters are the radius R_{PM} of the PM poles, the height h of the truncated octahedron structure, the rotor pole eccentricity δ , which is the distance between the rotor center O_{B} and the pole center O_{PM} , as well as the back-iron thickness H_{R} . Finally, R_{rot} is the outer radius of the spherical rotor. This new concept of spherical rotor based on bulk PM poles was preferred to the firstly proposed discrete approach for a variety of reasons including an improved mechanical stability, manufacturing repeatability, and a reduced assembly time. On the other hand, the proposed monoblock concept has a more distorted magnetic flux density profile, which

originates from the use of eight permanent magnets that can only be parallel-magnetized. Moreover, with respect to the discrete cylindrical magnets, in the monoblock concepts PMs have a truncated spherical shape, which increases the part and tooling costs.

In this chapter we present a procedure to find optimal design parameters for a given set of specifications concerning the new monoblock reaction sphere rotor. Because a pure analytical approach was not practicable due to the highly complex geometry of the rotor, the optimization was performed using FEM simulations. In Section 6.2 we define the rotor specifications and formulate the design optimization problem. Then, in Section 6.3 we present the design optimization performed using FEM simulations. As it will be seen, because of the highly complex problem to solve and of manufacturability aspects and constraints, the design optimization is separated into different subproblems, which eventually result in a set of design parameters making the rotor compliant with the specifications.

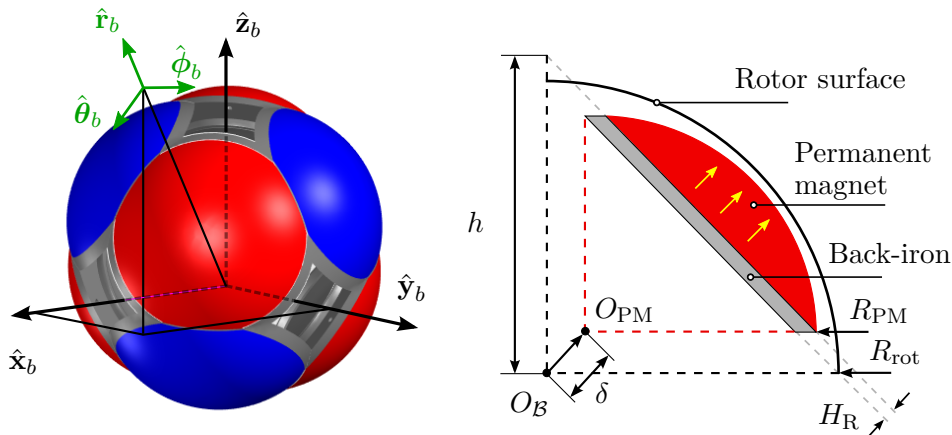


Figure 6.1. Schematic illustration of the optimized spherical rotor of the RS.

6.2 Rotor Specifications and Design Optimization Problem Definition

6.2.1 Rotor Magnetic Flux Density over Mass Ratio

The $B_{r_b}^{\text{RMS}}/m_{\text{rot}}$ is the ratio between the radial component of the magnetic flux density and the rotor mass. A minimum value of $B_{r_b}^{\text{RMS}}/m_{\text{rot}}$ will be specified so that the interaction of the rotor magnetic flux density with the stator coil currents produces sufficient force to levitate the rotor in presence of gravity. The value of $B_{r_b}^{\text{RMS}}$ is computed using the

6.2. Rotor Specifications and Design Optimization Problem Definition

Root Mean Square (RMS) value of the radial component of the magnetic flux density evaluated along a horizontal parametric circular path defined in spherical coordinates as $r_{b,p}\hat{\mathbf{r}}_b + \theta_{b,p}\hat{\boldsymbol{\theta}}_b + \phi_b\hat{\boldsymbol{\phi}}_b$, where $r_{b,p} = 95.5$ mm is the radial center of the coils, which span a distance from $R_{\text{in}} = 92$ mm to $R_{\text{out}} = 99$ mm, and $\theta_{b,p} = \tan^{-1} \sqrt{2}$ is the polar angle of a pole. Therefore, yielding

$$B_{r_b}^{\text{RMS}} = \sqrt{2} \sqrt{\frac{1}{2\pi} \int_0^{2\pi} B_{r_b}(r_{b,p}, \theta_{b,p}, \phi_b)^2 d\phi_b}. \quad (6.1)$$

6.2.2 Model Agreement Criterion

As discussed in Chapter 4, the real-time estimation strategy of the rotor magnetic flux density can reconstruct only the rotated fundamental spherical harmonic of degree $n = 3$ and $m = 2$. Consequently, spherical harmonics with higher degree introduce force and torque errors. Therefore, in order to minimize these errors, the model agreement criterion d is introduced as a quantitative evaluation of the global distortion of the magnetic flux density with respect to the spherical harmonic of degree 3 and order 2. To compute d , the radial component of the simulated magnetic flux density $B_{r_b}(r_{b,p}, \theta_b, \phi_b)$, evaluated at $r_{b,p} = 95.5$ mm, is decomposed on the basis of spherical harmonics up to the maximum degree $N_h = 20$ as

$$B_{r_b}(r_{b,p}, \theta_b, \phi_b) = \sum_{n=3}^{N_h} \sum_{m=-n}^n c_{n,\text{imm}}^m Y_n^m(\theta_b, \phi_b), \quad (6.2)$$

where $Y_n^m(\theta_b, \phi_b)$ is a complex-valued spherical harmonic of degree n and order m , while $c_{n,\text{imm}}^m$ the decomposition coefficients computed as (see also Chapter 4)

$$c_{n,\text{imm}}^m = \int_0^{2\pi} \int_0^\pi B_{r_b}(r_{b,p}, \theta_b, \phi_b) \overline{Y_n^m(\theta_b, \phi_b)} \sin \theta_b d\theta_b d\phi_b. \quad (6.3)$$

Therefore, the model agreement criterion d is defined as the ratio between the desired harmonic coefficient $c_{3,\text{imm}}^2$ and the sum of the other harmonic coefficients up to $N_h = 20$ as

$$d = \frac{|c_{3,\text{imm}}^2|}{\sqrt{\sum_{n=3}^{N_h} \sum_{m=0}^n |c_{n,\text{imm}}^m|^2}}. \quad (6.4)$$

Note that, thanks to the properties of spherical harmonic functions under rotation studied in Chapter 2, maximizing the model agreement d for the immobile rotor will automatically minimize the magnetic flux density distortions for any possible orientation of the rotor. Finally, since $c_{n,\text{imm}}^{-m} = (-1)^m \overline{c_{n,\text{imm}}^m}$, where $\overline{c_{n,\text{imm}}^m}$ denotes the complex conjugate of $c_{n,\text{imm}}^m$, only the one-sided spectrum ($m \geq 0$) is considered in (6.4).

6.2.3 Rotor Specifications and Problem Definition

The reaction sphere rotor specifications are summarized in Table 6.1. These specifications are defined taking into account the previously developed stator and power electronics presented in Chapter 1. The rotor optimization consists in finding suitable design parameter values h , δ , R_{PM} , and H_{R} , so as to maximize the model agreement $d \in [0, 1]$ while taking into account the constraints imposed by the specifications.

Table 6.1. Specifications of the monoblock spherical rotor.

Maximum rotor mass m_{rot}	10 kg
Maximum rotor outer radius R_{rot}	90 mm
Minimum magnetic flux density over mass ratio $B_{r_b}^{\text{RMS}}/m_{\text{rot}}$	0.04 T/kg
Minimum angular momentum	7.1 Nms
Model agreement $d \in [0, 1]$	to be maximized

6.3 Design Optimization with FEM Simulations

6.3.1 Influence of Rotor Pole Eccentricity and Permanent Magnet Mass on the Radial Component of the Flux Density

The objective of these simulations is to study the influence of the rotor pole eccentricity δ and the PM mass m_{PM} on the flux density $B_{r_b}^{\text{RMS}}$. Neodymium iron boron (NdFeB) PMs are modeled by applying their linear constitutive relation $B = \mu_{\text{PM}}\mu_0 H + B_{\text{rem}}$, where B and H are the magnetic flux density and the magnetic field, respectively. The relative magnetic permeability μ_{PM} is fixed to 1 while the remanent magnetic flux density B_{rem} is equal to 1.4 T. Finally, μ_0 is the vacuum permeability. The back-iron is modeled using the linear B-H relation $B = \mu_{\text{R}}\mu_0 H$, with the relative magnetic permeability μ_{R} equal to 10000. No saturation is taken into account at this stage of the design (saturation will be considered from Section 6.3.3 to optimize the back-iron geometry).

Simulations are repeated for several values of design variables h and δ ranging from 90 mm to 122 mm and from 0 mm to 30 mm, respectively. The radius R_{PM} of the magnets is adjusted consequently to satisfy the constraint $R_{\text{PM}} + \delta = 88.5$ mm, which is introduced to reduce the number of degree of freedoms for the design parameters.

The radial component of the magnetic flux density computed using (6.1) as a function of the PM mass m_{PM} for various values of the rotor pole eccentricity δ is reported in Fig. 6.2. As it can be observed, the value of $B_{r_b}^{\text{RMS}}$ increases with the PM mass m_{PM} . However, $B_{r_b}^{\text{RMS}}$ is not significantly influenced by the rotor pole eccentricity δ for a fixed permanent mass within the region where $m_{\text{PM}} \leq 6$ kg. Therefore, within this region, the magnetic

flux density distortion can be minimized by varying δ without significantly affecting $B_{r_b}^{\text{RMS}}/m_{\text{PM}}$. Finally, notice that a m_{PM} equal to 6 kg was identified as the maximum permanent magnet mass to obtain a rotor with total mass $m \leq 10$ kg. This maximum permanent magnet mass was estimated using the simplified computer-aided design (CAD) geometry and by taking into consideration a back-iron thickness proportionally scaled with respect to the one employed in our current prototype (back-iron thickness equal to 5 mm for $B_{r_b}^{\text{RMS}} = 0.18$ T [122]).

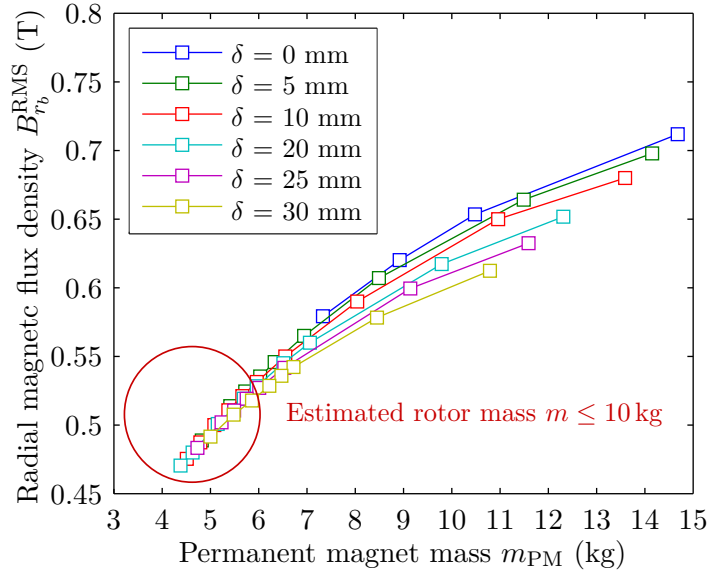


Figure 6.2. Radial component of the magnetic flux density $B_{r_b}^{\text{RMS}}$ as a function of PM mass m_{PM} and rotor pole eccentricity δ .

6.3.2 Influence of Rotor Pole Eccentricity on Model Agreement Criterion and Rotor Magnetic Flux Density over PM Mass Ratio

The objective of this section is to study the influence of the rotor pole eccentricity parameter δ on the $B_{r_b}^{\text{RMS}}/m_{\text{PM}}$ ratio (at this stage only the PM mass m_{PM} is considered) and on the model agreement d . Three different sets (A, B, and C) of configurations with the same PM mass m_{PM} and with the rotor magnetic outer radii ($R_{\text{PM}} + \delta$) summarized in Table 6.2 are analyzed. Sets of different $R_{\text{PM}} + \delta$ are defined with the purpose of studying the influence of the rotor magnetic outer radius on the $B_{r_b}^{\text{RMS}}/m_{\text{PM}}$ ratio and the model agreement d .

For set A, simulations are performed for a rotor pole eccentricity δ ranging from 0 mm to 35 mm with steps of 5 mm. The octahedron base-structure height h is adjusted to maintain $m_{\text{PM}} = 6$ kg, which is the maximum permanent magnet mass to obtain a rotor with total estimated mass compliant with specifications (less than 10 kg). Notice that, for set A, we have selected this maximum permanent mass to obtain the highest rotor

Chapter 6. Design Optimization of a Spherical Rotor

Table 6.2. Definition of sets A, B, and C for design optimization of monoblock rotor.

	set A	set B	set C
$R_{\text{PM}} + \delta$ (mm)	88.5	86.0	83.5
m_{PM} (kg)	6.0	5.5	5.0

inertia. As a matter of fact, the higher the rotor inertia the lower is the maximum angular velocity to obtain the minimum required angular momentum (see Table 6.1). A lower maximum angular velocity has several beneficial effects for the design including reduced back-EMF voltages, lower controller bandwidths, and weaker centrifugal forces (that are critical for the retention of PMs on the back-iron). Finally, note that with $m_{\text{PM}} = 6$ kg, the estimated total rotor mass is approximately 10 kg, but $B_{r_b}^{\text{RMS}}/m_{\text{rot}}$ is larger than the required value of 0.04 T/kg (see Fig. 6.2).

For set B and set C, the rotor pole eccentricity δ and the octahedron structure height h of the different configurations of set A are proportionally scaled (shrunk) as follows:

$$\begin{cases} \frac{\delta_{\text{set B,C}}}{\delta_{\text{set A}}} = \frac{(R_{\text{PM}} + \delta)_{\text{set B,C}}}{(R_{\text{PM}} + \delta)_{\text{set A}}} \\ \frac{h_{\text{set B,C}}}{h_{\text{set A}}} = \frac{(R_{\text{PM}} + \delta)_{\text{set B,C}}}{(R_{\text{PM}} + \delta)_{\text{set A}}} \end{cases} \quad (6.5)$$

Finally, simulations are performed using linear constitutive material relations as described in Section 6.3.1.

A summary of the model agreement d and the $B_{r_b}^{\text{RMS}}/m_{\text{PM}}$ ratio as a function of the rotor pole eccentricity δ for all the three sets is reported in Fig. 6.3 and Fig. 6.4, respectively. For set A, the model agreement d reaches its maximum at approximately $\delta = 25$ mm (corresponding to a height $h = 112$ mm). The maximum value of d can be increased by decreasing the outer rotor radius (set B and C) and is obtained for slightly lower eccentricities δ . Thus, the smaller the rotor the better is the model agreement. The $B_{r_b}^{\text{RMS}}/m_{\text{PM}}$ behavior in Fig. 5 shows that varying the eccentricity parameter δ does not influence $B_{r_b}^{\text{RMS}}/m_{\text{PM}}$ significantly and that the smaller the rotor is the worse is the $B_{r_b}^{\text{RMS}}/m_{\text{PM}}$. Hence, $B_{r_b}^{\text{RMS}}/m_{\text{PM}}$ and d show opposing trends in the sense that, for instance, the highest model agreement d achieved within set C has the poorest scores in terms of $B_{r_b}^{\text{RMS}}/m_{\text{PM}}$. Finally, the three configurations with the highest model agreement within each set are summarized in Table 6.3.

6.3.3 Back-iron Thickness Optimization with Nonlinear Simulations

The mass of the back-iron plays an important role on the total rotor mass. This mass shall be reduced to obtain a total mass of the rotor $m_{\text{rot}} < 10$ kg, but without affecting

6.3. Design Optimization with FEM Simulations

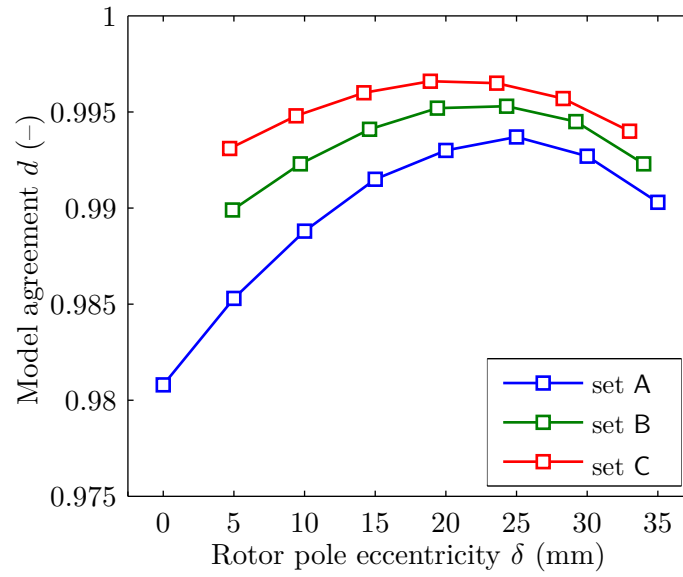


Figure 6.3. Summary of model agreement d as a function of rotor pole eccentricity δ for set A, set B, and set C.

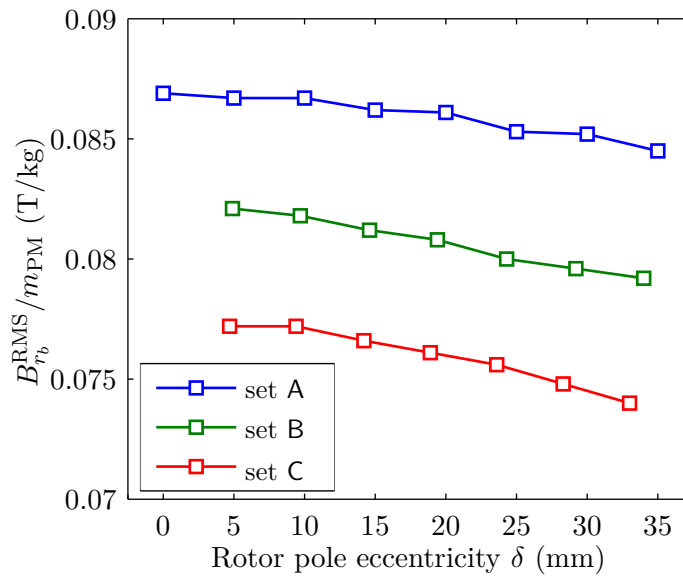


Figure 6.4. Summary of $B_{r_b}^{\text{RMS}}/m_{\text{PM}}$ as a function of rotor pole eccentricity δ for set A, set B, and set C.

Table 6.3. Optimal Conifugations for set A, B, and C.

	set A	set B	set C
$R_{\text{PM}} + \delta$ (mm)	88.5	86.0	83.5
Rotor pole eccentricity δ (mm)	25.0	24.3	18.9
Height h (mm)	112.0	108.8	107.4
$B_{r_b}^{\text{RMS}}/m_{\text{PM}}$	0.085	0.080	0.076
Model agreement d	0.9937	0.9953	0.9966

$B_{r_b}^{\text{RMS}}/m$ and the model agreement d negatively. In this section, the influence of the back-iron thickness H_{R} on $B_{r_b}^{\text{RMS}}/m_{\text{rot}}$ and the model agreement d is analyzed. The total mass of the rotor m_{rot} including also the back-iron is considered and calculated using the CAD model. Simulations are performed for the three preferred configurations within set A, B, and C reported in Table 6.3. The nonlinear magnetic properties of the back-iron material X46Cr13 are modeled by its nonlinear B-H curve and its relative permeability, taking into account saturation.

The model agreement d and the $B_{r_b}^{\text{RMS}}/m_{\text{rot}}$ ratio as a function of the back-iron thickness H_{R} are reported in Fig. 6.5 and Fig. 6.6, respectively. Reducing the back-iron thickness H_{R} has a negative effect on the model agreement d but allows increasing the $B_{r_b}^{\text{RMS}}/m_{\text{rot}}$ ratio. Notice that the simulated configurations for set B and C, although having good model agreement values, have in most of the cases an insufficient $B_{r_b}^{\text{RMS}}/m_{\text{rot}}$ (< 0.04 T/kg). Configurations of set A give encouraging results in terms of $B_{r_b}^{\text{RMS}}/m_{\text{rot}}$. However, the rotor mass of configurations of set A is above specifications (> 10 kg). An additional simulation effort is therefore required to reduce the mass. This is the topic of the next section.

6.3.4 Back-iron Mass Optimization with Non-linear Simulations

The norm of the magnetic flux density at the back-iron surface for the optimal configuration of set A in Table 6.3 (with $H_{\text{R}} = 5$ mm) is depicted in Fig. 6.7, where its value ranges from 0.04 T (blue) to 2.10 T (red). As one can observe, the flux is significantly lower in the center of the pole than at the external edges. Therefore, the mass of the back-iron could be reduced by removing some material at the center of the pole. Hence, as proposed in Fig. 6.8, the amount of material to be removed is parameterized by an additional design variable H_{C} , which denotes the depth of the conical cut. Thus the larger H_{C} is, the more material will be removed. In this section, non-linear simulations are performed to study the impact of H_{C} on the $B_{r_b}^{\text{RMS}}/m_{\text{rot}}$ ratio and on the model agreement d .

During the rotor optimization process, measurements of the inner radius of the existing stator showed that the radius of the rotor had to be reduced by 1 mm with respect to

6.3. Design Optimization with FEM Simulations

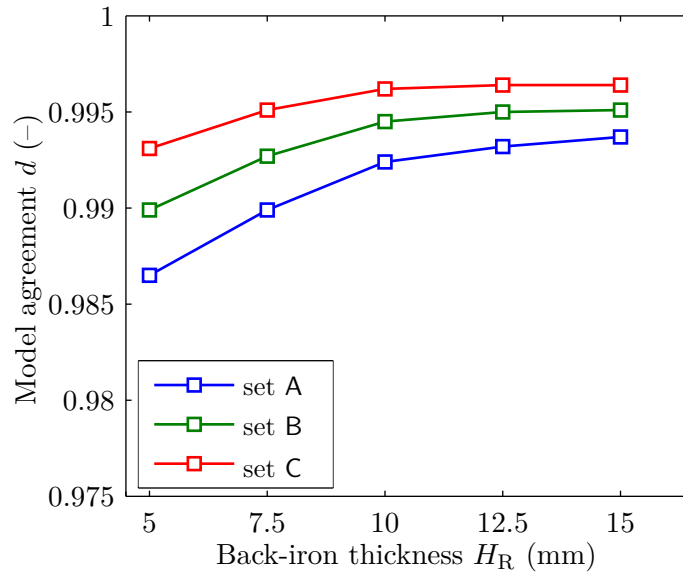


Figure 6.5. Model agreement d as a function of back-iron thickness H_R for set A, set B, and set C.

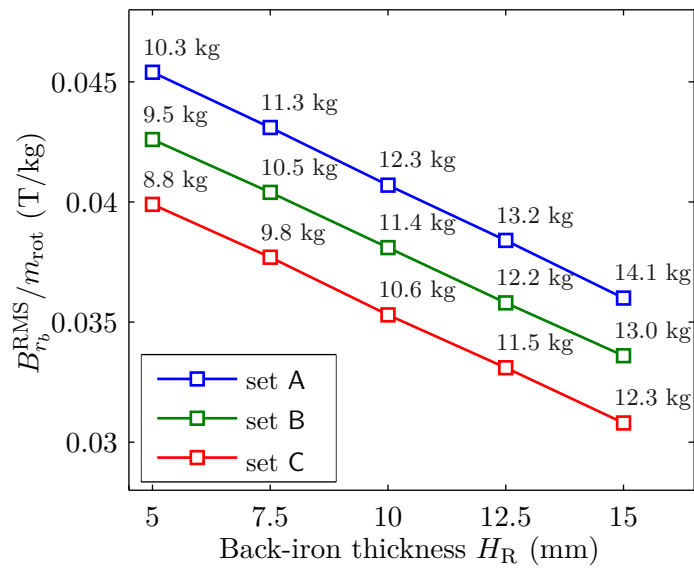


Figure 6.6. $B_{r_b}^{RMS}/m_{rot}$ ratio as a function of back-iron thickness H_R with total rotor mass m_{rot} for set A, set B, and set C.

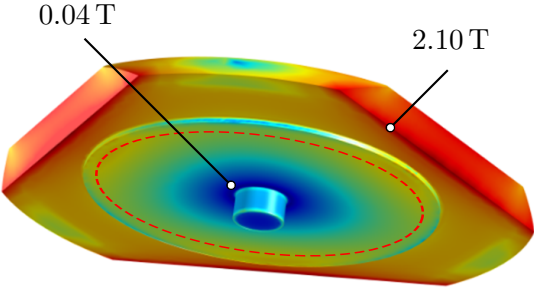


Figure 6.7. Magnetic flux density norm evaluated at the surface of the rotor back-iron surface.

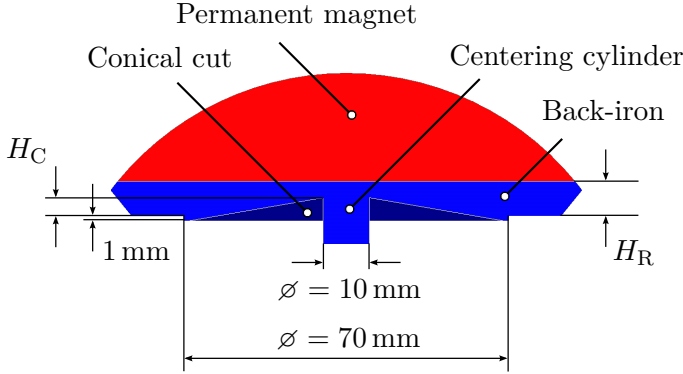


Figure 6.8. Geometry of the rotor back-iron and PM with relevant dimensions and indicating the design variables H_R and H_C .

6.3. Design Optimization with FEM Simulations

the value specified in Table 6.1. Therefore, the remaining part of the study is performed introducing a new configuration, which is a scaled version of the preferred configurations in Table 6.2, and which has an outer radius $R_{PM} + \delta$ equal to 87.5 mm. The octahedron height h is equal to 111.1 mm while the rotor pole eccentricity δ , obtained through interpolation, is equal to 23.7 mm.

Graphical illustrations of the model agreement d and the $B_{r_b}^{RMS}/m_{rot}$ ratio for various values of H_R and H_C are reported in Fig. 6.9 and Fig. 6.10, respectively. We observe that, for a given H_R , the model agreement criterion d remains unchanged for all values of H_C . Furthermore, as desired, the $B_{r_b}^{RMS}/m_{rot}$ ratio increases for higher values of H_C . Hence, removing material from the center of the back-iron has a beneficial effect on the $B_{r_b}^{RMS}/m_{rot}$ leaving the model agreement d unaffected. As it can be noticed in Fig. 6.10, the simulated configurations with $H_R = 7.5$ mm and $H_R = 10$ mm have to be discarded because their mass is higher than 10 kg, which is not compliant with the specifications in Table 6.1. Hence, the only acceptable configurations from those simulated are relative to H_R equal to 5 mm and the optimal configuration would be with H_C equal to 4 mm. Using these values results in a $B_{r_b}^{RMS}/m_{rot} = 0.0444$ T/kg and a model agreement $d = 0.9883$.

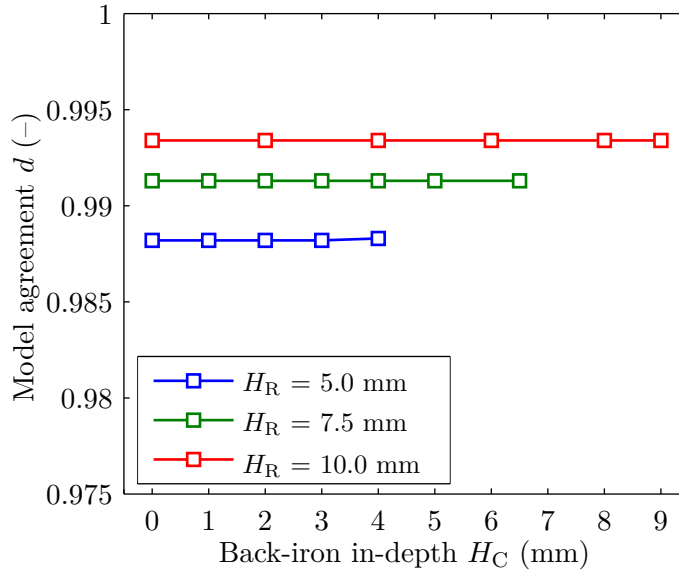


Figure 6.9. Model agreement d as a function of back-iron in-depth H_C and for various values of the back-iron thickness H_R .

Since the model agreement d decreases rapidly if H_R tends to 5 mm (see Fig. 6.5) and that model agreement d is nearly unaffected by the cut of the back-iron (see Fig. 6.9), an H_R of 6 mm instead of 5 mm is chosen and the shape of the back-iron is adapted as depicted in Fig. 6.11. Notice that in this back-iron geometry we have removed the pole centering cylinder, initially foreseen to mount and center the pole (see Fig. 6.8). In the back-iron design of Fig. 6.11, the mounting and centering of the pole are directly

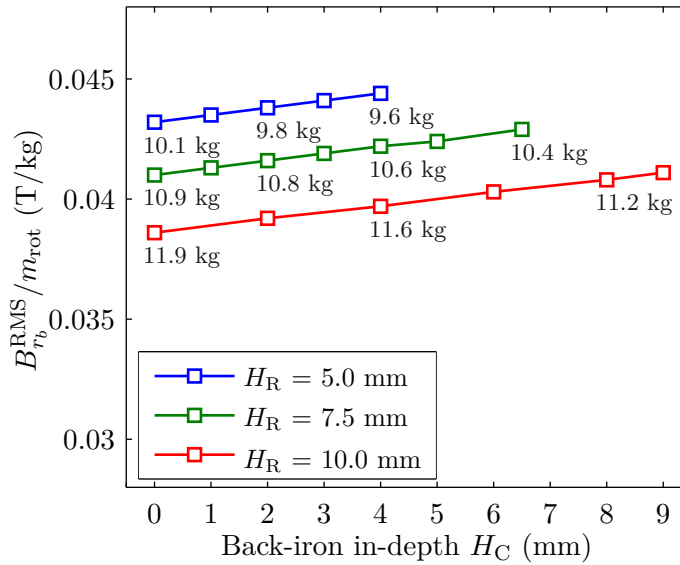


Figure 6.10. $B_{r_b}^{RMS}/m_{rot}$ ratio as a function of back-iron in-depth H_C and for various values of the back-iron thickness H_R .

implemented using a thicker centering ring and three mounting holes. Moreover, a cut of H_C equal to 3.5 mm was decided so as to guarantee enough mechanical stability near the pole center. Finally, this design was not further optimized but verified by simulation against the previously computed $B_{r_b}^{RMS}/m_{rot}$ and d . With the selected back-iron shape, the resulting values are $B_{r_b}^{RMS}/m_{rot} = 0.0433$ T/kg and $d = 0.9901$. The design of the rotor compliant with the specifications has the parameters listed in Table 6.4.

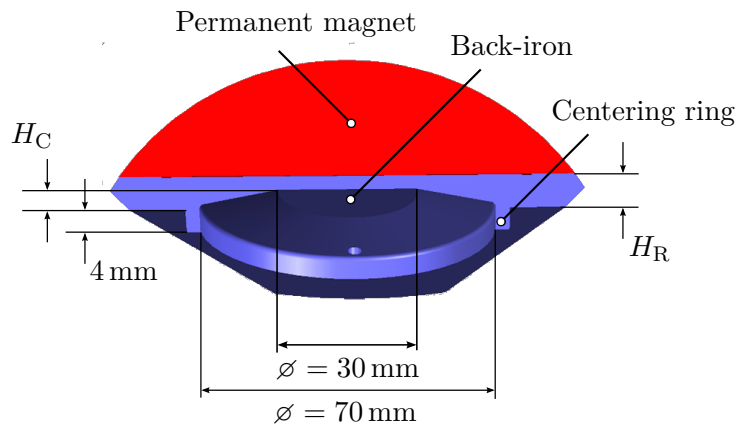


Figure 6.11. Final geometry of the rotor back-iron and PM with relevant dimensions and indicating the design variables H_R and H_C .

The manufactured optimized rotor is presented in Fig. 6.12 (top). To obtain a spherical rotor surface, which is necessary for position measurement, two hemispherical shells (bottom-right) are glued on the rotor.

6.3. Design Optimization with FEM Simulations

Table 6.4. Parameters of the selected design after optimization.

	Selected Value
Outer magnetic radius $R_{PM} + \delta$	87.5 mm
Rotor pole eccentricity δ	23.7 mm
Magnet radius R_{PM}	63.8 mm
Octahedron structure height h	111.1 mm
Back-iron thickness H_R	6 mm
Back-iron in-depth H_C	3.5 mm
Rotor mass m_{rot}	9.64 kg
Rotor angular momentum	7.1 Nms at 1842 rpm

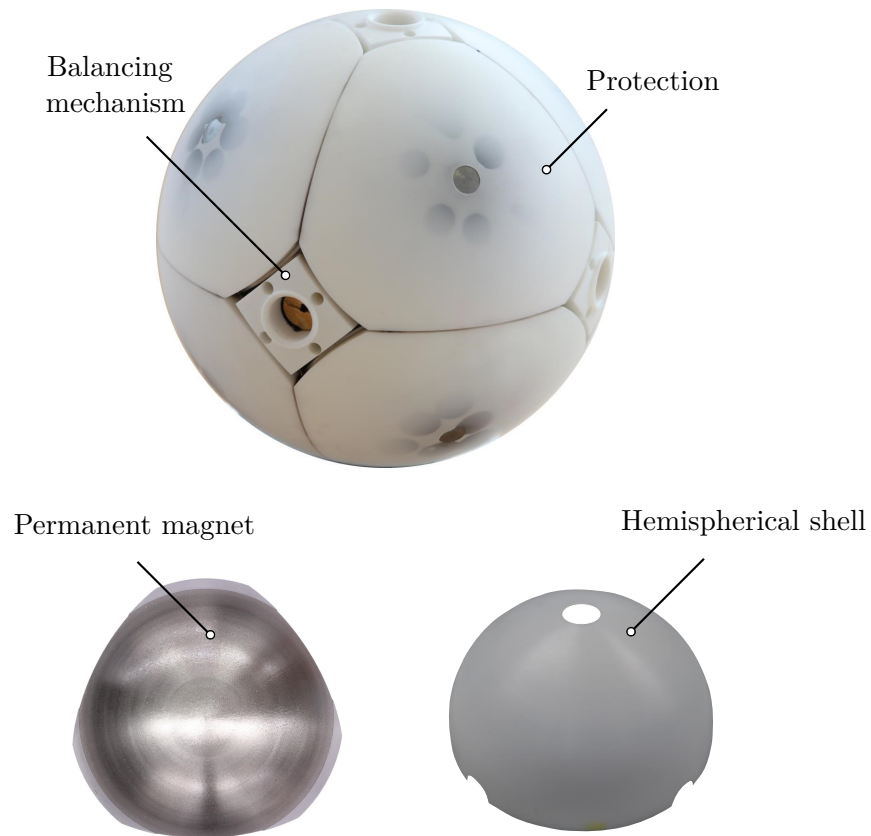


Figure 6.12. (Top) Manufactured rotor without hemispherical shells. (Bottom-left) Machined permanent magnet. (Bottom-right) Hemispherical shell.

6.4 Spherical Harmonic Analysis

In this section we perform a spherical harmonic analysis of the rotor magnetic flux density. As discussed in Section 2.4, to compute the harmonic content we consider the simulated magnetic flux density B_{4,r_b}^{dec} available on the entire spherical surface at $r_b = R_{\text{dec}} = 97.345$ mm and we decompose it on a spherical harmonic basis as

$$B_{4,r_b}^{\text{dec}} = \sum_{n=0}^{N_h} \sum_{m=-n}^n c_{n,\text{imm}}^m(R_{\text{dec}}) Y_n^m(\theta_b, \phi_b), \quad (6.6)$$

where $c_{n,\text{imm}}^m$ are spherical harmonic decomposition coefficients for the immobile rotor computed using integration as

$$c_{n,\text{imm}}^m(R_{\text{dec}}) = \int_0^{2\pi} \int_0^\pi B_{4,r_b}^{\text{dec}}(R_{\text{dec}}, \theta_b, \phi_b) \overline{Y_n^m(\theta_b, \phi_b)} \sin \theta_b d\theta_b d\phi_b. \quad (6.7)$$

The module of the normalized spherical harmonic decomposition coefficients with $N_h = 20$ is illustrated in Fig. 6.13. As it can be observed, the fundamental component of the magnetic flux density corresponds, as desired, to the spherical harmonic of degree 3 and order 2 (octupole). However, as it was studied in Section 2.4.6 and expression (2.64), high-order harmonics with degree n equal to 7, 9, 11, 13, 15, 17, and 19, and order m equal to 2, 6, 10, 14, and 18 also appear in the spectrum.

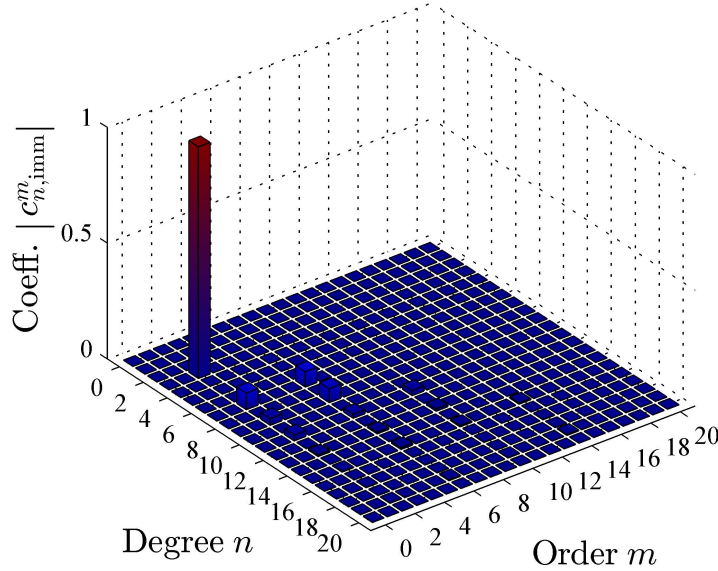


Figure 6.13. Spherical harmonic analysis using optimized monoblock rotor.

6.5 Summary

In this chapter we presented the design optimization of a permanent magnet spherical rotor for the proposed reaction sphere actuator. Contrary to the first developed spherical rotor introduced in Chapter 1, where the eight permanent magnet poles were discretized using a mosaic of 728 cylindrical magnets to approximate the desired fundamental spherical harmonic, the new rotor consists of eight bulk poles with truncated spherical shape that are parallel-magnetized and positioned on the back-iron structure.

Given a set of specifications on the mass, the flux density strength, the outer radius, and the angular momentum, the rotor design optimization problem consisted in finding suitable design parameters to minimize the distortion of the magnetic flux density with respect to the desired fundamental harmonic. Because a pure analytical approach was not practicable due to the highly complex geometry of the rotor, the optimization was performed using FEM simulations. Several linear and nonlinear simulations have been performed allowing us to obtain a design compliant with the specifications.

Experimental verification on the magnetic flux density as well as closed-loop rotor position and orientation control using the manufactured rotor have been performed and will be presented in the next chapter.

7 Experimental Results

In this chapter we present a variety of experimental activities related to the material developed throughout the document. We start with measurements of the magnetic flux density of the rotor and compare them to the developed analytical model and to FEM simulated values. Then, force and torque inverse models combined with the proposed magnetic state estimation procedure are experimentally validated demonstrating the capability of producing a current vector to generate a given pair of forces and torques. Next, we validate the developed magnetic state estimation method and show how the rotor magnetic flux density can be reconstructed starting from a finite number of magnetic flux density measurements. Subsequently, we validate the developed algorithm to estimate the back-EMF voltage and the rotor angular velocity. After that, by using measured flux density values, we will show that the newly developed monoblock rotor is indeed compliant with the specifications. Finally, we will present results obtained during the first closed-loop experimental validation campaign showing the ability of simultaneously levitating the rotor while rotating it about a given axis.

7.1 Introduction

This chapter is dedicated to experimental activities performed using the reaction sphere developed prototype. On one hand, these activities will provide an experimental validation of the theoretical models and techniques developed in this thesis. On the other hand, practical challenges will also be unveiled providing a perspective for future research.

To begin with, we focus on validating the hybrid FEM-analytical magnetic flux density model with both measurements and FEM simulations using the newly developed monoblock rotor presented in Chapter 6. Subsequently, force and torque inverse models are validated using both the discrete rotor and the monoblock rotor. In particular, for different orientations of the rotor inside the stator, we apply the proposed magnetic state estimation and compute a current vector to satisfy a given force and torque ref-

erence pair. Then, we report results concerning magnetic state estimation in which the optimal sensor placement technique is applied to select a number of sensors among various locations available in the prototype. Moreover, in this activity, we present a procedure to calibrate the radial and angular position of the operating magnetic flux density sensors and conclude with an illustration on how the magnetic flux density distribution can be reconstructed using flux measurements. After that, we validate the developed algorithm to estimate the rotor angular velocity. Next, with the magnetic flux density measurements, we compare the model agreement and the magnetic flux density over mass ratio to FEM values showing that the developed rotor is compliant with specifications. Finally, all the developed techniques are combined together in an illustrative closed-loop campaign. In this activity, we develop dynamic controllers for the magnetic bearing and the angular velocity and show that the rotor can simultaneously be levitated and rotated about a given axis. Closed-loop measurements are performed using the optimized monoblock rotor.

7.2 Magnetic Flux Density Model - Monoblock Rotor

7.2.1 Introduction

The objective of this section is to validate the hybrid FEM-analytical magnetic flux density model. To this end, we employ both measurements and FEM simulations performed with the developed monoblock rotor and compare them to the proposed model about horizontal and vertical paths for different number of harmonics N_h . Finally, to compare measurements and values computed using the hybrid FEM-analytical model we introduce the Mean Normalized Relative Error (MNRE) metrics and study the relation between this error and the number of harmonics N_h taken into consideration in the model.

7.2.2 Experimental Setup

The experimental setup for the magnetic flux density measurement is depicted in Fig. 7.1. The magnetic flux density is measured with a teslameter (MAGNET-PHYSIK FH55) equipped with an axial Hall probe (HS-AGB5) that can be placed at multiple declination angles θ_b and at various distances from the rotor surface. The axial probe can be positioned to measure the radial component of the magnetic flux density B_{r_b} and both tangential components B_{θ_b} and B_{ϕ_b} , which all contribute to generate the Lorentz force.

The magnetic flux density is measured at 8 polar angles $\theta_b = \{15^\circ, 25^\circ, \dots, 85^\circ\}$. The rotor is supported by a rigid guiding axis and connected to an AC electric motor so that, for each angle θ_b , a total of 600 points equally distributed on the interval $\phi_b \in [0^\circ, 360^\circ]$ are recorded. The radial component of the magnetic flux density is measured at 4 radial distances $r_b = \{92 \text{ mm}, 94 \text{ mm}, 96 \text{ mm}, 98 \text{ mm}\}$. Finally, at $r_b = 95.7 \text{ mm}$ both the radial

7.2. Magnetic Flux Density Model - Monoblock Rotor

component B_{r_b} and the tangential components B_{θ_b} and B_{ϕ_b} are recorded.

For FEM simulations, parameters are identical to those used in Chapter 6.

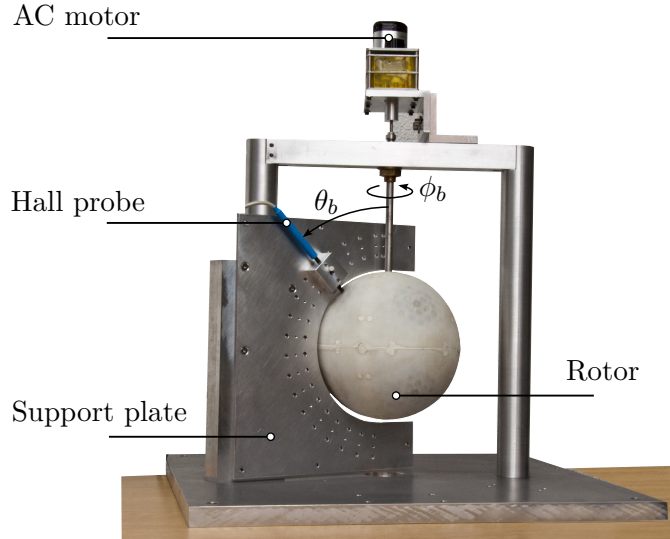


Figure 7.1. Experimental setup used to measure the magnetic flux density of the rotor.

7.2.3 Results

Horizontal Profiles

From Fig. 7.2 to Fig. 7.7 we report the three components of the measured magnetic flux density at $r_b = 95.7$ mm as a function of the azimuthal angle ϕ_b compared to FEM simulations and values derived using the developed model at polar angles θ_b equal to 25, 35, 45, 55, 65, and 75°. Values computed using the developed model are reported for maximum spherical harmonics degrees $N_h = 3$ and $N_h = 19$. As can be observed, measurements are in good agreement with the expected simulated values. Furthermore, the magnetic flux density profiles are sinusoidal although higher order harmonics are observed for θ_b equal to 65 and 75°. These fluctuations are due to the gaps at the vertexes of the truncated octahedron structure. Finally, notice that the profiles computed using the hybrid FEM-analytical model with $N_h = 3$ and $N_h = 19$ are in good agreement with measured values for θ_b equal to 55 and 65°. For θ_b equal to 65 and 75°, where fluctuations due to the vertexes occur more significantly, with $N_h = 3$ the model can only capture the fundamental component of the profile, which is completely approximated using $N_h = 19$.

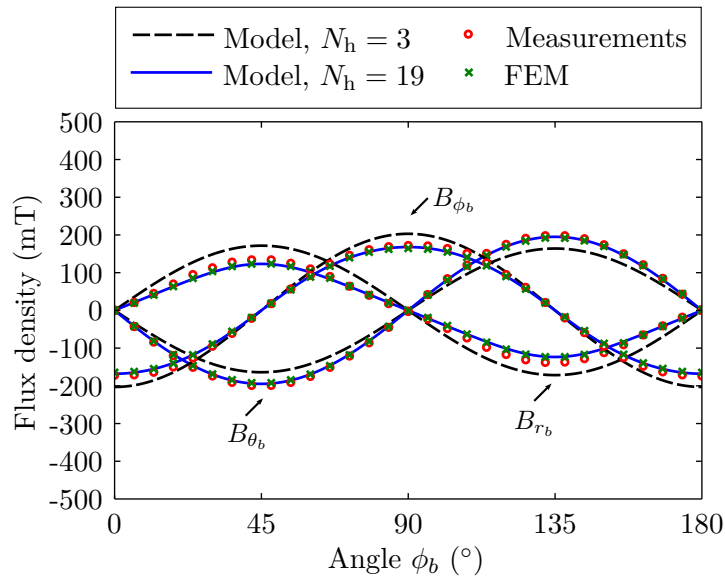


Figure 7.2. Measured magnetic flux density compared to FEM simulations and values derived using the developed model at polar angle $\theta_b = 25^\circ$.

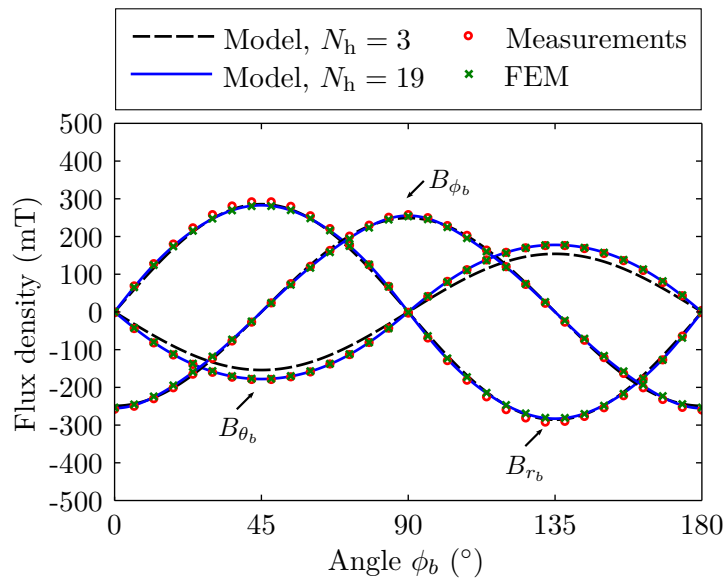


Figure 7.3. Measured magnetic flux density compared to FEM simulations and values derived using the developed model at polar angle $\theta_b = 35^\circ$.

7.2. Magnetic Flux Density Model - Monoblock Rotor

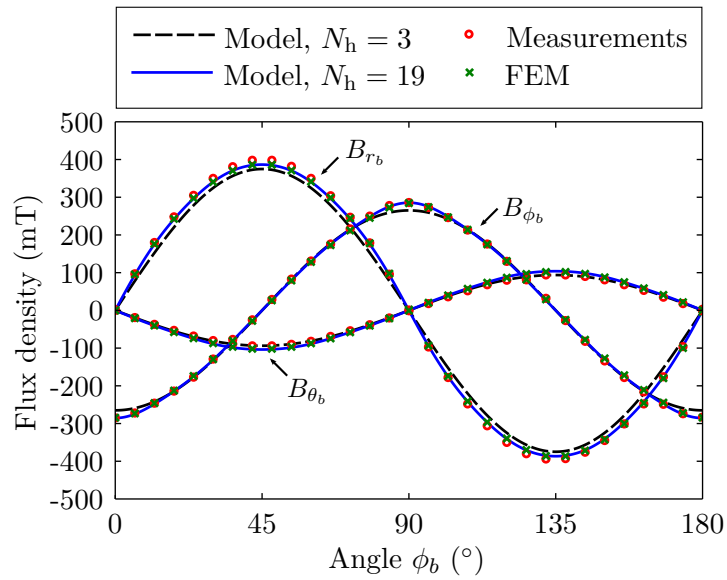


Figure 7.4. Measured magnetic flux density compared to FEM simulations and values derived using the developed model at polar angle $\theta_b = 45^\circ$.

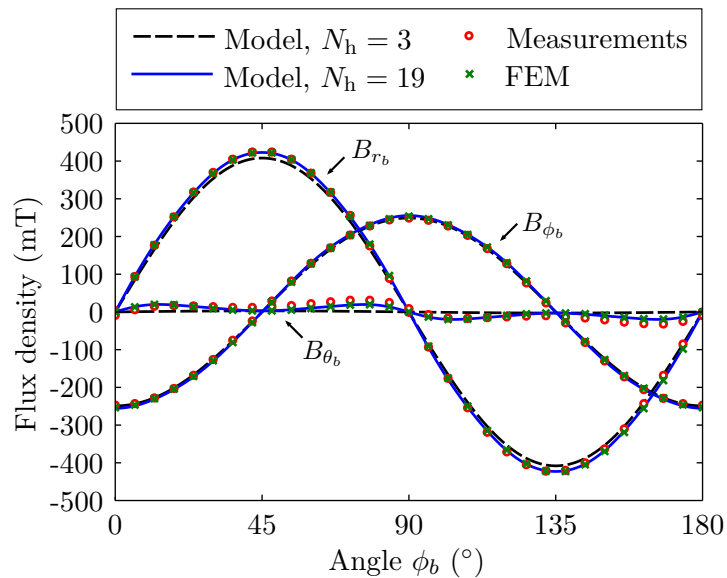


Figure 7.5. Measured magnetic flux density compared to FEM simulations and values derived using the developed model at polar angle $\theta_b = 55^\circ$.

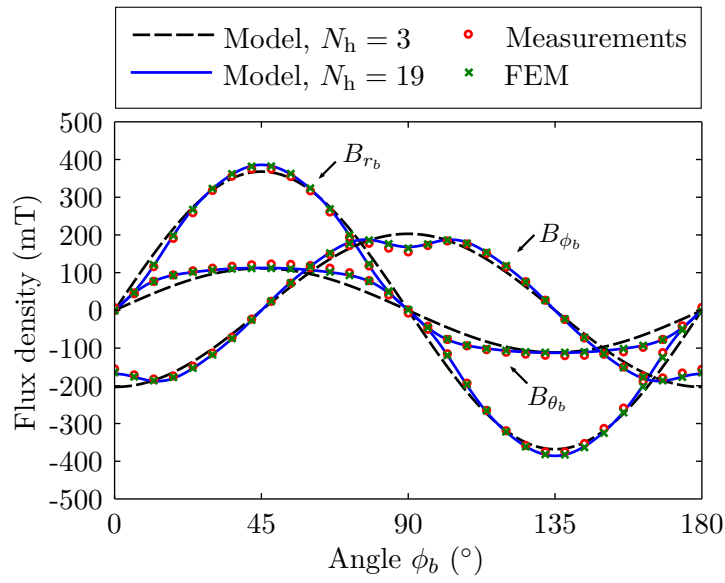


Figure 7.6. Measured magnetic flux density compared to FEM simulations and values derived using the developed model at polar angle $\theta_b = 65^\circ$.

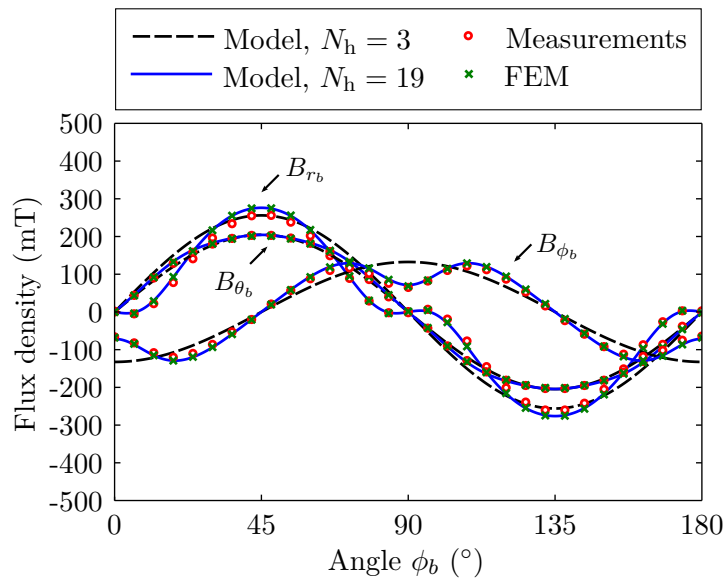


Figure 7.7. Measured magnetic flux density compared to FEM simulations and values derived using the developed model at polar angle $\theta_b = 75^\circ$.

Vertical Profiles

In Fig. 7.8 we display the radial component of the measured magnetic flux density as a function of the polar angle θ_b compared to FEM simulations and values derived using the developed model at azimuthal angle $\phi_b = 45^\circ$. In this image we can clearly observe the fluctuation due to the gap at the vertex of the rotor. Measurements are in close agreement with simulated values. With $N_h = 3$, the proposed model does not capture the fluctuation originating from the gap at the vertex (between 0 and 30°), but is completely captured using $N_h = 19$.

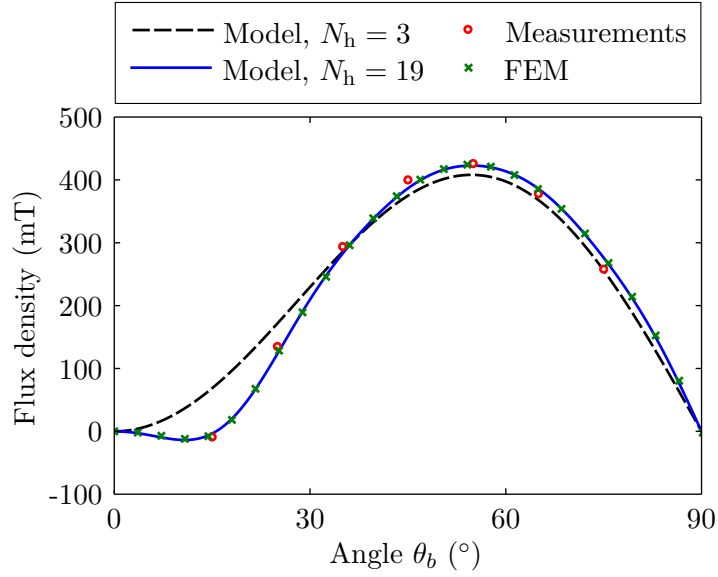


Figure 7.8. Measured magnetic flux density compared to FEM simulations and values derived using the developed model at azimuthal angle $\phi_b = 45^\circ$.

Profiles at a Pole

In Fig. 7.9 we report the radial component of the measured magnetic flux density at a pole ($\theta_b \approx 55^\circ$ and $\phi_b = 45^\circ$) as a function of the radial distance r_b ranging from 90 mm to 100 mm. The measured magnetic flux density is compared to FEM simulations and values derived using the developed model.

Mean Normalized Relative Error

Given values of the radial component of the measured magnetic flux density $B_{r_b, \text{meas}}(r, \theta_b, \phi_b)$ and values of the developed model $B_{r_b}^{N_h}(r_b, \theta_b, \phi_b)$ computed as in (2.68), we define a MNRE as

$$\text{MNRE} (\%) = \sum_{i=1}^4 \sum_{j=1}^8 \sum_{k=1}^{600} \frac{\epsilon(r_{b,i}, \theta_{b,j}, \phi_{b,k})}{4 \cdot 8 \cdot 600} \cdot 100 \%, \quad (7.1)$$

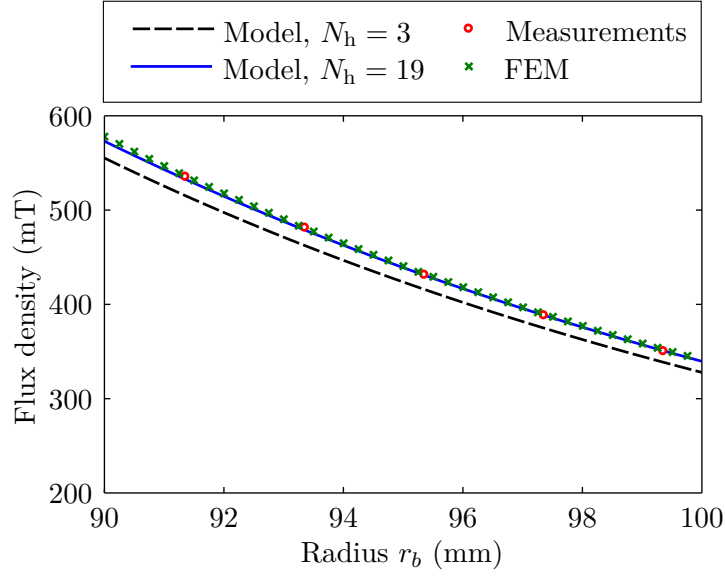


Figure 7.9. Measured magnetic flux density compared to FEM simulations and values derived using the developed model at pole.

where

$$\epsilon(r_{b,i}, \theta_{b,j}, \phi_{b,k}) = \frac{|B_{r_b}^{N_h}(r_{b,i}, \theta_{b,j}, \phi_{b,k}) - B_{r_b, \text{meas}}(r_{b,i}, \theta_{b,j}, \phi_{b,k})|}{\max_{j,k} |B_{r_b, \text{meas}}(r_{b,i}, \theta_{b,j}, \phi_{b,k})|}. \quad (7.2)$$

The MNRE can be computed similarly for the remaining tangential components of the flux density, which are evaluated using FEM simulations.

In Fig. 7.10 we report the MNRE values computed using (7.1) as a function of the maximum spherical harmonic reconstruction degree N_h . As expected, the higher the number of harmonics taken into account in the model is, the smaller the MNRE becomes.

7.2.4 Conclusions

In this section magnetic flux density measurements and FEM simulated values are compared to the proposed hybrid FEM-analytical model. We have observed that measurements are in good agreement with values calculated using the hybrid model although distortions of the measured field are observed in the proximity of the rotor vertexes, which require a higher number of harmonics to be fully approximated. Finally, the MNRE metric was introduced to analyze the global error between measurements and values given by the model for different maximum spherical harmonic reconstruction degrees N_h taken into account in the model. We observed that this MNRE becomes smaller as we increase the maximum spherical harmonic degree N_h .

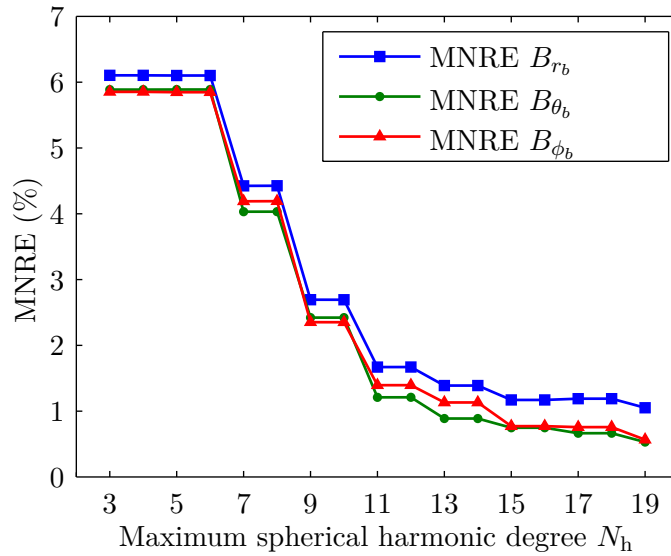


Figure 7.10. MNRE as a function of the maximum spherical harmonic degree.

7.3 Force and Torque Models

7.3.1 Introduction

The objective of this section is to verify force and torque inverse models using both the developed prototype and FEM simulations. This experimental program is divided into three parts. In the first phase, force and torque inverse models are verified using the discrete spherical rotor and estimation of the spherical harmonics coefficients (magnetic state) is performed using an external teslameter. Then, because in the experimental setup we can only measure forces and torques parallel to the guiding axis, in the second phase we employ FEM simulations to verify force and torque models about several randomly generated rotor orientations and corresponding random force and torque vectors. Finally, in the third phase, force and torque models are verified using the optimized monoblock rotor and estimation of the spherical harmonic coefficients is carried out using embedded flux density sensors.

7.3.2 Experiments with Discrete Rotor

Introduction

Force and torque models have first been validated using the discrete spherical rotor in [122]. In this reference, we have employed the analytical model with ideal octupole cubic magnetization presented in Section 2.3. Notice that, however, because in this section we validate force and torque inverse models employing magnetic state estimation,

Chapter 7. Experimental Results

the same results would have been obtained by using the hybrid FEM-analytical model, since the magnetic state estimation does solve the Laplace equation using measured boundary conditions. Before concentrating on force and torque model validation, we present measured and simulated magnetic flux density values corresponding to the discrete rotor. Then, the experimental setup and procedure to validate force and torque models is described. Finally, we present results obtained using the laboratory prototype.

Magnetic Flux Density

The experimental setup and procedure for the magnetic flux density measurement is the same presented in Fig. 7.1.

In Fig. 7.11 we report the three components of the measured magnetic flux density measured at $r_b = 95.5$ mm as a function of the azimuthal angle ϕ_b compared to FEM simulations at polar angles θ_b equal to 45, 55, 65, and 75°. As can be observed, measurements are in good agreement with the expected simulated values.

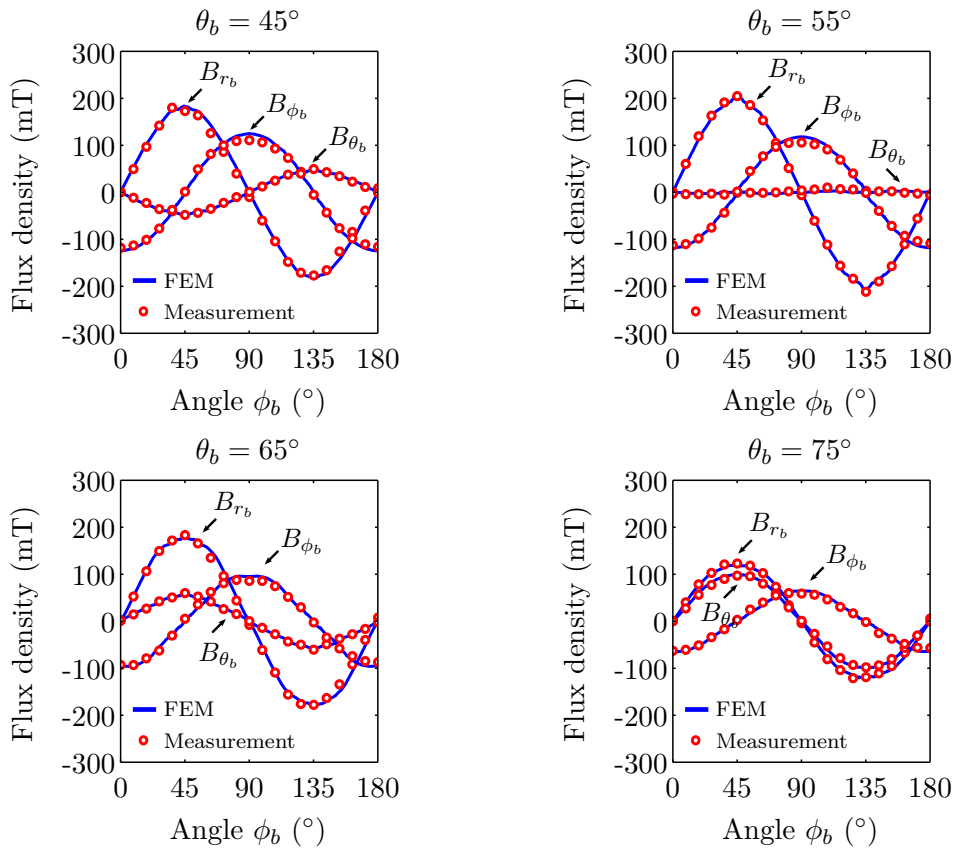


Figure 7.11. Measured magnetic flux density compared to FEM simulations at polar angles θ_b equal to 45°, 55°, 65°, and 75°.

Experimental Setup and Procedure

The experimental setup for force and torque measurements is reported in Fig. 7.12. The sphere is maintained centered inside the stator by a temporary rigid guiding axis to allow the measurement of forces and torques. Only force and torque components parallel to the axis will be measured. We emphasize, however, that this test axis is purely arbitrary and that the procedure to obtain force and torque models is applied as presented in Chapter 4 without *a priori* information on the choice of the rotation axis. For force measurements, the rotor is suspended to a load cell (HMB Typ Z8) that continuously measures the rotor weight. The permanent magnet rotor is mounted inside a plastic stator that also supports the coils. To measure the torque, the rotor is suspended and the torque is measured with a load cell through a cantilever of length d equal to 14.3 cm.

The measurement procedure consists in illustrating the ability of the developed force and torque analytical models to produce suitable current vectors to obtain the desired forces and torques for the rotor about various orientations. For each orientation, described by a rotation of α about the axis, the magnetic flux density is measured at the center of each stator coil \mathbf{P}_1 to \mathbf{P}_9 at $R_{\text{sens}} = 99$ mm and the online procedure in Section 4.2.4 is followed to compute K_F and K_T . For each orientation, a set of currents \mathbf{i}_F and \mathbf{i}_T is computed using the inverse model to produce vertical forces of 9.81 N and torques of 0.4 Nm as

$$\mathbf{i}_F = K_F^T (K_F K_F^T)^{-1} \cdot \begin{bmatrix} 0 & 0 & 9.81 \end{bmatrix}^T k_p \quad (7.3)$$

$$\mathbf{i}_T = K_T^T (K_T K_T^T)^{-1} \cdot \begin{bmatrix} 0 & 0 & 0.4 \end{bmatrix}^T k_p \quad (7.4)$$

where k_p is a scalar factor, which will be varied to verify the linearity.

Results

The measured radial components of the magnetic flux density at the center of the nine coils for various values of the angle α are summarized in Table 7.1.

Then, in Table 7.2 and 7.3 we report the current vector for angle α computed to satisfy the requested forces and torques, respectively, and considering a proportionality factor $k_p = 3$. The same current vectors are displayed in Fig. 7.14 and 7.15, respectively. As discussed in Section 3.5, because two facing coils \mathbf{P}_k and \mathbf{P}_{20+1-k} produce the same force, one has $\mathbf{i}_{F,k} = \mathbf{i}_{F,20+1-k}$, $k = 1, 2, \dots, 10$. Therefore, since coil \mathbf{P}_{10} and \mathbf{P}_{11} are not used in this experiment, only current from \mathbf{P}_1 to \mathbf{P}_9 are displayed. For each angle α , Fig. 7.14 and Fig. 7.15 indicate the maximum current intensity defined by the vector infinity-norm as $|\mathbf{i}_F| = \max |i_k|$, $k = 1, 2, \dots, 10$, and the total electric power P relative to all 20 stator currents. As can be noticed, the current of each coil depends on the orientation of the rotor described by α . Moreover, although the current vector \mathbf{i}_F is computed to minimize

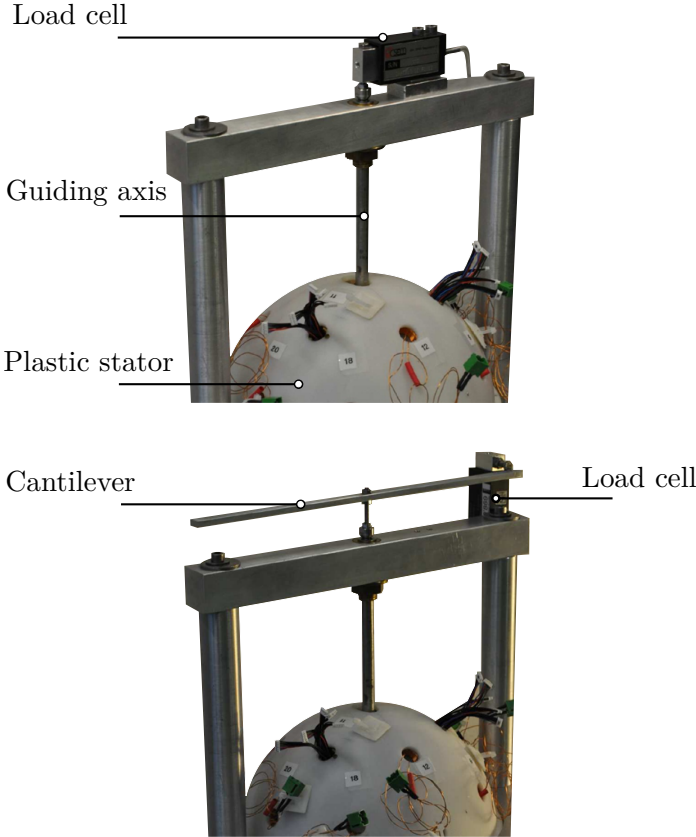


Figure 7.12. Force and torque experimental setup.

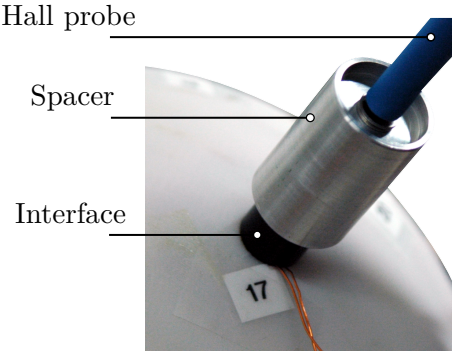


Figure 7.13. Setup to measure the radial component of the magnetic flux density at the center of a coil for experimental validation of force and torque inverse models.

7.3. Force and Torque Models

the dissipated energy for each orientation α , the total electric power varies among the orientations indicating the existence of preferred configurations.

Finally, measured forces and torques for different values of the proportionality factor k_p and for the rotor about different orientations are reported in Fig. 7.16 and 7.17, respectively. Measured values confirm the linearity between stator currents and forces and torques. Moreover, forces and torques obtained about various orientations of the rotor are in good agreement with the analytical models. Differences between the experimental values and the analytical model are mainly caused by fabrication and measurement errors as well as residual features due to the discretization of the magnet.

Table 7.1. Measured radial components of the magnetic flux densities at sensor locations for various orientation of the rotor.

Angle α ($^\circ$)	B_{4,r_b} (mT)								
	S_1	S_2	S_3	S_4	S_5	S_6	S_7	S_8	S_9
0	-25.4	-129.9	141.5	-65.8	3.9	68.3	131.1	140.1	22.5
20	-92.6	-74.6	98.5	-100.6	-49.6	15.6	134.5	132.7	-44.9
40	-133.5	3.2	19.3	-88.9	-91.4	-46.3	78.8	65.9	-110.3
60	-112.5	84.0	-69.5	-43.3	-93.7	-92.8	-2.6	-20.0	-124.8
80	-30.3	138.5	-137.0	28.3	-47.0	-94.0	-87.2	-109.5	-74.1

Table 7.2. Currents computed to satisfy given reference torques for various orientations of the rotor ($k_p = 3$).

Angle α ($^\circ$)	Current (A)								
	i_1	i_2	i_3	i_4	i_5	i_6	i_7	i_8	i_9
0	-0.014	0.033	-0.167	-2.121	2.062	0.179	-0.422	0.386	-0.035
20	0.125	0.405	0.177	-2.560	1.106	0.265	-0.845	0.042	1.021
40	0.171	0.465	0.349	-1.624	-0.050	0.098	-1.436	-0.833	2.442
60	0.523	0.132	0.108	0.003	-1.688	0.315	-0.741	-1.352	2.438
80	0.336	0.091	0.250	1.371	-2.588	0.003	0.207	-0.648	0.846

Table 7.3. Currents computed to satisfy given reference torques for various orientations of the rotor ($k_p = 3$).

Angle α ($^\circ$)	Current (A)								
	i_1	i_2	i_3	i_4	i_5	i_6	i_7	i_8	i_9
0	1.521	-1.286	-1.183	0.223	-0.521	1.206	0.756	-0.927	0.305
20	1.317	-0.488	0.096	-0.203	-0.650	0.360	-0.438	-1.089	-0.678
40	0.233	-0.696	1.342	-0.720	-0.445	1.088	-0.592	-0.245	-0.144
60	-0.701	0.329	1.041	-0.441	-0.753	1.302	-0.253	-0.632	0.148
80	-0.450	1.473	0.581	-0.823	-0.294	-0.205	-1.214	-0.267	0.464

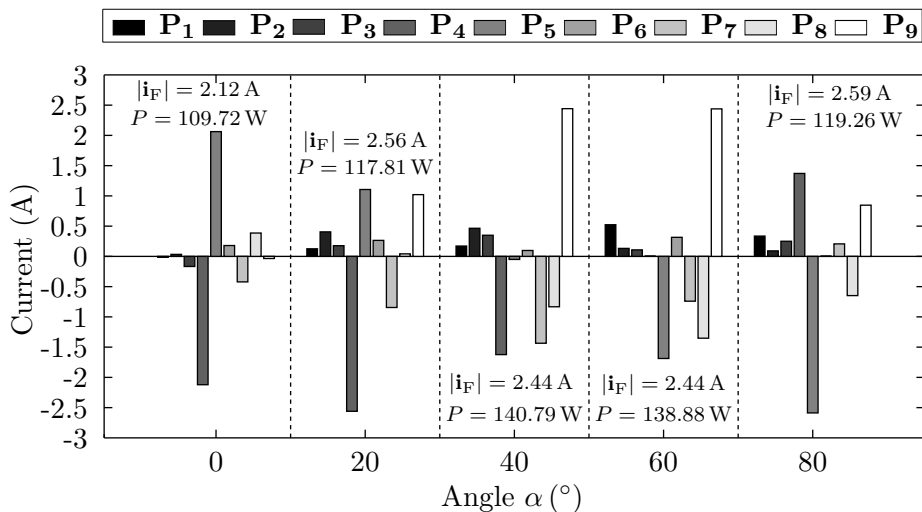


Figure 7.14. Currents computed to satisfy given reference forces for various orientations of the rotor ($k_p = 3$).

Conclusions

In this section we performed measurements to validate force and torque inverse models together with the magnetic estimation procedure. We have shown that given measurements of the magnetic flux density collected at multiple locations equidistant from the rotor surface we can compute a current vector to generate a force and torque reference pair along the guiding axis. Finally, we demonstrated the linearity between the applied current vector and the measured forces and torques.

7.3.3 Simulations with Discrete Rotor

Introduction

In this section we employ FEM simulations to verify force and torque models about several randomly generated rotor orientations and corresponding random force and torque vectors. This FEM validation is complementary to the experimental measurements presented in the previous section. As a matter of fact, at present, with the current laboratory prototype we can only measure forces and torques parallel to the guiding axis. Moreover, the possible rotor orientations are constrained about the guiding axis.

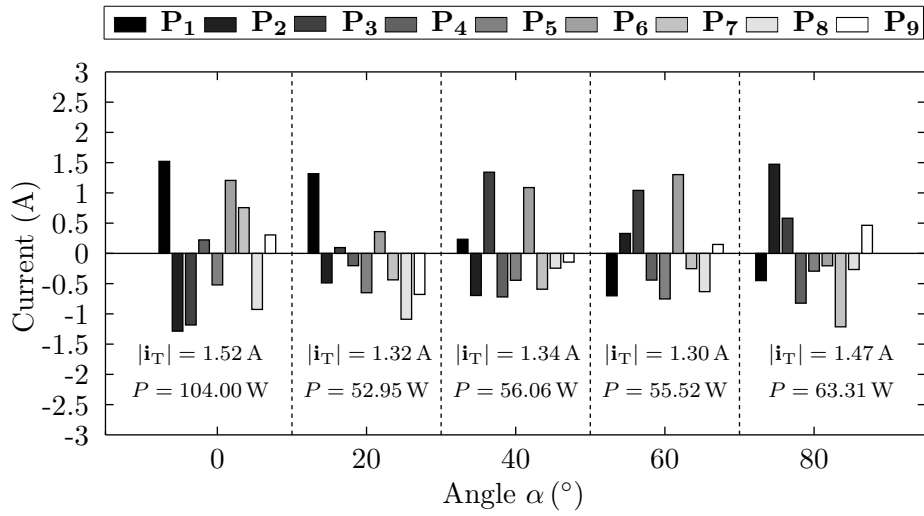


Figure 7.15. Currents computed to satisfy given reference torques for various orientations of the rotor ($k_p = 3$).

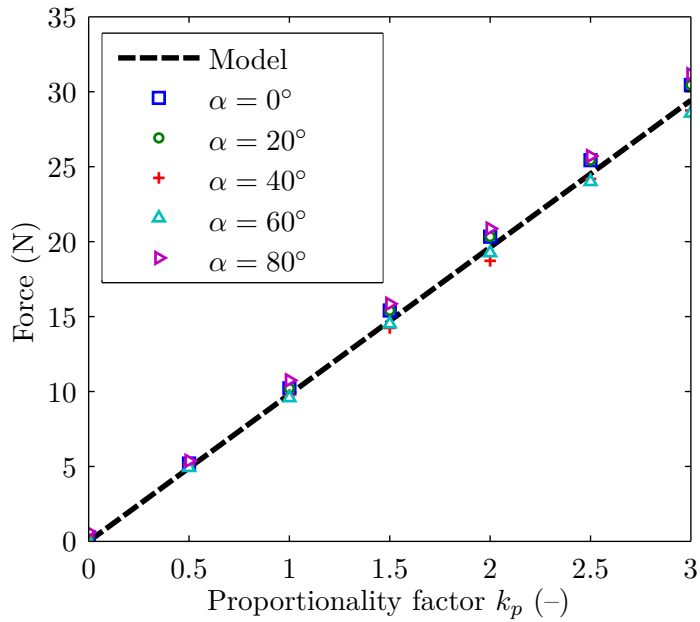


Figure 7.16. Measured forces for different orientations of the rotor and different magnitudes of the current vector. Measurements performed with discrete rotor.

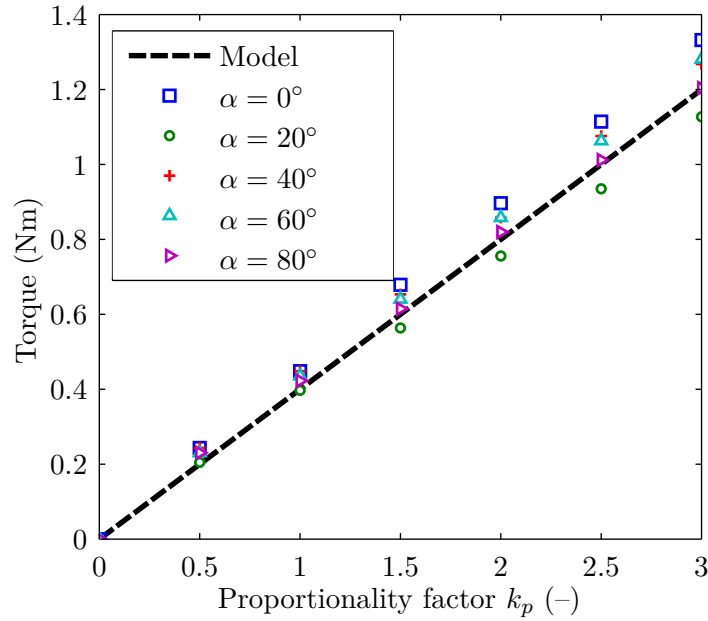


Figure 7.17. Measured torques for different orientations of the rotor and different magnitudes of the current vector. Measurements performed with discrete rotor.

Simulation Setup and Procedure

In this simulation we illustrate the ability of the developed force and torque analytical models to produce suitable current vectors to satisfy reference forces and torques for 4 randomly-generated orientations of the rotor. For illustrative purposes, 10 single-axis magnetic flux density sensors are placed at the center of each stator coil \mathbf{P}_1 to \mathbf{P}_{10} . Hence, the projection matrix P as well as force and torque characteristic matrices K_F^m and K_T^m are computed as presented in the offline procedure in Section 4.2.4. Subsequently, the simulated magnetic flux density is used to compute matrices K_F and K_T as described in the online procedure. Then, for each of the 4 orientations, force and torque characteristic matrices are employed to compute a suitable current vector by applying the inverse model (3.48) to satisfy 3 randomly-generated pairs of reference forces and torques. Forces and torques are chosen with random direction but with norm equal to 25 N and 1 Nm respectively. Therefore, force and torque inverse models are verified for a total of 12 configurations. Simulations are performed by applying to the stator coils the current vector generated with the inverse model. Finally, simulated forces and torques are computed using the Lorentz integral in COMSOL Multiphysics and compared to the expected reference values. In these simulations, permanent magnets are modeled applying their linear constitutive relations $\mathbf{B} = \mu_{PM}\mu_0\mathbf{H} + \mathbf{B}_{rem}$, where the relative permeability μ_{PM} is fixed to 1 and the norm of the remanent magnetic flux density \mathbf{B}_{rem} is equal to 1.4 T. The back-iron is simulated using a linear B-H relationship $\mathbf{B} = \mu_R\mu_0\mathbf{H}$, with the relative permeability μ_R equal to 10000. For illustration, in Fig. 7.18 we report the

meshed model used for the simulations.

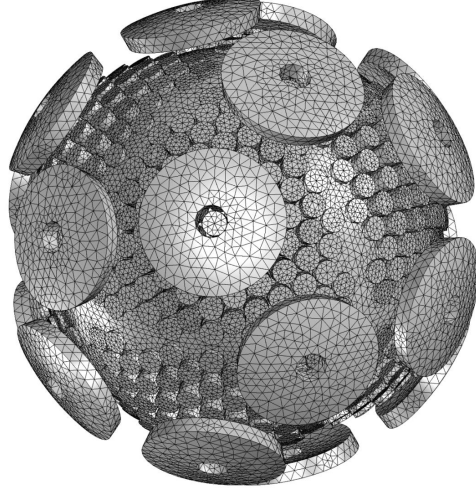


Figure 7.18. Meshed model used for FEM validation of force and torque models using discrete rotor.

Results

The three components of the reference and simulated forces and torques for the studied configurations are reported in Fig. 7.19 and 7.20, respectively. As can be observed, forces and torques resulting from the proposed simulated model are in agreement with the reference values. To compare the randomly-generated reference forces \mathbf{F}_{ref} to the simulated vectors \mathbf{F}_{FEM} , we introduce the norm relative error defined as

$$\text{Relative error (\%)} = \frac{\|\mathbf{F}_{\text{FEM}}\| - \|\mathbf{F}_{\text{ref}}\|}{\|\mathbf{F}_{\text{ref}}\|} \cdot 100\%, \quad (7.5)$$

and the angle error defined as

$$\text{Angle error (}^\circ\text{)} = \cos^{-1} \left(\frac{\mathbf{F}_{\text{FEM}}^T \mathbf{F}_{\text{ref}}}{\|\mathbf{F}_{\text{FEM}}\| \|\mathbf{F}_{\text{ref}}\|} \right) \cdot \frac{180}{\pi}. \quad (7.6)$$

The norm relative and angle errors corresponding to the torque are defined similarly.

Norm relative errors and angle errors corresponding to the studied configurations for force and torques are reported in Fig. 7.21 and 7.22, respectively. As it can be observed, the norm relative error is below 5% whereas the angle error is below 3°. Possible reasons of these differences include numerical errors in FEM simulations and distortions of the rotor magnetic flux density due to the discretization of the permanent magnets.

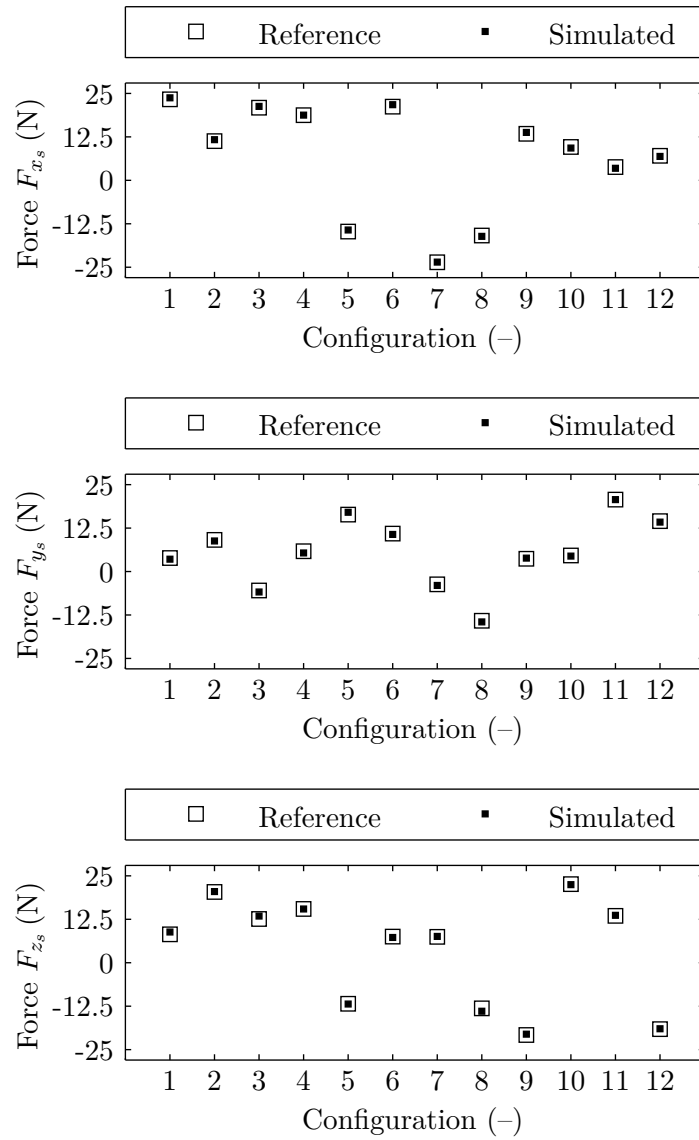


Figure 7.19. Three components of reference and simulated forces for FEM validation of force inverse model with discrete rotor.

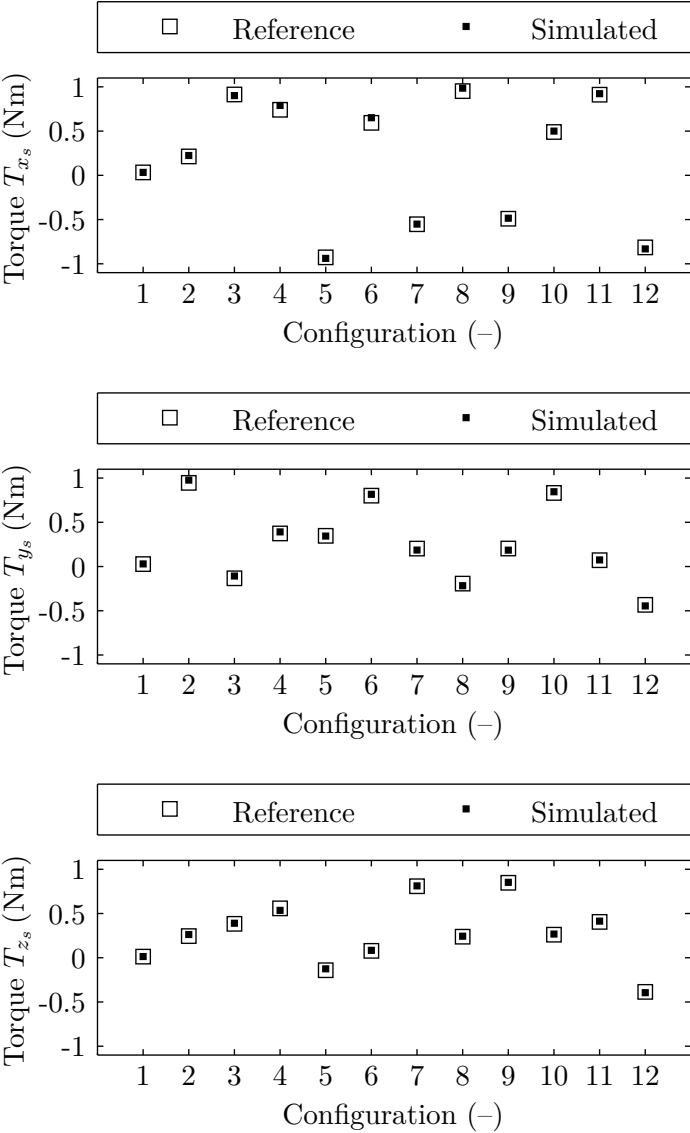


Figure 7.20. Three components of reference and simulated torques for FEM validation of torque inverse model with discrete rotor.

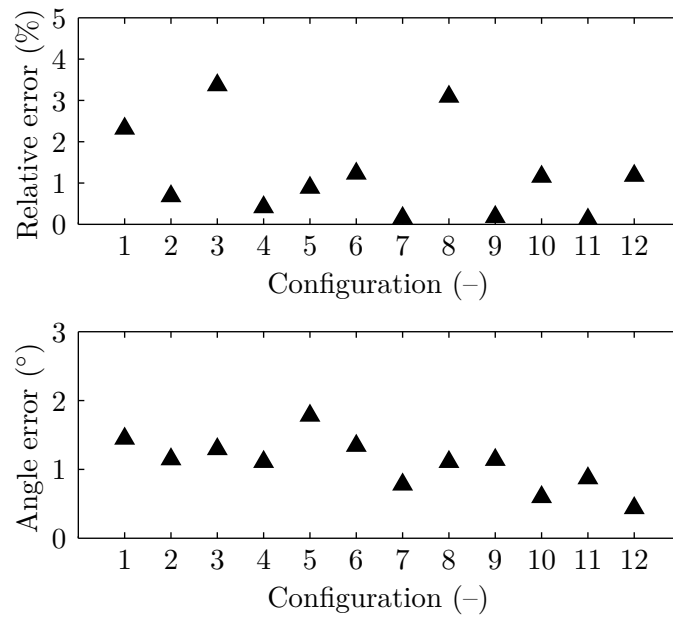


Figure 7.21. Norm and angle errors between reference and simulated forces for FEM validation of force inverse model with discrete rotor.

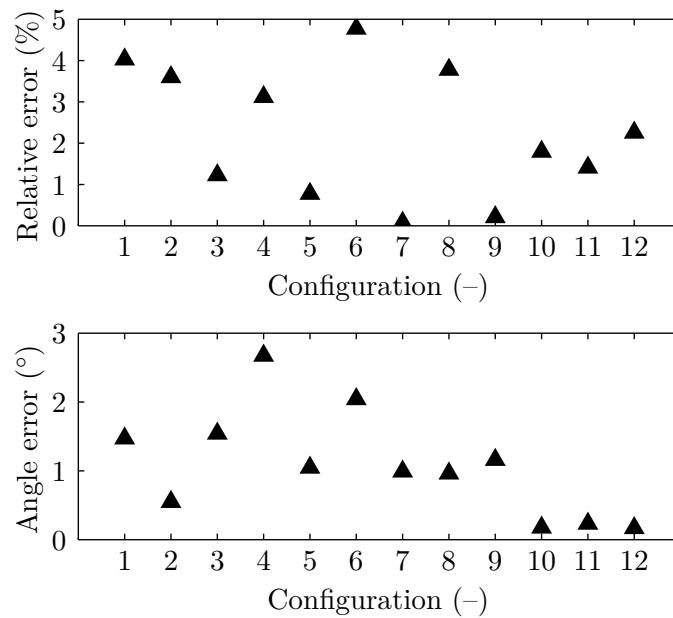


Figure 7.22. Norm and angle errors between reference and simulated torques for FEM validation of torque inverse model with discrete rotor.

Conclusions

In this section numerical FEM simulations have been performed to validate force and torque inverse models and the magnetic state procedure for various randomly-generated rotor orientations and force and torque pairs. As a comparison metrics between reference and simulated force and torque vectors we employed the relative error of the norms and the angle between these vectors.

7.3.4 Experiments with Monoblock Rotor

Introduction

In this section we report force measurements performed using the newly developed monoblock rotor to validate the force inverse model employing magnetic state estimation similarly to activities reported in Section 7.3.2. Note, however, that torque measurements have not been performed in this activity due to constraints in the experimental setup.

Experimental Setup and Procedure

The experimental setup for force measurement is similar to the one presented in Fig. 7.12 in Sec. 7.3.2. Likewise, we verify the ability of producing suitable current vectors to obtain desired forces for the rotor about various orientations about the guiding axis. However, contrary to the previous experiments, where the magnetic flux density was measured at the center of each stator coil \mathbf{P}_1 to \mathbf{P}_9 using an external teslameter, here we will use the embedded magnetic flux density sensors arranged as described in Fig. 7.24 in Section 7.4.2. This is a necessary verification in view of closed-loop experiments that will be presented in Section 7.7. Therefore, for each orientation of the rotor about the guiding axis, which is again described with an angle α , the magnetic flux density is measured and the online procedure in Section 4.2.4 is followed to compute K_F . For each orientation, a set of currents \mathbf{i}_F is computed using the inverse model to produce vertical forces of magnitude 9.81 N.

Results

Measured forces for different values of the proportionality factor k_p and for the rotor about different orientations are reported in Fig. 7.23. As it can be observed, the measured forces are in good agreement with the reference forces.

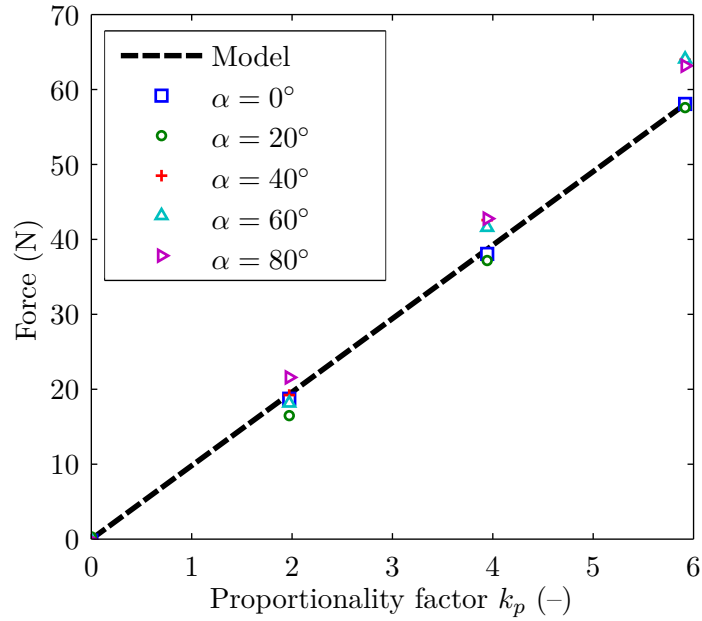


Figure 7.23. Measured forces for different orientations of the rotor and different magnitudes of the current vector. Measurements performed with monoblock rotor.

Conclusions

In this section we validated the force inverse model using the monoblock rotor. In particular, the magnetic state estimation to compute the force characteristic matrix was employed with measurements collected through magnetic flux density sensors embedded in the enclosing stator. This validation is of pivotal importance for closed-loop operation as it will be described in Section 7.7 below.

7.3.5 Conclusions

Force and torque inverse models and the magnetic state estimation procedure for offline (Section 7.3.2) and online (Section 7.3.4) operation have been validated using measurements and FEM simulations. We have shown that we can compute a current vector to generate force and torque reference pairs given any orientation of the rotor. Moreover, the linearity between the applied current vector and generated forces and torques was demonstrated with measurements.

7.4 Magnetic State Estimation

7.4.1 Introduction

In this section we report general results concerning magnetic state estimation and optimal sensor placement developed in Chapter 4. We begin by presenting the Hall sensor arrangement computed using the proposed placement strategy. Then, because both the angular and radial positions of each sensor inside the stator are only known approximately, we propose a model-based calibration procedure relying on multiple measurements of the radial component of the magnetic flux density at multiple rotor orientations. This calibration provides us with the sensor coordinates that best describe the observed data and are computed by minimizing a certain error criterion. Finally, we conclude by showing the reconstructed magnetic flux density about various orientations of the rotor.

7.4.2 Optimal Sensor Placement

The proposed optimal sensor placement strategy is applied to arrange nine magnetic flux density sensors similarly to the illustrative activity in Section 4.3. Here, because of pre-processing constraints, sensors can only be arranged in three different sensors stars. The selected optimal configuration is depicted in Fig. 7.24 and has a condition number $\kappa_2 = 4.06$.

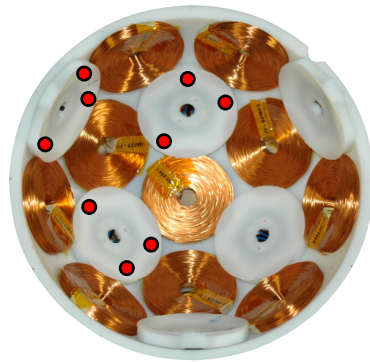


Figure 7.24. Optimal configuration of magnetic flux density sensors after optimization.

7.4.3 Sensor Position Calibration

The experimental setup for the calibration of the angular and radial position of the magnetic flux density sensors is presented in Fig. 7.25. In this setup, the rotor is supported by a rigid guiding axis and is free to rotate about it. The orientation of the rotor about the guiding axis is measured with a magnetic angle sensor. In this setup, magnetic flux density sensors are arranged as described above and depicted in Fig. 7.24. Measurements

7.4. Magnetic State Estimation

are collected by the real-time embedded platform DSpace and recorded manually by the test operator.

Starting from the general expression in (4.3) and (4.4) and taking into account only the fundamental spherical harmonic of degree $n = 3$, the radial component of the magnetic flux density within the airgap for a non-magnetic stator can be formulated as

$$B_{4,r_s}(r_s, \theta_s, \phi_s) = \left(\frac{r_s}{R_{\text{dec}}} \right)^{-5} \sum_{m=-3}^3 c_3^m(\alpha, \beta, \gamma) Y_3^m(\theta_s, \phi_s). \quad (7.7)$$

Therefore, the proposed calibration procedure consists in finding optimal sensor coordinates $\{R_{\text{sens},k}, \varsigma_k\}$, with $\varsigma_k = (\theta_k, \phi_k)$, $k = 1, 2, \dots, N_m$, by solving the following optimization problem

$$\{R_{\text{sens},k}, \varsigma_k\} = \underset{R_{\text{sens},k}, \varsigma_k}{\text{argmin}} \left\| \mathbf{B}_{4,k}^\perp - \hat{\mathbf{B}}_{4,r_s}(R_{\text{sens},k}, \varsigma_k) \right\|_2^2, \quad (7.8)$$

where $\mathbf{B}_{4,k}^\perp$ is a vector containing measurements corresponding to sensor k and collected for various orientations of the rotor, whereas $\hat{\mathbf{B}}_{4,r_s}(R_{\text{sens},k}, \varsigma_k)$ is the measurement model evaluated at the respective rotor orientations where the measurements are taken and parametrized by sensor radial position $R_{\text{sens},k}$ and angular coordinates ς_k . Measurements are performed for angles ranging from 0° to 352.8° with steps of 7.2° for a total of 50 rotor orientations about the guiding axis. The optimization problem is solved for each sensor independently using nonlinear least-squares implemented in the MATLAB[®] function `lsqnonlin`.

Sensor coordinates before and after calibration are summarized in Table 7.4 and 7.5, respectively. Then, the magnetic flux density measurements taken by the nine sensors are compared to the values computed using the developed model with and without calibration in Fig. 7.26

Table 7.4. Coordinates of magnetic flux density sensors before calibration.

	S_1	S_2	S_3	S_4	S_5	S_6	S_7	S_8	S_9
R_{sens} (mm)	95.00	95.00	95.00	95.00	95.00	95.00	95.00	95.00	95.00
θ_s ($^\circ$)	90.0	75.2	99.0	133.7	115.9	106.2	134.9	135.0	164.0
ϕ_s ($^\circ$)	-16.2	-26.8	-44.4	-77.4	-106.4	-90.0	12.8	-12.8	0

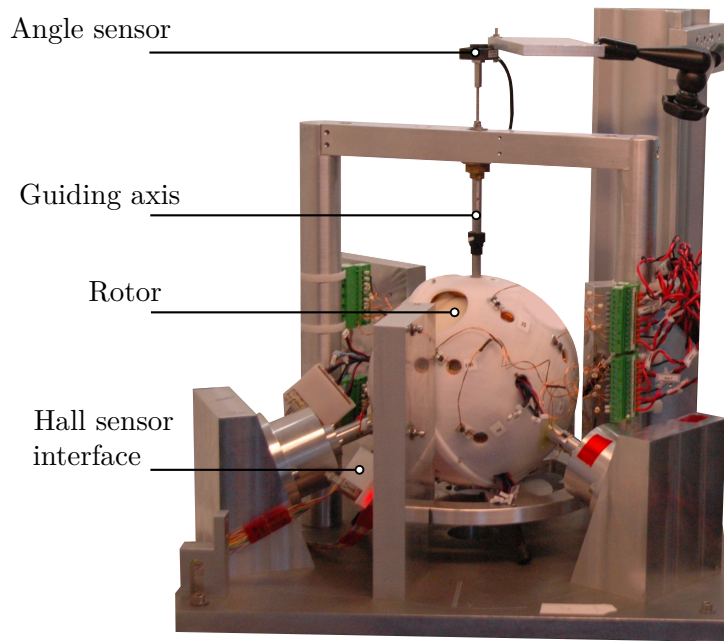


Figure 7.25. Experimental setup for calibration of the angular and radial position of magnetic flux density sensors.

Table 7.5. Coordinates of magnetic flux density sensors after calibration.

	S_1	S_2	S_3	S_4	S_5	S_6	S_7	S_8	S_9
R_{sens} (mm)	94.99	94.98	94.98	94.96	95.11	94.97	94.98	95.00	95.32
θ_s ($^\circ$)	92.7	73.8	101.6	137.9	115.5	105.1	132.6	129.0	167.4
ϕ_s ($^\circ$)	-13.11	-26.2	-46.5	-73.9	-115.1	-88.3	15.4	-16.1	9.2

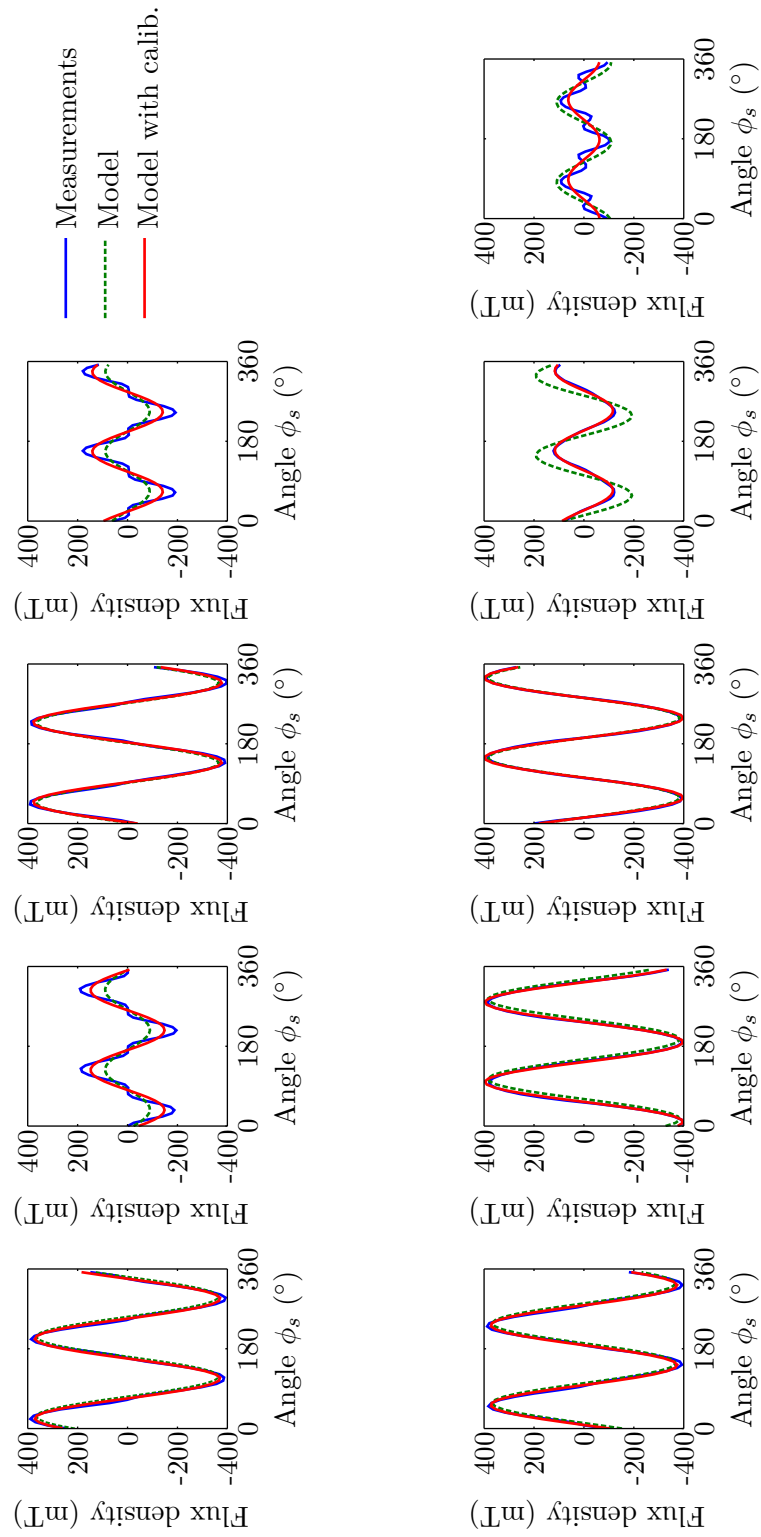


Figure 7.26. Measured magnetic flux density compared to model with and without calibration for various orientations of the rotor about the guiding axis.

7.4.4 Magnetic Flux Density Reconstruction

In this section, starting from the magnetic flux density measurements collected about various orientations of the rotor, spherical harmonics decomposition coefficients c_3^m are estimated using the magnetic state estimation strategy. Then, using the developed magnetic flux density model in (7.7), the radial component of the magnetic flux density can be reconstructed about the entire rotor surface. The reconstructed magnetic flux density for three different rotor orientations is compared to the true magnetic flux density in Fig. 7.27, where the true flux density is computed using (7.7) but with spherical harmonics decomposition coefficients computed by rotating the immobile coefficients.

7.4.5 Conclusions

In this section we have presented general results concerning the magnetic state estimation and the optimal sensor placement procedures. We started by employing the optimal sensor placement strategy to select a set of nine magnetic flux density sensors among all possible sensor locations available on the stator. This arrangement of sensors was used in Section 7.3.4 to validate the force inverse model and will be adopted also in the following sections for rotor angular velocity estimation and closed-loop experiments. Then, we also provided a model-based procedure to calibrate the position of each magnetic flux density sensor. Finally, given measurements of the radial component of the magnetic flux density collected at these nine sensor locations, we have illustrated how the field distribution can be reconstructed on the entire spherical surface.

7.5 Back-EMF and Rotor Angular Velocity Estimation

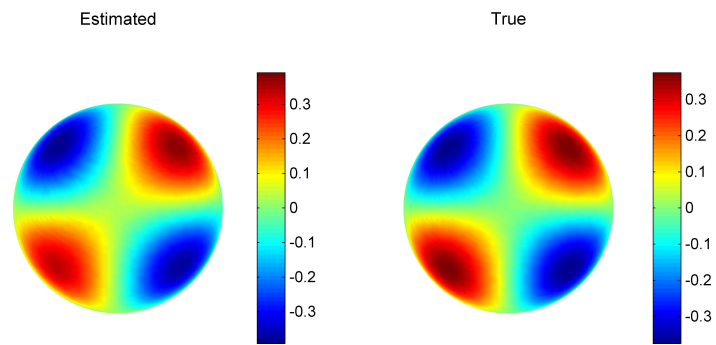
7.5.1 Introduction

In this section we present a preliminary evaluation of the rotor angular velocity estimation technique presented in Chapter 5. Experimental measurements are performed using the monoblock spherical rotor.

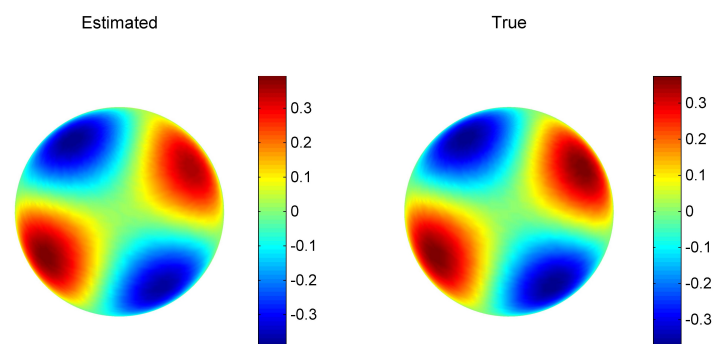
7.5.2 Experimental Setup

The reaction sphere setup used for this activity is similar to the one displayed in Fig. 7.25. In this test setup, the rotor is centered inside the stator with a rigid guiding axis along the gravity direction and it is free to rotate about it. In this framework, the reaction sphere is controlled by a DSpace platform at sampling frequency of 5 kHz. For this experimental validation, the rotor will be accelerated about its guiding axis using the open-loop rotating field proposed in [153]. Nine single-axis Hall sensors are employed to measure the radial component of the magnetic flux density at different locations, which allows computing the

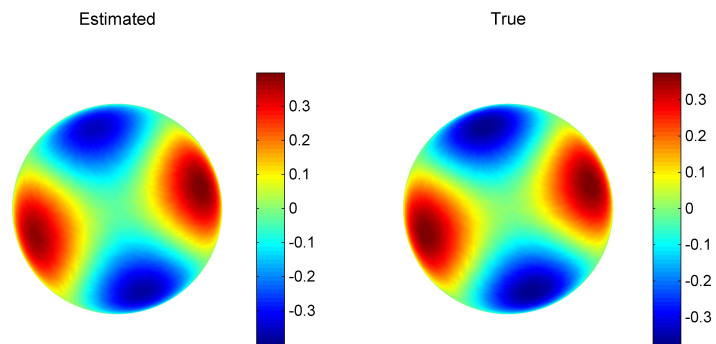
7.5. Back-EMF and Rotor Angular Velocity Estimation



(a) Angle 0° .



(b) Angle 14.4° .



(c) Angle 28.8° .

Figure 7.27. Surface plots of the estimated and true radial component of magnetic flux density about various rotor orientations.

spherical harmonic coefficients c_3^m using least-square techniques developed in Chapter 4, and to compute the torque characteristic matrix K_T at each sample interval. Then, given the estimated coefficients c_3^m , the angular velocity is computed using (5.10), in which \mathbf{u}_{emf} is computed according to (5.20), where derivation is approximated using finite differences.

The estimated angular velocity is affected by rotor magnetic flux density high-order harmonics. Consequently, the derivative acting on coefficients c_3^m in (5.20) has a negative effect on the estimated angular velocity. Therefore, to reduce the error, a low-pass filter is applied to the estimated angular velocity (note that for a fixed rotation axis the estimation error is a periodic function whose average should be closed to the actual angular velocity). A cut-off frequency of 5 rad/s was identified as the lowest possible frequency to avoid perturbing the ADCS, which also requires measurement of the angular velocity.

Since the test bench is currently not equipped with a reference measurement of the angular velocity (the angle sensor is not connected to our real-time platform), the latter will be computed from Hall sensor measurements taking into account that the rotation axis is fixed and the flux density measurements are periodic for a constant angular velocity. As a matter of fact, since the direction of the angular velocity is known, we only need to compute its magnitude, which can be easily computed using zero-crossing techniques on the flux density measurements. Notice, however, that the rotation axis is not taken into account for the validation of the developed algorithm, which is applied identically as presented in Chapter 5.

7.5.3 Results

The measured angular velocity along the guiding axis is compared to the estimated angular velocity in Fig. 7.28. We notice that the estimated values are in agreement with the measured angular velocity. However, the estimated profile undergoes undesired residual oscillations, which result from the approximation of the derivative operation and from residual rotor magnetic flux density high-order harmonics. The measured angular velocity in Fig. 7.28 is computed using zero-crossing techniques on the flux density measurements as illustrated in Fig. 7.29.

7.5.4 Conclusions

We have reported preliminary experimental results to validate the rotor angular velocity estimation technique. This activity serves to complement the FEM simulations in Chapter 5, where the ideal octupole model of the rotor was employed to validate the algorithm. Contrary to the ideal model, here the estimation is affected by high-order harmonics that can partially be suppressed using low-pass filtering. For future

7.5. Back-EMF and Rotor Angular Velocity Estimation

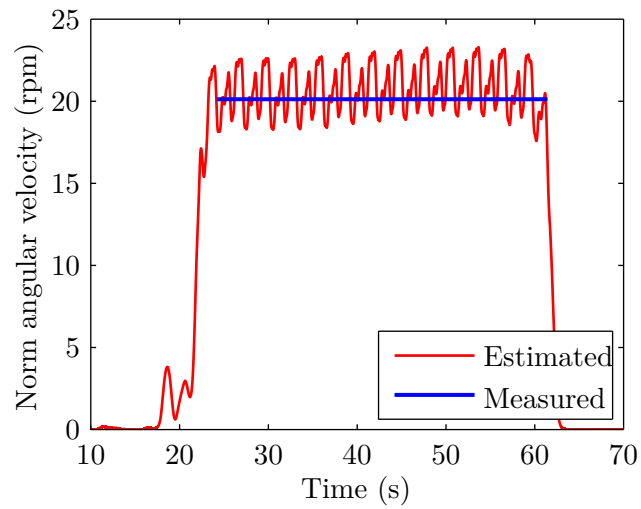


Figure 7.28. Measured angular velocity compared to estimated value.

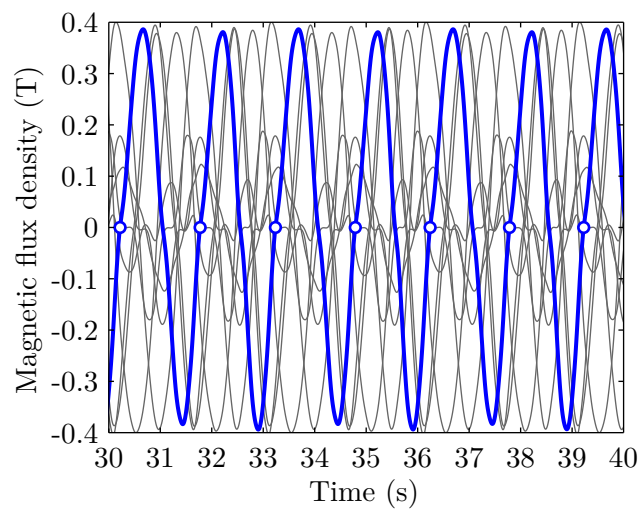


Figure 7.29. Measured magnetic flux density profiles to determine the reference angular velocity using zero-crossing.

investigations, the test bench setup should be equipped with a rotary encoder to provide a reference value of the angular velocity, which in the presented validation has been derived offline from zero-crossing intervals in the measured magnetic flux density profiles.

7.6 Design Optimization of a Spherical Rotor

7.6.1 Introduction

In this section we present experimental results aiming at verifying the FEM characteristics of the manufactured optimized rotor. Specifically, the radial component of the magnetic flux density of the rotor is measured and compared to FEM simulations of the optimized rotor introduced in Chapter 6. Finally, from these measurements, the $B_{r_b}^{\text{RMS}}/m_{\text{rot}}$ ratio and model agreement criterion d are computed and also compared to their expected values given by the optimization.

7.6.2 Experimental Setup and Method

The setup for the rotor magnetic flux density measurement is the same as the one displayed in Fig. 7.1. The rotor is supported by a rigid guiding axis and connected to an AC-electric motor to measure the flux about $\phi_b \in [0^\circ, 360^\circ]$. An axial Hall probe, which can be adjusted on a support plate at 16 inclination angles $\theta = \{15^\circ, 25^\circ, \dots, 165^\circ\}$, measures the radial component of the magnetic flux density. The flux is recorded using a teslameter (MAGNET-PHYSIK FH55) connected to a computer. For each angle θ_b , a total of 600 points equally distributed on the interval $\phi_b \in [0^\circ, 360^\circ]$ are recorded.

The magnetic flux density is measured at $r_b = 89.075 + 0.27 + \Delta r_b$, where $\Delta r_b = \{2 \text{ mm}, 4 \text{ mm}, 6 \text{ mm}, 8 \text{ mm}\}$. Therefore, each sample of the measured radial magnetic flux density of the rotor can be denoted as $B_{r_b, \text{meas}}(\theta_{b,j}, \phi_{b,k})$, with $j = 1, 2, \dots, 16$ and $k = 1, 2, \dots, 600$. In order to evaluate the error between measured $B_{r_b, \text{meas}}(\theta_{b,j}, \phi_{b,k})$ and simulated $B_{r_b, \text{FEM}}(\theta_{b,j}, \phi_{b,k})$ data, similarly to (7.1), we use a MNRE metric defined as

$$\text{MNRE}(\theta_{b,j}) = \frac{1}{600} \sum_{k=1}^{600} |\text{LNRE}(\theta_{b,j}, \phi_{b,k})|, \quad (7.9)$$

where $\text{LNRE}(\theta_{b,j}, \phi_{b,k})$ is the Local Normalized Relative Error (LNRE) defined as

$$\text{LNRE}(\theta_{b,j}, \phi_{b,k}) = \frac{B_{r_b, \text{meas}}(\theta_{b,j}, \phi_{b,k}) - B_{r_b, \text{FEM}}(\theta_{b,j}, \phi_{b,k})}{\max |B_{r_b, \text{FEM}}|}, \quad (7.10)$$

where $\max |B_{r_b, \text{FEM}}|$ is the maximum radial component of the magnetic flux density attained about a rotor pole at $\theta_b = \tan^{-1} \sqrt{2}$ and $\phi_b = 45^\circ$.

7.6.3 Results

The horizontal profiles have been reported in Section 7.2 above and compared to the developed hybrid FEM-analytical model. The MNRE computed using (7.9) at different polar angles and various distances from the rotor is summarized in Table 7.6. As can be read in this table, the MNRE for various polar angles θ_b is always below 1%.

Finally, the global model agreement d resulting from projecting the magnetic flux density measurements on the basis of spherical harmonics and the $B_{r_b}^{\text{RMS}}/m_{\text{rot}}$ ratio are compared with the simulated values in Table 7.7. As observed, both the measured $B_{r_b}^{\text{RMS}}/m_{\text{rot}}$ ratio and the model agreement d are in strong correspondence with the respective simulated values.

Table 7.6. Computed MNRE at different declination angles expressed in (%)

Distance Δr_b (mm)	θ_b ($^\circ$)					
	25	35	45	55	65	75
2	0.4296	0.7210	0.7461	1.0018	0.6792	0.7086
4	0.4493	0.7524	0.8597	0.9880	0.7258	0.6137
6	0.3498	0.7299	0.8481	1.0429	0.6348	0.5864
8	0.3479	0.6620	0.8712	1.0602	0.6993	0.5507

Table 7.7. Simulated and measured $B_{r_b}^{\text{RMS}}/m_{\text{rot}}$ and model agreement d

	FEM	Measured
$B_{r_b}^{\text{RMS}}/m_{\text{rot}}$ (T/kg)	0.0433	0.0447
Model agreement d	0.9901	0.9934

7.6.4 Conclusions

In this section we reported experimental investigations on the optimized monoblock spherical rotor. Specifically, the radial component of the magnetic flux density is measured about horizontal profiles at various polar angles and distances from the rotor surface. As a comparison metric, a MNRE is evaluated showing a good correspondence between measurements performed on the manufactured rotor and expected values computed using FEM simulations. Then, using these measurements we derived the model agreement d and the $B_{r_b}^{\text{RMS}}/m_{\text{rot}}$ ratio showing a strong correspondence with the respective simulated values.

7.7 Closed-loop Levitation and Angular Velocity Control

7.7.1 Introduction

In this section we report results obtained during the first closed-loop experimental validation campaign. The objective of this campaign is to first illustrate the ability of levitating the rotor inside the stator at zero angular velocity and then to rotate it about a given axis. We begin by describing the main control scheme, a strategy to measure the position of the rotor inside the stator, as well as designs of magnetic bearing and angular velocity controllers. Then, we present the experimental setup and discuss a calibration procedure to center the rotor inside the stator. Finally, we report experimental results for the two activities described above and provide a conclusion.

7.7.2 Control Scheme and Design

Control Scheme

A simplified control scheme is presented in Fig. 7.30. The goal of the closed-loop control is to levitate the rotor inside the stator and to rotate it about some desired axis. In this control scheme there are two loops. The first loop controls the rotor position inside the stator (magnetic bearing), and it is based on a state-space controller with displacement velocity estimator. Then, a second loop controls the angular velocity of the rotor. To validate rotation, we initially employed a proportional controller with an angular velocity estimator. The inputs of the magnetic bearing controller are the reference position \mathbf{p}_{ref} (in nominal operation this should correspond to the center of the stator), the estimated rotor position $\hat{\mathbf{p}}$, which is measured according to the method presented below in Section 7.7.2, and the estimated force characteristic matrix K_{F} , which is computed as presented in Chapter 4. The force output \mathbf{F} is subsequently transformed into a vector of currents \mathbf{i}_{F} through the general inverse matrix M_{F} according to the inverse model (3.48). The inputs of the angular velocity controller are the reference $\boldsymbol{\omega}_{\text{ref}}$, the magnetic state $\hat{\mathbf{c}}$, estimated as described in Chapter 4, and the torque characteristics matrix K_{T} . The torque output \mathbf{T} is multiplied with the torque general inverse matrix M_{T} to produce the relative vector of currents \mathbf{i}_{T} , which summed with \mathbf{i}_{F} gives the total control current $\mathbf{i}_{\text{F,T}}$.

7.7. Closed-loop Levitation and Angular Velocity Control

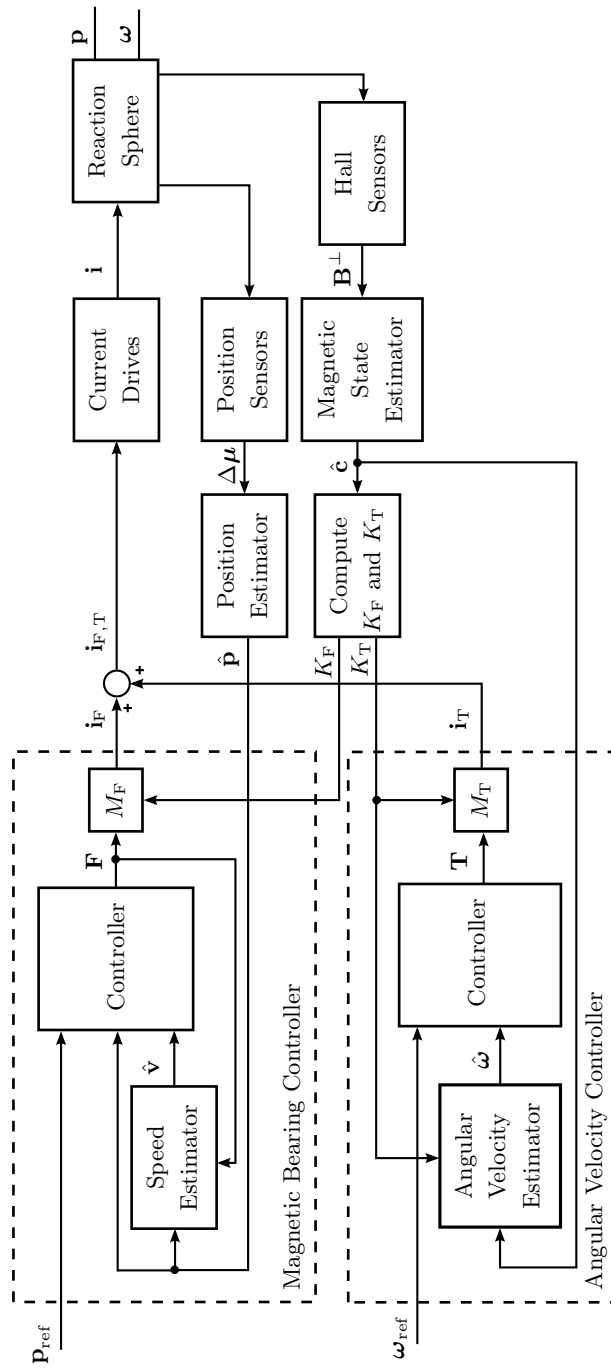


Figure 7.30. Main control scheme for experimental validation.

Rotor Position Measurement

The position of the rotor inside the stator is necessary for closed-loop control. In this section, we present a method to measure the rotor position based on optical linear displacement sensors. To illustrate the process of rotor position measurement, we consider the 2-D schematics in Fig. 7.31. In this figure, the position $\mathbf{p} = [p_{x_s} \ p_{y_s} \ p_{z_s}]^T$ of the sphere is expressed with respect to the orthonormal stator reference frame \mathcal{S} .

To measure the rotor position, we consider a set of three laser displacement sensors (μ Epsilon optoNCDT 2300 LL) placed in a tetrahedral configuration at a distance R_{psens} along \mathbf{P}_a , \mathbf{P}_b , and \mathbf{P}_c , such that $\|\mathbf{P}_i\| = 1$ with $i = a, b, c$.

These sensors measure the distance between a sensor and the rotor surface, which in Fig. 7.31 we express as $\mu_i^0 + \Delta\mu_i$, μ_i^0 being reference measurements corresponding to a centered rotor ($\mathbf{p} = \mathbf{0}$). Then, we can define the distance λ_i as

$$\begin{aligned} \lambda_i &= R_{\text{psens}} - (\mu_i^0 + \Delta\mu_i) \\ &= R_{\text{rot}} + \mu_i^0 - (\mu_i^0 + \Delta\mu_i) \\ &= R_{\text{rot}} - \Delta\mu_i. \end{aligned} \tag{7.11}$$

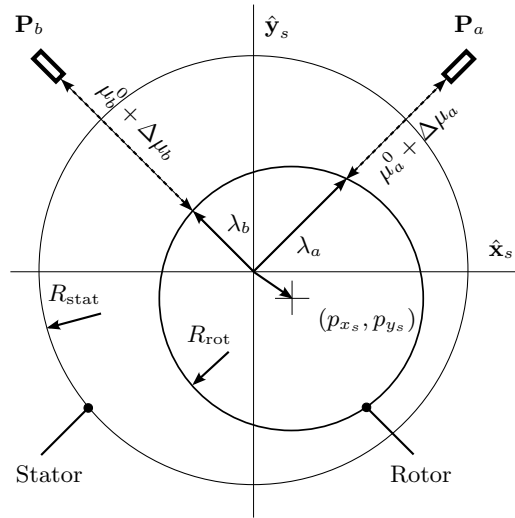


Figure 7.31. Schematic illustration of the rotor position measurement.

Three methods of computing the rotor position \mathbf{p} are proposed and briefly introduced in the following list. The first method is an exact method in the sense that it takes into account the real spherical geometry of the rotor. The remaining methods are approximations.

Method 1 The first method consists in computing the exact center \mathbf{p} of the sphere given

7.7. Closed-loop Levitation and Angular Velocity Control

three points λ_a , λ_b , and λ_c , which can be easily reconstructed from the values $\Delta\mu_a$, $\Delta\mu_b$, and $\Delta\mu_c$ according to (7.11). Therefore, using the equation of a sphere, the center \mathbf{p} is computed by solving the following system of three nonlinear equations

$$(\lambda_i \mathbf{P}_i - \mathbf{p})^\top (\lambda_i \mathbf{P}_i - \mathbf{p}) - R_{\text{rot}}^2 = 0, \quad i = a, b, c. \quad (7.12)$$

The solution of this system of equations can be easily computed using a program of symbolic computation.

Method 2 The second method aims at linearizing the three equations given in method 1 about the origin and solving the resulting linear system. Linearization should be fairly accurate because the feasible displacement of the sphere (airgap) is very little compared to its radius. Therefore, defining

$$F_i(\mathbf{p}) = (\lambda_i \mathbf{P}_i - \mathbf{p})^\top (\lambda_i \mathbf{P}_i - \mathbf{p}) - R_{\text{rot}}^2, \quad i = a, b, c, \quad (7.13)$$

and linearizing it about the origin yields

$$F_i(\mathbf{p}) = F_i(\mathbf{0}) + \frac{\partial F_i}{\partial p_{x_s}}(\mathbf{0}) p_{x_s} + \frac{\partial F_i}{\partial p_{y_s}}(\mathbf{0}) p_{y_s} + \frac{\partial F_i}{\partial p_{z_s}}(\mathbf{0}) p_{z_s}, \quad i = a, b, c, \quad (7.14)$$

whose solution can be expressed in matrix form as

$$\mathbf{p} = \begin{bmatrix} p_{x_s} \\ p_{y_s} \\ p_{z_s} \end{bmatrix} = -\frac{1}{2} \begin{bmatrix} \lambda_a \mathbf{P}_a^\top \\ \lambda_b \mathbf{P}_b^\top \\ \lambda_c \mathbf{P}_c^\top \end{bmatrix}^{-1} \begin{bmatrix} \lambda_a^2 - R_{\text{rot}}^2 \\ \lambda_b^2 - R_{\text{rot}}^2 \\ \lambda_c^2 - R_{\text{rot}}^2 \end{bmatrix}. \quad (7.15)$$

Method 3 In the third method, the center of the rotor \mathbf{p} is projected directly on the three unit-norm axes to retrieve the three sensor readings. This is again motivated by the fact that the feasible displacements of the rotor are small compared to its radius. Therefore,

$$-\begin{bmatrix} \Delta\mu_a \\ \Delta\mu_b \\ \Delta\mu_c \end{bmatrix} = \begin{bmatrix} \mathbf{P}_a^\top \\ \mathbf{P}_b^\top \\ \mathbf{P}_c^\top \end{bmatrix} \mathbf{p} \quad (7.16)$$

and the center of the rotor can be expressed as

$$\mathbf{p} = -\begin{bmatrix} \mathbf{P}_a^\top \\ \mathbf{P}_b^\top \\ \mathbf{P}_c^\top \end{bmatrix}^{-1} \begin{bmatrix} \Delta\mu_a \\ \Delta\mu_b \\ \Delta\mu_c \end{bmatrix}. \quad (7.17)$$

Clearly, the inverse matrix is constant and can be computed offline.

We have performed numerical simulations considering 5000 randomly-generated rotor displacements with maximum norm equal to 1 mm, which is approximately the airgap length. Results show that method 2 has a mean error of approximately $16.9 \pm 8.2 \mu\text{m}$ whereas method 3 has an error of $11.6 \pm 6.3 \mu\text{m}$. Method 1 is error-free because is exact. Considering its computational simplicity and taking into account results of numerical simulations, method 3 was selected for the following experimental activity.

Design of a Magnetic Bearing Controller

To begin with, the dynamic model of the translational motion of the reaction sphere rotor can be described using Newton's law as

$$m_{\text{rot}} \frac{d^2}{dt^2} \mathbf{p} = \mathbf{F} + \mathbf{F}_g, \quad (7.18)$$

where m_{rot} is the mass of the rotor, $\mathbf{p} = [p_{x_s} \ p_{y_s} \ p_{z_s}]^T$ is the rotor position expressed in stator coordinates, \mathbf{F} the electromagnetic force applied to the rotor, and \mathbf{F}_g the force of gravity. The design of the magnetic bearing controller is carried out by considering each of the three axis independently. Define the state vector $[p \ v]^T$, where p and v are the position and velocity of the rotor, respectively, with $p = p_{x_s}$ and $v = v_{x_s}$ if we consider the x_s -axis, $p = p_{y_s}$ and $v = v_{y_s}$ for the y_s -axis, and $p = p_{z_s}$ and $v = v_{z_s}$ if we consider the z_s -axis. Then, the continuous-time second-order state-space model corresponding to the translational motion along any of the three axis can be expressed as

$$\frac{d}{dt} \begin{bmatrix} p \\ v \end{bmatrix} = A_c \begin{bmatrix} p \\ v \end{bmatrix} + B_c F, \quad (7.19)$$

where F is the applied force along the considered axis and

$$A_c = \begin{bmatrix} 0 & 1 \\ 0 & 0 \end{bmatrix}, \quad B_c = \begin{bmatrix} 0 \\ 1/m_{\text{rot}} \end{bmatrix}. \quad (7.20)$$

The corresponding discrete-time state-space model can be expressed as

$$\begin{bmatrix} p_{k+1} \\ v_{k+1} \end{bmatrix} = A_d \begin{bmatrix} p_k \\ v_k \end{bmatrix} + B_d F, \quad (7.21)$$

where

$$A_d = e^{A_c T_s} = \begin{bmatrix} 1 & T_s \\ 0 & 1 \end{bmatrix}, \quad B_d = \left(\int_0^{T_s} e^{A_c \tau} d\tau \right) B_c = \begin{bmatrix} 1/2 T_s^2 / m_{\text{rot}} \\ T_s / m_{\text{rot}} \end{bmatrix}, \quad (7.22)$$

7.7. Closed-loop Levitation and Angular Velocity Control

and T_s is the sampling time. Since only the rotor position can be measured, the output equation becomes

$$y_k = C_d \begin{bmatrix} p_k \\ v_k \end{bmatrix}, \quad (7.23)$$

with

$$C_d = \begin{bmatrix} 1 & 0 \end{bmatrix}. \quad (7.24)$$

The Bode diagram of the transfer function between the force and the position of the state-space model (7.19) is displayed in Fig. 7.33 and corresponds to a double-integrator plant.

Numerous techniques have been proposed to control the rotor position in the literature of active magnetic bearings [92]. PD controllers are among the most common and simplest schemes available to stabilize an active magnetic bearing system [92, 154, 155]. In this case, controller parameters can be selected equivalently to a mass spring damper system. However, to compensate for static disturbances, such as gravity or modeling errors, a Proportional-Integral-Derivative (PID) solution is frequently proposed [87, 92, 154]. In this experimental section, the magnetic bearing controller is based on a state-feedback controller with integral control as depicted in Fig. 7.32. This control architecture is equivalent to a PID scheme. In Fig. 7.32, the controller parameters are the integral gain $K_e \in \mathbb{R}$ and the state-feedback matrix $K_s \in \mathbb{R}^{1 \times 2}$. The speed estimator is a reduced-order observer and will be explained below. Details concerning this kind of controller and observer design can be found in [156, 157]. Controller parameters K_e and K_s are computed so that $\tilde{A}_d - \tilde{B}_d \begin{bmatrix} K_s & K_e \end{bmatrix}$ has poles corresponding to the desired closed-loop dynamics, where

$$\tilde{A}_d = \begin{bmatrix} A_d & 0 \\ -C_d T_s & 0 \end{bmatrix}, \quad \text{and} \quad \tilde{B}_d = \begin{bmatrix} B_d \\ 0 \end{bmatrix}. \quad (7.25)$$

Therefore, two dominant poles are placed to satisfy a generic second-order dynamics specified with natural frequency ω_n and damping ξ . The integral pole is placed so that it does not influence the desired dynamics. Hence, we select the following poles

$$\nu_{1,2} = e^{\left(-\xi\omega_n \pm i\omega_n \sqrt{1-\xi^2}\right)T_s} \quad (7.26)$$

$$\nu_3 = e^{4\text{Re}\left[\left(-\xi\omega_n + i\omega_n \sqrt{1-\xi^2}\right)T_s\right]}. \quad (7.27)$$

In our design, the sampling time is equal to $T_s = 1/f_s$, where $f_s = 3.5$ kHz. The desired closed-loop bandwidth is $f_{cl} = 10$ Hz, thus $\omega_n = 2\pi f_{cl}$. The damping ξ is 0.95.

The discrete-time reduced-order observer estimates the rotor displacement speed given the measured position and applied force. Considering the plant model in (7.21) and

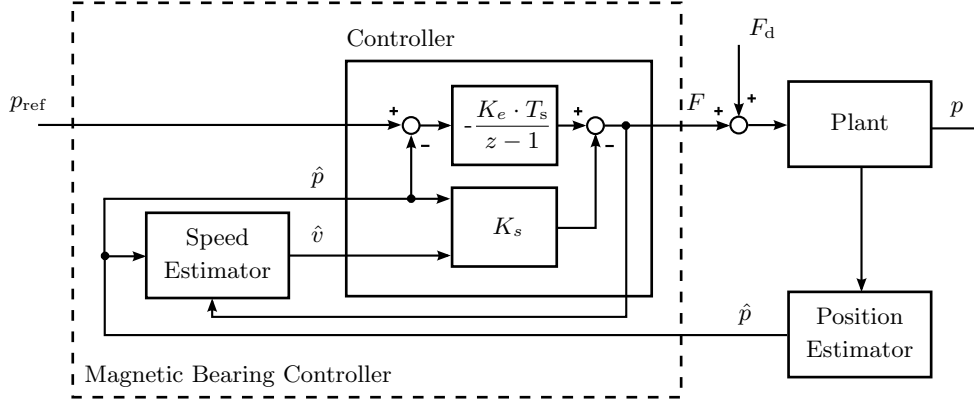


Figure 7.32. Schematic diagram of the magnetic bearing controller.

(7.23), the observer takes the form of

$$\begin{cases} w_{k+1} = (1 - LT_s) w_k + \left(\frac{T_s}{m_{\text{rot}}} - L \frac{1}{2} \frac{T_s^2}{m_{\text{rot}}} \right) F_k + (-L^2 T_s) p_k \\ \hat{v}_k = w_k + L p_k \end{cases} \quad (7.28)$$

where w_k is the state, \hat{v}_k the estimated speed, and $L \in \mathbb{R}$ the observer gain. The observer gain is selected so that its pole is located 1.2 times to the left with respect to the closed-loop plant dynamics (ideally higher than 1.2 but limited by noise). Thus

$$\nu_{\text{redobs}} = e^{1.2 \text{Re} \left[\left(-\xi \omega_n + i \omega_n \sqrt{1 - \xi^2} \right) T_s \right]}. \quad (7.29)$$

Then, the observer gain can be computed as

$$L = \frac{-\nu_{\text{redobs}} + 1}{T_s}. \quad (7.30)$$

In Fig. 7.33 we depict the Bode diagram corresponding to the closed-loop transfer function from reference position p_{ref} to output position p , which also includes the reduced-order observer. Then, the Bode plot of the open-loop transfer function with controller and reduced-order observer is reported in Fig. 7.35. The corresponding gain and phase margins are -15 dB and 47.7° , respectively. Next, the Bode of the dynamic stiffness transfer function is illustrated in Fig. 7.36. The dynamic stiffness is the inverse of the dynamic compliance, which is the transfer function between the disturbance input F_d and output position p [92, 154]. The higher the gain of the dynamic stiffness, the lower the amplification of an external disturbance excitation at a particular frequency becomes [92]. Finally, in Fig. 7.37 we report the step responses of the closed-loop system from the reference input $p_{\text{ref}} = 1$ mm (left) and from the disturbance force $F_d = 1$ N (right) to the output position.

7.7. Closed-loop Levitation and Angular Velocity Control

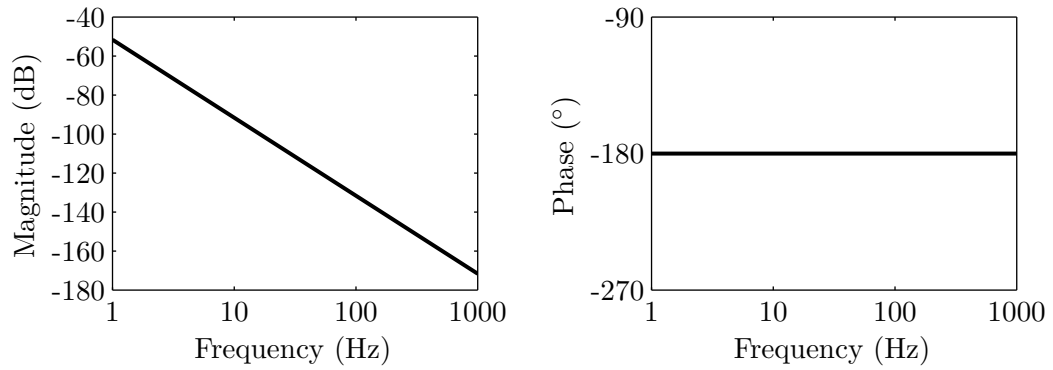


Figure 7.33. Bode plot of the plant.

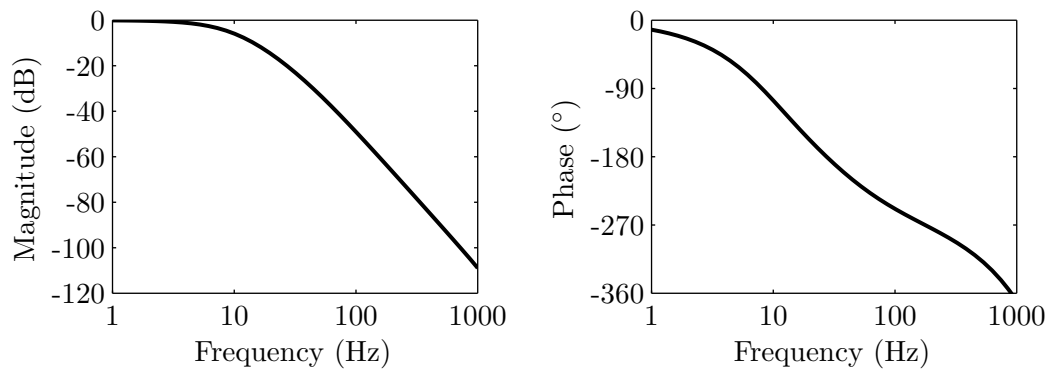


Figure 7.34. Bode plot of closed-loop system with reduced-order observer.

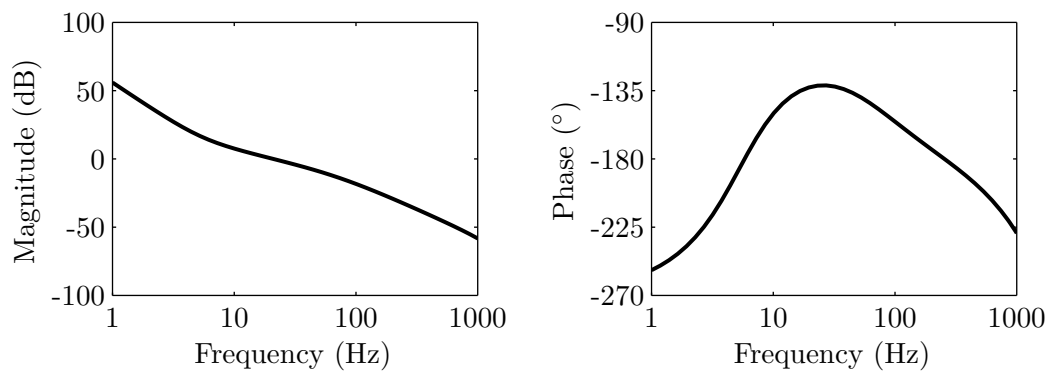


Figure 7.35. Bode plot of open-loop system with reduced-order observer. The gain and phase margins are -15 dB and 47.7° , respectively.

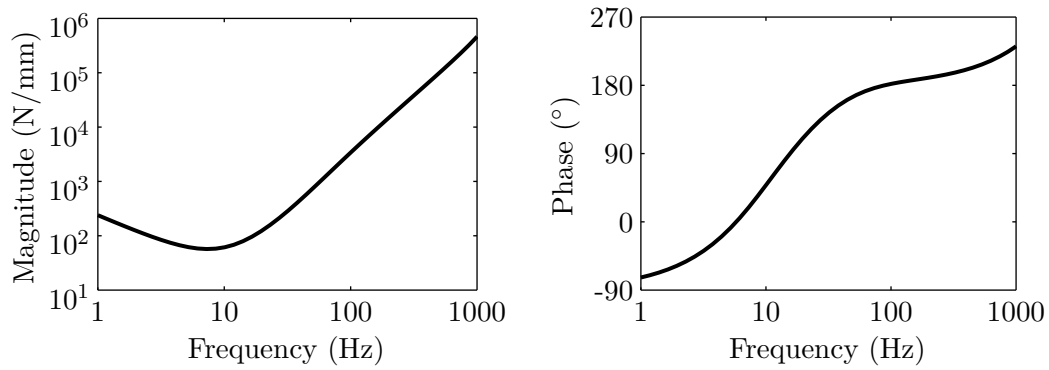


Figure 7.36. Bode plot of closed-loop dynamic stiffness with reduced-order observer.

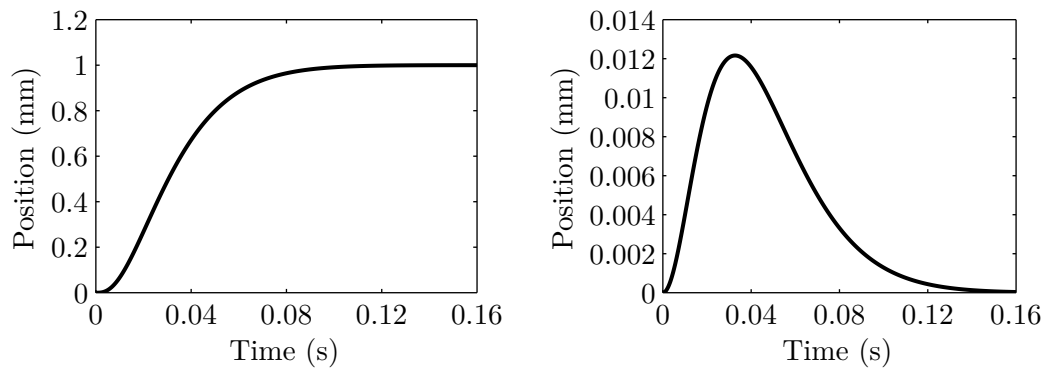


Figure 7.37. (Left) Step response with reference equal to $p_{\text{ref}} = 1$ mm. (Right) Force disturbance rejection with step disturbance force $F_d = 1$ N.

Design of an Angular Velocity Controller

The dynamic model of the rotating rotor was proposed in Section 5.2 and is reported here for convenience

$$J_{\text{rot}} \frac{d}{dt} \boldsymbol{\omega} = \mathbf{T}, \quad (7.31)$$

where J_{rot} is the inertia tensor of the rotor, $\boldsymbol{\omega}$ is the angular velocity of the rotor expressed in stator coordinates, and \mathbf{T} is the torque applied to the rotor. As above, the design of controller will be carried out by considering each of the three axis independently. Then,

$$J \frac{d}{dt} \omega = T, \quad (7.32)$$

where $J = 0.0368 \text{ kg m}^2$ is the inertia of the rotor about the considered axis, ω the angular velocity, and T the torque. The discrete-time open-loop transfer function becomes

$$\frac{\omega(z)}{T(z)} = \frac{T_s/J}{z-1}. \quad (7.33)$$

For illustration, a simple proportional controller is employed to control the angular velocity of the rotor. The closed-loop transfer function is

$$\frac{\omega(z)}{\omega_{\text{ref}}(z)} = \frac{T_s/JK_p}{z - (1 - T_s/JK_p)}. \quad (7.34)$$

For this experiments, we selected $K_p = 4$, which corresponds to a closed-loop bandwidth of approximately 6 Hz.

7.7.3 Experimental Setup

The test bench setup for closed-loop validation is displayed in Fig. 7.38. The test bench is equipped with three optical sensors for position measurements and nine Hall sensors to estimate in real-time the spherical harmonic decomposition coefficients, which are necessary to update force and torque models and to estimate the rotor angular velocity.

For closed-loop position control, the rotor position inside the stator is measured using three optical sensors. As discussed in Section 7.7.2, each optical sensor delivers a relative distance $\Delta\mu_i$ from a programmed zero position μ_i^0 , which should correspond to the center of the stator. Therefore, to program the zero position in each of the three sensors, the rotor has to be positioned precisely at the center of the stator. The rotor centering is a crucial activity as it will have a direct impact on the performance in closed-loop. Ideally, the center of the stator corresponds to the center of the rotor, its center of gravity and its magnetic center. Any error between these four centers will generate undesired vibrations and other negative effects during operation.

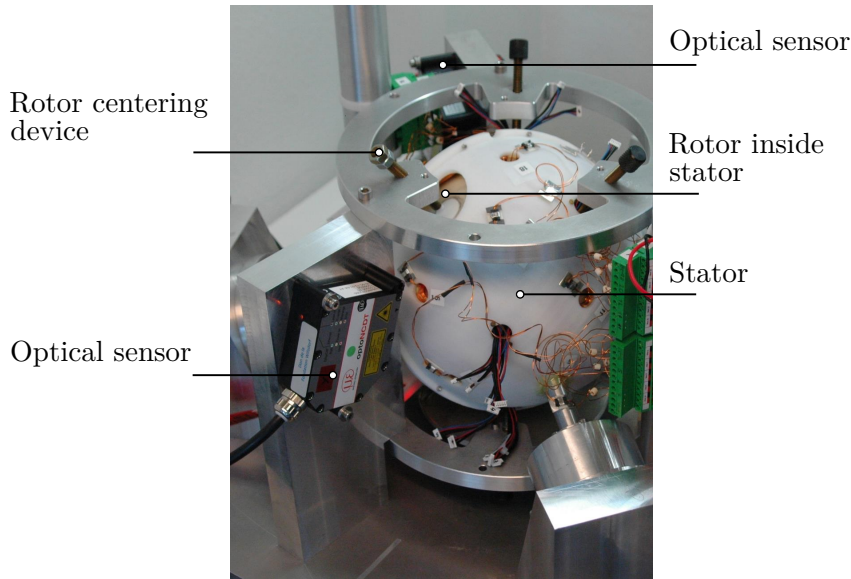


Figure 7.38. Experimental setup for closed-loop magnetic bearing and angular velocity control.

The procedure to perform this activity is briefly described. As depicted in Fig. 7.39, using a coordinate measuring machine (FARO), we collect several measurements on the stator and on the rotor, with respect to a predefined reference system (situated on the test bench). Then, we perform a fitting of a sphere using the points collected from the stator and do the same thing with the points collected from the rotor. These two fittings provide the centers of the spheres with respect to an absolute reference system on the test bench. If the error between the two centers is not satisfactory, the rotor is guided manually through its axis so as to reduce the error and the acquisition of the rotor points is performed again. The process is repeated until a satisfactory result is obtained. Finally, the guiding axis connected to the rotor is removed. Ideally, the stator and rotor centers coincide. However, measurements taken on the sphere allowed us to estimate the stator non-sphericity, which is defined as the maximum variation of its radius, and is approximately 0.50 mm. The non-sphericity of the rotor is 0.28 mm. One consequence of these non-sphericities is that during rotation the rotor center depends on the orientation of the rotor.

7.7.4 Results

Magnetic Bearing at Zero Angular Velocity

The first test consists in levitating the rotor inside the stator at zero angular velocity and subsequently in changing its position by providing position references along the three orthogonal axes. This is certainly something not foreseen during normal operation of the

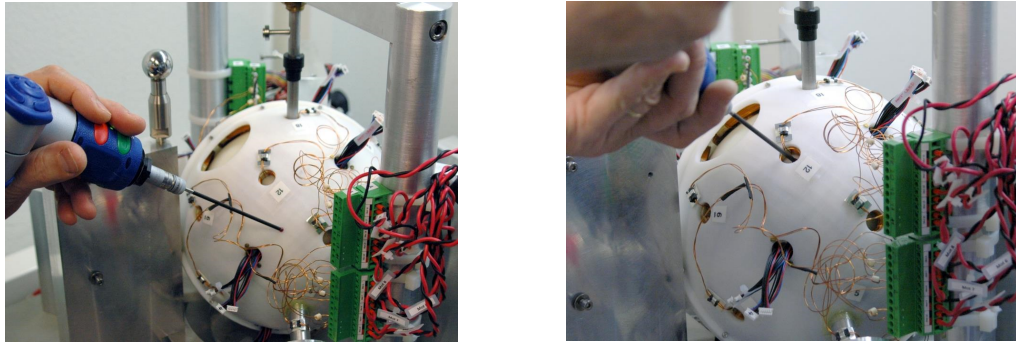


Figure 7.39. Illustration of the rotor centering procedure. (Left) Acquisition of points on the stator. (Right) Acquisition of points on the rotor.

reaction sphere, where the rotor should remain centered inside the stator. However, this activity allows us to verify the magnetic bearing.

The three measured rotor positions as a function of time are reported in Fig. 7.40. Taking into account this figure, the procedure of this test can be summarized in three phases:

1. The rotor is initially supported by the centering devices and its center is located at approximately 0.7 mm below the stator center.
2. At 10 seconds we activate the position closed-loop and from 15 to 30 s we provide a gentle trajectory to bring the rotor to the center. It is important to observe that, because of asymmetries and coupling between force and torque for an uncentered rotor, once the rotor starts levitating it begins to tumble randomly. Therefore, at approximately 25 s we activate the angular velocity loop at 0 rpm, which will maintain the angular velocity near to zero.
3. Once the rotor is immobile we provide references along the three axes (variation of ± 0.7 mm). As we can notice, the measured position and reference are in a good agreement.

The estimated angular velocity as a function of time is depicted in Fig. 7.41. Once again we can observe the random tumbling after levitation between 20 and 30 s and the effect of the angular velocity controller.

Magnetic Bearing and Angular Velocity

The objective of this second test is to levitate the rotor and simultaneously make it rotate about a given axis. The three measured rotor positions as a function of time are reported in Fig. 7.42. The procedure is similar to the one presented above:

1. The rotor is initially located at approximately 0.9 mm below the stator center.

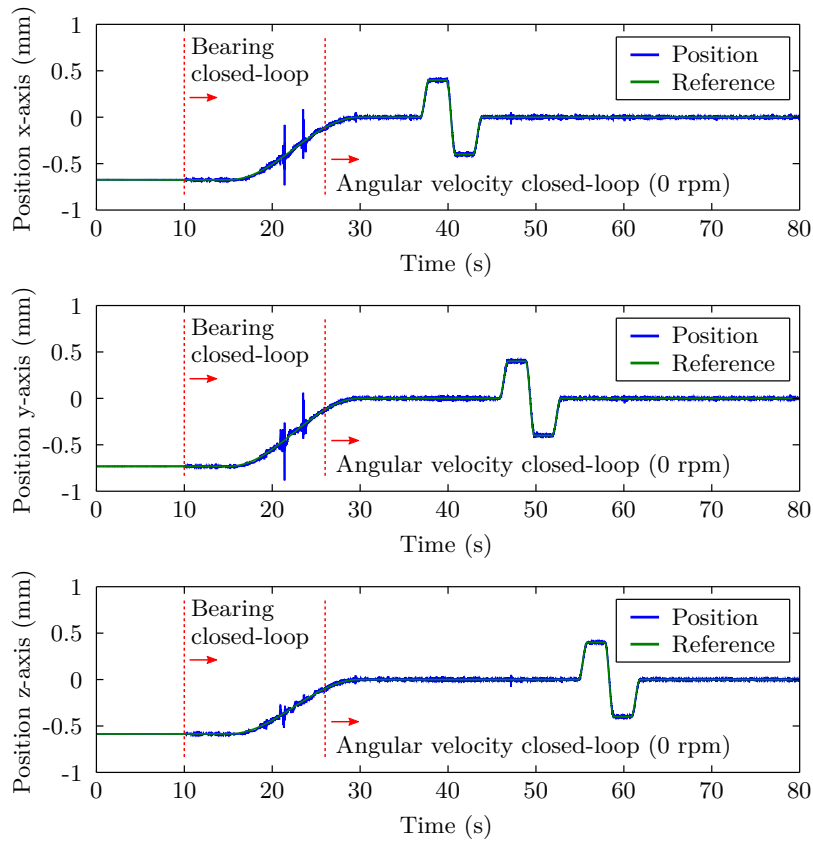


Figure 7.40. Rotor position as a function of time for the magnetic levitation at zero angular velocity.

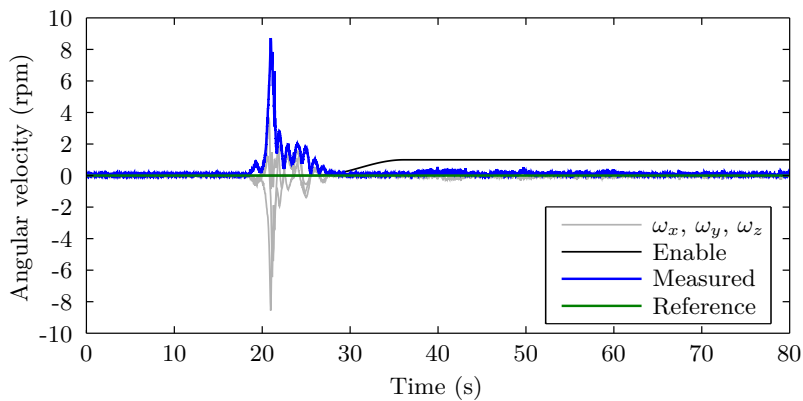


Figure 7.41. Rotor angular velocity as a function of time for the magnetic levitation at zero angular velocity.

7.7. Closed-loop Levitation and Angular Velocity Control

2. At 10 s we activate the position closed-loop and from 15 seconds to 30 s we gently bring the reference to the center of the stator.
3. At 30 s we activate the angular velocity controller at 0 rpm (this stops the random tumbling).
4. Finally, at 50 s we give a reference angular velocity along the vertical axis of 12 rpm.

As we can observe in Fig. 7.42, the magnetic bearing performance is severely affected by rotation. There are several possible sources of this performance degradation:

1. Force and torque errors due to rotor distortion. As we have discussed in previous chapters, high-order harmonics of the magnetic flux density of the rotor, which cannot be taken into account into our estimation procedure due to the limited number of flux density sensors, introduce errors in force and torque models. Moreover, these errors are rotor-orientation-dependent, which means that the position controller has to compensate for them.
2. Rotor non-sphericity, zero position, and mechanical/magnetic unbalance. As we have mentioned above, the rotor and stator are not perfectly spherical. Therefore, during rotation, the center of gravity of the rotor is continuously displaced, which could possibly lead to undesired behavior.
3. Cross-coupling between force and torque when the rotor is not centered. This could be a serious issue although we expect a higher coupling from force to torque than from torque to force (the force-generating currents are higher than torque-generating currents). To clarify this issue, we point out that force and torque models are derived considering a perfectly centered rotor (see Chapter 3). In this condition, we concluded that no coupling occurs between force and torque. In other words, a current vector to generate a torque will not produce any force and vice versa. However, when the rotor is not centered in the stator, this condition is no longer satisfied and a coupling will occur (we do not know the severity of this coupling since there is no analytical model for an uncentered rotor).
4. Test bench alignment problems.
5. Deformation of the stator due to rotor weight.

In Fig. 7.42 we also note that, during rotation, variations of the rotor position are periodic for a constant angular velocity. Adaptive control techniques could be used in future research.

Finally, the rotor estimated angular velocity and the reference angular velocity as a function of time are reported in Fig. 7.43. Similarly to the previous experiment, the

angular velocity is initially equal to 0 rpm. Then, once the rotor start levitating it begins to rotate randomly. The angular velocity goes back to 0 rpm once we activate the controller. Finally, the angular velocity follows the reference up to 12 rpm. It is important to mention that, contrary to the position of the rotor, the angular velocity is not directly measurable but it can only be estimated using flux density sensors. Consequently, the estimated angular velocity using the proposed method is affected by rotor magnetic flux density high-order harmonics. Hence, errors in the estimated angular velocity will automatically be propagated in the loop. As a matter of fact, the estimation of the rotor angular velocity is based on the estimated spherical harmonic coefficients, which in turn are estimated from rotor magnetic flux density measurements. Since the magnetic estimation procedure can only take into account the fundamental harmonic, the estimated spherical harmonic coefficients will be affected by high-order harmonics. The derivative operation acting on these coefficients has a negative effect on the estimated angular velocity. A low-pass filter at approximately 5 rad/s reduces the estimation error (observe that for a fixed rotation axis the estimation error is a periodic function whose average should be closed to the actual angular velocity). In parallel to these efforts, advanced filtering techniques such as the Kalman filtered should be assessed as alternative methods for angular velocity estimation.

7.7.5 Conclusions

Closed-loop tests have been performed. First, we validated the magnetic bearing loop using time-varying position references along the three orthogonal axes. The performance is qualitatively good when the rotor angular velocity is zero. However, we observed that the performance of the bearing deteriorates for non-zero angular velocities. Several possible reasons have been outlined to explain this degradation including force and torque errors due to rotor distortion, rotor non-sphericity and mechanical/magnetic unbalance, cross-coupling between force and torque when the rotor is not centered, test bench alignment problems, and deformations of the stator due to rotor weight.

7.8 Summary

This chapter was dedicated to experimental activities performed using the manufactured prototypes with the aim of validating the developed techniques.

First, we focused on the hybrid FEM-analytical magnetic flux density model and reported measurements and FEM simulations that showed a good correspondence to values computed using the proposed model. The MNRE between experimental and values provided by the proposed model is approximately 6% when only the fundamental harmonic is taken into account. We observed that this error can be reduced below 1% by increasing the number of harmonics taken into account.

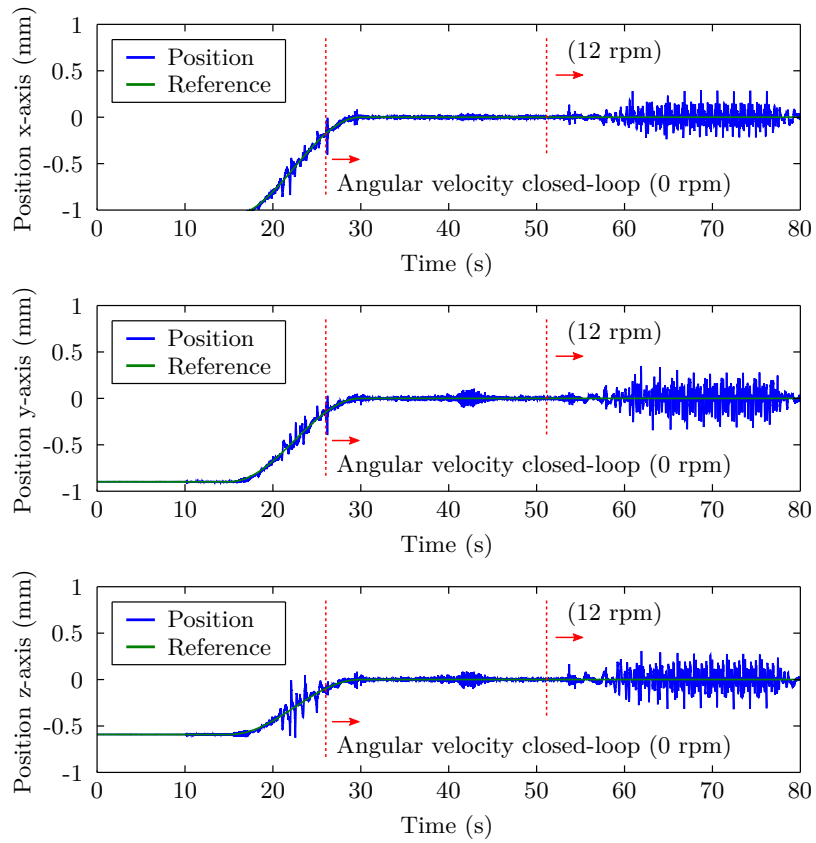


Figure 7.42. Rotor position and position norm as a function of time for the magnetic levitation with rotation.

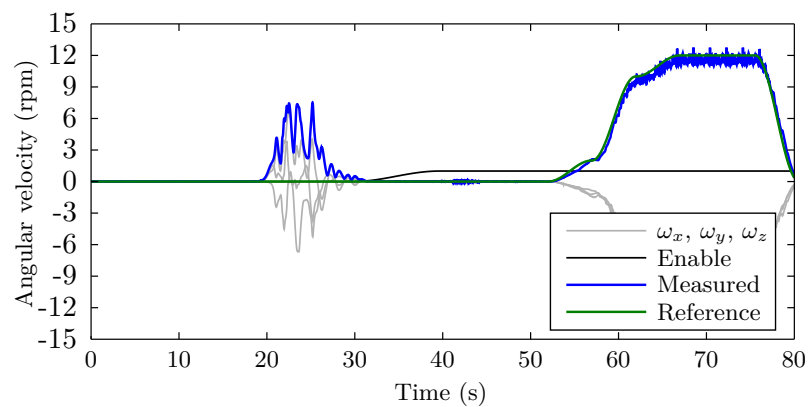


Figure 7.43. Rotor angular velocity as a function of time for the magnetic levitation with rotation.

Second, experimental and simulation activities were performed to validate force and torque inverse models and the magnetic state estimation procedure. Given measurements of the radial component of the magnetic flux density collected at several locations equidistant from the rotor surface, a current vector was computed to generate given force and torque references. Measured forces and torques are in good agreement with their reference values. As expected, we observed that the electrical power necessary to produce a given force or torque varies as a function of the rotor orientation. Moreover, the linearity between the applied current vector and the resulting forces and torques was confirmed by experiments.

Then, we looked at experimental aspects related to magnetic state estimation. Specifically, we introduced a model-based calibration procedure to determine the position of each magnetic flux density sensor, which is initially only approximately known. With these calibrated coordinates and taking into consideration a finite number of measurements only, we illustrated the ability of reconstructing the distribution of the magnetic flux density on the entire spherical surface at a desired distance. Distributions computed using the reconstructing technique were compared to those computed using the analytical method and a good correspondence was observed.

Subsequently, we performed preliminary experimental measurements to examine the algorithm proposed to estimate the angular velocity of the rotor. Although further investigations are required to completely validate this method (e.g. rotations at higher angular velocity), we observed that the proposed algorithm is capable of providing estimated values of the angular velocity. To alleviate the influence of high-order harmonics, low-pass filtering has been applied to the estimated values.

Afterwards, we reported measurements performed using the monoblock rotor recently developed. Specifically, we evaluated the MNRE metric between magnetic flux density values computed using FEM simulations and experimental measurements on the manufactured rotor. The MNRE is below 1 % for all the polar angles and radial distances.

Finally, for illustrative purposes, we performed the first experimental closed-loop measurements using the developed prototype. First, we executed magnetic bearing tests and demonstrated that position of the rotor inside the stator can be controlled adequately. These tests were performed keeping the angular velocity regulated to 0 rpm. Then, with the rotor levitated, rotations of 12 rpm were achieved about an arbitrary axis. During rotation, we observed that the performance of the bearing deteriorates importantly. Possible reasons that have been identified include force and torque errors due to rotor distortion, rotor non-sphericity and mechanical/magnetic unbalance, cross-coupling between force and torque when the rotor is not centered, test bench alignment problems, and deformations of the stator due to rotor weight. We observed that the variation of rotor position during rotations seems to be periodic for a constant angular velocity, which in future research could be addressed with advanced adaptive control techniques.

8 Conclusions

In this final chapter we summarize the main results achieved throughout this thesis and outline our technical and experimental contributions. Finally, we provide a list of possible future directions of research.

8.1 Overview

In this thesis we addressed electromagnetic modeling and control aspects of a reaction sphere actuator for satellite attitude control.

As discussed in the introduction in Chapter 1, reaction spheres are multi-axis momentum exchange devices and consist of a single spherical mass that can be torqued about any direction to provide three-axis attitude control with a unique device. Reaction spheres were firstly proposed in 1960, however, none of the presented designs or concepts have reached the technology readiness level needed for a commercial product, especially due to the complexity of the 3-D motor, the bearing, and its combination.

Although aiming at a different application, we have seen that reaction spheres can be classified under the family of spherical actuators, which are devices studied in robotics and are capable of performing 3-DOF rotational motion in a single joint. Consequently, the study of electromagnetic modeling and control aspects of reaction sphere shares many challenges and related techniques with the spherical actuator literature, to which we believe this thesis was mostly addressed. As a matter of fact, the majority of models and developed solutions can directly be transferred to this field of research.

The reaction sphere studied in this thesis is based on invention [1]. The proposed reaction sphere is a permanent magnet spherical actuator whose rotor is magnetically levitated and can be accelerated about any desired axis. The actuator is composed of an 8-pole

permanent magnet spherical rotor and of a 20-coil stator. Initially, a reaction sphere laboratory prototype was manufactured to validate force and torque analytical models presented in Chapter 3. In this prototype, the eight PM poles of the spherical rotor were discretized using a mosaic of 728 cylindrical magnets to approximate the desired fundamental spherical harmonic. However, closed-loop experiments using this rotor were at that time not possible due to manufacturing issues.

More recently, a new spherical rotor optimized to improve its manufacturability was designed and manufactured. The design optimization was presented in Chapter 6. This monoblock rotor has eight bulk permanent magnet poles with truncated spherical shape that are parallel-magnetized and adjusted on the back-iron structure, which has truncated octahedral shape. Because of the highly complex geometry of this newly manufactured rotor, a pure analytical method to express the magnetic flux density of the rotor was not practicable. For this reason, in Chapter 2 we adopted a hybrid FEM-analytical approach, in which FEM or measured derived values are combined with other boundary conditions on a known analytical structure. Thanks to this approach, high-order spherical harmonics of the rotor can be taken into account in the magnetic flux density, force, and torque models.

One of the most critical aspects of the proposed reaction sphere, and of spherical actuators in general, is that forces and torques depend on the orientation of the rotor inside the stator, which needs to be determined for closed-loop control. In this thesis, rather than using the “mechanical” orientation of the rotor, which generally requires solving a nonlinear and iterative process with possible non-uniqueness and convergence problems, we focused on the “magnetic” orientation and introduced the term “magnetic state”. The magnetic state is a set of spherical harmonic decomposition coefficients that parametrize the magnetic flux density, and thus the force and torque, for any possible orientation of the rotor. More specifically, thanks to spherical harmonic properties under rotation, the magnetic flux density of the rotor can be “decomposed into a direct sum of orthogonal subspaces which are globally invariant under rotation [123]”. Consequently, the magnetic flux density for any possible orientation of the rotor can be expressed as a linear combination between spherical harmonics coefficients (the magnetic state) and spherical harmonic functions. As described in Chapter 4, the proposed method to determine the magnetic state is based on measuring the radial component of the magnetic flux density at multiple locations equidistant from the rotor surface and project them on a basis of spherical harmonic functions. In other words, the proposed method consists in solving the Laplace equation (online) with its general solution expressed as a series of spherical harmonic functions (invariant under rotation) and with boundary conditions expressed using measurements of the radial component of the magnetic flux density. The advantage is that the magnetic estimation procedure is linear and it is expressed in closed-form.

As studied in this thesis, measurement of the rotor angular velocity is necessary for closed-

loop control and it is also required by the ADCS for angular momentum management. A possible solution to determine the angular velocity was proposed in Chapter 5. The underlying idea behind the proposed principle was to exploit the magnetic state of the rotor and avoid computing the rotor “mechanical” orientation. Therefore, the proposed approach is based on determining the angular velocity from the back-EMF voltage induced in the coils, which can be determined using Faraday’s law of electromagnetic induction, in which the time-varying magnetic flux density is parametrized with the magnetic state.

Finally, in Chapter 7 we reported experimental results to validate the proposed techniques and we discussed preliminary experiments of closed-loop magnetic bearing and angular velocity control.

8.2 Summary of Results and Contributions

Main results and contributions of this thesis can be summarized in the following points:

- ***An analytical magnetic flux density model of an eight-pole permanent magnet spherical rotor:*** an analytical model of an eight-pole permanent magnet spherical rotor with ideal octupole magnetization was presented. The novelty consists in exploiting powerful properties of spherical harmonic functions under rotation to express the magnetic scalar potential corresponding to a rotated rotor as an expansion of spherical harmonic functions, in which spherical harmonic decomposition coefficients (the magnetic state) convey to the model all the information relative to the orientation of the rotor. The advantage with respect to traditional models parametrized using the rotor orientation (e.g. Euler angles or quaternions), which generally require solving nonlinear and iterative problems or using bulky external apparatuses, is that these coefficients can be measured using linear techniques and that force and torque characteristic matrices can be expressed in closed-form for any possible orientation of the rotor. These results were published in the IEEE Transactions on Mechatronics [122]. More recently, parametrization of the rotated magnetic flux density using spherical harmonic coefficients was also adopted by our colleagues to develop a model of the eddy currents generated in presence of a ferromagnetic stator. Results were reported in the IEEE Transactions on Magnetics [158].
- ***A Hybrid FEM-analytical magnetic flux density model of an eight-pole permanent magnet spherical rotor with complex geometry:*** this model was proposed to obtain an accurate description of the magnetic flux density distribution of a permanent magnet spherical rotor with complex pole geometry for which an analytical approach is inadequate. The innovation is to combine FEM simulations performed to compute boundary conditions (typically inside the airgap) for the

immobile rotor and spherical harmonic properties under rotation to obtain a generic structure of the flux density distribution, in which spherical harmonic decomposition coefficients carry all the information relative to the orientation of the rotor. The proposed method allows taking into account high-order spherical harmonics of the rotor. Results were presented at the 2013 IEEE Electrical Machines and Drives Conference (IEMDC) [159]. Finally, we point out that the proposed procedure to obtain the magnetic flux density model is also a powerful tool for design optimization. Specifically, for a given potential design, instead of performing a large number of time-consuming FEM simulations to study the effect of rotor distortions on forces and torques, here we only perform one FEM simulation to generate the complete magnetic flux density model and then the force and torque models. Therefore, we can perform numerical simulations using a large number of randomly-generated rotor orientations and evaluate the effect of rotor high-order harmonics on force and torque errors. In this case, we use a reference model in which all the harmonics are taken into account and study the errors with a working model, in which only a subset of harmonics are considered. The advantage is that we can predict the performance of a given design in a shorter time.

- ***Force and torque models for an 8-pole permanent magnet spherical rotor and 20-pole stator with coils:*** force and torque forward/inverse models for the proposed rotor/stator architecture were developed. Thanks to the parametrization of the rotated magnetic flux density with spherical harmonic coefficients, forces and torques for any orientation of the rotor are expressed as a linear combination of force and torque characteristic matrices provided by each spherical harmonic of given degrees and orders (these matrices are computed offline), with the spherical harmonic coefficients delivering to the models all the necessary information relative to the orientation of the rotor (these coefficients can be determined online non-iteratively and in a linear fashion by measuring the radial component of the magnetic flux density from at least seven different locations). Force and torque models are linear and are expressed in closed-form. These results were published in the IEEE Transactions on Mechatronics [122].
- ***A magnetic state estimation as relevant procedure to express the orientation of the rotor inside the stator:*** a procedure to estimate the magnetic state of the rotor was proposed and it is based on measuring the radial component of the magnetic flux density at multiple locations equidistant from the rotor surface to subsequently solve a linear inverse problem using least-squares. Conversely from the estimation of the rotor orientation, the estimation of the magnetic state is linear, it is expressed in closed-form, and it implicitly takes into consideration non-uniqueness of solutions due to the cubic symmetry of the rotor magnetic flux density. The magnetic state corresponding to the ideal ocutpole model can be reconstructed with a minimum of seven measurements that can be collected using single-axis magnetic flux density sensors. The magnetic state estimation procedure

for an ideal octupole magnetization was presented in the IEEE Transactions on Mechatronics [122]. A discussion relative to the influence of high-order harmonics is proposed in [159].

- ***An optimal placement of magnetic flux density sensors:*** we have presented an optimization strategy to position magnetic flux density sensors necessary for magnetic state estimation. The proposed optimization procedure consists in minimizing the condition number related to the linear estimation problem of the coefficients so as to minimize the influence of the measurement noise and high-order harmonics on force and torque relative errors. The proposed placement strategy can be used in the design phase to study the impact of both the number of sensors and their arrangement. Results have been presented at the 2012 International Conference on Electrical Machines (ICEM) [160].
- ***An algorithm to estimate the back-EMF voltage and the rotor angular velocity:*** the proposed algorithm to estimate the back-EMF voltage induced in the coils is based on Faraday's law of electromagnetic induction. Application of the law of electromagnetic induction to compute the back-EMF voltage had already been proposed for example for a brushless DC motor [161]. In this reference, for instance, the time-varying component of the magnetic flux density within the coils is parametrized with the angular velocity of the rotor. In our approach, this method is extended to the case of 3-DOF rotations and the novelty is to parametrize the time-varying component of the magnetic flux density with the magnetic state, which can readily be determined as mentioned above. The proposed approach to determine the back-EMF voltage does not require additional measurements of the coil voltages or actuations. Subsequently, we have shown that the rotor angular velocity can be determined using the energy conservation principle by multiplying the estimated back-EMF voltage vector with the transpose of the torque characteristics matrix, which is a multidimensional equivalence to classical motor theory. Both procedures to determine the back-EMF voltages and the rotor angular velocity are linear and are expressed in closed-form where several components are computed offline. Results will be presented at the 2014 IEEE/ASME International Conference on Advanced Intelligent Mechatronics (AIM) [162].
- ***Optimization of a permanent magnet spherical rotor:*** the design of a new permanent magnetic spherical rotor with eight poles was presented. The optimization was performed using FEM simulations in which several linear and nonlinear simulations have been performed allowing us to obtain a design compliant with the specifications. In order to minimize high-order harmonics, the model agreement criterion d is introduced as a quantitative evaluation of the global distortion of the magnetic flux density with respect to the spherical harmonic of degree three and order two (octupole). These results were presented at the 2012 International Conference on Electrical Machines and Systems (ICEMS) [163] and published in the IEEE Transactions on Industry Applications [164].

- **Algorithms to determine the position of the rotor inside the stator:** methods to determine the rotor position inside the stator were presented based on a set of three optical linear displacement sensors. For instance, in the preferred method, the rotor position is computed in closed-form through a simple change of coordinates, which relates the sensor position expressed in the stator frame and measurements provided by the three optical sensors (the change of coordinates is a matrix multiplication and the matrix is computed offline).
- **Closed-loop experimental validation:** using dedicated dynamic controllers for the magnetic bearing and the angular velocity, we showed that the rotor can simultaneously be levitated and rotated about a given axis in closed-loop. To the best of our knowledge, there is no evidence of closed-loop magnetic bearing and rotation in the PM-based spherical actuator literature. Results have been submitted to the IEEE Transactions on Mechatronics [165].
- **Numerical FEM simulations of spherical actuators:** FEM simulations have been extremely useful to validate the developed methods and to design the new spherical rotor. To this end, we first created a 3-D simulation model of the discrete rotor, which consists of a pavement of 728 permanent cylindrical magnets fixed to an iron sphere and a set of 20 coils. Then, for design optimization we developed also the 3-D simulation model of the monolock rotor. Results were presented at the 2011 and 2013 COMSOL conferences [166, 167].

8.3 Research Perspectives

In this thesis we touched several aspects related to modeling and control of the reaction sphere actuator. These opened new possibilities of future research among which we identify the the following list.

- **Force and torque inverse models:** force and torque inverse models have been presented in Chapter 3. Considering the force only, the current vector \mathbf{i} to satisfy a given reference force \mathbf{F} can be computed as (see equation 3.48)

$$\mathbf{i} = M_{\mathbf{F}} \mathbf{F} \quad (8.1)$$

where

$$M_{\mathbf{F}} = K_{\mathbf{F}}^{\top} (K_{\mathbf{F}} K_{\mathbf{F}}^{\top})^{-1}. \quad (8.2)$$

Considering the fundamental harmonic only, force and torque characteristic matrix in (8.2) can be computed as (see equation (8.3))

$$K_{\mathbf{F}} = \sum_{m=-3}^3 c_3^m(\alpha, \beta, \gamma) K_{\mathbf{F},3}^m. \quad (8.3)$$

Therefore, to compute \mathbf{i} , a 3×3 matrix inversion is required in (8.2) at each iteration. It would be interesting to study the possibility of avoiding this matrix inversion by looking at alternative structures, for instance,

$$\mathbf{i} = \sum_{m=-3}^3 f(c_3^m(\alpha, \beta, \gamma)) \tilde{M}_{F,3}^m \mathbf{F}, \quad (8.4)$$

where $f(\cdot)$ is a generic (possibly simple) function and $\tilde{M}_{F,3}^m$ are matrices computed offline.

- ***Design of advanced controllers for magnetic bearing and angular velocity:*** presently, closed-loop magnetic bearing is achieved with a state-feedback controller in combination with an integral compensation. Control of the angular velocity is performed with a proportional controller. As we have observed, magnetic bearing performances deteriorate significantly for non-zero angular velocities. We noticed that variation of the rotor position during rotations seems to be periodic for a constant angular velocity. As mentioned, among the various reasons for this behavior, we identified force and torque errors due to rotor distortion, rotor non-sphericity, and mechanical/magnetic unbalance. Therefore, in future research these challenges could be addressed with advanced adaptive control techniques in a way to automatically adapt the model/controller online using closed-loop measured values. Moreover, vibrations could be minimized by intelligently filtering actuations to avoid changing the position of the center of gravity due to rotor mechanical and magnetic non-sphericity [11, 12, 92].
- ***Extended Kalman filter framework:*** in this thesis we have presented non-iterative models to estimate the magnetic state and the angular velocity of the rotor. These methods have the advantage of being computationally simple and straightforwardly implementable in real-time. An alternative and powerful approach for estimation of the magnetic state, the rotor angular velocity, and possibly the rotor position is based on the EKF, which is a recursive state estimator for nonlinear processes and does not require differentiation of the measurements [140]. In parallel to the work presented in this thesis, some preliminary work was performed to introduce the EKF as a control framework for the reaction sphere. In one of the proposed structures, the EKF is based on the following nonlinear state space differential equation

$$\begin{aligned} \frac{d}{dt} \boldsymbol{\omega} &= J_{\text{rot}}^{-1} (g \mathbf{T}_c + \mathbf{w}) \\ \frac{d}{dt} \mathbf{q} &= \frac{1}{2} \Omega \mathbf{q} \\ \frac{d}{dt} g &= 0, \end{aligned}$$

where $\boldsymbol{\omega}$ is the angular velocity, J_{rot} is the rotor tensor of inertia, \mathbf{q} is the quaternion vector corresponding to the orientation of the rotor, \mathbf{T}_c is the command torque, \mathbf{w} is the process noise vector, and the matrix Ω is given by

$$\Omega = \begin{bmatrix} 0 & -\omega_x & -\omega_y & -\omega_z \\ \omega_x & 0 & \omega_z & -\omega_y \\ \omega_y & -\omega_z & 0 & \omega_x \\ \omega_z & \omega_y & -\omega_x & 0 \end{bmatrix}.$$

An additional state variable g is included in this model to partially overcome the fact that the difference between the torque generated and the command torque $\mathbf{T} - \mathbf{T}_c$ does not have zero mean. The measurement equation is given by

$$\mathbf{z} = h_3(\mathbf{q}) + \mathbf{v},$$

where $h_3(\cdot)$ is a function relating rotor orientation to measurements and takes into account only the fundamental spherical harmonic of degree 3. Finally, \mathbf{v} is the output noise vector. The noise vector \mathbf{v} represents the measurement noise of the sensors, which is probably white and therefore well filtered by the EKF, and the noise produced by unmodeled high-order harmonics of the rotor. One attractive approach proposed to reduce the negative influence of unmodeled high-order harmonics is to use a covariance matrix in the EKF measurement update that is expressed as the difference between the estimated sensor output, which is computed taking into account high-order harmonics starting from the estimated quaternion, and the estimated output taking into account the fundamental harmonic only. Although not consistent with the definition of the noise covariance matrix (defined for white noise), this method allows “weighting” the measurements in a smart way. Some preliminary simulations show the stability of this method.

- ***Rotor position determination with magnetic flux density measurements:*** in this thesis we proposed to measure the rotor position using three optical displacement sensors. This approach is computationally simple and the theoretical accuracy seems adequate. However, the proposed measurement procedure relies on the assumption that the rotor is perfectly spherical, which is not the case in practice. The consequence of rotor non-sphericity are orientation-dependent measurement errors, which may have a dramatic impact on the magnetic bearing performance. One highly challenging alternative is to measure the rotor position using magnetic flux density sensors, which are already necessary to determine the magnetic state. The complexity of this approach lies on the fact that the relation between the radial component of the magnetic flux density measured at a given point and the position of the rotor depends on the orientation of the latter. Therefore, to process flux density measurements for position determination one has to first compute the rotor orientation (the EKF above is a possible solution). Finally, errors related to rotor

orientation measurement are propagated in the magnetic bearing loop introducing unwanted couplings.

- ***Force/torque coupling for uncentered rotor:*** in Chapter 3 we showed that if the rotor is perfectly centered inside the stator then force and torque are uncoupled, allowing us to control magnetic bearing and angular velocity independently. This assumption is based on the fact that, in nominal operation, the magnetic bearing loop maintains the rotor centered. However, in the experimental chapter we stated that coupling between forces and torques is among the possible reasons of magnetic bearing performance degradation during rotation. Hence, a possible future activity is to perform a quantitative evaluation of this coupling between currents generating forces and currents generating torques. To this end, FEM simulations could be used. Coupling between forces and torques is a particularly important aspect for on-earth performance validation of the reaction sphere. As a matter of fact, on earth, the currents necessary to levitate the rotor are significantly higher than those requested to produce a given torque for precise attitude control. Consequently, for an uncentered rotor, the current generating forces (magnetic bearing) are going to influence negatively the torque production. A possible solution to counteract this limitation is to employ hydrostatic bearing to partially compensate for the weight of the rotor in presence of gravity.

A Spherical Harmonics

A.1 Introduction

Spherical harmonics are a frequency-space basis for representing functions defined over the sphere. They are the spherical analogue of the 1-D Fourier series [168].

Spherical harmonics are important in a variety of theoretical and practical applications including computational chemistry [124], quantum mechanics, where they are used to model the electron configuration in atoms and to model quantum angular momentum [168–170], and geomagnetics, where they appear to model magnetic field of the earth as well as other planetary bodies [171]. Spherical harmonics are also widely employed in 3-D computer graphics for example in interactive graphics and lighting [168, 169, 172], image registration [123, 173, 174], and surface parameterization [127, 175], which include several applications in biomedical imaging [131, 176–179] and signal processing [128]. The authors of these references make an extensive use of spherical harmonics properties under rotation, which represent an essential instrument for the development of the magnetic flux density model in Chapter 2. Finally, in the spherical actuators literature, as mentioned in Section 2.1, spherical harmonics characterize the angular portion of the solution to Laplace’s equations, which result from Maxwell’s equations [50, 52, 55, 58, 71, 72, 75, 76, 93–97, 180].

In this Appendix, we briefly discuss the spherical harmonics and introduce several important properties for the thesis.

A.2 Definition

Let (θ, ϕ) be spherical coordinates and $\eta(\theta, \phi) = (\cos \phi \sin \theta, \sin \phi \sin \theta, \cos \theta)$ a point on the 2-D unit sphere. Then, $\theta \in [0, \pi]$ is the polar angle, which is the angle between the z -axis and the vector corresponding to η ; $\phi \in [0, 2\pi]$ is the azimuthal angle and is defined

Appendix A. Spherical Harmonics

as the angle between the positive x -axis and the projection of η onto the x - y plane. Then, for any integer $n \geq 0$ and integer m , with $|m| \leq n$, the complex-valued spherical harmonic of degree n and order $m \geq 0$ is defined in spherical coordinates (θ, ϕ) as [181]

$$Y_n^m(\theta, \phi) = K_n^m P_n^m(\cos \theta) e^{im\phi}, \quad (\text{A.1})$$

where K_n^m are normalization constants

$$K_n^m = \left[\frac{(2n+1)(n-m)!}{4\pi(n+m)!} \right]^{1/2}, \quad (\text{A.2})$$

and $P_n^m(x)$ are the associated Legendre polynomials defined as [181]

$$P_n^m(x) = (1-x^2)^{m/2} \frac{d^m}{dx^m} P_n(x) \quad (\text{A.3})$$

$$= \frac{(-1)^m}{2^n n!} (1-x^2)^{m/2} \frac{d^{n+m}}{dx^{n+m}} [(x^2-1)^n]. \quad (\text{A.4})$$

In expression (A.3), $P_n(x)$ are Legendre polynomials, and are defined using Rordigues formula as [181]

$$P_n(x) = \frac{1}{2^n n!} \frac{d^n}{dx^n} [(x^2-1)^n]. \quad (\text{A.5})$$

A numerically robust evaluation of these polynomials can be obtained through a set of recurrence relations [168, 172]. The degree n determines the frequency band of the basis functions over the sphere. Each band is equivalent to polynomials of that degree and there are $2n+1$ functions in a given band [168, 169]. For $m < 0$, spherical harmonics are expressed as [181]

$$Y_n^{-m}(\theta, \phi) = (-1)^m \overline{Y_n^m(\theta, \phi)}, \quad (\text{A.6})$$

where $\overline{Y_n^m(\theta, \phi)}$ is the complex conjugate of $Y_n^m(\theta, \phi)$.

Spherical harmonics of degree $n = 3$, whose relevance is pivotal in the proposed reaction sphere models, are summarized in Table A.1 in both spherical and Cartesian coordinates.

Spherical harmonics are complex-valued functions and, as will be seen in the following section, provide a complete basis of orthonormal functions over the sphere. In the 3-D computer graphics literature, authors have adopted real-valued spherical harmonics, which are defined as [124, 168, 172]

$$y_n^m(\theta, \phi) = \begin{cases} [Y_n^m(\theta, \phi) + (-1)^m Y_n^{-m}(\theta, \phi)]/\sqrt{2}, & \text{if } m > 0, \\ Y_n^0(\theta, \phi), & \text{if } m = 0, \\ -i[Y_n^{|m|}(\theta, \phi) - (-1)^m Y_n^{-|m|}(\theta, \phi)]/\sqrt{2}, & \text{if } m < 0, \end{cases} \quad (\text{A.7})$$

$$= \begin{cases} \sqrt{2} \text{Re} \{Y_n^m(\theta, \phi)\}, & \text{if } m > 0, \\ Y_n^0(\theta, \phi), & \text{if } m = 0, \\ \sqrt{2} \text{Im} \{Y_n^m(\theta, \phi)\}, & \text{if } m < 0. \end{cases} \quad (\text{A.8})$$

Table A.1. Spherical harmonics of degree $n = 3$ in spherical and Cartesian coordinates.

	Spherical	Cartesian
$Y_3^{-3}(\theta, \phi)$	$\frac{1}{8} \sqrt{\frac{35}{\pi}} e^{-3i\phi} \sin^3 \theta$	$\frac{1}{8} \sqrt{\frac{35}{\pi}} \frac{(x - iy)^3}{r^3}$
$Y_3^{-2}(\theta, \phi)$	$\frac{1}{4} \sqrt{\frac{105}{2\pi}} e^{-2i\phi} \sin^2 \theta \cos \theta$	$\frac{1}{4} \sqrt{\frac{105}{2\pi}} \frac{(x - iy)^2 z}{r^3}$
$Y_3^{-1}(\theta, \phi)$	$\frac{1}{8} \sqrt{\frac{21}{\pi}} e^{-i\phi} \sin \theta (5 \cos^2 \theta - 1)$	$\frac{1}{8} \sqrt{\frac{21}{\pi}} \frac{(x - iy) (4z^2 - x^2 - y^2)}{r^3}$
$Y_3^0(\theta, \phi)$	$\frac{1}{4} \sqrt{\frac{7}{\pi}} (5 \cos^3 \theta - 3 \cos \theta)$	$\frac{1}{4} \sqrt{\frac{7}{\pi}} \frac{z (2z^2 - 3x^2 - 3y^2)}{r^3}$
$Y_3^1(\theta, \phi)$	$\frac{-1}{8} \sqrt{\frac{21}{\pi}} e^{i\phi} \sin \theta (5 \cos^2 \theta - 1)$	$\frac{-1}{8} \sqrt{\frac{21}{\pi}} \frac{(x + iy) (4z^2 - x^2 - y^2)}{r^3}$
$Y_3^2(\theta, \phi)$	$\frac{1}{4} \sqrt{\frac{105}{2\pi}} e^{2i\phi} \sin^2 \theta \cos \theta$	$\frac{1}{4} \sqrt{\frac{105}{2\pi}} \frac{(x + iy)^2 z}{r^3}$
$Y_3^3(\theta, \phi)$	$\frac{-1}{8} \sqrt{\frac{35}{\pi}} e^{3i\phi} \sin^3 \theta$	$\frac{-1}{8} \sqrt{\frac{35}{\pi}} \frac{(x + iy)^3}{r^3}$

Real-valued spherical harmonics from degree $n = 0$ to degree $n = 3$ are displayed in Fig. A.1. However, even though in this thesis we are concerned with real-valued functions, complex-valued spherical harmonics will be employed in accordance to the magnetic community [106, 180] and the literature of spherical actuators (see references in the introduction of this section). After all, as can be read in (A.7), real-valued spherical harmonics are expressed as linear combinations of complex-valued harmonics.

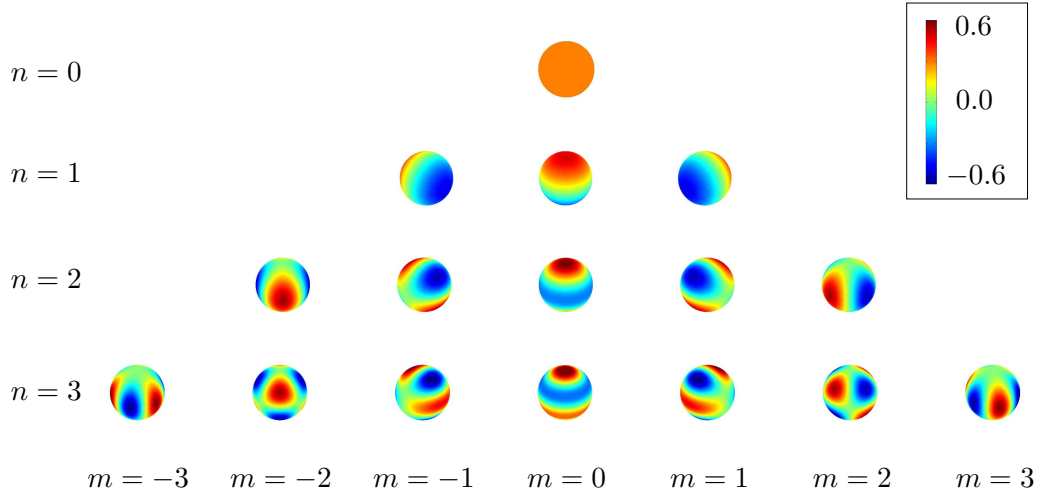


Figure A.1. Real-valued spherical harmonics from degree $n = 0$ to degree $n = 3$.

A.3 Properties

A.3.1 Orthonormality

Spherical harmonics $Y_n^m(\theta, \phi)$ are orthogonal for different n and m on the 2-D unit sphere. Therefore [181],

$$\int_0^\pi \int_0^{2\pi} Y_n^m(\theta, \phi) \overline{Y_k^j(\theta, \phi)} \sin \theta \, d\theta \, d\phi = \begin{cases} 1, & n = k, m = j, \\ 0, & \text{otherwise.} \end{cases} \quad (\text{A.9})$$

A.3.2 Projection and Expansion/Reconstruction

Spherical harmonics define a complete basis of orthonormal functions over the sphere. Hence, any suitable function f defined over the sphere can be expanded in a spherical harmonics series of the form [181]

$$f(\theta, \phi) = \sum_{n=0}^{\infty} \sum_{m=-n}^n c_{n,\text{imm}}^m Y_n^m(\theta, \phi), \quad (\text{A.10})$$

where the coefficients $c_{n,\text{imm}}^m$ of expansions are calculated by projecting the function f onto each basis function $Y_n^m(\theta, \phi)$ as

$$c_{n,\text{imm}}^m = \int_0^{2\pi} \int_0^\pi f(\theta, \phi) \overline{Y_n^m(\theta, \phi)} \sin \theta \, d\theta \, d\phi. \quad (\text{A.11})$$

Notice that if f is a real function, then $c_{n,\text{imm}}^{-m} = (-1)^m \overline{c_{n,\text{imm}}^m}$. As a matter of fact [125],

$$\begin{aligned} c_{n,\text{imm}}^{-m} &= \int_0^{2\pi} \int_0^\pi f(\theta, \phi) \overline{Y_n^{-m}(\theta, \phi)} \sin \theta \, d\theta \, d\phi \\ &= \int_0^{2\pi} \int_0^\pi f(\theta, \phi) [(-1)^m Y_n^m(\theta, \phi)] \sin \theta \, d\theta \, d\phi \\ &= (-1)^m \overline{\int_0^{2\pi} \int_0^\pi f(\theta, \phi) Y_n^m(\theta, \phi) \sin \theta \, d\theta \, d\phi} \\ &= (-1)^m \overline{\int_0^{2\pi} \int_0^\pi f(\theta, \phi) \overline{Y_n^m(\theta, \phi)} \sin \theta \, d\theta \, d\phi} \\ &= (-1)^m \overline{c_{n,\text{imm}}^m}. \end{aligned} \quad (\text{A.12})$$

Equivalently to Fourier series, expansion in (A.10) is exact as long as n goes to infinity. However, by limiting the number of bands to $n = N_h - 1$, we obtain the N_h -th order band-limited approximation \tilde{f} of the original function f as [168]

$$\tilde{f}(\theta, \phi) = \sum_{n=0}^{N_h-1} \sum_{m=-n}^n c_{n,\text{imm}}^m Y_n^m(\theta, \phi). \quad (\text{A.13})$$

As can be observed, an N_h -th order approximation requires N_h^2 coefficients.

A.3.3 Rotation

Properties of spherical harmonics under rotation are particularly important for the development of rotation invariant magnetic flux density, force, and torque models.

Consider (θ, ϕ) to be spherical coordinates corresponding to a rotating reference frame (for instance a frame fixed to the rotor). Similarly, (θ', ϕ') are spherical coordinates corresponding to a fixed reference frame (for instance a frame fixed to the stator). Let $\eta(\theta, \phi) = (\cos \phi \sin \theta, \sin \phi \sin \theta, \cos \theta)$ be a point on the 2-D unit sphere expressed in rotating spherical coordinates. The rotation of a point $\eta'(\theta, \phi)$ from the fixed reference frame to the rotated reference frame is performed by an element $R \in \mathbb{R}^{3 \times 3}$ of the rotation group $SO(3)$, which is defined as the group of all rotations about the origin of three-dimensional Euclidean space, or equivalently as the group of all matrices R such that $R^T R = I$ with $\det R = 1$. Using ZYZ Euler's angles, this rotation operator can be expressed as [173]

$$R(\alpha, \beta, \gamma) = R_z(\gamma) R_y(\beta) R_z(\alpha), \quad (\text{A.14})$$

where $R_z(\alpha)$ and $R_y(\beta)$ are rotation matrices representing a rotation around the z -axis by α and y -axis by β . Hence, for any $R \in SO(3)$ and a function $f(\eta')$, we define $f'(\eta')$ as the rotated version of $f(\eta')$ with the operator Λ_R such that

$$f'(\eta') = \Lambda_R f(\eta') = f(R^{-1}\eta'), \quad (\text{A.15})$$

where

$$\eta = R^{-1}\eta' \quad (\text{A.16})$$

corresponds to the point η' expressed in the rotating reference frame.

We are interested in examining the effect that a rotation of the function f has on its representation in the frequency space. Spherical harmonic functions transform among themselves under rotation according to [124, 173, 182]

$$\Lambda_R Y_n^m(\eta') = Y_n^m(R^{-1}\eta') = \sum_{m'=-n}^n D_{m'm}^n(R) Y_n^{m'}(\eta'), \quad (\text{A.17})$$

where $D_{m'm}^n$ are unitary rotation matrices due to Wigner and are expressed as

$$D_{m'm}^n(\alpha, \beta, \gamma) = e^{-im'\alpha} d_{m'm}^n(\beta) e^{-im\gamma}, \quad (\text{A.18})$$

Appendix A. Spherical Harmonics

where

$$d_{m'm}^n = [(n+m')!(n-m')!(n+m)!(n-m)!]^{1/2} \times \sum_{k=\max(0, m-m')}^{\min(n-m', n+m)} \frac{(-1)^{m'-m+k} (\cos \beta/2)^{2n+m-m'-2k} (\sin \beta/2)^{m'-m+2k}}{(n+m-k)!(m'-m-k)!(n-m'-k)!k!}. \quad (\text{A.19})$$

Substituting (A.17) into (A.10) gives f expressed in fixed frame spherical coordinates

$$f(\eta') = \sum_{n=0}^{\infty} \sum_{m=-n}^n c_{n,\text{imm}}^m \sum_{m'=-n}^n D_{m'm}^n(\alpha, \beta, \gamma) Y_n^{m'}(\eta'). \quad (\text{A.20})$$

Now, taking into account (A.10), the function f can be expanded in fixed coordinates as

$$\begin{aligned} \sum_{n=0}^{\infty} \sum_{m=-n}^n c_n^m(\alpha, \beta, \gamma) Y_n^m(\eta') &= f'(\eta') \\ &= \Lambda_R f(\eta') \\ &= \Lambda_R \sum_{n'=0}^{\infty} \sum_{m'=-n'}^{n'} c_{n',\text{imm}}^{m'} Y_{n'}^{m'}(\eta') \\ &= \sum_{n'=0}^{\infty} \sum_{m'=-n'}^{n'} c_{n',\text{imm}}^{m'} \Lambda_R Y_{n'}^{m'}(\eta') \\ &= \sum_{n'=0}^{\infty} \sum_{m'=-n'}^{n'} c_{n',\text{imm}}^{m'} \sum_{l=-n'}^{n'} D_{lm'}^{n'}(\alpha, \beta, \gamma) Y_{n'}^l(\eta'). \quad (\text{A.21}) \end{aligned}$$

Then, multiplying both sides by $\overline{Y_k^j(\eta')}$, with k varying from 0 to ∞ and j from $-k$ to k , and integrating over the sphere, all terms vanish except at $k = n' = n$ and $j = m = l$. Therefore,

$$c_n^m(\alpha, \beta, \gamma) = \sum_{m'=-n}^n D_{m'm}^n(\alpha, \beta, \gamma) c_{n,\text{imm}}^{m'}. \quad (\text{A.22})$$

This result tells us that coefficients in one frequency band of the unrotated function f only influence the same band of coefficients in its rotated version.

Equation (A.22) has the following block diagonal sparse structure [123]

$$\begin{bmatrix} c_0^0 \\ c_1^{-1} \\ c_1^0 \\ c_1^1 \\ c_2^{-2} \\ c_2^{-1} \\ c_2^0 \\ c_2^1 \\ c_2^2 \\ \vdots \end{bmatrix} = \begin{bmatrix} D^0(\alpha, \beta, \gamma) & 0 & 0 & 0 & 0 & 0 & 0 & 0 & \dots \\ 0 & & & & 0 & 0 & 0 & 0 & \dots \\ 0 & D^1(\alpha, \beta, \gamma) & & & 0 & 0 & 0 & 0 & \dots \\ 0 & & & & 0 & 0 & 0 & 0 & \dots \\ \hline 0 & 0 & 0 & 0 & & & & & \dots \\ 0 & 0 & 0 & 0 & & & & & \dots \\ 0 & 0 & 0 & 0 & D^2(\alpha, \beta, \gamma) & & & & \dots \\ 0 & 0 & 0 & 0 & & & & & \dots \\ 0 & 0 & 0 & 0 & & & & & \dots \\ \hline \vdots & \vdots & \vdots & \vdots & \vdots & \vdots & \vdots & \vdots & \ddots \end{bmatrix} \begin{bmatrix} c_{0,imm}^0 \\ c_{1,imm}^{-1} \\ c_{1,imm}^0 \\ c_{1,imm}^1 \\ c_{2,imm}^{-2} \\ c_{2,imm}^{-1} \\ c_{2,imm}^0 \\ c_{2,imm}^1 \\ c_{2,imm}^2 \\ \vdots \end{bmatrix} \quad (A.23)$$

Hence, the spherical harmonic basis functions are decomposed into a direct sum of orthogonal subspaces that are globally invariant under rotation. Properties of spherical harmonics under rotations are widely exploited in computer graphics for example to compute the orientation between two objects (images, organs, molecules, or other shapes) [123,124,173,174], to construct rotation invariant representations of 3-D shape descriptors [175], or in 3-D interactive graphics to provide stable lighting under rotations [169,172].

B Illustration of Propositions

B.1 Illustration of Proposition 1

To begin with, we will show that, for any orientation of the rotor, two opposite coils produce the same forces but opposite torques. In other words, we will show that $\mathbf{F}_k = \mathbf{F}_{20+1-k}$ and that $\mathbf{T}_k = -\mathbf{T}_{20+1-k}$, for $k = 1, 2, \dots, 10$. The force produced by coil k can be described in a spherical coordinate frame attached to the coil as

$${}^c \mathbf{F}_k = \int_{V_{\text{coil}}} {}^c \mathbf{J}_k \times {}^c \mathbf{B}_4 dV, \quad (\text{B.1})$$

where V_{coil} is the volume of the coil, ${}^c \mathbf{J}_k$ is the current density vector with norm J_k in spherical coordinates defined as

$${}^c \mathbf{J}_k = J_k \hat{\phi}_c, \quad (\text{B.2})$$

and ${}^c \mathbf{B}_4$ is the magnetic flux density of the rotor in the airgap defined as

$${}^c \mathbf{B}_4 = B_{r_c} \hat{r}_c + B_{\theta_c} \hat{\theta}_c + B_{\phi_c} \hat{\phi}_c. \quad (\text{B.3})$$

Similarly, the torque produced by coil k is calculated as

$${}^c \mathbf{T}_k = \int_{V_{\text{coil}}} r_c \hat{r}_c \times {}^c \mathbf{J}_k \times {}^c \mathbf{B}_4 dV. \quad (\text{B.4})$$

The force and torque produced by coil $20 + 1 - k$ can be calculated in the reference frame of coil k as

$${}^c \mathbf{F}_{20+1-k} = \int_{V_{\text{coil}}} \left(-{}^c \mathbf{J}_k \right) \times \left(-{}^c \mathbf{B}_4 \right) dV = {}^c \mathbf{F}_k. \quad (\text{B.5})$$

In equation (B.5), the current density is taken with minus sign because coil $20 + 1 - k$ is facing coil k . Furthermore, the magnetic flux density is also taken with minus sign because of the cubic symmetry of the rotor magnetic flux density. Similarly, the torque

Appendix B. Illustration of Propositions

produced by coil 20 is calculated in the reference frame of coil 1 as

$$c^S \mathbf{T}_{20+1-k} = \int_{V_{\text{coil}}} (-r_c \hat{\mathbf{r}}_c) \left(-c^S \mathbf{J}_k \right) \times \left(-c^S \mathbf{B}_4 \right) dV = -c^S \mathbf{T}_k. \quad (\text{B.6})$$

Therefore, $\mathbf{F}_k = \mathbf{F}_{20+1-k}$ and $\mathbf{T}_k = -\mathbf{T}_{20+1-k}$, for $k = 1, 2, \dots, 10$. Hence, the total force produced by the actuator can be described as

$$\mathbf{F} = \mathbf{F}_1 + \mathbf{F}_2 + \dots + \mathbf{F}_{20} = K_{F,1}i_1 + K_{F,2}i_2 + \dots + K_{F,20}i_{20} = K_{\mathbf{F}}\mathbf{i}, \quad (\text{B.7})$$

where i_k is the current flowing in coil k and where

$$K_{\mathbf{F}} = \begin{bmatrix} K_{F,1} & K_{F,2} & \dots & K_{F,20} \end{bmatrix} \quad (\text{B.8})$$

$$= \begin{bmatrix} K_{F,1} & K_{F,2} & \dots & K_{F,10} & K_{F,10} & \dots & K_{F,2} & K_{F,1} \end{bmatrix} \in \mathbb{R}^{3 \times 20} \quad (\text{B.9})$$

is the force characteristic matrix. Similarly, the torque characteristic matrix can be expressed as

$$K_{\mathbf{T}} = \begin{bmatrix} K_{T,1} & K_{T,2} & \dots & K_{T,20} \end{bmatrix} \quad (\text{B.10})$$

$$= \begin{bmatrix} K_{T,1} & K_{T,2} & \dots & K_{T,10} & -K_{T,10} & \dots & -K_{T,2} & -K_{T,1} \end{bmatrix} \in \mathbb{R}^{3 \times 20}. \quad (\text{B.11})$$

Therefore, defining the entries of $K_{\mathbf{F}}K_{\mathbf{T}}^{\top} \in \mathbb{R}^{3 \times 3}$ as

$$K_{\mathbf{F}}K_{\mathbf{T}}^{\top} = \begin{bmatrix} K_{\mathbf{F}}K_{\mathbf{T}}^{\top}(1,1) & K_{\mathbf{F}}K_{\mathbf{T}}^{\top}(1,2) & K_{\mathbf{F}}K_{\mathbf{T}}^{\top}(1,3) \\ K_{\mathbf{F}}K_{\mathbf{T}}^{\top}(2,1) & K_{\mathbf{F}}K_{\mathbf{T}}^{\top}(2,2) & K_{\mathbf{F}}K_{\mathbf{T}}^{\top}(2,3) \\ K_{\mathbf{F}}K_{\mathbf{T}}^{\top}(3,1) & K_{\mathbf{F}}K_{\mathbf{T}}^{\top}(3,2) & K_{\mathbf{F}}K_{\mathbf{T}}^{\top}(3,3) \end{bmatrix} \quad (\text{B.12})$$

and the entries of $K_{\mathbf{F},k} \in \mathbb{R}^{3 \times 1}$ and $K_{\mathbf{T},k} \in \mathbb{R}^{3 \times 1}$, $k = 1, 2, \dots, 10$, as

$$K_{\mathbf{F},k} = \left[K_{F,k}(1) \quad K_{F,k}(2) \quad K_{F,k}(3) \right]^{\top} \quad (\text{B.13})$$

and

$$K_{\mathbf{T},k} = \left[K_{T,k}(1) \quad K_{T,k}(2) \quad K_{T,k}(3) \right]^{\top}, \quad (\text{B.14})$$

it is verified that

$$\begin{aligned}
 K_{\text{F}}K_{\text{T}}^{\text{T}}(1, 1) &= \begin{bmatrix} K_{\text{F},1}(1) & K_{\text{F},2}(1) & \dots & K_{\text{F},20}(1) \end{bmatrix} \cdot \begin{bmatrix} K_{\text{T},1}(1) \\ K_{\text{T},2}(1) \\ \vdots \\ K_{\text{T},20}(1) \end{bmatrix} \\
 &= \begin{bmatrix} K_{\text{F},1}(1) & K_{\text{F},2}(1) & \dots & K_{\text{F},10}(1) & K_{\text{F},10}(1) & \dots & K_{\text{F},2}(1) & K_{\text{F},1}(1) \end{bmatrix} \\
 &\quad \cdot \begin{bmatrix} K_{\text{T},1}(1) \\ K_{\text{T},2}(1) \\ \vdots \\ K_{\text{T},10}(1) \\ -K_{\text{T},10}(1) \\ \vdots \\ -K_{\text{T},2}(1) \\ -K_{\text{T},1}(1) \end{bmatrix} \\
 &= 0,
 \end{aligned} \tag{B.15}$$

and that

$$\begin{aligned}
 K_{\text{F}}K_{\text{T}}^{\text{T}}(1, 2) &= \begin{bmatrix} K_{\text{F},1}(1) & K_{\text{F},2}(1) & \dots & K_{\text{F},20}(1) \end{bmatrix} \cdot \begin{bmatrix} K_{\text{T},1}(2) \\ K_{\text{T},2}(2) \\ \vdots \\ K_{\text{T},20}(2) \end{bmatrix} \\
 &= \begin{bmatrix} K_{\text{F},1}(1) & K_{\text{F},2}(1) & \dots & K_{\text{F},10}(1) & K_{\text{F},10}(1) & \dots & K_{\text{F},2}(1) & K_{\text{F},1}(1) \end{bmatrix} \\
 &\quad \cdot \begin{bmatrix} K_{\text{T},1}(2) \\ K_{\text{T},2}(2) \\ \vdots \\ K_{\text{T},10}(2) \\ -K_{\text{T},10}(2) \\ \vdots \\ -K_{\text{T},2}(2) \\ -K_{\text{T},1}(2) \end{bmatrix} \\
 &= 0.
 \end{aligned} \tag{B.16}$$

It can be easily verified that also the remaining entries of $K_{\text{F}}K_{\text{T}}^{\text{T}}$ are zero. Therefore, $K_{\text{F}}K_{\text{T}}^{\text{T}} = 0$ confirming that force and torque characteristic matrices are mutually orthogonal.

B.2 Illustration of Proposition 2

For this illustration see for example [183].

To see that \mathbf{i}_{LS} is the unique solution minimizing $\|\mathbf{i}\|_2^2$, suppose there is another solution \mathbf{i} satisfying (3.44). Hence, $K_{\text{F},\text{T}}(\mathbf{i} - \mathbf{i}_{\text{LS}}) = 0$ and

$$(\mathbf{i} - \mathbf{i}_{\text{LS}})^\top \mathbf{i}_{\text{LS}} = (\mathbf{i} - \mathbf{i}_{\text{LS}})^\top K_{\text{F},\text{T}}^\top \left(K_{\text{F},\text{T}} K_{\text{F},\text{T}}^\top \right)^{-1} \begin{bmatrix} \mathbf{F} \\ \mathbf{T} \end{bmatrix} \quad (\text{B.17})$$

$$= [K_{\text{F},\text{T}}(\mathbf{i} - \mathbf{i}_{\text{LS}})]^\top \left(K_{\text{F},\text{T}} K_{\text{F},\text{T}}^\top \right)^{-1} \begin{bmatrix} \mathbf{F} \\ \mathbf{T} \end{bmatrix} \quad (\text{B.18})$$

$$= 0, \quad (\text{B.19})$$

which means that $(\mathbf{i} - \mathbf{i}_{\text{LS}})^\top$ is orthogonal to \mathbf{i}_{LS} . Therefore,

$$\|\mathbf{i}\|_2^2 = \|\mathbf{i}_{\text{LS}} + \mathbf{i} - \mathbf{i}_{\text{LS}}\|_2^2 = \|\mathbf{i}_{\text{LS}}\|_2^2 + \|\mathbf{i} - \mathbf{i}_{\text{LS}}\|_2^2 \geq \|\mathbf{i}_{\text{LS}}\|_2^2, \quad (\text{B.20})$$

i.e., \mathbf{i}_{LS} is the minimum-energy solution of (3.44). Hence, the resulting current vector is the minimum-norm solution and the unique vector minimizing the dissipated energy.

B.3 Illustration of Proposition 3

In Proposition 1 we have shown that $\mathbf{F}_k = \mathbf{F}_{20+1-k}$ and that $\mathbf{T}_k = -\mathbf{T}_{20+1-k}$, for $k = 1, 2, \dots, 10$. Therefore, from (B.8) and (B.10) we can write

$$K_{\text{F}}^3 = \begin{bmatrix} K_{\text{F},1}^3 & K_{\text{F},2}^3 & \dots & K_{\text{F},20}^3 \end{bmatrix} \quad (\text{B.21})$$

$$= \begin{bmatrix} K_{\text{F},1}^3 & K_{\text{F},2}^3 & \dots & K_{\text{F},10}^3 & K_{\text{F},10}^3 & \dots & K_{\text{F},2}^3 & K_{\text{F},1}^3 \end{bmatrix} \in \mathbb{R}^{3 \times 20} \quad (\text{B.22})$$

and

$$K_{\text{T}}^{N_{\text{h}}} = \begin{bmatrix} K_{\text{T},1}^{N_{\text{h}}} & K_{\text{T},2}^{N_{\text{h}}} & \dots & K_{\text{T},20}^{N_{\text{h}}} \end{bmatrix} \quad (\text{B.23})$$

$$= \begin{bmatrix} K_{\text{T},1}^{N_{\text{h}}} & K_{\text{T},2}^{N_{\text{h}}} & \dots & K_{\text{T},10}^{N_{\text{h}}} & -K_{\text{T},10}^{N_{\text{h}}} & \dots & -K_{\text{T},2}^{N_{\text{h}}} & -K_{\text{T},1}^{N_{\text{h}}} \end{bmatrix} \in \mathbb{R}^{3 \times 20}. \quad (\text{B.24})$$

Therefore, similarly to (B.12) defining

$$K_{\text{T}}^{N_{\text{h}}} \left(K_{\text{F}}^3 \right)^\top = \begin{bmatrix} K_{\text{T}}^{N_{\text{h}}} (K_{\text{F}}^3)^\top (1, 1) & K_{\text{T}}^{N_{\text{h}}} (K_{\text{F}}^3)^\top (1, 2) & K_{\text{T}}^{N_{\text{h}}} (K_{\text{F}}^3)^\top (1, 3) \\ K_{\text{T}}^{N_{\text{h}}} (K_{\text{F}}^3)^\top (2, 1) & K_{\text{T}}^{N_{\text{h}}} (K_{\text{F}}^3)^\top (2, 2) & K_{\text{T}}^{N_{\text{h}}} (K_{\text{F}}^3)^\top (2, 3) \\ K_{\text{T}}^{N_{\text{h}}} (K_{\text{F}}^3)^\top (3, 1) & K_{\text{T}}^{N_{\text{h}}} (K_{\text{F}}^3)^\top (3, 2) & K_{\text{T}}^{N_{\text{h}}} (K_{\text{F}}^3)^\top (3, 3) \end{bmatrix} \quad (\text{B.25})$$

and the entries of $K_{\text{F},k}^3 \in \mathbb{R}^{3 \times 1}$ and $K_{\text{T},i}^{N_{\text{h}}} \in \mathbb{R}^{3 \times 1}$, $k = 1, 2, \dots, 10$, as

$$K_{\text{F},k}^3 = \left[K_{\text{F},k}^3(1) \quad K_{\text{F},k}^3(2) \quad K_{\text{F},k}^3(3) \right]^\top \quad (\text{B.26})$$

and

$$K_{T,k}^{N_h} = \left[K_{T,k}^{N_h}(1) \quad K_{T,k}^{N_h}(2) \quad K_{T,k}^{N_h}(3) \right]^T \quad (\text{B.27})$$

it is verified that

$$\begin{aligned} K_T^{N_h} \left(K_F^3 \right)^T (1, 1) &= \left[K_{T,1}^{N_h}(1) \quad K_{T,2}^{N_h}(1) \quad \dots \quad K_{T,20}^{N_h}(1) \right] \cdot \begin{bmatrix} K_{F,1}^3(1) \\ K_{F,2}^3(1) \\ \vdots \\ K_{F,20}^3(1) \end{bmatrix} \\ &= \left[K_{T,1}^{N_h}(1) \quad K_{T,2}^{N_h}(1) \quad \dots \quad K_{T,10}^{N_h}(1) \quad K_{T,10}^{N_h}(1) \quad \dots \quad K_{T,2}^{N_h}(1) \quad K_{T,1}^{N_h}(1) \right] \\ &\quad \cdot \begin{bmatrix} K_{F,1}^3(1) \\ K_{F,2}^3(1) \\ \vdots \\ K_{F,10}^3(1) \\ -K_{F,10}^3(1) \\ \vdots \\ -K_{F,2}^3(1) \\ -K_{F,1}^3(1) \end{bmatrix} \\ &= 0, \end{aligned} \quad (\text{B.28})$$

and that

$$\begin{aligned} K_T^{N_h} \left(K_F^3 \right)^T (1, 2) &= \left[K_{T,1}^{N_h}(1) \quad K_{T,2}^{N_h}(1) \quad \dots \quad K_{T,20}^{N_h}(1) \right] \cdot \begin{bmatrix} K_{F,1}^3(2) \\ K_{F,2}^3(2) \\ \vdots \\ K_{F,20}^3(2) \end{bmatrix} \\ &= \left[K_{T,1}^{N_h}(1) \quad K_{T,2}^{N_h}(1) \quad \dots \quad K_{T,10}^{N_h}(1) \quad K_{T,10}^{N_h}(1) \quad \dots \quad K_{T,2}^{N_h}(1) \quad K_{T,1}^{N_h}(1) \right] \\ &\quad \cdot \begin{bmatrix} K_{F,1}^3(2) \\ K_{F,2}^3(2) \\ \vdots \\ K_{F,10}^3(2) \\ -K_{F,10}^3(2) \\ \vdots \\ -K_{F,2}^3(2) \\ -K_{F,1}^3(2) \end{bmatrix} \\ &= 0. \end{aligned} \quad (\text{B.29})$$

Appendix B. Illustration of Propositions

It can be easily verified that also the remaining entries of $K_T^{N_h} (K_F^3)^\top$ are zero. Therefore, $K_T^{N_h} (K_F^3)^\top = 0$ confirming our proposition. Finally, by applying the same illustration we can show that a current vector computed to generate a desired reference torque using the torque model taking into account only the fundamental harmonics of degree $n = 3$ does not generate any force.

B.4 Illustration of Proposition 4

We start with the energy balance relation [106]

$$dW_e = dW_{\text{loss}} + dW_{\text{fld}} + dW_{\text{mech}}, \quad (\text{B.30})$$

where W_e is the electrical energy input, W_{loss} the energy dissipated, W_{fld} the energy stored in the magnetic field, and W_{mech} the mechanical energy. Using (5.5) we can write

$$\frac{d}{dt}W_e = \mathbf{u}^\top \mathbf{i} = R_c \mathbf{i}^\top \mathbf{i} + \frac{d}{dt} \frac{1}{2} \mathbf{i}^\top L_c \mathbf{i} + \mathbf{u}_{\text{emf}}^\top \mathbf{i}, \quad (\text{B.31})$$

where $R_c \mathbf{i}^\top \mathbf{i} = \frac{d}{dt}W_{\text{loss}}$ is the dissipated power while $\frac{d}{dt} \frac{1}{2} \mathbf{i}^\top L_c \mathbf{i} = \frac{d}{dt}W_{\text{fld}}$ is the variation of the energy stored in the magnetic field (coils). Therefore, $\mathbf{u}_{\text{emf}}^\top \mathbf{i}$ is equal to the mechanical power, i.e.

$$\frac{d}{dt}W_{\text{mech}} = \mathbf{u}_{\text{emf}}^\top \mathbf{i}. \quad (\text{B.32})$$

Then, by employing proposition in (5.9) and the inverse model in (3.48), where the force is equal to zero since we only consider rotational motion, expression (B.32) can be reformulated as

$$\begin{aligned} \frac{d}{dt}W_{\text{mech}} &= \boldsymbol{\omega}^\top K_T \mathbf{i} \\ &= \boldsymbol{\omega}^\top K_T M_T \mathbf{T} = \boldsymbol{\omega}^\top \mathbf{T}, \end{aligned} \quad (\text{B.33})$$

which is indeed the mechanical power calculated in (5.4) and confirms Proposition 4.

Bibliography

- [1] O. Chételat, “Torquer apparatus,” U.S. Patent 8 164 294, 04 24, 2012.
- [2] A. K. Maini and V. Agrawal, *Satellite technology : principles and applications*. Chichester: John Wiley, 2007.
- [3] P. Fortescue and J. Stark, *Spacecraft Systems Engineering*, 2nd ed. Chichester: John Wiley, 1995.
- [4] W. J. Larson and J. R. Wertz, Eds., *Space Mission Analysis and Design*, 3rd ed. Torrance, CA: Microcosm, Inc., 1999.
- [5] C. D. Brown, *Elements of Spacecraft Design*. Reston: AIAA (American Institute of Aeronautics & Astronautics), 2002.
- [6] J. R. Wertz, *Spacecraft attitude determination and control*, 2002nd ed. Dordrecht, Boston, Reidel: Springer Netherlands, 1978.
- [7] A. H. de Ruiter, C. J. Damaren, and J. R. Forbes, *Spacecraft dynamics and control: an introduction*. Oxford: Wiley, 2013.
- [8] M. J. Sidi, *Spacecraft Dynamics and Control: A Practical Engineering Approach*. Cambridge: Cambridge University Press, 2000.
- [9] V. L. Pisacane and R. C. Moore, *Fundamentals of space systems*. New York: Oxford University Press, 1994.
- [10] U. J. Bichler, “A magnetic bearing momentum wheel for high pointing accuracy and vibration sensitive space applications,” in *4th Annual AAS Guidance and Control Conference*, Keystone, Colorado, United States, 1991.
- [11] B. Gerlach, M. Ehinger, H. K. Raue, and R. Seiler, “Gimballing magnetic bearing reaction wheel with digital controller,” in *Proc. 11th European Space Mechanisms and Tribology Symposium (ESMATS)*, Lucerne, Switzerland, Sep. 2005.
- [12] B. Gerlach, M. Ehinger, and R. Seiler, “Low noise five-axis magnetic bearing reaction wheel,” in *4th IFAC Symposium on Mechatronic Systems*, Ruprecht-Karls-University, Germany, Sep. 2006.

Bibliography

- [13] J. Lyman Spitzer, "Space telescopes and components," *The Astronomical Journal*, vol. 65, no. 5, pp. 242–263, 1960.
- [14] R. D. Ormsby, "A free reaction sphere satellite attitude control system," in *Proc. IAS National Specialists Meeting on Guidance of Aerospace Vehicles*, Boston, Massachusetts, United States, May 1960, pp. 53–55.
- [15] W. Haeussermann, "The spherical control motor for three axis attitude control of space vehicles," Tech. Rep., 1959.
- [16] K. W. Henring and R. E. Hufnagel, "An inertial sphere system for complete attitude control of earth satellites," *ARS Journal*, vol. 31, no. 6, pp. 1074–1079, 1960.
- [17] R. D. Ormsby, "Capabilities and limitations of reaction spheres for attitude control," *ARS Journal*, vol. 31, no. 6, pp. 808–812, 1961.
- [18] T. Tierney and R. Curran, "Development of an electrostatic suspension reaction sphere," Tech. Rep., 1964.
- [19] H. Schröpl, "Attitude stabilization of satellites by means of the free reaction sphere," Tech. Rep., 1965.
- [20] W. H. Isely, "Magnetically supported and torqued momentum reaction sphere," U.S. Patent 4 611 863, 09 16, 1986.
- [21] J. R. Downer, D. B. Eisenhaure, R. L. Hockney, and B. G. Johnson, "Magnetic bearing and suspension system," U.S. Patent 4 961 352, 10 09, 1990.
- [22] T. Nakanishi, Y. Ando, K. Sakakibara, and A. Mitsukane, "Control moment gyro having spherical rotor with permanent magnets," U.S. Patent 5 476 018, 12 19, 1995.
- [23] J. Doty, "Reaction sphere for spacecraft attitude control," WO Patent Application 2010/117 819, 10 14, 2010.
- [24] L. Yan, I.-M. Chen, C. K. Lim, G. Yang, and K.-M. Lee, *Design, Modeling and Experiments of 3-DOF Electromagnetic Spherical Actuators*. Reading, MA: Springer, 2011.
- [25] M. Aoyagi, T. Nakajima, Y. Tomikawa, and T. Takano, "Examination of disk-type multidegree-of-freedom ultrasonic motor," *Japanese Journal of Applied Physics*, vol. 43, no. 5B, pp. 2884–2890, 2004.
- [26] Y. Goda, D. Koyama, and K. Nakamura, "Design of multi-degree-of-freedom ultrasonic micromotors," *Japanese Journal of Applied Physics*, vol. 48, 2009.

-
- [27] M. Hoshina, T. Mashimo, and S. Toyama, "Development of spherical ultrasonic motor as a camera actuator for pipe inspection robot," in *Intelligent Robots and Systems, 2009. IROS 2009. IEEE/RSJ International Conference on*, 2009, pp. 2379–2384.
- [28] B. Lu, M. Aoyagi, H. Tamura, and T. Takano, "Development of a novel rotor-embedded-type multidegree-of-freedom spherical ultrasonic motor," in *Mechatronics and Automation (ICMA), 2011 International Conference on*, 2011, pp. 795–800.
- [29] T. Mashimo, S. Toyama, and H. Ishida, "Design and implementation of spherical ultrasonic motor," *Ultrasonics, Ferroelectrics and Frequency Control, IEEE Transactions on*, vol. 56, no. 11, pp. 2514–2521, 2009.
- [30] K. Takemura and T. Maeno, "Design and control of an ultrasonic motor capable of generating multi-DOF motion," *Mechatronics, IEEE/ASME Transactions on*, vol. 6, no. 4, pp. 499–506, 2001.
- [31] K. Takemura, Y. Ohno, and T. Maeno, "Design of a plate type multi-DOF ultrasonic motor and its self-oscillation driving circuit," *Mechatronics, IEEE/ASME Transactions on*, vol. 9, no. 3, pp. 474–480, 2004.
- [32] F. Williams, E. Laithwaite, and J. Eastham, "Development and design of spherical induction motors," in *Proceedings of the Institution of Electrical Engineers*, vol. 106, December 1959, p. 471–484.
- [33] K. Davey, G. Vachtsevanos, and R. Powers, "The analysis of fields and torques in spherical induction motors," *Magnetics, IEEE Transactions on*, vol. 23, no. 1, pp. 273–282, 1987.
- [34] G. Vachtsevanos, K. Davey, and K.-M. Lee, "Development of a novel intelligent robotic manipulator," *Control Systems Magazine, IEEE*, vol. 7, no. 3, pp. 9–15, 1987.
- [35] J. Ruan, S. Huang, and K. Zhou, "Computation of 3d electromagnetic field and torques in spherical motors," *The International Journal for Computation and Mathematics in Electrical and Electronic Engineering*, vol. 17, no. 1/2/3, pp. 106–110, 1998.
- [36] B. Dehez, G. Galary, D. Grenier, and B. Raucent, "Development of a spherical induction motor with two degrees of freedom," *Magnetics, IEEE Transactions on*, vol. 42, no. 8, pp. 2077–2089, 2006.
- [37] J. Zentner, "Induction motors with several degrees of freedom: Applications, design, modelling," in *ACTUATOR 2010, 12th International Conference on New Actuators*, Bremen, Germany, June 2010, pp. 208–511.

Bibliography

- [38] M. Kumagai and R. Hollis, “Development and control of a three DOF spherical induction motor,” in *Robotics and Automation (ICRA), 2013 IEEE International Conference on*, 2013, pp. 1528–1533.
- [39] K.-M. Lee, G. Vachtsevanos, and C. Kwan, “Development of a spherical stepper wrist motor,” *Journal of Intelligent and Robotic Systems*, vol. 1, no. 3, pp. 225–242, 1988.
- [40] K.-M. Lee and C.-K. Kwan, “Design concept development of a spherical stepper for robotic applications,” *Robotics and Automation, IEEE Transactions on*, vol. 7, no. 1, pp. 175–181, 1991.
- [41] K.-M. Lee, R. B. Roth, and Z. Zhou, “Dynamic modeling and control of a ball-joint-like variable-reluctance spherical motor,” *Journal of Dynamic Systems, Measurement, and Control*, vol. 118, pp. 29–40, 1996.
- [42] Z. Zhou and K.-M. Lee, “Real-time motion control of a multi-degree-of-freedom variable reluctance spherical motor,” in *Robotics and Automation, 1996. Proceedings, 1996 IEEE International Conference on*, vol. 3, 1996, pp. 2859–2864 vol.3.
- [43] K.-M. Lee, R. A. Sosseh, and Z. Wei, “Effects of the torque model on the control of a VR spherical motor,” *Control Engineering Practice*, vol. 12, no. 11, pp. 1437 – 1449, 2004.
- [44] K.-M. Lee, Z. Wei, and J. Joni, “Parametric study on pole geometry and thermal effects of a VRSM,” in *Robotics, Automation and Mechatronics, 2004 IEEE Conference on*, vol. 1, 2004, pp. 548–553 vol.1.
- [45] K.-M. Lee, J. Loni, and H. Son, “Design method for prototyping a cost-effective VR spherical motor,” in *Robotics, Automation and Mechatronics, 2004 IEEE Conference on*, vol. 1, 2004, pp. 542–547 vol.1.
- [46] K.-M. Lee, H. Son, J. Joni, K.-M. Lee, H. Son, and J. Joni, “Concept development and design of a spherical wheel motor (SWM),” in *Robotics and Automation, 2005. ICRA 2005. Proceedings of the 2005 IEEE International Conference on*, 2005, pp. 3652–3657.
- [47] K.-M. Lee and H. Son, “Torque model for design and control of a spherical wheel motor,” in *Advanced Intelligent Mechatronics. Proceedings, 2005 IEEE/ASME International Conference on*, 2005, pp. 335–340.
- [48] K.-M. Lee, K. Bai, and J. Lim, “Dipole models for forward/inverse torque computation of a spherical motor,” *Mechatronics, IEEE/ASME Transactions on*, vol. 14, no. 1, pp. 46–54, 2009.
- [49] H. Son and K.-M. Lee, “Open-loop controller design and dynamic characteristics of a spherical wheel motor,” *Industrial Electronics, IEEE Transactions on*, vol. 57, no. 10, pp. 3475–3482, 2010.

-
- [50] L. Yan, I.-M. Chen, G. Yang, and K.-M. Lee, "Analytical and experimental investigation on the magnetic field and torque of a permanent magnet spherical actuator," *Mechatronics, IEEE/ASME Transactions on*, vol. 11, no. 4, pp. 409–419, 2006.
- [51] L. Yan, I.-M. Chen, C. K. Lim, G. Yang, W. Lin, and K.-M. Lee, "Design and analysis of a permanent magnet spherical actuator," *Mechatronics, IEEE/ASME Transactions on*, vol. 13, no. 2, pp. 239–248, 2008.
- [52] L. Yan, I.-M. Chen, C. K. Lim, G. Yang, and K.-M. Lee, "Modeling and iron-effect analysis on magnetic field and torque output of electromagnetic spherical actuators with iron stator," *Mechatronics, IEEE/ASME Transactions on*, vol. 17, no. 6, pp. 1080–1087, 2012.
- [53] L. Yan, I.-M. Chen, C. K. Lim, G. Yang, and K.-M. Lee, "Empirical formulation of torque output for spherical actuators with low-cost rotor poles," in *Advanced Intelligent Mechatronics, 2009. AIM 2009. IEEE/ASME International Conference on*, 2009, pp. 1625–1630.
- [54] L. Yan, I.-M. Chen, C. K. Lim, G. Yang, W. Lin, and K.-M. Lee, "Hybrid torque modeling of spherical actuators with cylindrical-shaped magnet poles," *Mechatronics*, vol. 21, no. 1, pp. 85 – 91, 2011.
- [55] L. Yan, I.-M. Chen, H. Son, C. K. Lim, and G. Yang, "Analysis of pole configurations of permanent-magnet spherical actuators," *Mechatronics, IEEE/ASME Transactions on*, vol. 15, no. 6, pp. 986–989, 2010.
- [56] K. Bai, J. Ji, K.-M. Lee, and S. Zhang, "A two-mode six-DOF motion system based on a ball-joint-like spherical motor for haptic applications," *Computers and Mathematics with Applications*, vol. 64, no. 5, pp. 978 – 987, 2012.
- [57] K. Bai and K.-M. Lee, "Direct field-feedback control of a ball-joint-like permanent-magnet spherical motor," *Mechatronics, IEEE/ASME Transactions on*, vol. PP, no. 99, pp. 1–12, 2013.
- [58] W. Wang, J. Wang, G. Jewell, and D. Howe, "Design and control of a novel spherical permanent magnet actuator with three degrees of freedom," *Mechatronics, IEEE/ASME Transactions on*, vol. 8, no. 4, pp. 457–468, 2003.
- [59] G. Chirikjian and D. Stein, "Kinematic design and commutation of a spherical stepper motor," *Mechatronics, IEEE/ASME Transactions on*, vol. 4, no. 4, pp. 342–353, 1999.
- [60] D. Stein and G. S. Chirikjian, "Experiments in the commutation and motion planning of a spherical stepper motor," in *ASME 2000 Design Engineering Technical Conferences and Computers and Information in Engineering Conference*, Baltimore, Maryland, September 2000.

Bibliography

- [61] D. Stein, G. Chirikjian, and E. Scheinerman, "Theory, design, and implementation of a spherical encoder," in *Robotics and Automation, 2001. Proceedings 2001 ICRA. IEEE International Conference on*, vol. 2, 2001, pp. 1773–1779 vol.2.
- [62] D. Stein, E. Scheinerman, and G. Chirikjian, "Mathematical models of binary spherical-motion encoders," *Mechatronics, IEEE/ASME Transactions on*, vol. 8, no. 2, pp. 234–244, 2003.
- [63] Q. Wang, Z. Li, Y. Ni, and W. Jiang, "Magnetic field computation of a PM spherical stepper motor using integral equation method," *Magnetics, IEEE Transactions on*, vol. 42, no. 4, pp. 731–734, 2006.
- [64] Z. Li and Q. Wang, "Modeling and control of a permanent magnet spherical stepper motor," in *Electrical Machines and Systems, 2007. ICEMS. International Conference on*, 2007, pp. 1574–1579.
- [65] Z. Li, "Intelligent control for permanent magnet spherical stepper motor," in *Automation and Logistics, 2008. ICAL 2008. IEEE International Conference on*, 2008, pp. 1807–1812.
- [66] Z. Li and Q. Wang, "Robust neural network controller design for permanent magnet spherical stepper motor," in *Industrial Technology, 2008. ICIT 2008. IEEE International Conference on*, 2008, pp. 1–6.
- [67] Z. Li, "Robust control of pm spherical stepper motor based on neural networks," *Industrial Electronics, IEEE Transactions on*, vol. 56, no. 8, pp. 2945–2954, 2009.
- [68] Y. Öner, "A permanent magnet spherical rotor design and three dimensional static magnetic analysis," *Sensors and Actuators A: Physical*, vol. 137, no. 2, pp. 200 – 208, 2007.
- [69] Z. Li, Y. Wang, and Z. Zhao, "Computation and analysis of a novel spherical actuator based on 3D finite element simulation," *Journal of Information and Computational Science*, vol. 7, no. 12, pp. 2410–2419, 2010.
- [70] M. Rashid and Z. Khalil, "Configuration design and intelligent stepping of a spherical motor in robotic joint," *Journal of Intelligent and Robotic Systems*, vol. 40, no. 2, pp. 165–181, 2004.
- [71] J. Wang, G. Jewell, and D. Howe, "Analysis, design and control of a novel spherical permanent-magnet actuator," *Electric Power Applications, IEE Proceedings -*, vol. 145, no. 1, pp. 61–71, 1998.
- [72] J. Wang, W. Wang, G. Jewell, and D. Howe, "A novel spherical permanent magnet actuator with three degrees-of-freedom," *Magnetics, IEEE Transactions on*, vol. 34, no. 4, pp. 2078–2080, 1998.

- [73] B. Ackermann, H. Steinbusch, T. Vollmer, J. Wang, G. Jewell, and D. Howe, "A spherical permanent magnet actuator for a high-fidelity force-feedback joystick," *Mechatronics*, vol. 14, no. 3, pp. 327 – 339, 2004.
- [74] K. Kahlen, I. Voss, C. Priebe, and R. De Doncker, "Torque control of a spherical machine with variable pole pitch," *Power Electronics, IEEE Transactions on*, vol. 19, no. 6, pp. 1628–1634, 2004.
- [75] C. Xia, H. Li, and T. Shi, "3-d magnetic field and torque analysis of a novel halbach array permanent-magnet spherical motor," *Magnetics, IEEE Transactions on*, vol. 44, no. 8, pp. 2016–2020, 2008.
- [76] C. Xia, J. Xin, H. Li, and T. Shi, "Design and analysis of a variable arc permanent magnet array for spherical motor," *Magnetics, IEEE Transactions on*, vol. 49, no. 4, pp. 1470–1478, 2013.
- [77] W. Chen, L. Zhang, L. Yan, and J. Liu, "Design and control of a three degree-of-freedom permanent magnet spherical actuator," *Sensors and Actuators A: Physical*, vol. 180, no. 0, pp. 75 – 86, 2012.
- [78] G. Jinjun, D.-H. Kim, and H. Son, "Effects of magnetic pole design on orientation torque for a spherical motor," *Mechatronics, IEEE/ASME Transactions on*, vol. 18, no. 4, pp. 1420–1425, 2013.
- [79] T. Yano, Y. Kubota, T. Shikayama, and T. Suzuki, "Basic characteristics of a multi-pole spherical synchronous motor," in *Micro-NanoMechatronics and Human Science, 2007. MHS '07. International Symposium on*, 2007, pp. 383–388.
- [80] T. Yano, "Development of a high torque spherical motor (2nd report: Proposal of a hexahedron-octahedron based spherical stepping motor)," in *Electrical Machines, 2008. ICEM 2008. 18th International Conference on*, 2008, pp. 1–6.
- [81] T. Yano, "Design of a hexahedron-octahedron based spherical stepping motor," in *Micro-NanoMechatronics and Human Science, 2008. MHS 2008. International Symposium on*, 2008, pp. 519–524.
- [82] T. Yano, "Simulation results of a hexahedron-octahedron based spherical stepping motor," *Journal of Mechanical Science and Technology*, vol. 24, no. 1, pp. 33–36, 2010.
- [83] T. Yano, "Proposal of polyhedron based spherical stepping motors," in *Power Electronics, Electrical Drives, Automation and Motion, 2008. SPEEDAM 2008. International Symposium on*, 2008, pp. 1433–1438.
- [84] Y. Um, T. Yano, and B. Hur, "3 axes rotational and frequency characteristics of a hexahedron-octahedron based spherical stepping motor," in *Micro-NanoMechatronics and Human Science, 2009. MHS 2009. International Symposium on*, 2009, pp. 27–32.

Bibliography

- [85] A. Gofuku, R. Sasaki, T. Yano, and M. Shibata, “Basic experimental results of a 14-12 spherical motor,” in *Power Electronics, Electrical Drives, Automation and Motion (SPEEDAM), 2012 International Symposium on*, 2012, pp. 832–836.
- [86] A. Gofuku, R. Sasaki, T. Yano, Y. Wada, and M. Shibata, “Development of a spherical stepping motor rotating around six axes,” *International Journal of Applied Electromagnetics and Mechanics*, vol. 39, pp. 905–911, 2012.
- [87] A. Boletis, “High speed micromotor on a three axis active magnetic bearing,” Ph.D. dissertation, Ecole Polytechnique Fédérale de Lausanne (EPFL), 2004.
- [88] B. Van Ninhuijs, T. E. Motoasca, and E. A. Lomonova, “Accurate analytical computation of magnetic flux density of spherical permanent magnet arrays,” in *Electrical Machines (ICEM), 2012 XXth International Conference on*, 2012, pp. 2746–2751.
- [89] B. van Ninhuijs, T. Motoasca, B. Gysen, and E. Lomonova, “Modeling of spherical magnet arrays using the magnetic charge model,” *Magnetics, IEEE Transactions on*, vol. 49, no. 7, pp. 4109–4112, 2013.
- [90] E. Onillon, O. Chételat, L. Rossini, L. Lisowski, S. Droz, and J. Moerschell, “Reaction sphere for attitude control,” in *Proceedings of the 13th European Space Mechanisms and Tribology Symposium (ESMATS 2009)*, Vienna, Austria, 2009.
- [91] O. Chételat, “Study of a reaction sphere for attitude control (sphere) - reaction sphere design,” CSEM CH-2002 Neuchâtel, Tech. Rep. SPH.CSE.TN2.iss6, 2009.
- [92] H. Bleuler, M. Cole, P. Keogh, R. Larsonneur, E. Malsen, R. Nordmann, Y. Okada, G. Schweitzer, and A. Traxler, *Magnetic Bearings: Theory, Design, and Application to Rotating Machinery*, G. Schweitzer and E. H. Malsen, Eds. Springer, 2011.
- [93] L. Yan, I.-M. Chen, C. K. Lim, G. Yang, W. Lin, and K.-M. Lee, “Experimental investigation on the magnetic field of a permanent magnet spherical actuator,” in *Advanced Intelligent Mechatronics. Proceedings, 2005 IEEE/ASME International Conference on*, 2005, pp. 347–352.
- [94] L. Yan, I.-M. Chen, C. K. Lim, G. Yang, W. Lin, and K.-M. Lee, “Torque modeling of a spherical actuator based on lorentz force law,” in *Robotics and Automation, 2005. ICRA 2005. Proceedings of the 2005 IEEE International Conference on*, 2005, pp. 3646–3651.
- [95] H. Li, C. Xia, P. Song, and T. Shi, “Magnetic field analysis of a halbach array PM spherical motor,” in *Automation and Logistics, 2007 IEEE International Conference on*, 2007, pp. 2019–2023.
- [96] H. Li, C. Xia, and T. Shi, “Spherical harmonic analysis of a novel halbach array pm spherical motor,” in *Robotics and Biomimetics, 2007. ROBIO 2007. IEEE International Conference on*, 2007, pp. 2085–2089.

-
- [97] J. Wang, G. Jewell, and D. Howe, “Modelling of a novel spherical permanent magnet actuator,” in *Robotics and Automation, 1997. Proceedings., 1997 IEEE International Conference on*, vol. 2, 1997, pp. 1190–1195 vol.2.
- [98] H. Son and K.-M. Lee, “Distributed multipole models for design and control of pm actuators and sensors,” *Mechatronics, IEEE/ASME Transactions on*, vol. 13, no. 2, pp. 228–238, 2008.
- [99] H. Son and K.-M. Lee, “Two-DOF magnetic orientation sensor using distributed multipole models for spherical wheel motor,” *Mechatronics*, vol. 21, no. 1, pp. 156 – 165, 2011.
- [100] K.-M. Lee and H. Son, “Distributed multipole model for design of permanent-magnet-based actuators,” *Magnetics, IEEE Transactions on*, vol. 43, no. 10, pp. 3904–3913, 2007.
- [101] K.-M. Lee, J. Lim, and K. Bai, “Magnetic dipoles for electromagnetic multi-DOF actuator design,” in *Robotics and Automation, 2009. ICRA '09. IEEE International Conference on*, 2009, pp. 3335–3340.
- [102] H. Son, K. Bai, J. Lim, and K.-M. Lee, “Design of multi-DOF electromagnetic actuators using distributed multipole models and image method,” *International Journal of Applied Electromagnetics and Mechanics*, vol. 34, no. 3, pp. 195–210, 2010.
- [103] B. Li, G.-D. Li, and H.-F. Li, “Magnetic field analysis of 3-DOF permanent magnetic spherical motor using magnetic equivalent circuit method,” *Magnetics, IEEE Transactions on*, vol. 47, no. 8, pp. 2127–2133, 2011.
- [104] H. Kim, H. Kim, and D. Gweon, “Magnetic field analysis of a VCM spherical actuator,” *Sensors and Actuators A: Physical*, vol. 195, no. 0, pp. 38 – 49, 2013.
- [105] H. Kim, H. Kim, D. Ahn, and D. Gweon, “Design of a new type of spherical voice coil actuator,” *Sensors and Actuators A: Physical*, vol. 203, no. 0, pp. 181 – 188, 2013.
- [106] E. P. Furlani, *Permanent Magnet and Electromechanical Devices: Materials, Analysis and Applications*. San Diego: Academic Press, 2001.
- [107] L. Yan, F. Liang, M. Yuan, H. Hu, C.-Y. Chen, and I.-M. Chen, “Analysis of novel three-dimensional pole arrays for electromagnetic spherical actuators,” in *Advanced Intelligent Mechatronics (AIM), 2013 IEEE/ASME International Conference on*, 2013, pp. 780–785.
- [108] M. Tsukano, Y. Sakaidani, K. Hirata, N. Niguchi, S. Maeda, and A. Zaini, “Analysis of 2-degree of freedom outer rotor spherical actuator employing 3-D finite element method,” *Magnetics, IEEE Transactions on*, vol. 49, no. 5, pp. 2233–2236, 2013.

Bibliography

- [109] J. Wang, G. Jewell, and D. Howe, "A novel spherical actuator: design and control," *Magnetics, IEEE Transactions on*, vol. 33, no. 5, pp. 4209–4211, 1997.
- [110] L. Hu, K.-M. Lee, and X. Fu, "A method based on measured boundary conditions for reconstructing the magnetic field distribution of an electromagnetic mechatronic system," *Mechatronics, IEEE/ASME Transactions on*, vol. 15, no. 4, pp. 595–602, 2010.
- [111] L. Hu, K.-M. Lee, and X. Fu, "Analytical torque model for a permanent magnet spherical motor using magnetic field reconstruction from measured boundary conditions," in *Advanced Intelligent Mechatronics (AIM), 2013 IEEE/ASME International Conference on*, 2013, pp. 762–767.
- [112] J. Healy, D.M., D. Rockmore, P. Kostelec, and S. Moore, "Ffts for the 2-sphere-improvements and variations," *Journal of Fourier Analysis and Applications*, vol. 9, no. 4, pp. 341–385, 2003.
- [113] H.-J. Weber and G. B. Arfken, *Essential Mathematical Methods for Physicists*, 5th ed. Academic Press, 2004.
- [114] K.-M. Lee, H. Son, and J. K. Park, "Design analysis of a spherical magnetic bearing for multi-DOF rotational stage applications," in *International Manufacturing Science And Engineering Conference (MSEC) 2007*, Atlanta, Georgia, USA, October 2007.
- [115] J. Wang, G. Jewell, and D. Howe, "Analysis of a spherical permanent magnet actuator," *Journal of Applied Physics*, vol. 81, no. 8, pp. 4266–4268, 1997.
- [116] J. Wang, K. Mitchell, G. Jewell, and D. Howe, "Multi-degree-of-freedom spherical permanent magnet motors," in *Robotics and Automation, 2001. Proceedings 2001 ICRA. IEEE International Conference on*, vol. 2, 2001, pp. 1798–1805 vol.2.
- [117] L. Yan, I.-M. Chen, C. K. Lim, G. Yang, W. Lin, and K.-M. Lee, "Torque modeling and analysis of spherical actuators with iron stator," in *Robotics and Automation, 2009. ICRA '09. IEEE International Conference on*, 2009, pp. 164–169.
- [118] K. Bai and K.-M. Lee, "Magnetic field model for direct field-feedback control of a permanent magnet spherical motor," in *Advanced Intelligent Mechatronics (AIM), 2013 IEEE/ASME International Conference on*, 2013, pp. 768–773.
- [119] L. Yan, I.-M. Chen, Z. Guo, Y. Lang, and Y. Li, "A three degree-of-freedom optical orientation measurement method for spherical actuator applications," *Automation Science and Engineering, IEEE Transactions on*, vol. 8, no. 2, pp. 319–326, April 2011.
- [120] W. Fang and H. Son, "Optimization of measuring magnetic fields for position and orientation tracking," *Mechatronics, IEEE/ASME Transactions on*, vol. 16, no. 3, pp. 440–448, June 2011.

- [121] S. Foong, K.-M. Lee, and K. Bai, "Magnetic field-based sensing method for spherical joint," in *Robotics and Automation (ICRA), 2010 IEEE International Conference on*, May 2010, pp. 5447–5452.
- [122] L. Rossini, O. Chélat, E. Onillon, and Y. Perriard, "Force and torque analytical models of a reaction sphere actuator based on spherical harmonic rotation and decomposition," *Mechatronics, IEEE/ASME Transactions on*, vol. 18, no. 3, pp. 1006–1018, 2013.
- [123] G. Burel and H. Henocq, "Determination of the orientation of 3D objects using spherical harmonics." *CVGIP: Graphical Model and Image Processing*, vol. 57, no. 5, pp. 400–408, 1995.
- [124] D. W. Ritchie and G. J. L. Kemp, "Fast computation, rotation, and comparison of low resolution spherical harmonic molecular surfaces," *Journal of Computational Chemistry*, vol. 20, no. 4, pp. 383–395, 1999.
- [125] B. Yeo, "Computing spherical transform and convolution on the 2-sphere," 2005, accessed: 2014-01-15. [Online]. Available: <http://people.csail.mit.edu/ythomas/unpublished/6869.pdf>
- [126] R. Hoover, A. Maciejewski, and R. Roberts, "Eigendecomposition of images correlated on S^1 , S^2 , and $SO(3)$ using spectral theory," *Image Processing, IEEE Transactions on*, vol. 18, no. 11, pp. 2562–2571, 2009.
- [127] C. Brechbühler, G. Gerig, and O. Kübler, "Parametrization of closed surfaces for 3-D shape description," *Computer Vision and Image Understanding*, vol. 61, no. 2, pp. 154 – 170, 1995.
- [128] S. Taulu and M. Kajola, "Presentation of electromagnetic multichannel data: The signal space separation method," *Journal of Applied Physics*, vol. 97, no. 12, pp. –, 2005.
- [129] L. Rouve, L. Schmerber, O. Chadebec, and A. Foggia, "Optimal magnetic sensor location for spherical harmonic identification applied to radiated electrical devices," *Magnetics, IEEE Transactions on*, vol. 42, no. 4, pp. 1167–1170, 2006.
- [130] M. Chung, K. Dalton, L. Shen, A. Evans, and R. Davidson, "Weighted Fourier series representation and its application to quantifying the amount of gray matter," *Medical Imaging, IEEE Transactions on*, vol. 26, no. 4, pp. 566–581, 2007.
- [131] A. B. Abdallah, F. Ghorbel, K. Chatti, H. Essabbah, and M. Bedoui, "A new uniform parameterization and invariant 3D spherical harmonic shape descriptors for shape analysis of the heart's left ventricle – a pilot study," *Pattern Recognition Letters*, vol. 31, no. 13, pp. 1981 – 1990, 2010.

Bibliography

- [132] S. Padula, R. Kincaid, and L. R. Center, “Optimization strategies for sensor and actuator placement,” Tech. Rep., 1999.
- [133] S. Lau, R. Eichardt, L. Di Rienzo, and J. Haueisen, “Tabu search optimization of magnetic sensor systems for magnetocardiography,” *Magnetics, IEEE Transactions on*, vol. 44, no. 6, pp. 1442–1445, 2008.
- [134] S. Borguet and O. Léonard, “The Fisher information matrix as a relevant tool for sensor selection in engine health monitoring,” *International Journal of Rotating Machinery*, vol. 2008, 2008.
- [135] D. Uciński, *Optimal measurement methods for distributed parameter system identification*, ser. Taylor & Francis systems and control book series. CRC Press, 2005.
- [136] B. Siciliano and O. Khatib, Eds., *Springer Handbook of Robotics*. Berlin, Heidelberg: Springer, 2008.
- [137] D. C. Kammer and L. Yao, “Enhancement of on-orbit modal identification of large space structures through sensor placement,” *Journal of Sound and Vibration*, vol. 171, no. 1, pp. 119–139, 1994.
- [138] A. Bicchi and G. Canepa, “Optimal design of multivariate sensors,” *Meas. Sci. Technol.*, vol. 5, pp. 319–332, 1994.
- [139] G. H. Golub and C. F. Van Loan, *Matrix Computations*, 3rd ed. Baltimore, MD: John Hopkins University Press, 1996.
- [140] S. Kay, *Fundamentals of Statistical Signal Processing: Estimation theory*, ser. Prentice Hall signal processing series. Prentice-Hall PTR, 1993.
- [141] R. Eichardt and J. Haueisen, “Influence of sensor variations on the condition of the magnetostatic linear inverse problem,” *Magnetics, IEEE Transactions on*, vol. 46, no. 8, pp. 3449–3452, 2010.
- [142] A. C. A. Cintrón-Arias, H. T. Banks and A. L. Lloyd, “A sensitivity matrix based methodology for inverse problem formulation,” *Journal of Inverse and Ill-Posed Problems*, vol. 17, p. 545 – 564, 2009.
- [143] D. Lee and S. Velinsky, “Analysis and experimental verification of a three-dimensional noncontacting angular motion sensor,” *Mechatronics, IEEE/ASME Transactions on*, vol. 12, no. 6, pp. 612–622, Dec 2007.
- [144] J. L. Crassidis, F. L. Markley, and Y. Cheng, “Survey of nonlinear attitude estimation methods,” *Journal of Guidance, Control, and Dynamics*, vol. 30, no. 1, pp. 12–28, 2007.

-
- [145] J. M. Benet, “Swisscube attitude determination algorithm design and validation,” Master’s thesis, Ecole Polytechnique Fédérale de Lausanne, 2007.
- [146] O. Scaglione, M. Markovic, and Y. Perriard, “On-line parameter estimation for improved sensorless control of synchronous motors,” in *Electrical Machines (ICEM), 2012 XXth International Conference on*, Sept 2012, pp. 2229–2237.
- [147] X. Yun and E. Bachmann, “Design, implementation, and experimental results of a quaternion-based kalman filter for human body motion tracking,” *Robotics, IEEE Transactions on*, vol. 22, no. 6, pp. 1216–1227, Dec 2006.
- [148] A. Sabatini, “Quaternion-based extended Kalman filter for determining orientation by inertial and magnetic sensing,” *Biomedical Engineering, IEEE Transactions on*, vol. 53, no. 7, pp. 1346–1356, July 2006.
- [149] J. R. Taylor, *Classical Mechanics*. University Science Books, 2005.
- [150] N. Chaturvedi, A. Sanyal, and N. McClamroch, “Rigid-body attitude control,” *Control Systems, IEEE*, vol. 31, no. 3, pp. 30–51, 2011.
- [151] H. Schaub and J. Junkins, *Analytical Mechanics of Space Systems (AIAA Education Series)*, 2nd ed. AIAA, 2009.
- [152] T. Overboom, “Design and optimization of a rotary actuator for a two degree-of-freedom $z\phi$ -module,” Master’s thesis, Technische Univeristeit Eindhoven, 2009.
- [153] L. Rossini, O. Chételat, E. Onillon, and Y. Perriard, “An open-loop control strategy of a reaction sphere for satellite attitude control,” in *Electrical Machines and Systems (ICEMS), 2011 International Conference on*, Aug 2011, pp. 1–4.
- [154] F. Barrot, “Acceleration and inclination sensors based on magnetic levitation. application in the particular case of structural health monitoring in civil engineering.” Ph.D. dissertation, Ecole Polytechnique Fédérale de Lausanne (EPFL), 2008.
- [155] P. Berkelman and M. Dzadovsky, “Magnetic levitation over large translation and rotation ranges in all directions,” *Mechatronics, IEEE/ASME Transactions on*, vol. 18, no. 1, pp. 44–52, Feb 2013.
- [156] S. Balemi and R. Bucher, “Lecture notes for course “progettazione di controllori”,” 2002, University of Applied Sciences of Southern Sitzerland.
- [157] G. F. Franklin, D. J. Powell, and A. Emami-Naeini, *Feedback Control of Dynamic Systems*, 3rd ed. Upper Saddle River, NJ, USA: Prentice Hall PTR, 1995.
- [158] M. Strumik, R. Wawrzaszek, M. Banaszkiwicz, K. Seweryn, M. Sidz, E. Onillon, and L. Rossini, “Analytical model of eddy currents in a reaction sphere actuator,” *Magnetics, IEEE Transactions on*, vol. PP, no. 99, pp. 1–1, 2014.

Bibliography

- [159] L. Rossini, E. Onillon, O. Chételat, and Y. Perriard, “Hybrid fem-analytical force and torque models of a reaction sphere actuator,” in *Electric Machines Drives Conference (IEMDC), 2013 IEEE International*, May 2013, pp. 694–700.
- [160] L. Rossini, E. Onillon, O. Chételat, and Y. Perriard, “An optimal sensor placement strategy for force and torque analytical models of a reaction sphere actuator for satellite attitude control,” in *Electrical Machines (ICEM), 2012 XXth International Conference on*, Sept 2012, pp. 2545–2551.
- [161] M. Markovic and Y. Perriard, “Simplified design methodology for a slotless brushless dc motor,” *Magnetics, IEEE Transactions on*, vol. 42, no. 12, pp. 3842–3846, Dec 2006.
- [162] L. Rossini, E. Onillon, O. Chételat, and Y. Perriard, “Back-emf and rotor angular velocity estimation for a reaction sphere actuator,” in *Advanced Intelligent Mechatronics (AIM), 2014 IEEE/ASME International Conference on*, Accepted.
- [163] L. Rossini, S. Mingard, A. Boletis, E. Forzani, E. Onillon, and Y. Perriard, “Rotor design optimization for a reaction sphere actuator,” in *Electrical Machines and Systems (ICEMS), 2012 15th International Conference on*, Oct 2012, pp. 1–6.
- [164] L. Rossini, S. Mingard, A. Boletis, E. Forzani, E. Onillon, and Y. Perriard, “Rotor design optimization for a reaction sphere actuator,” *Industry Applications, IEEE Transactions on*, vol. PP, no. 99, pp. 1–1, 2013.
- [165] L. Rossini, E. Onillon, O. Chételat, and Y. Perriard, “Closed-loop magnetic bearing and angular velocity control of a reaction sphere actuator,” *Mechatronics, IEEE/ASME Transactions on*, Under review.
- [166] L. Rossini, E. Onillon, and O. Chételat, “Electromagnetic force and torque simulations on a reaction sphere laboratory prototype.” Presented at COMSOL Conference, Stuttgart, Germany, 2011.
- [167] M. Sidz, R. Wawrzaszek, K. Seweryn, M. Strumik, A. Boletis, S. Mingard, L. Rossini, and E. Onillon, “Optimization of a rotor shape for spherical actuator with magnetically levitating rotor to match octupole field distribution.” Presented at COMSOL Conference, Rotterdam, The Netherlands, 2013.
- [168] W. Jarosz, “Efficient monte carlo methods for light transport in scattering media,” Ph.D. dissertation, UC San Diego, La Jolla, CA, USA, Sep. 2008.
- [169] P.-P. Sloan, “Stupid spherical harmonics (SH) tricks,” 2008.
- [170] W. Wilcox, *Quantum Principles and Particles*. CRC Press, 2012.
- [171] G. Backus, R. Parker, and C. Constable, *Foundations of Geomagnetism*. Cambridge University Press, 2005.

-
- [172] R. Green, "Spherical Harmonic Lighting: The Gritty Details," Mar. 2003. [Online]. Available: <http://www.research.scea.com/gdc2003/spherical-harmonic-lighting.pdf>
- [173] A. Makadia and K. Daniilidis, "Direct 3D-rotation estimation from spherical images via a generalized shift theorem," in *Computer Vision and Pattern Recognition, 2003. Proceedings. 2003 IEEE Computer Society Conference on*, vol. 2, 2003, pp. II-217–24 vol.2.
- [174] R. Hoover, A. Maciejewski, and R. Roberts, "Pose detection of 3-D objects using images sampled on $SO(3)$, spherical harmonics, and wigner-d matrices," in *Automation Science and Engineering, 2008. CASE 2008. IEEE International Conference on*, 2008, pp. 47–52.
- [175] M. Kazhdan, T. Funkhouser, and S. Rusinkiewicz, "Rotation invariant spherical harmonic representation of 3D shape descriptors," in *Proceedings of the 2003 Eurographics/ACM SIGGRAPH Symposium on Geometry Processing*, ser. SGP '03. Aire-la-Ville, Switzerland, Switzerland: Eurographics Association, 2003, pp. 156–164.
- [176] H. Huang, L. Shen, R. Zhang, F. Makedon, A. Saykin, and J. Pearlman, "A novel surface registration algorithm with biomedical modeling applications," *Information Technology in Biomedicine, IEEE Transactions on*, vol. 11, no. 4, pp. 474–482, 2007.
- [177] J. L. Dillenseger, H. Guillaume, and J. J. Patard, "Spherical harmonics based intra-subject 3-D kidney modeling/registration technique applied on partial information," *Biomedical Engineering, IEEE Transactions on*, vol. 53, no. 11, pp. 2185–2193, 2006.
- [178] G. Gerig, M. Styner, D. Jones, D. Weinberger, and J. Lieberman, "Shape analysis of brain ventricles using spharm," in *Mathematical Methods in Biomedical Image Analysis, 2001. MMBIA 2001. IEEE Workshop on*, 2001, pp. 171–178.
- [179] M. K. Chung, R. Hartley, K. M. Dalton, , and R. J. Davidson, "Encoding cortical surface by spherical harmonics," *Statistica Sinica*, vol. 18, no. 4, pp. 1269–1291, 2008.
- [180] J. D. Jackson, *Classical electrodynamics*, 3rd ed. New York, NY: Wiley, 1999.
- [181] C. Constanda, *Solution Techniques for Elementary Partial Differential Equations*, 2nd ed. CRC Press, 2010.
- [182] L. C. Biedenharn and J. D. Louck, *Angular momentum in quantum physics: theory and application*, ser. Encyclopaedia of mathematics and its applications. Reading, MA: Addison-Wesley, 1981, companion vol. to : The Racah-Wigner algebra in quantum theory. Reading, Mass., Addison-Wesley, 1981.

Bibliography

- [183] S. Boyd, "Lecture notes for EE263 course," 2012, Stanford.

Nomenclature

Acronyms

<i>Symbol</i>	<i>Description</i>
ABS	Acrylonitrile Butadiene Styrene.
AC	Alternating Current.
ADCS	Attitude Determination and Control System.
CAD	Computer-Aided Design.
CMG	Control Moment Gyroscope.
CSEM	Centre Suisse d'Electronique et de Microtechnique.
DC	Direct Current.
DMP	Distributed Multipoles.
DOF	Degree-of-freedom.
EKF	Extended Kalman Filter.
EM	Electro Magnet.
EMF	Electromotive-Force.
EPFL	École Polytechnique Fédérale de Lausanne.
ESA	European Space Agency.
FEA	Finite Element Analysis.
FEM	Finite Element Method.
LAI	Laboratoire d'actionneurs Intégrés.
LNRE	Local Normalized Relative Error.

Bibliography

MEC	Magnetic Equivalent Circuit.
MNRE	Mean Normalized Relative Error.
NdFeB	Neodymium iron boron.
PD	Proportional-Derivative.
PI	Proportional-Integral.
PID	Proportional-Integral-Derivative.
PM	Permanent Magnet.
RMS	Root Mean Square.
RS	Reaction Sphere.
RW	Reaction Wheel.
SWM	Spherical Wheel Motor.
VRSM	Variable Reluctance Spherical Motor.

List of symbols

<i>Symbol</i>	<i>Unit</i>	<i>Description</i>
A		Matrix with spherical harmonics evaluated at magnetic flux density sensor locations.
A_b	m^2	Section of a coil.
α, β, γ	rad	ZYZ Euler angles.
\mathcal{B}		Rotor reference frame.
\mathcal{B}^S		Rotor spherical coordinate system.
\mathbf{B}	T	Magnetic flux density vector.
\mathbf{B}^\perp	T	Vector of Magnetic flux density measurements.
B_{rem}	T	Permanent magnet remanence.
\mathbf{B}_{rem}		Permanent magnet remanence vector.
δ	m	Rotor pole eccentricity.
\mathcal{C}		Coil reference frame.
\mathcal{C}^S		Coil spherical coordinate system.

c		Vector of spherical harmonic coefficients.
c_n^m		Spherical harmonic coefficient of degree n and order m .
$c_{n,imm}^m$		Spherical harmonic coefficient of degree n and order m of immobile rotor.
D		Unitary rotation matrix.
d		Model agreement.
F	N	Force vector.
f		Generic function.
Γ		Parameter set of sensor spherical angular coordinates.
H	A/m	Magnetic field vector.
h	Nms	Angular momentum vector.
H_C	m	Depth of the conical cut.
h	m	Height of the truncated octahedron structure.
H_R	m	Thickness of back-iron.
i	A	Vector of currents.
I		Identity matrix.
\mathbb{I}_n		Set of spherical harmonic degrees n .
J	A/m ²	Current density vector.
J_{rot}	kgm ²	Tensor of inertia of the rotor.
κ		Coefficient of general solution of Laplace's equation.
K_n^m		Normalization factor of degree n and order m .
k_p		Proportionality factor for force and torque experiments.
K_F		Force characteristic matrix.
K_T		Torque characteristic matrix.
Λ_R		Rotation operator.
L_c	H	Electrical inductance of a coil.
m		Spherical harmonic order.

Bibliography

M_F		Pseudoinverse of force characteristic matrix.
m_{rot}	kg	Mass of the rotor.
M_T		Pseudoinverse of torque characteristic matrix.
μ_0	Vs/(Am)	Vacuum permeability.
$\Delta\mu_a, \Delta\mu_b, \Delta\mu_c$	m	Relative position of rotor displacement sensors a , b , and c .
$\mu_a^0, \mu_b^0, \mu_c^0$	m	Calibrated zero of rotor displacement sensors a , b , and c .
μ_{PM}		Relative permeability of permanent magnet.
μ_{R}		Relative permeability of iron.
n		Spherical harmonic degree.
N_{h}		Maximum spherical harmonic degree.
N_{t}		Number of turns of the coil.
N_{m}		Number of magnetic flux density measurements.
ω	rad/s	Angular velocity vector.
$O_{\mathcal{B}}$		Origin rotor reference frame.
$O_{\mathcal{C}}$		Origin coil reference frame.
$O_{\mathcal{S}}$		Origin stator reference frame.
O_{PM}		Center of the permanent magnet with truncated spherical shape.
\mathbf{P}		Normalized coordinate of a stator coil.
P		Spherical harmonic projection matrix.
P_n		Legendre polynomials of degree n and order m .
P_n^m		Associated Legendre polynomials of degree n and order m .
Φ	Wb	Matrix of average magnetic flux.
\mathbf{p}	m	Position of the rotor with respect to the center of the stator.
Ψ	Wb	Magnetic flux.
$\hat{\mathbf{r}}_b, \hat{\boldsymbol{\theta}}_b, \hat{\boldsymbol{\phi}}_b$		Unit vectors rotor spherical coordinate system.
$\hat{\mathbf{r}}_c, \hat{\boldsymbol{\theta}}_c, \hat{\boldsymbol{\phi}}_c$		Unit vectors coil spherical coordinate system.
$\hat{\mathbf{r}}_s, \hat{\boldsymbol{\theta}}_s, \hat{\boldsymbol{\phi}}_s$		Unit vectors stator spherical coordinate system.

R		Rotation matrix.
r, θ, ϕ		Generic spherical coordinates.
R_c	Ω	Electrical resistance of a coil.
r_b, θ_b, ϕ_b		Rotor spherical coordinates.
r_c, θ_c, ϕ_c		Coil spherical coordinates.
r_s, θ_s, ϕ_s		Stator spherical coordinates.
R_1	m	Inner radius of back-iron.
R_2	m	Outer radius of back-iron.
R_3	m	Outer radius of permanent magnet.
R_4	m	Inner radius of stator.
R_5	m	Outer radius of stator.
$R_{C \rightarrow \mathcal{B}}$		Rotation matrix between coil and rotor reference frames.
$R_{C \rightarrow \mathcal{S}}$		Rotation matrix between coil and stator reference frames.
R_{dec}	m	Radius of spherical harmonics decomposition.
R_{in}	m	Inner radius of the coil.
R_{out}	m	Outer radius of the coil.
R_{PM}	m	Radius of permanent magnet with truncated spherical shape.
R_{rot}	m	Radius of the rotor.
$R_{\mathcal{S} \rightarrow \mathcal{B}}$		Rotation matrix between rotor and stator reference frames.
R_{sens}	m	Hall sensor radial location.
\mathcal{S}		Stator reference frame.
\mathcal{S}^S		Stator spherical coordinate system.
σ		Singular value.
ϕ_{pole}	rad	Azimuthal angle relative to a permanent magnet pole.
θ_{pole}	rad	Polar angle relative to a permanent magnet pole.
\mathbf{T}	Nm	Torque vector.
t	s	Time.

Bibliography

θ_{in}	rad	Inner angle of the coil.
θ_{out}	rad	Outer angle of the coil.
T_s	s	Sampling time.
\mathbf{u}_{EMF}	V	Back-EMF voltage vector.
φ_i	Vs/m	Magnetic scalar potential in region i .
V_c	m ³	Volume of a coil.
$\hat{\mathbf{x}}_b, \hat{\mathbf{y}}_b, \hat{\mathbf{z}}_b$		Unit vectors rotor reference frame.
$\hat{\mathbf{x}}_c, \hat{\mathbf{y}}_c, \hat{\mathbf{z}}_c$		Unit vectors coil reference frame.
$\hat{\mathbf{x}}_s, \hat{\mathbf{y}}_s, \hat{\mathbf{z}}_s$		Unit vectors stator reference frame.
ξ		Coefficient of general solution of Laplace's equation.
x_b, y_b, z_b		Rotor cartesian coordinates.
x_c, y_c, z_c		Rotor cartesian coordinates.
x_s, y_s, z_s		Stator cartesian coordinates.
Y_n^m		Spherical harmonic function of degree n and order m .

Mathematical operators

<i>Symbol</i>	<i>Description</i>
$\text{Im}(\cdot)$	Imaginary part operator.
$\kappa_2(\cdot)$	2-norm condition number.
$\nabla(\cdot)$	Gradient operator.
$\nabla^2(\cdot)$	Laplace operator.
$\nabla \times (\cdot)$	Curl operator.
$\nabla \cdot (\cdot)$	Divergence operator.
$(\cdot)^+$	Pseudoinverse matrix.
$\text{Re}(\cdot)$	Real part operator.

Curriculum Vitae

Leopoldo Rossini

I Runch di Guèra 6
6528 Camorino, Switzerland
✉ leopoldo.rossini@alumni.epfl.ch
Swiss citizen. Born on December 12, 1980

Work Experience

- 2010–2014 **Ph.D. Student**, CSEM SA, Neuchâtel, Switzerland.
- 2007–2010 **R&D Engineer**, CSEM SA, Neuchâtel, Switzerland.
 - 2006 **Summer Internship**, Contraves Space AG, Zürich, Switzerland.
- 2005–2006 **Research Assistant**, Purdue University, West Lafayette, United States.
 - 2005 **Research Assistant**, Institute for Solar Research, Locarno, Switzerland.
- 2003–2004 **Research Assistant**, University of Applied Sciences of Southern Switzerland, Manno, Switzerland.
- 1996–2000 **Electronic Apprentice**, Invertomatic Technology SA, Riazzino, Switzerland.

Education

- 2010–2014 **Ph.D. Student**, Ecole Polytechnique Fédérale de Lausanne, Lausanne, Switzerland.
Laboratory of Integrated Actuators (LAI).
- 2005–2007 **Master of Science in Electrical and Computer Engineering**, Purdue University, West Lafayette, United States.
- 2000–2003 **Bachelor of Science in Electrical Engineering**, University of Applied Sciences of Southern Switzerland, Manno, Switzerland.

Publications

Journal Articles

- L. Rossini, E. Onillon, O. Chételat, and Y. Perriard, "Closed-loop magnetic bearing and angular velocity control of a reaction sphere actuator," *Mechatronics, IEEE/ASME Transactions on*, Submitted.
- M. Strumik, R. Wawrzaszek, M. Banaszkiwicz, K. Seweryn, M. Sidz, E. Onillon, and L. Rossini, "Analytical model of eddy currents in a reaction sphere actuator," *Magnetics, IEEE Transactions on*, vol. 50, no. 6, pp. 1–7, June 2014.
- L. Rossini, S. Mingard, A. Boletis, E. Forzani, E. Onillon, and Y. Perriard, "Rotor design optimization for a reaction sphere actuator," *Industry Applications, IEEE Transactions on*, vol. 50, no. 3, pp. 1706–1716, May 2014.
- L. Rossini, O. Chételat, E. Onillon, and Y. Perriard, "Force and torque analytical models of a reaction sphere actuator based on spherical harmonic rotation and decomposition," *Mechatronics, IEEE/ASME Transactions on*, vol. 18, no. 3, pp. 1006–1018, 2013.

Conference Publications

- L. Rossini, E. Onillon, O. Chételat, and Y. Perriard, "Back-EMF and rotor angular velocity estimation for a reaction sphere actuator," in *Advanced Intelligent Mechatronics (AIM), 2014 IEEE/ASME International Conference on*, Accepted.
- L. Rossini, E. Onillon, O. Chételat, and Y. Perriard, "Hybrid FEM-analytical force and torque models of a reaction sphere actuator," in *Electric Machines Drives Conference (IEMDC), 2013 IEEE International*, May 2013, pp. 694–700.

- L. Rossini, E. Onillon, O. Chételat, and Y. Perriard, "An optimal sensor placement strategy for force and torque analytical models of a reaction sphere actuator for satellite attitude control," in *Electrical Machines (ICEM), 2012 XXth International Conference on*, Sept 2012, pp. 2545–2551.
- L. Rossini, S. Mingard, A. Boletis, E. Forzani, E. Onillon, and Y. Perriard, "Rotor design optimization for a reaction sphere actuator," in *Electrical Machines and Systems (ICEMS), 2012 15th International Conference on*, Oct 2012, pp. 1–6.
- L. Rossini, O. Chételat, E. Onillon, and Y. Perriard, "An open-loop control strategy of a reaction sphere for satellite attitude control," in *Electrical Machines and Systems (ICEMS), 2011 International Conference on*, Aug 2011, pp. 1–4.
- L. Rossini, O. Chételat, E. Onillon, and Y. Perriard, "Analytical and experimental investigation on the force and torque of a reaction sphere for satellite attitude control," in *Advanced Intelligent Mechatronics (AIM), 2011 IEEE/ASME International Conference on*, July 2011, pp. 487–492.
- R. Ramelli, R. Bucher, L. Rossini, M. Bianda, and S. Balemi, "Adaptive optics system for the IRSOL solar observatory," in *Proc. SPIE*, vol. 7736, 2010, pp. 77 363K–77 363K–9.
- E. Onillon, O. Chételat, L. Rossini, L. Lisowski, S. Droz, and J. Moerschell, "Reaction sphere for attitude control," in *Proc. of the European Space Mechanisms and Tribology Symposium (ESMATS)*, Sept 2009.
- M. Bertschi and L. Rossini, "Wrist-worn fall detection device - development and preliminary evaluation." in *BIODEVICES*. INSTICC Press, 2009, pp. 368–371.
- L. Rossini, R. Vetter, C. Verjus, P. Theurillat, P. Renevey, M. Bertschi, and J. Krauss, "Robust ear located heart rate monitor." in *BIODEVICES*. INSTICC Press, 2009, pp. 214–219.
- R. Vetter, L. Rossini, A. Ridolfi, J. Sola, O. Chételat, M. Correvon, and J. Krauss, "Frequency domain SpO₂ estimation based on multichannel photoplethysmographic measurements at the sternum," in *World Congress on Medical Physics and Biomedical Engineering*, ser. IFMBE Proceedings, vol. 25/4, Sept 2009, pp. 326–329.